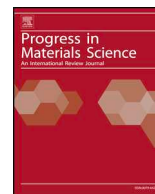




Contents lists available at ScienceDirect

Progress in Materials Science

journal homepage: www.elsevier.com/locate/pmatsci

Functionalized graphene and targeted applications – Highlighting the road from chemistry to applications



Anastasios Stergiou^{a,*}, Rubén Cantón-Vitoria^a, Maria N. Psarrou^b,
Solon P. Economopoulos^{b,*}, Nikos Tagmatarchis^{a,*}

^a Theoretical and Physical Chemistry Institute, National Hellenic Research Foundation, 48 Vassileos Constantinou Avenue, Athens 11635, Greece

^b Department of Chemistry, Norwegian University of Science and Technology (NTNU), NO-7491 Trondheim, Norway

ABSTRACT

Chemical functionalization of graphene aims at tailoring its properties and to promote its use in an array of different application fields through the attachment of different functional groups. In this review, we attempt to detail the major synthetic routes that are employed for the covalent functionalization of graphene. Additionally, we aim to present the different applications that chemically-tailored graphene has shown potential uses such as in optoelectronics, photocatalysis and nanomedicine alongside the performance of the hybrid materials in said fields. We aspire that the interested readers will find, not only, the general synthetic rules towards functionalization of graphene nanoparticles but, more importantly, guidance and inspiration on the trends for the specific choice of organic addends towards applications of interest.

1. Introduction

Graphene is defined by the IUPAC as a single carbon layer of graphite, analogous to a polycyclic aromatic hydrocarbon of quasi infinite size [1]. The atomic layer is formed by sp^2 -hybridized carbons arranged in a honeycomb structure, with a C-C distance of 0.142 nm. However, this definition is frequently expanded to include graphene nanoparticles with multiple layers, typically up to 10. Similarly, a large sheet of graphene is often comprised of small (tens of nanometers) fragments of single or few-layered graphene joined together at the grain boundaries that may include a certain number of heteroatoms, sp^3 carbon atoms and/or physical holes in the structure.

Graphene is produced by employing a variety of methods. These methods differ in both the quality of the graphene sheets produced as well as the amount. As with many other materials, the synthetic approaches for graphene can generally be divided into two main categories, the bottom-up and the top-down. The bottom-up approach includes methods such as classical organic synthesis [2–5], chemical vapour deposition (CVD) [6] and epitaxial growth [7,8]. The top-down approach, on the other hand, houses micro-mechanical [9], liquid [10,11] and electrochemical [12] exfoliation and the reduction of graphene oxide [13]. We could not omit from these two major categories, the production of graphene nanoribbons through the unzipping of carbon nanotubes (CNTs) [14,15]. From a chemist's standpoint, some methods appear significantly more attractive than others. The bottom-up classical organic synthetic approach stresses the chemical ingenuity, forcing the researcher to come up with efficient ways to synthesize polyaromatic compounds, mimicking the continuous planar graphitic backbone. On the other hand, the liquid and electrochemical exfoliation along with the production of graphene oxide, of course, offers chemists significant amounts of starting material as a blank canvas to decorate and functionalize graphene towards hybrid materials. So far, the two methods that seem to show the most promise towards commercialization, are CVD for high quality single-layer and liquid exfoliation for high volume/low-cost production [16].

The mechanical properties of graphene have been extensively studied. Exhibiting a tensile strength measured at 130 GPa, a

* Corresponding authors.

E-mail addresses: astergiou@eie.gr (A. Stergiou), solon.oikonomopoulos@ntnu.no (S.P. Economopoulos), tagmatar@eie.gr (N. Tagmatarchis).

Young's modulus of 1.0 TPa, while possessing a (hypothetical) density of 0.77 mg/m², graphene becomes extremely attractive as a reinforcing agent [17,18]. The pristine material is practically transparent absorbing, on average, 2.3% of all incident light [19]. The charge-transport in graphene has been reported to be as high as 200000 cm²/V s [20–22], but this value is strongly dependent on the number of layers and defects present.

Although graphene's application range is remarkable, researchers are still actively working on the origin and understanding of this material's properties as well as the link between these and the ripples that a single graphene sheet inherently possesses [23–25]. Properties such as ballistic charge transport [26] have been studied for "limited" models such as graphene nanoribbons [27]. Gu and coworkers showed that the material enters a "ballistic-state" regime as the length of the nanoribbons increases [28], while Ackerman studied the Brownian motion of free-standing graphene sheets and suggested that this interaction of carbon molecules with their environment, that potentially causes the concave-convex ripple effect, could be harnessed into producing a limitless source of electricity [29].

The chemistry of graphene and the covalent decoration of the graphene lattice with organic species is a continuously growing field creating an inter-disciplinary space of knowledge exchange. Evidently, a series of reviews have been published in the last decade meeting the demand for an up-to-date overview of the efforts taking place [30–49]. Given the constant evolution in the graphene arena, which is accompanied by the development of a series of doped-analogues, it is appropriate and timely to expand and update, in the form of a new review article, the progress achieved. Considering that graphene can find uses in diverse areas ranging from energy to biomedical related, the exploration of new hybrid materials that will enable breakthroughs is increasingly attractive. Among the different synthetic routes that enable production, solubilization and functionalization, the research community strives for the realization of novel materials that will bring graphene closer to applications. However, the members of graphene nanomaterials, that include single- and multilayer graphene, graphene oxide, chemical/thermal reduced graphene oxide and graphene quantum dots, possess different physicochemical properties owing to their defect composition, different surface chemistry and different electrical and mechanical properties. These aspects are what make this family of materials ideal for a vast number of applications but can also prove chaotic to a researcher trying to explore its possibilities. Our perspective, is to collectively present the chemistry of graphene and its variables (graphene oxide, N-doped graphene, S-doped graphene, fluorographene etc) and the application of such functionalized graphenes in (opto)electronics, nanomedicine and environmental applications.

2. Preparing graphene sheets for real applications – An ongoing challenge

For a material that can be synthesized from so many fundamentally different methods, it is expected that each of these come with advantages and drawbacks. Micromechanical exfoliation does produce high quality single-layer graphene, however, the nanoparticle size is limited e.g. to the parent graphite flake from whence it was exfoliated. Moreover, this method is not easily scalable, although researchers have been working towards overcoming this obstacle [9]. Similarly, CVD and epitaxial approaches produce very high quality graphene sheets. The keys to the success of these methods lie in the catalyst used, the purity of the carbon source and the conditions in the production chamber (pressure, temperature etc). Tour and coworkers proposed a CVD-based approach, where a virtually "infinite" variety of carbon sources can be used to produce equally high-quality material [50,51]. In the case of CVD, the area of the graphene produced is "limited" by the area of the catalyst on which the growth occurs. Scientists in South Korea, in collaboration with Samsung, were successful in growing graphene nanoparticles in a large catalyst surface forming essentially a functional continuous layer of graphene that retained the desired optical and electronic properties [52,53]. On the other hand, graphene with relatively lower-quality but at higher amount, such as the one obtained through exfoliation, can be used in diverse array of devices such as the well-known "Graphene-Silly Putty", where a cross-linked polymer and graphene composite formed an electrically conductive sensor with multiple applications [54]. Similarly, when considering applications such as the construction industry, where graphene can be used as an additive to cement to enhance e.g. mechanical properties [55–57], the critical factor is cost efficiency of the product i.e. in the order of ~\$20/Kg. As such, graphene oxide is a prime candidate for this market. It is clear at this stage that no single production method is set to monopolize the growing need for graphene as a raw material. Rather, each of the production methods quietly finds its niche market, catering to specific applications (Fig. 1).

A large number of chemists within the carbon nanoscience community are actively involved in the functionalization of graphene, with the end-goal of coupling graphene's attractive characteristics with various organic addends and achieving a hybrid material with enriched properties. Concerning functionalized graphene, the vast number of hybrid materials synthesized can, in turn, be divided into two main categories. The ones obtained through covalent functionalization of graphene, where defects are introduced on the graphitic backbone, and the ones obtained through non-covalent approaches, where the careful selection of reagents allows functionalization by taking advantage of the π - π^* interactions of the organic moiety and the graphene sheet. The interested reader can delve more into the extent that covalent and non-covalent attachment affect the properties of graphene [58].

A simple search on "Scopus" with the key-words "graphene" and "nanomedicine", "sensors", optoelectronics" or "catalysis" yields a rapid, exponential increase of the number of publications (Fig. 2), progressing from a few hundred in the period 2008–2012 and quickly exceeding several thousand papers, for each of the following years. This, clearly, shows an increasing interest in graphene-based applications. The vast majority of graphene-based materials used in this indicative sample are based on functionalized graphene. During the last decade, several groups have pioneered the chemistry of graphene functionalization resulting in interesting properties and new applications. In this review, we present the high number of covalent hybrids synthesized during the last years, while focusing in these four areas and elaborating on the type of graphene used, the functionalization reaction, the properties and finally the potential applications. The desired outcome is that the interested reader should obtain a clear idea on the synthetic route and basic family of functional moieties used in order to target specific applications.

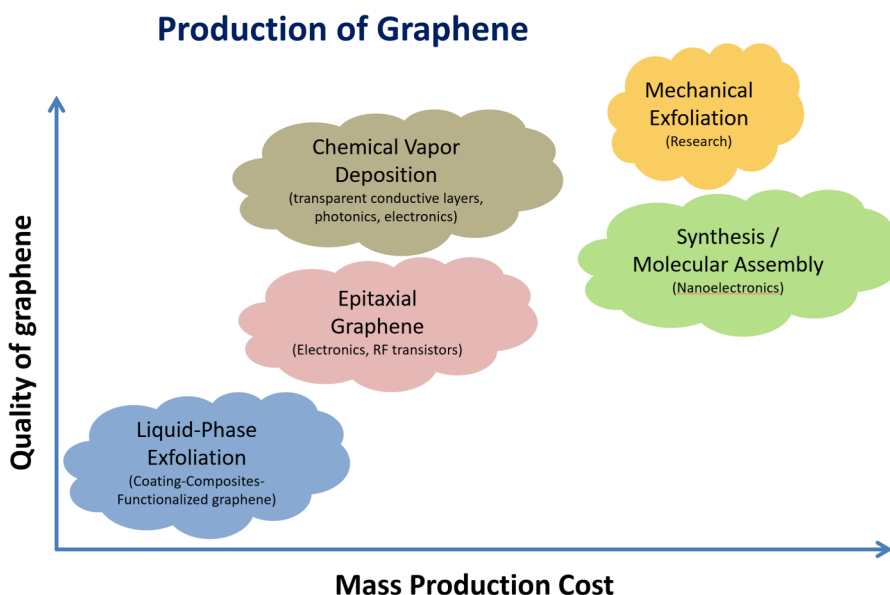


Fig. 1. Schematic representation of various methods of graphene production and the subsequent quality of produced graphene vs cost of mass-producing.

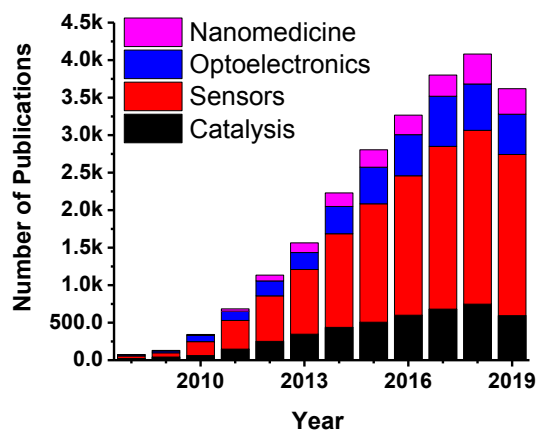


Fig. 2. Number of yearly publications with the key-words “graphene” and “catalysis” (black), “sensors” (red), “optoelectronics” (blue), and “nanomedicine” (pink).

Source: www.scopus.com (October 2019).

3. The covalent chemistry of graphene

Functionalization of graphene nanosheets can be realized either through physisorption of molecules and complexes or through formation of covalent bonds between the lattice and the organic moiety. Non-covalent approaches offer the advantage of minimal damage to the graphene sp^2 network, since the immobilization on the surface of the nanocarbon is via multiple weak π - π attractive interactions [59]. Representative examples of this methodology involve graphene-based ensembles featuring oligothiophenes [60,61], porphyrins [62–65], pyrene-derivates [66,67], coronene carboxylates [68], phthalocyanine derivatives [69–74], azobenzene-derivatives [75], *para*-phenylenevinylene (PPV) derivatives [76], perylene-derivatives [77,78], osmium(II)-bipyridine complexes [79] and methylene blue [80].

Herein, we briefly present the most prominent functionalization routes reported for the preparation of covalent graphene-based hybrids, focusing in the fundamental mechanisms taking place. In this context, the reader will acquire an overview of the available chemical tools and some insights from the standpoint of a chemist for each protocol. It should be noted here that all the described methods and protocols presented in this section can be -in principle- easily applied to all types of graphene-based derivatives, e.g. liquid-assisted or mechanically exfoliated graphene, epitaxial graphene, graphene grown by chemical vapor diffusion (CVD), graphene oxide (GO), reduced graphene oxide (rGO), heteroatom doped graphenes, graphene nanoribbons etc, while also to pristine natural graphite, high ordered pyrolytic graphite (HOPG) etc.

A variety of characterization tools provide complementary information for the success of the chemical functionalization of graphene. A series of spectroscopic methods allows the identification of the species inserted on the graphene lattice: a) FT-IR (Fourier-transform infra-red) spectroscopy allows the detection of characteristic vibrational and stretching modes due to the introduced species, b) XPS (X-ray photoelectron) spectroscopy enables the quantitative determination of atoms, as well as the nature of bonds formed, and c) EDS (electron diffraction spectroscopy) and EELS (electron energy loss spectroscopy) allow the in-situ atom-detection when coupled to a microscope. Raman spectroscopy is a prominent spectroscopic tool unveiling the distortion of the graphene lattice (the so-called D-band), p- or n-doping effects (from the position of the so-called G-band) and the thickness of the layered material (the so-called 2D-band). Additional spectral signatures of the chemically incorporated species can be also observed. Moreover, electronic absorption and fluorescence spectroscopy give information for the light capture and emission properties in the case of photoactive ensembles. Thermogravimetric analysis (TGA) assays complement the characterization of the covalently modified graphenes in terms of the thermal stability of the hybrid materials and subsequently assist the determination of the organic matter loaded on the graphitic lattice during the functionalization. Finally, microscopic imaging techniques implement the identification of the morphology of the starting material and the hybrids: a) atomic force microscopy (AFM) allows to determine the thickness of the layered material and construct the 3D-topography, while also is applied to study the elasticity, adhesion and other mechanical properties of the material, b) scanning electron microscopy (SEM) and transmission electron microscopy (TEM) are essential for imaging the material in a non-invasion way (in contrast to the cantilever-mediated imaging of an AFM) as well as for in-situ elemental analysis, diffraction studies etc.

In this section, we will discuss the most common functionalization strategies focusing into the nature of the reactants and the chemical mechanisms taking place. A broad range of functionalization routes will be collectively presented to the interested reader, while the new and experienced researchers seeking to integrate graphene in their research will be provided with a roadmap of this fascinating carbon allotrope.

3.1. Covalent chemistry on the graphene sp^2 network

3.1.1. [2 + 1] cycloaddition of malonate derivatives

Reaction between graphene and malonate derivatives in the presence of 1,8-diazabicycloundec-7-ene (DBU) and carbon tetrabromide (CBr_4) results on the [2 + 1] cycloaddition addition furnishing graphene-malonate hybrids. The overall reaction scheme resembles the characteristics and mechanism of the so-called Bingel reaction of malonates with the cage of fullerene C_{60} [81] and takes place at the basal plane of the graphene network. Each malonate unit reacts with two adjacent carbons of the graphene backbone according to Fig. 3a, resulting to graphene-based hybrid materials decorated with symmetric and unsymmetric malonate derivatives [82]. It is a diverse approach since the synthesis of unsymmetric malonate derivatives carrying two discrete functional

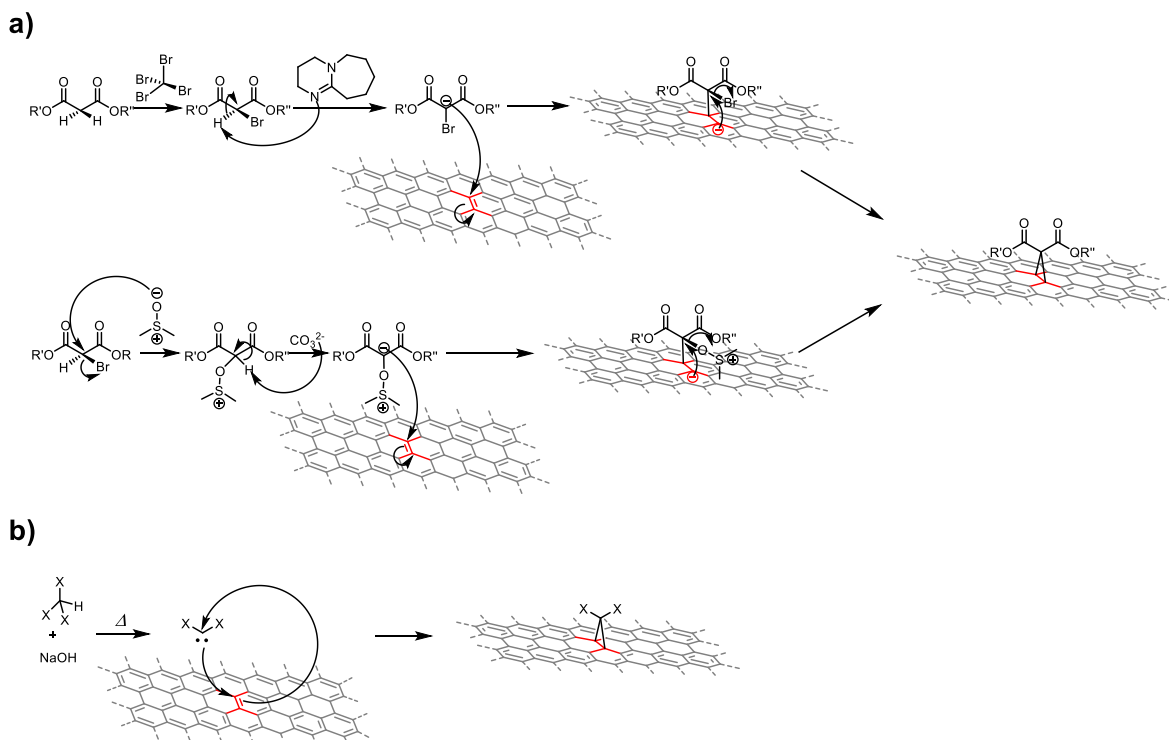


Fig. 3. [2 + 1] cycloaddition reaction of (a) malonate derivatives, and (b) carbenes, on graphene.

units is as feasible as the synthesis of symmetric malonates, by means of simple organic chemistry protocols. The functionalization reaction can also take place under milder conditions, employing dimethyl sulfoxide (DMSO) and α -bromo malonates in the presence of sodium carbonate (Na_2CO_3), at room temperature, affording highly functionalized hybrids, constituting a more attractive approach for scale up [83].

3.1.2. [2 + 1] cycloaddition of carbenes

Analogously to malonate cycloaddition on the graphene network, addition of carbenes results to the formation of fused cyclopropane rings on graphene. In the presence of sodium hydroxide and moderate heat at around 70 °C, bromoform and chloroform are transformed to the corresponding dibromo- and dichloro-carbenes, which are strong nucleophiles, attacking the carbon lattice and forming 1,1-dihalogen cyclopropanes [84,85]. This is a protocol applicable to dispersions of graphene in the presence of a phase transfer catalyst (i.e. triethylbenzylammonium chloride or trihexylamine) in order to surpass the negligible solubility of the inorganic base in the organic media used for the dispersion of the exfoliated nanosheets. As evidenced by spectroscopic studies [55], the mostly active sites are the edges of graphene, thus the presence of the addends is more dense at the periphery of the graphene flakes.

Another way to prepare functionalized graphene with the aid of carbene chemistry is by the thermal decomposition of *para*-toluene hydrazide derivatives [86]. This approach offers extended versatility since the required hydrazide derivatives are easily synthesized by condensation of *para*-toluene hydrazone with a variety of aryl-ketone derivatives. Density functional theory studies for the addition of dichlorocarbenes on graphene nanoribbons (GNRs) revealed that the insertion of extra molecules is an energetically favourable process and takes place at the same edge of the GNRs where the previous molecules were attached [87]. Moreover, carbene chemistry can be also realized by photoinduced in-situ generation of carbenes from the parent diazirines [88].

3.1.3. [2 + 1] cycloaddition of nitrenes

Nitrenes are the nitrogen analogues of carbenes. In contrast to carbenes, which are negatively charged, the nitrogen atom of nitrenes is neutral with six electrons and therefore a strong electrophile due to the unsatisfied octet rule. In this case, the sp^2 network

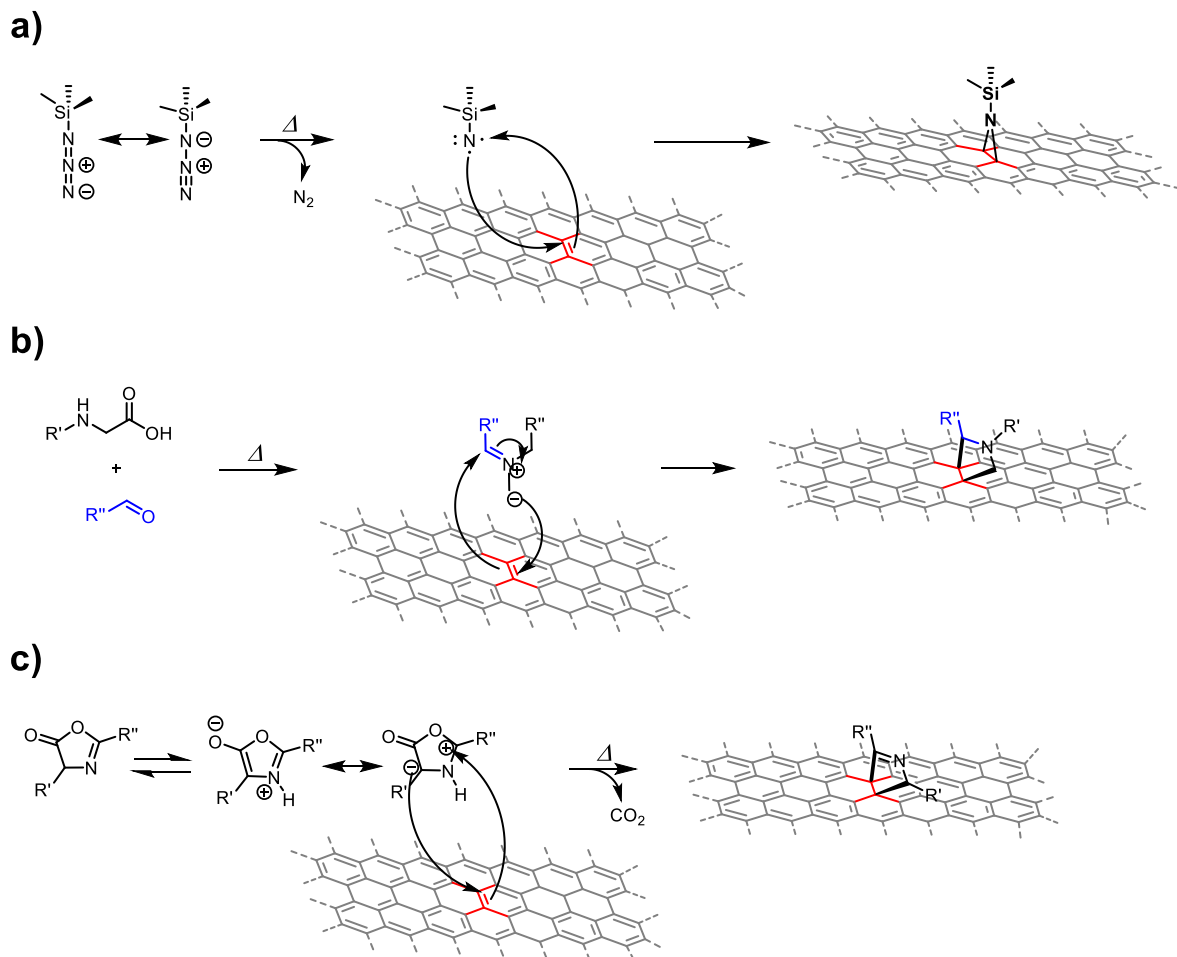


Fig. 4. (a) Cycloaddition reaction of nitrenes, (b) 1,3-dipolar cycloaddition reaction of azomethine ylides, and (c) 1,3-dipolar cycloaddition reaction of oxazolones, on graphene.

of graphene is considered as the nucleophile and an analogous reaction to cycloaddition of carbenes takes place (Fig. 4a). Nitrene species are generated in-situ by heating the corresponding azido-derivative. In this context, the commercially available azido-trimethylsilane in the presence of graphene, under moderate heating (70–100 °C), affords the corresponding aziridotrimethylsilane-functionalized nanosheets, namely an aziridine fused ring similar to cyclopropane [89].

3.1.4. 1,3-Dipolar cycloaddition

Azomethine ylides: Single or few-layer graphene was highly functionalized using the 1,3-dipolar cycloaddition reaction of azomethine ylides, to introduce fused pyrrolidine rings on graphene. The reaction sites can either be the basal plane or the edge of the graphene sheet. The highly reactive azomethine ylides are prepared by the condensation of an amino acid and an aldehyde in the presence of graphene dispersions [90]. Accordingly, graphene can be decorated with a great variety of functional units by tuning the structure of the amino acid and aldehyde reactants. The reaction proceeds under moderate high temperature (above 80 °C) in order to in-situ generate the azomethine ylides, which rapidly react with the graphene sp^2 network as shown in Fig. 4b.

Oxazolones: Another example of 1,3-dipolar cycloaddition reaction on the graphene lattice is the thermally-induced addition of mesoionic (dipolar) oxazolones [91]. In analogous fashion to azomethine ylides, the dipolar oxazolones react with the sp^2 network of graphene leading to the formation of fused 5-membered rings (Fig. 4c). The first report of this method was dealing with the subsequent exfoliation/functionalization of pristine graphite towards graphene nanosheets covalently decorated with 2H-pyrrole derivatives. Actually, this is a chemical functionalization protocol, which can be also adopted for the covalent grafting of such functionalities on the basal plane. Moreover, a series of different oxazolones (or münchnones) can be prepared according to known procedures [92].

Nitrile imines: Similarly to oxazolones, the dipolar cycloaddition reaction of nitrile imines results to the formation of fused 5-membered rings of pyrazolines on graphene. Initially, the precursor hydrazones are treated with N-chlorosuccinimide to afford the corresponding dipolar nitrile imine intermediate, followed by heating at 170 °C in the presence of graphene to proceed the cycloaddition reaction [93]. As evidenced by Raman spectroscopy, the insertion of the pyrazoline rings induced n-doping effect to the graphene sheets.

3.1.5. [4 + 2] cycloaddition of dienes and dienophiles

Haddon and coworkers adopted the classic Diels-Alder reaction [94] for the functionalization of graphene and graphite [95]. Reaction between dienophiles and dienes is a long-standing tool in the synthetic arsenal of organic chemists focused in total synthesis of valuable compounds [96,97], while also for the preparation of fullerene [98,99] and SWNT [100–102] derivatives. Graphene and graphite, due to their extended sp^2 network, are capable to act both as dienes or dienophiles (Fig. 5a). In this perspective, a Diels-Alder type reaction on the graphitic network can be proceed either by exploiting a diene or a dienophile, offering the advantage of two different routes but also the simultaneous functionalization of the nanosheets with dienes and dienophiles. Tetracyanoethylene (TCNE) is the most common dienophile employed for the functionalization of graphene, with the latter acting as diene. Notably, the reaction takes place at room temperature and by heating the TCNE-functionalized nanosheets the graphitic plane is restored through a retro Diels-Alder reaction. Graphene has been also tested as dienophile in reactions with 9-methylanthracene and 2,3-dimethoxy-1,3-butadiene (DMBD) being the dienes. The overall strategy is directly applicable to graphite sheets, affording exfoliated functionalized nanosheets, but also can be adopted to exfoliated graphene dispersions or other graphenes (GO, rGO, doped graphenes etc). Diels-Alder addition of tetracyanoethyleneoxide was also reported for the on-plane functionalization of graphene, as evidenced by Auger and Raman spectroscopy [103]. Moving to more sophisticated materials processing, CVD-graphene nanosheets covered by PMMA have been patterned to on-plane hexagons generating favourable on-plane sites for performing the addition reaction with the aid of two dihydronaphthalene backbones giving an alternative way of material design at the nanoscale [104].

3.1.6. [2 + 2] cycloaddition of arynes

Arynes are intermediates prepared in-situ by, among other ways, zwitterionic 2-diazoary-1-carboxylates (i.e. by heating anthranilic acid) [105] or at room temperature via 1,2-trimethylsilyl triflates [106]. The as formed triple bond within the parent arene is highly strained and consequently arynes are highly reactive intermediates capable to attack the sp^2 graphene network via [2 + 2] cycloaddition reactions (Fig. 5b). Beyond the commercially available aryne precursors, this route is also promising for the decoration of graphene sheets by introducing different functional units on the aryne skeleton. Taking into consideration that this protocol can be also performed at room temperature, this is a convenient method for sensitive or labile functional units.

3.1.7. Friedel-Crafts acylation

Carbonium anions have been also exploited for the chemical functionalization of graphene nanosheets, via the so-called Friedel-Crafts acylation reaction. As it was shown, such intermediates can be generated at moderate high temperature (130 °C) by employing a protocol based on the reaction of 4-aminobenzoic acid with phosphorous pentoxide in the presence of polyphosphoric acid. This method was firstly reported for the sequential exfoliation and functionalization of graphene, namely the production of acylated nanosheets starting from pristine graphene [107]. Within the graphitic superstructure, it is more likely for the reaction to proceed at the edges. Actually, the adoption of this method to exfoliated graphene showed the same results [108], indicating that the reactivity at the edges is higher. Such an acylation reaction can be also performed the opposite way, with graphene acting as the acylating agent by its activation with acidic alumina and trifluoroacetic anhydride at the same temperature range [109]. Following this approach, graphene oxide decorated with covalently grafted ferrocene has been isolated in good yields [110].

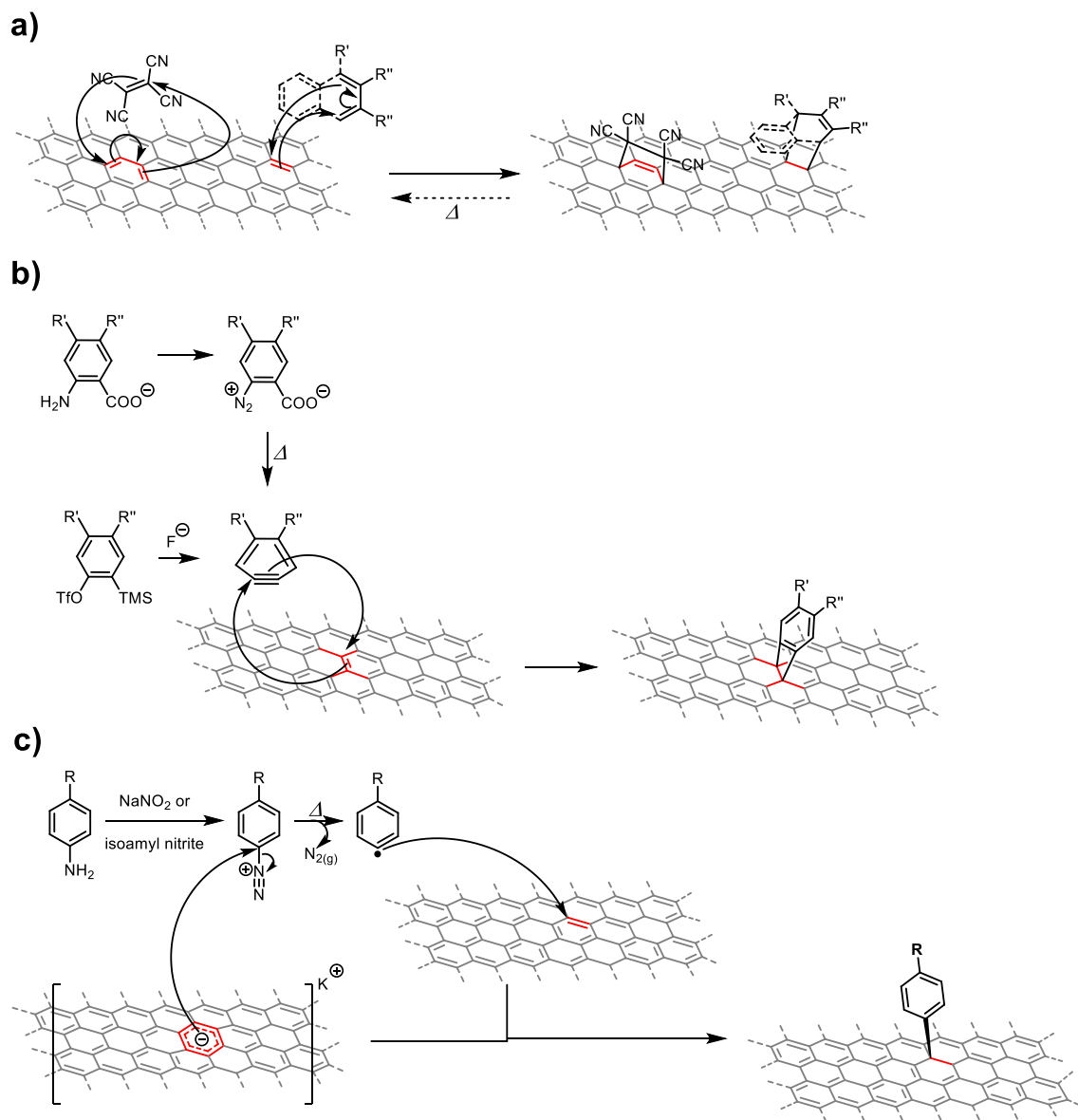


Fig. 5. (a) [4 + 2] Cycloaddition reaction of dienes/dienophiles on graphene. (b) [2 + 2] Cycloaddition reaction of arynes, and (c) addition reaction of aryl radicals, on graphene.

3.1.8. Kolbe-Schmitt oxidation

Handling the oxygen functionalities of graphene oxide is important towards the fine-tuning of its surface chemistry and properties, i.e. bandgap. A modified Kolbe-Schmitt reaction has been proposed for enriching the carboxylic acid functionalities (up to 11% atom) and at the same time reducing the content of the other oxygen groups [111]. GO is treated with potassium hydroxide at elevated temperatures (220–500 °C) in order to activate the hydroxyl functionalities, while calcium oxide absorbs the carbon dioxide produced by the elimination of the more labile oxygen functionalities (hydroxyl and epoxide groups) and the thermal healing of the distorted lattice. Accordingly, the activated graphene lattice undergoes nucleophilic attack to the carbon dioxide molecules furnishing the carboxylic acid functionalities. Along the same lines, reduction of the epoxides present on the basal plane of graphene oxide, towards the corresponding hydroxyls, by HBr followed by addition of oxalic acid, resulted to carboxylic acid enriched graphene nanosheets [112].

3.1.9. Electrochemical addition

Electropolymerization: Beyond conventional reactions, the use of electrochemical approaches for the functionalization of graphene was also demonstrated. In this way, electropolymerized polydiphenylamine was successfully covalently grafted on rGO with the aid of cyclic voltammetry assays [113]. As long as the polymer chain elongates, the nitrogen atoms connecting the diphenyl rings attack

the graphitic lattice furnishing covalent bonds, while counter anions provided by the electrolyte balance the charges generated across the polymer. By tuning the counter anions, it is possible to alter the properties of the polymer decorated graphene.

Electrooxidation: Electrochemical oxidation of aryl-carboxylates found to be a feasible way for the reversible functionalization of graphene electrodes with aryl-radical [114]. Specifically, during the oxidation of 1-naphthaleneacetate anions, a decarboxylation mechanism takes place resulting to methyl-naphthalene radicals which effectively react with the sp^2 network of the graphene-based electrode. Under reversed voltage conditions, the graphene electrode is restored by the electroreductive release of methyl-naphthalene cations.

3.1.10. Addition of radicals

Aryl diazonium salts: Diazonium salts are produced by the reaction of arylamines with sodium nitrate or isoamyl nitrite in a route known as diazotization. These derivatives are usually stable at room temperature, however, it is appreciated to be prepared in-situ for the covalent functionalization of graphene. Upon heating, the diazonium salts release nitrogen, which is a very good leaving group, furnishing a highly reactive arene radical able to react with the sp^2 network of graphene via an electron transfer mechanism (Fig. 5c). This functionalization protocol was found to be highly favorable for engineering the edges of graphene [115,116], especially for the case of graphene nanoribbons [117], or at locally strained areas [118] of the basal plane. Importantly, by the incorporation of arenes carrying electron withdrawing groups (i.e. nitroarenes), significant improvement on the electric properties of graphene was observed [66,119]. Moreover, different reactivity was observed for different types of graphenes, namely between surfactant-assisted liquid exfoliated graphene and the CVD grown ones, upon addition of propargyloxy-benzene [120]. CVD-graphene was found more reactive than few-layered graphene probably due to local fluctuations of the electron density in the monolayered nanosheets, leading to higher reactivity towards the substitution reaction. Interestingly, via Raman spectroscopy it is not only feasible to monitor the increment of the D/G ratio as a probe for the reaction's progress, but also to examine isolated nanosheets and study the success of the reaction at different areas. Actually, Raman mapping and analysis of the D/G ratio of CVD monolayers clearly showed that the diazonium addition is also likely on the basal plane (Fig. 6). Diazonium chemistry is also a versatile tool for the nanomanipulation of graphene and is compatible with already surfactant-decorated nanosheets [121–123]. Interestingly, amine-functionalized arenes carrying long alkyl chains reported to be efficient candidates for the electrochemical driven diazonium addition of the self-assembled hydrophobic molecules on the graphitic surface, furnishing patterned arrays in short reaction times, i.e. < 10 s [124]. Electrochemical-driven diazonium addition of fluorinated-arenes was demonstrated to afford a functionalization density of 1×10^{14} molecules/cm² [125]. Further, it was possible to access such covalently decorated graphene sheets directly from graphite via a sequential two-step approach, where initially graphite is intercalated by a sodium-potassium (NaK) alloy, resulting to negatively charged exfoliated graphene, immediately attacking the diazonium salts at room temperature [126]. The latter approach has been also proposed for the preparation of alkylated graphenes by employing alkyl iodides, namely the negatively charged graphene promoted nucleophilic attack to the iodides resulting to substitution reactions [127,128].

Xanthate derivatives: Following a thermal strategy for the activation of xanthate derivatives in the presence of an organic peroxide, graphene can be efficiently functionalized by the functional units carried by xanthates [129]. More specifically, the organic peroxides via heating are transformed to radicals activating the xanthate moiety towards the corresponding radical species of the xanthate derivatives, which finally attack the graphene lattice forming covalent C-C bonds.

Radical polymerization: Radical attack to the sp^2 network of graphene has been also proposed for the simultaneous exfoliation/functionalization of graphene [130]. Performing, for instance, a classic polystyrene synthesis in the presence of graphite, the generated radicals elongate the polymer chain, while also attack the edges of the graphene lattice furnishing exfoliated nanosheets carrying polystyrene chains.

Thiol-ene reaction: In the same context, the sp^2 lattice of graphene allows to perform the highly efficient click-reactions, likewise the thiol-ene reaction. More specific, the graphene network acts as an "alkene" in the presence of a thiol and a radical initiator (i.e. AIBN) forming covalent C-S bonds, mainly at the edges of the network [131]. Simple thiol-ene approaches enable the decoration of graphene nanosheets with ligands having affinity for metals, allowing the growth of metal nanoparticles. Moreover, the method can be applied to graphenes functionalized by arenes bearing alkenes or alkynes and thiol-terminated derivatives (i.e. polyethylene-SH) [132]. It should be noted that the employed click-chemistry approaches affect the electrical, thermal and mechanical properties of the hybrid materials [133].

3.2. Organometallic chemistry

Graphene nanosheets, due to the sp^2 hybridization of the honeycomb lattice, reserve a flat topography, allowing their exploitation as ligands for organometallic complexes. In this concept, a series of hexahapto-chromium complexes with graphene as ligand have been reported [134]. Accordingly, hexacarbonyl chromium was initially heated in the presence of graphene resulting to coordination of chromium to the graphene lattice. By employing $(\eta^6\text{-benzene})\text{Cr}(\text{CO})_3$ chromium complexes of graphene can be easily produced, where the benzene ring and the carbon lattice are in axial directions. Moreover, the process can be also performed with aid of illumination [135] in a reversible fashion, since the insertion of xylene induces the dissociation of the graphene complexes without disturbing the hybridization of the involved carbon atoms. The incorporation of metal centers on the basal plane of graphene is expected to fine-tune the properties of the nanosheets. The latter was investigated for the case of the analogous cyclopentadiene-based transition metal complexes of graphene by means of density functional theory approximations [136].

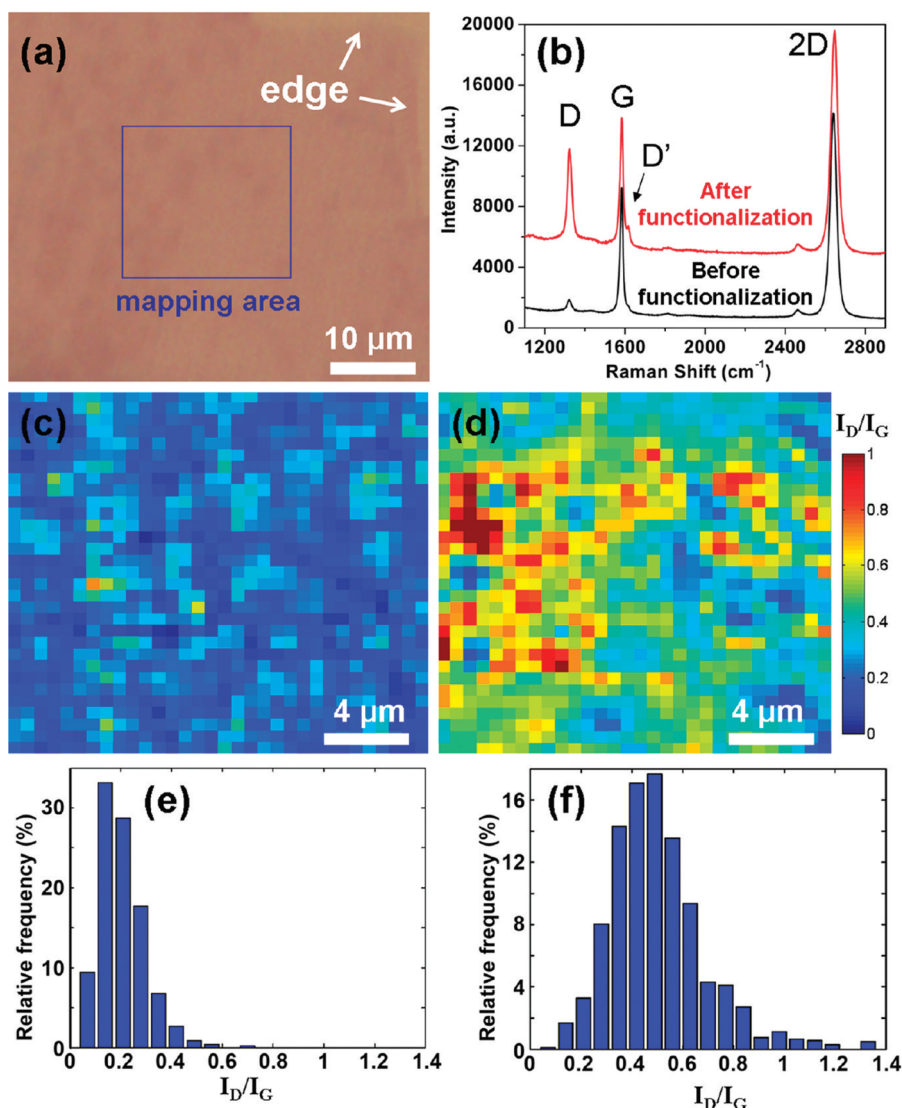


Fig. 6. (a) Optical image of a large-area monolayer CVD-graphene film transferred on a SiO₂/Si chip with 300-nm-thick thermally oxidized silica. (b) Typical Raman spectra taken at the same position of this CVD-graphene film before and after the two-step functionalization. Spatial maps of D/G from Raman spectra collected at the same position of this CVD-graphene film (c) before, and (d) after the two-step functionalization; the intensity values of D and G band were calculated after fitting the peaks to Lorentzians. The step length of Raman mapping was 0.6 μm for both x and y axes, and the laser excitation wavelength was 633 nm. The histograms (e and f) show the corresponding relative frequency of D/G values in the Raman spatial maps (c and d, respectively). Reproduced with permission from Ref. [120]. Copyright (2011) American Chemical Society.

3.3. Covalent chemistry of oxidized graphene

Oxidized graphenes are mostly prepared by the chemical oxidation of graphite under the conditions described by Hummers [137,138], although new insights considering the employed oxidants (KMnO₄, NO⁺) assist the control of the reaction [139]. In the harsh oxidative environment, the graphite is intercalated by the oxidants and yields oxidized graphene sheets. The common oxygen functionalities inserted on graphene are hydroxyl groups, carboxylic acids and epoxides [140]. The density of the carboxylic groups is higher at the edges, while the hydroxyl and epoxy functionalities are denser on the basal plane. It should be noted that via chemical reduction (i.e. hydrazine [141]) the graphene plane is partially restored and the loading of oxygen functionalities is controllable. The exploitation of the carboxylic acids is the most facile way to attach hydroxyl- or amine-terminated derivatives via condensation. These reactions are discussed in the next sections dealing with applications of graphene. Herein, we rather focus into the less-explored etherification of hydroxyl functionalities, the Claisen-type rearrangement and the nucleophilic attack to epoxides.

3.3.1. Etherification

Treating graphene oxide with a trimethoxysilane derivative results to substitution of the methoxy group by the hydroxyl group of

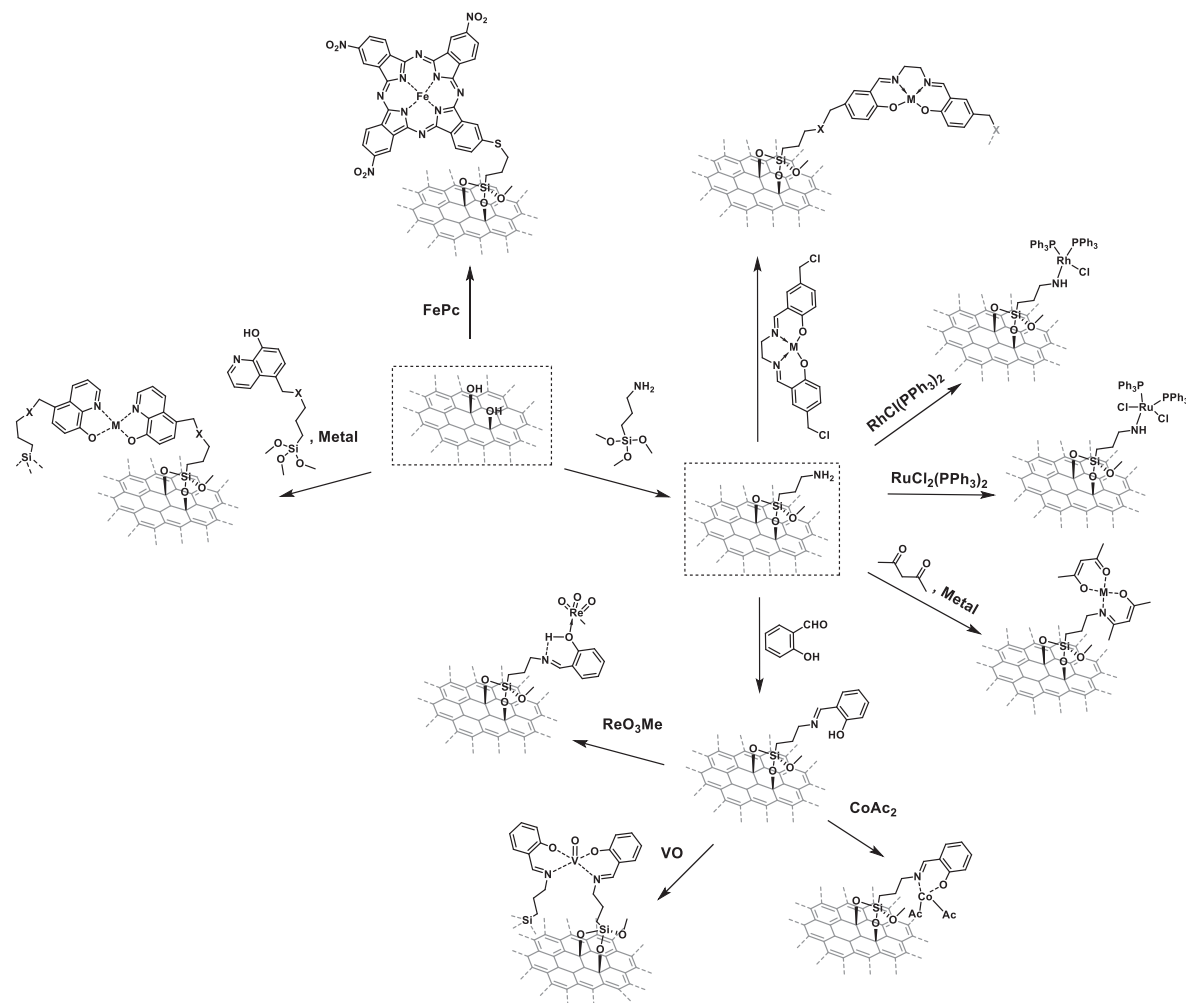


Fig. 7. Synthetic procedures for graphene-based covalent ensembles based on (aminopropyl)trimethoxysilane (APTMS)-functionalized nanosheets.

graphene [142]. The obtained silanized graphene is stable and different types of silane-derivatives can be covalently incorporated on the nanosheets in an analogous fashion, as shown in Fig. 7. Graphene oxide prepared by Hummer's method was treated with (aminopropyl)trimethoxysilane (APTMS) in order to proceed the covalent incorporation of the silane on the graphene substrate. The free primary amine group can then be used as ligand for the coordination of $\text{RuCl}_2(\text{PPh}_3)_3$ [143], $\text{RhCl}(\text{PPh}_3)_3$ [144] and other catalysts [145]. APTMS-functionalized GO nanosheets have been also employed for the covalent attachment of 2-hydroxybenzaldehyde forming a Schiff base for the immobilization of oxo-vanadium, [146] cobalt acetate [147] and a rhenium oxo-complex [148]. In analogous fashion, condensation of the APTMS units with acetylacetone enables the generation of a Schiff base for the efficient complexation of transition metal cations [149]. Covalent attachment of salen ligand on the APTMS-GO nanosheets has been also reported towards the formation of dioxomolybdenum(VI) [150] and copper (II) [151] complexes. Besides from pre-functionalization of GO with APTMS, there has been also reported the treatment of the oxidized nanosheets with photoactive units or ligands carrying a trimethoxysilane edge for the direct covalent incorporation of the desired dye [152] or ligand [153,154] on the graphene lattice. This functionalization strategy was utilized for the fabrication of graphene-based stationary phases for chromatographic separations [155].

Along the same lines, the successful covalent incorporation of boranes via etherification was demonstrated by treating graphene oxide with triphenylborane, where the hydroxyl functionalities of GO substitute the ligands of the borane, forming stable borane-functionalized graphene derivatives [156]. Furthermore, symmetric 1,2-diboronic arenes have been proposed for the synthesis of graphene organic frameworks, via the interconnection of the graphitic network through boronic ester formation [157,158].

3.3.2. Nucleophilic attack to epoxides

Across the oxidized network of GO, epoxide functionalities can be found, which are susceptible to nucleophilic attack under heating conditions. Addition of benzene radicals by pyrolysis of benzoyl peroxide in the presence of graphene oxide has been reported for the preparation of chemically modified graphenes via nucleophilic attack to the epoxide rings present on the basal plane [159].

Notably, under pyrolytic conditions the radical addition was found to promote restoration of the sp^2 network. Nucleophilic attack to epoxides is a profound strategy to covalently attach amines [160–162] or heteroatom radical species, such as the organic radical 2,2,6,6-tetramethyl-1-piperidinyloxy (TEMPO) [163] and thiols [164].

The susceptibility of epoxy functionalities is also a target for the preparation of azido-functionalized graphenes through treatment of graphene oxide with sodium azide [165,166]. This type of graphene derivative can be directly employed to copper-catalysed Huisgen “click” cycloaddition reactions [167]. An important insight, for this type of nucleophilic substitutions, is that the storage of graphene oxide prepared by the Hummer’s method at low temperatures ($< 10\text{ }^\circ\text{C}$), reserves a sulfur content in the form of sulfonates, which are exceptional leaving groups. Eventually, the as-prepared azido-graphene can be further reduced towards the preparation of amino-graphene [168]. Azido-graphene derived by treatment of acyl-activated graphene oxide has been reported for the preparation of amino-functionalized nanosheets [169].

Another efficient reaction is the addition of sulfides on the basal plane of graphene oxide by reacting the epoxides with potassium thioacetate (KSAc) as source of nucleophilic sulphur [170]. According to this protocol, sulfur atoms are inserted on the epoxidic carbons and upon addition of water geminal alcohol-thiol functionalities are yielded. In analogous way, substitution of KSAc by alkyl thiols under mild conditions resulted to alkyl-sulfide functionalized RGO. Under more harsh conditions, at elevated temperature (300–1000 $^\circ\text{C}$), the utilization of other organic sulfide sources, such as dibenzyl sulfide, furnishes sulfur functionalities embedded onto the graphene lattice or adsorbed at the edges in the form of SO_x oxides [171].

3.3.3. Rearrangement reactions

Oxidation of graphite results to a distorted honeycomb lattice at the exfoliated graphene oxide. Accordingly, there are regions where allylic alcohol functionalities are present. The exposed alcohols are able to react with a vinyl transfer agent, such as N,N-dimethylacetamide dimethyl acetal (DMDA), and undergo an intra-ensemble Eschenmoser–Claisen rearrangement furnishing the corresponding γ,δ -unsaturated N,N-dimethylamides [172]. In other words, the initially grafting of DMDA via an ether bond is finally attached via a C-C bond on the graphene lattice. This unique sigmatropic transformation demonstrates the diverse chemistry of graphene and introduces not only new ways to tune its properties [173], but also the potential to expand the chemistry toolbox with currently unexplored reactions. Allylic functionalities, although present in hydrogenated graphene, have been examined in dehydrogenative cross-coupling reactions resulting to tetrahydrothiophen-3-one functionalized nanosheets [174].

3.3.4. Chlorination

Sulfuryl chloride (SO_2Cl_2) is a superior source of chlorine for the conversion of alcohols to the corresponding chlorides. In this respect, chlorination of the hydroxyl functionalities of GO affords the corresponding Cl-functionalized graphene oxide [175]. Under the thermal conditions of the functionalization reaction, the final derivatized nanosheet is a chlorinated reduced graphene oxide, as evidenced by XPS elemental analysis.

3.4. Covalent chemistry on heteroatom doped-graphene

3.4.1. Fluorine-doped graphene

Ideally, fluorographene is a stoichiometric (C_1F_1) “graphene” with a Teflon-like structure [46]. Actually, for practical applications the use of graphite fluoride provides a significant amount of fluorine atoms, while reserving an extended graphitic network [176,177]. Accordingly, few-layered F-doped graphene can be prepared by exfoliation of graphite fluoride. Moreover, elemental doping of reduced graphene oxide is another route towards the preparation of F-doped graphene nanosheets. In both cases, the embedded fluorine atoms are susceptible to nucleophilic substitution enabling the covalent functionalization of the doped nanocarbon [178]. Below, we briefly present the major functionalization routes.

Incorporation of alcohols and secondary amines is a feasible way to chemically functionalize F-graphene [179], while sulfur functionalities may be introduced by reaction with hydrosulfides [180], or via xanthogenates [181]. Amine functionalization of fluorographene has attracted significant interest and a series of reports dealing with substitution reactions promoted by urea [182], ethylene diamine [183], poly(oxypropylene)diamine (PEA) [184] and the inorganic NaNH_2 salt [185] have been published. Interestingly, the insertion of amine-terminated substituents can be also promoted via the cyanofluorographene, prepared by treatment of fluorographene with NaCN [186]. These cyanofluorographenes can be oxidized to the corresponding carboxylic acid functionalized fluorographene and be coupled to amine derivatives via common amide condensation reactions. Another functionalization route for fluorographene is the reaction with dichlorocarbenes resulting to covalent addition of the carbene on the nanosheets, possibly in a two-step mechanism initiated by defluorination and followed by addition of the carbene [187]. Fluorographene also enabled the exploration of cross-coupling reactions with the halide being the active species. In this respect, the fluorine heteroatoms have successfully mediated the functionalization of fluorographene with Grignard reagents [188,189] or was covalently modified via Sonogashira-type cross coupling reactions [190].

3.4.2. Chlorine-doped graphene

Graphene oxide can effectively be transformed to chlorine-doped graphene via a radical reaction, by treatment with chlorine gas under ultraviolet irradiation. Cl-Graphene monolayers can be selectively alkylated by organomagnesium bromides at the basal plane. With this approach, methyl [191] and adamantyl [192] functionalities have been incorporated on graphene nanosheets by employing the corresponding Grignard reagents.

3.4.3. Bromine-doped graphene

Coupling reactions: Treating the structurally defected rGO nanosheets with bromine is a straightforward approach to prepare brominated graphene and take advantage of the introduced heteroatoms for further chemical manipulation. Actually, brominated graphene is able to act as a regular “aryl-bromide” in palladium cross-coupling reactions, likewise the Suzuki-Miyaura reaction [193]. Aryl mono- and bis-boronic acids can be exploited for such coupling reactions affording functionalized nanosheets carrying single molecules (*p*-hexylbenzene) or homopolymers (polyfluorene). Evidently, this is a method with potential towards a great variety of functional materials.

Nucleophilic substitution reactions: Bromide anions are excellent leaving groups in nucleophilic substitution reactions. Eventually, brominated graphenes, exfoliated by Na/naphthalene intercalation, participate in nucleophilic substitution of bromide by hydroxyl group of polyethyleneglycol, while also appear in the preparation of poly(methyl) methacrylate decorated nanosheets by in-situ polymerization [194]. It should be noted that these studies performed under moderate heating (70–90 °C) and strictly anaerobic and dry atmosphere to protect the sodium naphthalenide-intercalated nanosheets. In the presence of water molecules, nucleophilic substitution results to hydroxyl-functionalized graphenes. However, it is also anticipated to utilize other bromo-graphenes [195], stable to air, in order to perform the substitution of the bromide by the desired functionalities.

3.4.4. Nitrogen-doped graphene

Nitrogen-doped graphenes are another and more widespread member of the heteroatom doped graphenes, prepared by elemental doping of graphene, by pyrolyzing a carbon-nitrogen precursor at 800–1200 °C [196,197]. This type of doped-graphene allows to design functionalization strategies relying on the embedded nitrogen atom, which should be noted that it is mainly located on the basal plane and has pyridinic conformation [198]. N-alkylation is a promising route to covalently graft bromide-terminated precursors. Actually, a series of bromide-terminated molecules have been incorporated by N-alkylation in the presence of a base [199]. Depending on the N-substituents, the manipulation of the bandgap of functionalized N-graphene is a feasible task.

3.4.5. Phosphorous-doped graphene

Chemical doping of graphene with phosphorus is also known [200,201]. More specific, ball milling of graphite mixed with red phosphorous affords graphene nanoplatelets bearing phosphonic acid functionalities. It is believed that ball-milling of graphite promotes the mechanically cleavage of C–C bonds within the graphene lattice generating reactive carbon species which then react with phosphorous. This type of graphene has been tested as flame retardant, while also for C–C cross coupling reactions as a substrate for Pd catalysts [202].

3.4.6. Boron-doped graphene

Hydroboration of graphene oxide by BH₃ towards the preparation of graphols and hydroxygraphanes results to the incorporation of boron atoms (1.2–1.8%) on the lattice [203]. However, these graphenes have yet to be exploited for optoelectronics, nanomedicine or environmental applications.

3.5. Miscellaneous: Covalent approaches for graphene-polymer materials

Covalent functionalization of graphene with polymers (Fig. 8) has attracted significant interest since nanocarbons are exceptional nanofillers for the fabrication of polymer composites [204,205]. Further, polymer arrays covalently incorporated on graphene have been studied as electrochromic and optical limiting materials [206,207]. Moreover, functionalization of the nanosheets with water soluble polymers i.e. poly(3-aminobenzene sulfonic acid) [208] significantly improves the compatibility of graphene with aqueous processing protocols. A series of homopolymers have been reported as candidates for the covalent modification of graphene. Polyamide-6 was covalently grafted on graphene via a ring-opening polymerization reaction of ϵ -caprolactam as the monomer and 6-aminocaproic acid as the initiator [209]. The carboxylic acids utilized as grafting points for the amine-terminus of the polymer furnishing a new amide bond. An analogous azido-terminated poly(ϵ -caprolactone) was successfully incorporated on liquid-assisted exfoliated graphene via direct attack of the azido-terminus on the graphene network [210]. Azido-functionalized graphene was also used for the [3 + 2] Huisgen cycloaddition of an alkyne-terminated poly-(L-lactide) polymers [211].

Chemistry on the epoxide functionalities of GO offers another option for covalently modified nanosheets with polymers. Polyhedral oligomeric silsesquioxanes having an amine or thiol terminus have been successfully incorporated on the graphene surface through nucleophilic attack to GO epoxide rings and further utilized for the fabrication of epoxy [212] and poly-urethane composites [213]. Nucleophilic addition of 1,4-diaminobenzene on GO was used for the subsequent covalent attachment of cyanuric chloride followed by another 1,4-diaminobenzene molecules affording a V-shaped motif owed to the two free amino groups [214]. The latter design was used for the covalent grafting of polypropylene chains carrying maleic anhydride units. In another strategy, the epoxide groups of GO were initially activated followed by carboxylation with oxalic acid. The –COOH enriched GO were functionalized by the covalent incorporation of 1,4-diaminobenzene [215] and immersed into a polymerization mixture containing pyromellitic anhydride and 4,4'-diaminodiphenyl ether, furnishing GO nanosheets carrying a poly-imide array.

Activation of the GO carboxylic acids to the corresponding acyl chlorides has been exploited for the incorporation of amine-terminated poly-glutamate derivatives [216], while also utilized as primers for the preparation of alkyne-functionalized nanosheets for the click addition of poly(styrene-bethylene-co-butylene-b-styrene) (SEBS) triblock copolymers [217] and poly-pyrrole/poly-benzylsulfonate copolymers [218] by means of Huisgen cycloaddition chemistry.

Functionalization of graphene with N-(2-aminoethyl)-2-bromo-2-methylpropanamide, via nucleophilic attack of the amine group

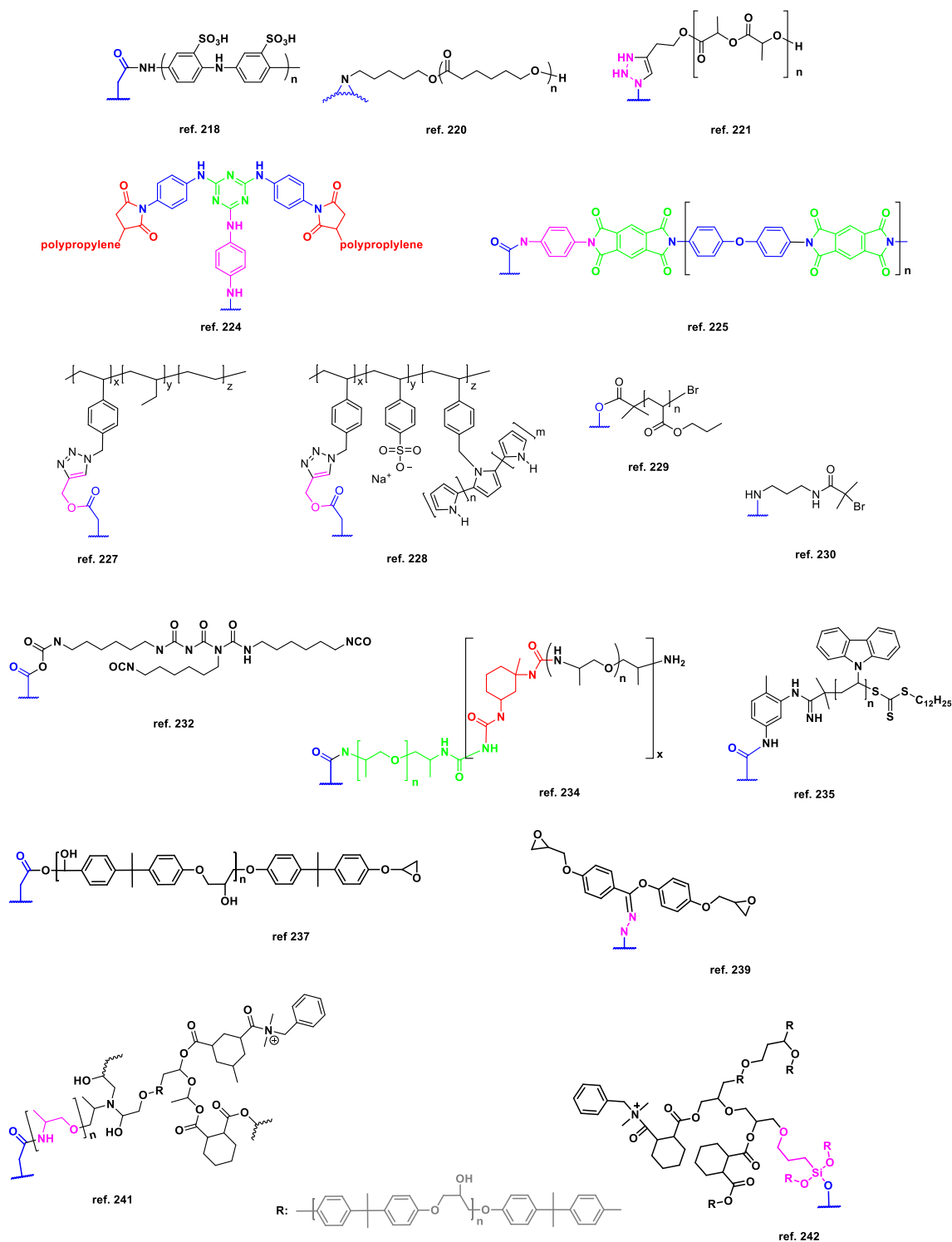


Fig. 8. Illustration of selected polymer structures employed for the chemical modification of graphene.

to GO epoxides was exploited as a graphene-based initiator for the atom transfer radical polymerization (ATRP) of styrene furnishing covalent graphene-polystyrene hybrids with various graft densities [219]. In an analogous manner, 2-bromo-2-methylpropionyl bromide was chemically attached on the hydroxyl functionalities of oxidized graphene and exploited as initiator for the growth of poly(2-hydroxyethyl acrylate) arrays grafted on the surface of GO [220].

Isocyanate derivatives can be directly attached on the carboxylic acid units of GO affording functionalized GO, which is

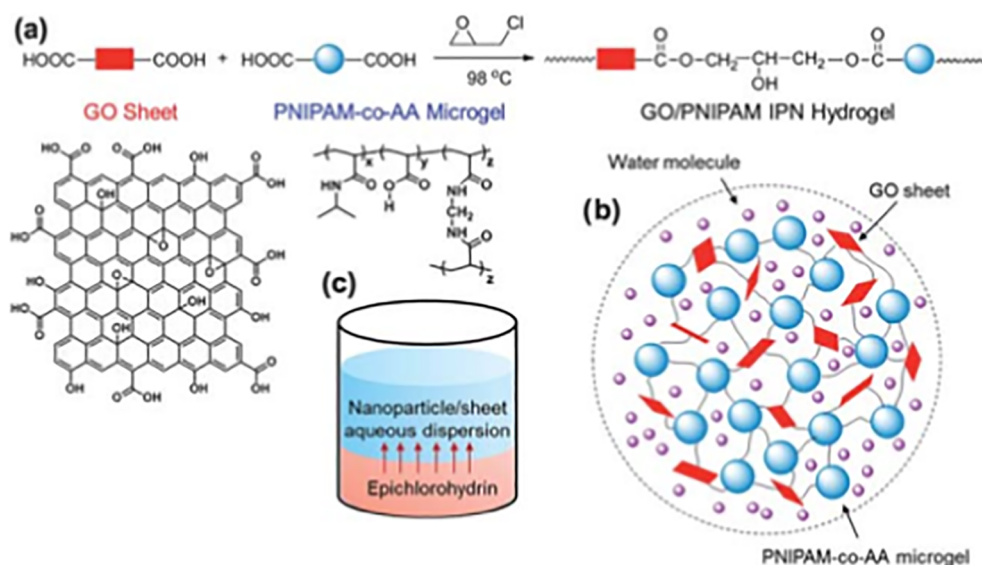


Fig. 9. (a) Formation of GO/PNIPAM interpenetrating hydrogel networks via the reaction between ECH and carboxyl groups in GO and PNIPAM-co-AA microgels. (b) Structural sketch of GO/PNIPAM IPN hydrogel. (c) The sealed reaction tube was placed at 98 °C for incubation while ECH would permeate into the aqueous phase to induce the cross-linking reaction. Reproduced Ref. [233]. Copyright 2011 Royal Society of Chemistry.

transformed to GO/PMMA [221] and GO/poly-urethane composites [222,223]. Moreover, thermal condensation of GO carboxylic acids with an amine-terminated polyether afforded graphene-polyether ensembles having a free amine group used for the elongation of the polymer with the aid of 3-isocyanatomethyl-3,5,5-trimethylcyclohexyl isocyanate [224]. Treating GO with toluene-2,4-diisocyanate enables the covalent attachment of this versatile species either on the hydroxyl or carboxylic functionalities of GO. Having a free isocyanate unit, the functionalized nanosheets were used as templates for the growth of a poly-(N-vinylcarbazole) macromolecule [225].

Attachment of epoxy polymers on GO can be easily achieved via the so-called grafting-to reaction on the carboxylic groups of GO [226]. In an analogous fashion, GO functionalized with the diglycidyl ether of bisphenol-A (DGEBA) can be used as template for the growth of covalently grafted epoxy resins [227,228]. Hydrazine-reduced GO was also reported to be able to host analogous resins via a condensation reaction between the diazine functionalities present on the nanosheets and the keto-groups of the DGEBA-like units [229]. Covalent addition of 4,4'-diaminophenylsulfone on graphene via nucleophilic attack of the amino groups on the epoxides of GO was reported as a graphene template for attaching DGEBA [230]. Pre-functionalization of GO by covalent attachment of polyetheramine (PEA) with different chain lengths [231] or by addition of hydroxyl terminated silanes [232] was proposed for the covalent incorporation of DGEBA accompanied by chemical attachment of 4-methylhexahydrophthalic anhydride and N,N-benzyl-dimethylamide, as hardener. The diverse chemistry of epoxy derivatives was also proposed for the preparation of graphene-based hydrogels [233]. Specifically, epichlorohydrin (ECH) mediated the covalent attachment of the carboxylic acids of GO to those of a PNIPAM-co-AA microgel, as presented in Fig. 9. The process is based on the slow diffusion of ECH into an aqueous mixture of GO and PNIPAM-co-AA microgel due to the formation of an azeotropic ECH/water mixture at 98 °C.

Silane-functionalized graphene oxide carrying a methacrylate terminus were utilized for the growth of grafted poly(methacrylic acid), PMAA, creating graphene foams, which effectively host polypyrrole arrays [234]. Finally, vinyl-terminated benzoxazine was directly introduced on the graphitic lattice via a radical addition reaction in the presence of AIBN and used as a grafting from moiety for preparing the corresponding branched homopolymer via free radical polymerization [235].

4. Applications of covalently functionalized graphene

A broad yet varied toolbox of chemical protocols for the functionalization of the graphene lattice enables the integration of graphene-based nanomaterials to real applications. It should be underlined that the selection of the functionalization route is usually related to the target application, while the utilized chemistry usually affects the properties of the covalently decorated graphene networks [58,236,237]. In this section we discuss the source of the graphene material (i.e. exfoliation or oxidation/reduction of graphite, epitaxial growth) and the employed chemical functionalization protocol. The surface of the graphene can be used to interact with a variety of chemical structures: nanoparticles, polymers, biological structures and organic molecules [238]. Graphene meets applications in areas such as solar cells, energy storage, light emitting diodes, photo detectors, or ultrafast lasers. Depending on the application, the role of graphene can vary as ultracapacitor [239], a semiconducting layer [240], a transparent conducting electrode (TCO) [241,242], an electrolyte [243], a counter electrode [244] or simply through its properties as a hybrid material in nanocomposites [37]. In this review, we discuss the preparation and implementation of covalent graphene-based ensembles in (opto) electronics, nanomedicine and environmental applications.

4.1. Covalently functionalized graphene for (opto)electronics

Mechanical exfoliation of graphite produces mono- and few-layered graphene of high chemical and structural quality. In this respect, the light-matter interactions were evaluated by fabricating transistors for the photodetection properties of the exfoliated nanosheets [240]. The photoresponse of graphene was exceptional and did not degrade for intensity modulations up to 40 GHz. This remarkable transport of photocarriers emerged graphene as a unique candidate for photonic applications. Compared to devices based on III-IV group elements, the photoresponse ability of graphene is lower, however, it can be countered by coupling to plasmonic nanostructures increasing its efficiency by 20-fold [245]. Further improvements resulted to responsivity of ~ 107 A/W and a high gain of $\sim 10^8$ electrons per photon [246]. Concerning exfoliation of graphite in liquid phase, tuning the solvent's surface energy is critical. Exfoliation in water solutions containing sodium deoxycholate (SDC) produces high quality mono- and few-layered graphene nanosheets, which can be embedded into polyvinyl alcohol solutions and further used as mode-locked ultrafast lasers. In this respect, an erbium-doped laser fiber (1559 nm) was passively mode-locked producing a 5.24 nm spectral band-width with ~ 460 fs pulse duration [247]. Liquid assisted exfoliation of graphite in organic solvents (NMP or o-DCB) via sonication also produced high quality of mono- and few-layered graphene nanosheets. Then, by mixing the as-prepared nanosheets with a polymer matrix -polyvinyl alcohol (PVA) for aqueous and styrene methyl methacrylate (SMMA) for organic solutions- graphene composites showing 5% non-linear saturable absorption allowed to mode-lock a laser with 630 fs pulses [248]. Decoration of graphene nanosheets with other functional components is currently a hot topic in materials chemistry.

Coordination of hexahapto (η^6 -) chromium atoms [$-\text{Cr}(\text{CO})_3$ moieties] on the surface of micro-mechanically exfoliated graphene allowed the preparation of transistors with a room-temperature field effect mobility in the range of $\mu \sim 200\text{--}2000$ $\text{cm}^2/\text{V s}$ and an on/off ratio of 5–13 [249]. Following the same coordination strategy, the preparation of interconnected graphene platelets, where the coordinated sandwiched chromium mediates the electrical interconnection of the nanosheets was reported [250]. Interestingly, treatment of these graphene complexes restores the graphitic lattice by elimination of the chromium ligands. A such reversible approach was also reported for the interconnection of graphene nanosheets functionalized with terpyridine ligands and antagonist coordination of iron cations in the presence of EDTA [251].

Apart from the functionalized graphenes owing excellent charge carrier performance, graphene derivatives similar to transparent fluorographene are potential candidates to perform as insulators and dielectric materials [252]. CVD-grown graphene with a thickness of 5 nm was doped by CF_4 plasma and characterized by Raman and XPS spectroscopy. Structural defects emerging from the networks' growth and chemical defects due to the doping were evident, while also it was shown that the fluorine content at the surface (15.9 at.%) was extremely higher than the bottom (0.06 at.%) of the functionalized nanocarbon. The latter is a fascinating result as even 60 min of plasma treatment reserves this unique junction, where the top layers are insulators and the bottom are conductive and actually a bifunctional layered framework is observed. Leakage current between the two phases was diminutive (0.5 nA) even at 5 V. Evidently, new horizons have yet to be unveiled by combining such frameworks with the above discussed methodologies.

4.1.1. Optical limiting

Optical limiting materials have been prepared by covalently grafting strong visible light absorbing molecules on the graphene lattice. Strong intra-hybrid electron and/or energy transfer phenomena play important role in the optical limiting performance and a variety of light-harvesting molecules can be combined with graphene. In a first example, a six-ring conjugated oligothiophene (6 T) having an amine group was chemically attached on graphene oxide via carbodiimide chemistry furnishing 6 T-GO owing a broad absorption band centred at 410 nm, due to the grafted oligothiophene molecules [253]. FT-IR revealed the characteristic vibrations at 1636 and 1576 cm^{-1} related to the newly formed amide bond between the individuals, while in the magic angle spinning (MAS) ^{13}C NMR spectrum the carbon atoms of the 6 T thiophene were evident, accompanied by a partial reduction of the graphitic lattice due to the coupling agent ($\text{N,N}'$ -diisopropylcarbodiimide, DIC), which has dehydrating properties. Moving to the optical properties of the 6 T-GO ensembles, the light absorption of 6 T-GO was linearly dependent to the concentration in the range of 0–25 mg/L and the fluorescence emission of 6 T within the ensembles was found quenched by 98% suggesting electronic communication under excitation. Moreover, the hybrid material was evaluated as an optical limiter, namely for its ability to strongly attenuate strong electron beams. For these studies a pulsed laser source of 532 nm was employed and the thickness of the samples was adjusted to equal linear transmittance (65%) and fullerene C_{60} used as a reference. The sample was moved close to the tightly focused laser beam and measured the transmittance for two photon absorption (TPA). The dip of the curve observed by plotting the transmittance vs the sample distance was higher for the 6 T-GO indicating that the hybrid material possesses better properties than the individual components (6 T and GO) and the reference (C_{60}).

Another example of such a system scrutinized a covalently grafted tetraphenylporphyrin (TPP) derivative [254]. Firstly, graphene oxide was activated by thionyl chloride in order to promote the conversion of the carboxylic acids to the corresponding highly reactive acyl chlorides and an amino derivative of TPP (TPP-NH_2) was added in order to perform the amide condensation reaction affording TPP-GO. The formation of the amide bond was evidenced by FT-IR and the intense absorption in the UV-Vis spectrum of the Soret band arising from the porphyrin unit. The absorbance of the ensemble was linear for up to 40 mg/L, better than the previous oligothiophene-based hybrid. As shown in Fig. 10, the open-aperture Z-scan results show the highest curve dip for TPP-GO and interestingly is much more intense than the control sample, being a 1:1 mass blend of TPP-NH_2 and GO. Similar studies have been also reported for a covalently grafted tetra(p-aminophenyl)porphyrin, TAPP, however the curve dip recorded for the TAPP-GO was

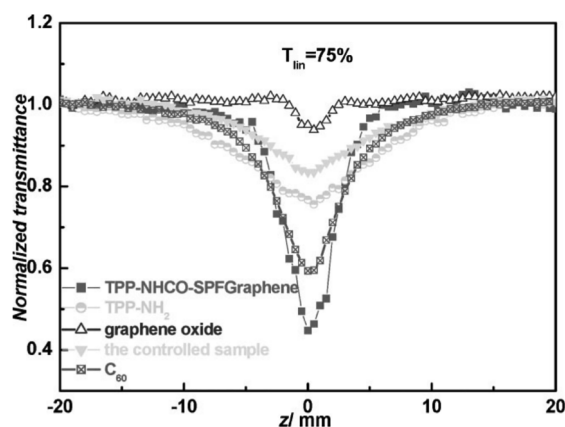


Fig. 10. Open-aperture Z-scan results of TPP-NHCO-SPF graphene, TPP-NH₂, graphene oxide, control sample, and C₆₀, with the same linear transmittance of 75% to 5 ns, 532 nm optical pulses. Reproduced with permission from Ref. [254]. Copyright 2009 Wiley.

moderate lower than the free TAPP [255]. Intra-hybrid electronic communication affects the non-linear properties of the ensemble and porphyrin provides a versatile template to explore such phenomena. More specific, the impact of the coordinated metal cation to a 5-(p-hydroxyphenyl)-10,15,20-tritoly porphyrin, MHTP, was employed for the study of the corresponding MHTP-GO ensemble containing Zn⁺², Cu⁺², Sn⁺⁴ and oxovanadium (II) [256]. The prepared metallo-MHTP dyes were chemically incorporated on GO-Cl via esterification as monitored by IR spectroscopy. Time-resolved fluorescence spectroscopy showed the fast deactivation of the excited macrocycle in the presence of coordinated metal, manifesting the strong interactions induced by the metal cations. Z-scan curves for the metallated MHTP-GO hybrids revealed negligible differences as compared to the non-metallated ensemble. In all cases the NLO behaviour of the covalent ensembles were orders of magnitude better than the corresponding free dyes and significant changes between the tested covalent ensembles were unveiled under 532 nm excitation at the nanosecond regime. Non-metallated porphyrin-GO had the best properties followed by the metallated ones in the order oxovanadium > Cu⁺² > Zn⁺² > Sn⁺⁴.

Concerning the chemistry employed for the covalent attachment of TPP molecules on the graphene lattice, in another approach the 1,3-cycloaddition reaction of azomethine ylides was scrutinized in two ways on chemically reduced graphene oxide: i) by 1,3-cycloaddition of a hydroxybenzaldehyde-terminated ylide, followed by alkylation of the hydroxybenzaldehyde by 5-[4-(2-bromoethoxy)phenyl]-10,15,20-triphenylporphyrin, and ii) by direct addition of a 4-formylphenoxyethoxy-triphenylporphyrin derivative [257], as shown in Fig. 11. Interestingly, the non-linear properties of the differently prepared TPP-rGO ensembles are almost identical, as evidenced by the open-aperture Z-scan results, indicating the independence of the chosen chemical protocol. Analogous results were obtained by performing the functionalization reactions adopting the diazonium chemistry [258].

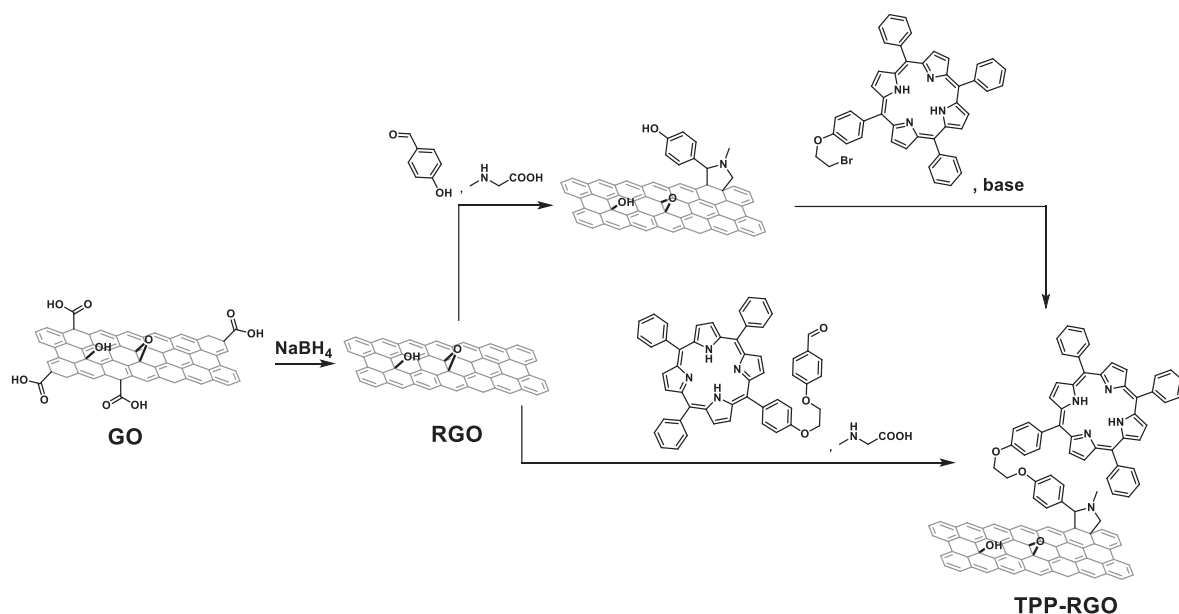


Fig. 11. Chemical routes to functionalize RGO with porphyrin molecules.

graphitic network. The generation of nanogaps drastically decreases the conductivity of the corresponding transistor devices. Reconnection of the nanogaps with the aid of conducting molecular wires restores the conductivity of the device and depending on the nature of the molecular wire photo- and/or chemical switching of conductivity is possible.

Organic molecules having free terminal amine groups covalently bridge graphene nanosheets. Oligophenylenes are the simplest candidate to connect the point contacts and regain the conductivity of the device [267,268]. The length of the molecular wire is depended on the distance of through space separating the patterned edges. In this respect, the nanogaps can be ultra short in a scale of ~ 1 nm and up to 10 nm, while also further modulation of the graphene electrodes can be realized by using ionic liquids as gate dielectric [269].

Among the most interesting molecular architectures is the integration of the photoresponsive symmetric diarylethylene derivative [265,266]. Under UV irradiation (about $100 \mu\text{W}/\text{cm}^2$, 365 nm) the molecules are found in the conjugated closed form, whereas under visible irradiation possess the non-conjugated opened form. Evidently, the charge mobility along the patterned graphene "islands" is mediated by the closed or opened form of the covalently grafted organic switch. Photoconductivity measurements have revealed that UV irradiation results to higher photocurrents, as a result of the good conductance provided by the delocalized π -orbitals of the closed form. The latter is supported by the zero-bias voltage transmission (T_0) assays. For the opened conformation no significant transmission channels at the energy range of -0.05 to 2.00 eV were observed. In contrast, the closed form generates an intense transmission peak at 1.2 eV corresponding to the perturbed LUMO level, closer to the Fermi level than the opened form (2.00 eV). Tuning the substituent atoms of the 5-membered ring hosting the ethylene unit gives further access to the HOMO-LUMO engineering of the molecule and on/off ratios ranging from 60 to 300 were recorded.

Along the same lines, azobenzene bridges have been utilized for their photochromic properties, namely the *trans* to *cis* conversion of the N=N bond geometry under ultraviolet irradiation [270] (Fig. 13a). Oxygen ion plasma etching of a PMMA coated graphene sheet generated contacts with a 10 nm gap. The carboxylic acid terminus of the graphene point contacts was covalently coupled to the aniline terminated symmetric azobenzene wire, furnishing the graphene-wire junction. Recording the source-to-drain current (I_{SD}) versus the gate voltage (V_G) allowed the characterization of the intact, cut and re-connected devices. Evidently, the reconnection of the graphene nanosheet with the wire recovers the conductivity of the device (Fig. 13b) and allows the study of its response to external stimuli such as light wavelength. Under visible light, the azobenzene-based wire has a *trans* configuration, whereas under UV reforms to the *cis* geometry. The latter photochromic response is depicted to the recorded I-V graph, showing lower conductivity for the *cis* configuration (Fig. 13c). Further insights of the photoswitching behavior of the azobenzene-connected device provided by recording the drain current via switching the irradiation source from visible to UV light and vice versa (Fig. 13d), demonstrating a stable reversible process. Taking advantage of the chemical properties of the azobenzene-based wire the chemical switch of conductivity was also evaluated. Since the molecular wire is in the form of a sulfonate-pyridine pair, low pH releases the pyridine and transforms the wire to the corresponding sulfonic acid. The recorded drain current at pH 1 was almost 60 times higher (~ 60 nA) than the corresponding recorded for the non-treated devices. A second step treatment with a base (pH 12) deprotonates the wire and results to slight decrement of the drain current in respect to the initial non-treated device. Repeating acid/base treatment of the device generates a stable chemical switching. Concerning the development of a chemical switch, covalent modification of the graphene point contacts with ligands enables the formation of coordination compounds which serve as conductive wires. Fig. 13e shows two possible ways to achieve the nanosheet interconnection by such assemblies. The ligand-functionalized graphene edges could be directly wired by the coordination of the metal center (for small distances) or another symmetric ligand may have been participated as a mediator (for higher distances). Adopting the coordination-mediated restore of conductivity is feasible for the preparation of on-off devices. The as prepared coordination compounds can be collapsed by extracting the metal cations by ethylenediaminetetraacetic acid (EDTA) or other chelates and turn-off the device conductivity. Actually, repeating cycles of treating the device with the cation followed by removal by EDTA demonstrated a stable chemical switch of conductivity [264].

By means of theoretical investigation, butadienimine [271], (E)- and (Z)- stilbene [272], polycyclic aromatic hydrocarbons [273,274], and 6,11-dioxo-5,6,11,12-tetrahydrobenzo[b]phenazine-1,4,7,10-tetracarbonitrile (DO-THbPA-TCN) [275] have been examined for their switching properties. Beyond wired nano-patterned graphene, strategies for the interconnection of graphene nanoribbons have been recently developed. As described in Fig. 14, the chemical attachment of a porphyrin on a graphene nanoribbon primer afforded GNRs branched around the porphyrin molecules [276]. This protocol ensures the chemical stability of the as-formed covalent hybrids and offer new insights into the preparation of efficient molecular junctions.

As previously discussed, chemical modification of graphene nanosheets with azobenzene derivatives [277–280] was introduced as handy probe for investigating photo-switching properties. Functionalization of a graphene monolayer with photoresponsive azobenzene derivatives via diazonium chemistry, generated nanosheets carrying a covalent columnar array, which can be sandwiched by a second monolayer [281]. The azobenzene units are in the *trans*-conformation under visible irradiation and switch to the *cis*-conformation under UV light. Changing the light source results to different conformation of the organic molecule and accordingly to different distances between the graphene monolayers accompanied by different light absorption properties. This structural switch results to different photocurrent gain. In this fashion, a highly efficient photo-switch device can be realized with highly reproducible photocurrents for the reversible *trans-cis* structural conformations. What should also be underlined is that the self-assembly of the second non-covalent graphene sheet is stable, highlighting the flexibility of the sandwich-like nanodevice. The same concept was also investigated for the case of solution processed graphene oxide nanosheets being modified with azobenzene units via diazonium chemistry [282]. In contrast to the previous study, the *trans-to-cis* transition was mediated by applying voltage.

Employing graphene oxide significantly reduces the cost of the fabricated devices and offer the advantage of solution processed device fabrication. Graphene oxide nanosheets have been also decorated by incorporating amine-terminated azobenzene units at their perimeter via condensation with the carboxylic acid functionalities [283]. XPS spectroscopy revealed a 3.7% percentage of N-atoms, which was sufficient in order to investigate the photo-switching properties of the azobenzene-graphene ensembles.

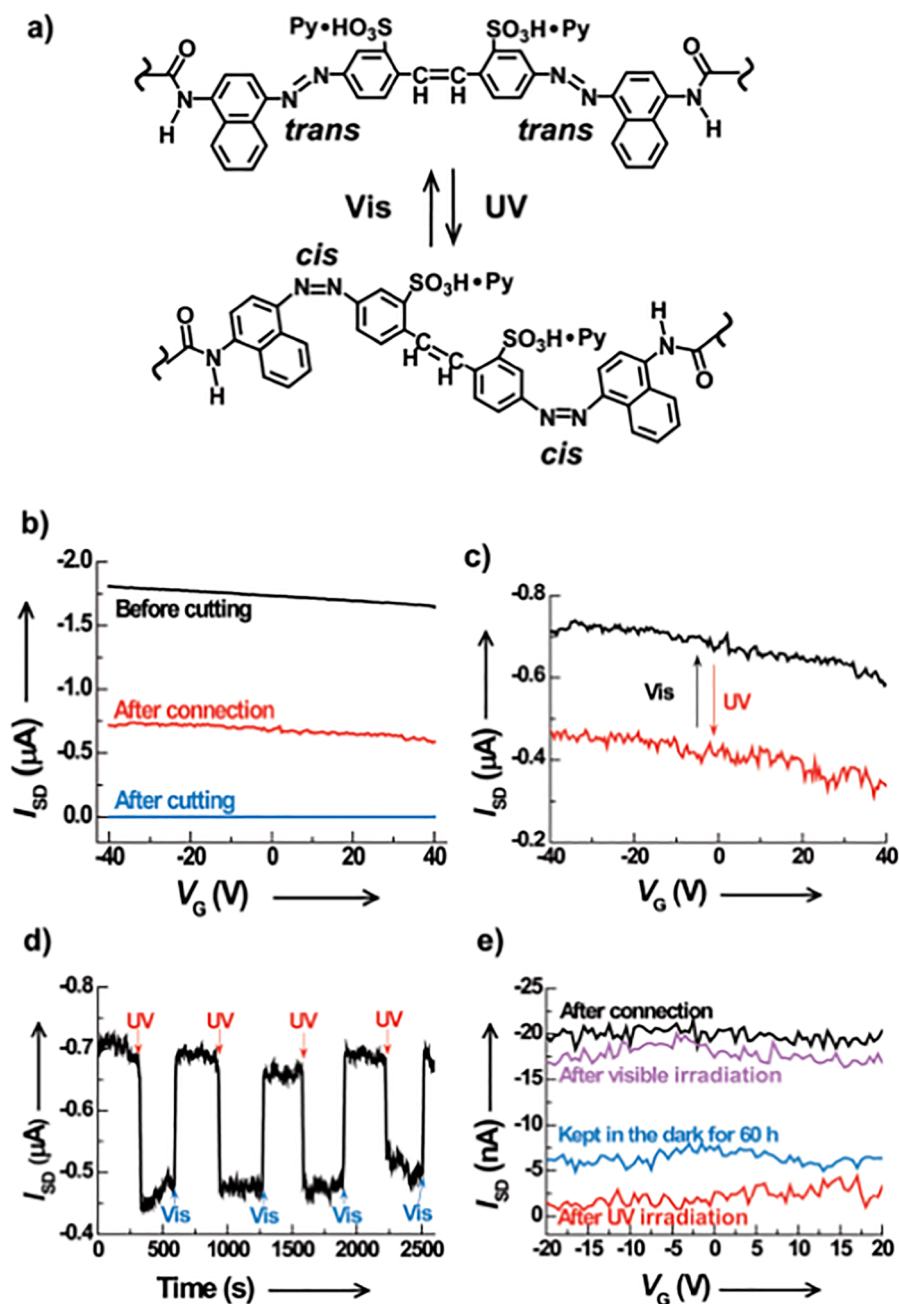


Fig. 13. Photoswitching properties of devices rejoined by azobenzene molecules. a) Schematic representation of the switching mechanism for the molecule responding to UV and visible light. b) Characteristics of a representative device reconnected with the azobenzene bridge before cutting (black curve, $V_{SD} = 1$ mV), after cutting (red curve, $V_{SD} = 50$ mV), and after connecting (blue curve, $V_{SD} = 50$ mV). c) Characteristics of the same device under UV ($\lambda = 254$ nm) and Vis-light irradiation ($\lambda > 460$ nm). $V_{SD} = 50$ mV. d) Time trace of the drain current for the same device showing the reversible photoswitching events under irradiation with UV light and Vis light. $V_{SD} = 50$ mV and $V_G = 0$ V. e) Characteristics of another reconnected device after connection (black curve), after UV irradiation (red curve), kept in the dark for 60 h (blue curve) and after further irradiation with visible light (magenta curve). $V_{SD} = 50$ mV. Reproduced with permission from Ref. [270]. Copyright 2013 Wiley.

Photoluminescence spectroscopy provided evidence for the effective electronic communication of the individual species, since the emission spectra of the excited azobenzene within the ensemble was found significantly quenched. The *trans*-to-*cis* transformation of the attached azobenzene units was monitored by irradiating the ensemble with UV pulses (365 nm) and subsequently recording the electronic absorption spectrum. Gradually, the absorption maxima at ~ 400 nm, owed to the *trans* configuration, decays, indicating the formation of the *cis*-conformer with a characteristic maxima at ~ 300 nm. Recording the I-V characteristics for the hybrid material, a clear photoresponsive behavior was observed. The latter was further validated by recording the generated photocurrents

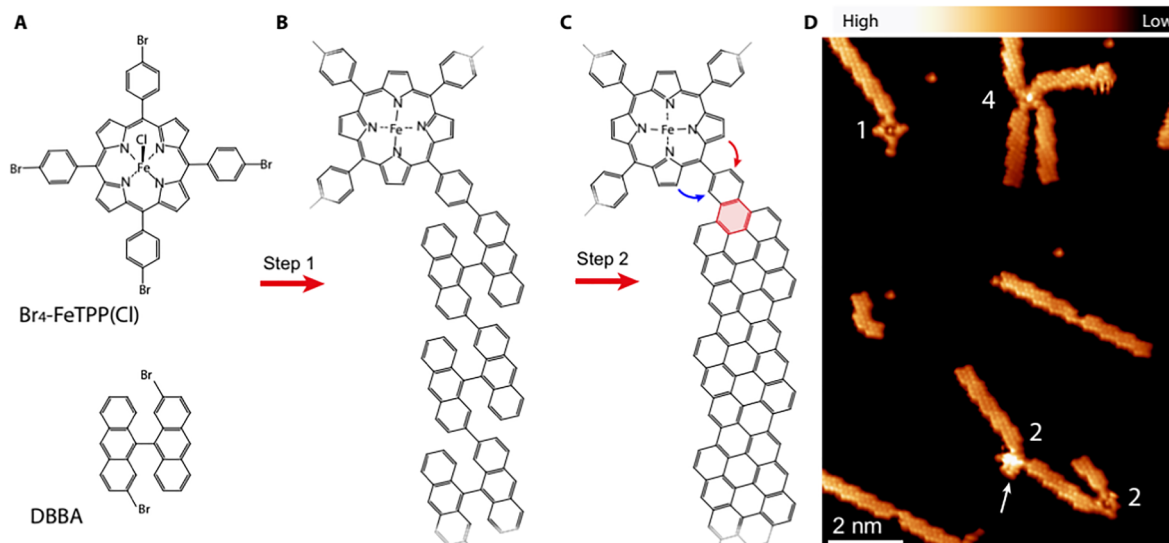


Fig. 14. Synthetic strategy to produce hybrid molecular systems composed of a magnetic FeTPP bonded to graphene nanoribbons. (A) Structure of the monomers DBBA and $\text{Br}_4\text{-FeTPP(Cl)}$ used for the on-surface reaction. DBBA is three-dimensional, appearing with two enantiomeric forms on the substrate. (B) Structure of a hybrid polymer of covalently linked monomers created after the Ullmann coupling step. At the annealing temperatures, the Cl ligand of the porphyrin is detached, whereas the DBBA molecule maintains its three-dimensional shape. (C) Structure of a molecular hybrid after the CDH step. The CDH reaction forms the new ring shadowed red in the image and can additionally fuse the porphyrin core in a clockwise (red arrow) or anticlockwise (blue arrow) manner to the contact phenyl. The fusion renders planar structures, in contrast to the known saddle shape of pristine FeTPP fragments. Note that two mirror-symmetric bonding configurations can form, depending on the chirality of the graphene nanoribbon. (D) High-resolution dI/dV image measured at constant height with a CO-terminated tip [$V_s = 5$ mV, $V_{ac} = 2$ mV root mean square (rms), and $R_t \sim 1$ gigaohm over pristine $\text{Au}(1\ 1\ 1)$ regions], showing several molecular hybrids created on a $\text{Au}(1\ 1\ 1)$ surface. Numbers quantify the graphene nanoribbons connections to each of the four porphyrin centers of the image. The arrow points to an FeTPP moiety with a three-dimensional structure, whereas the other three on the image are planar. Reproduced with permission from Ref. [276].

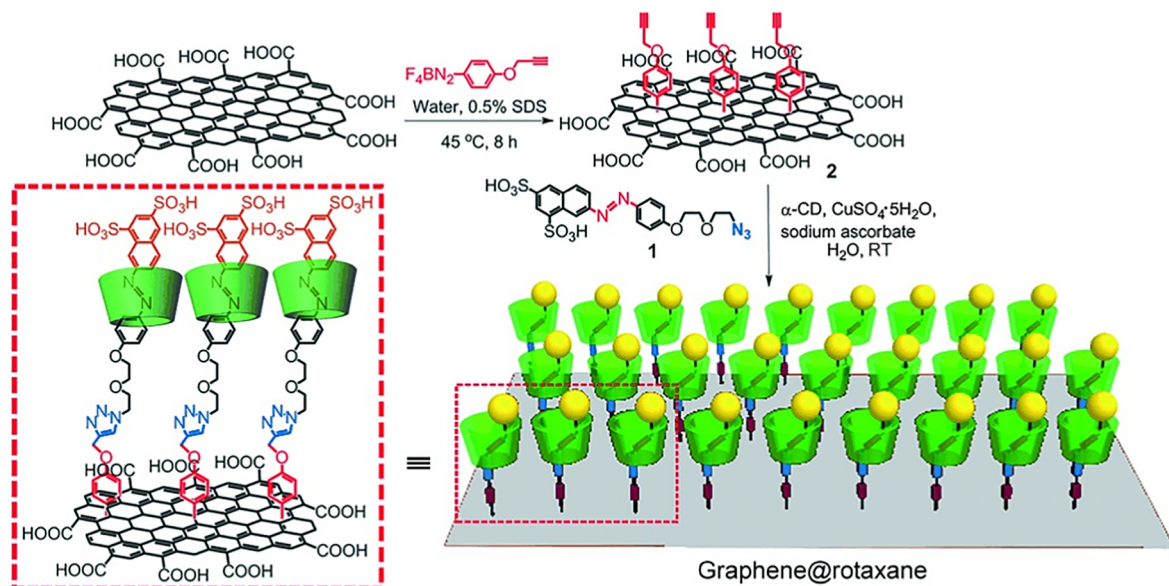


Fig. 15. A representation of the preparation of [2]rotaxane-functionalized GO. Reproduced with permission Ref. [284]. Copyright 2012 Wiley.

under on-off conditions. Under UV irradiation the generated photocurrent for the covalently bound azobenzene on graphene was 800% higher than that due to free azobenzene, suggesting that the photogenerated charges on azobenzene are efficiently scavenged by the nanosheets, which are excellent electron acceptors.

The versatile chemistry of azobenzene molecule allowed the exploration of rotaxane-like nanoarchitectures covalently immobilized on graphene oxide [284]. In this example, graphene oxide nanosheets were initially modified with an alkyne-terminated

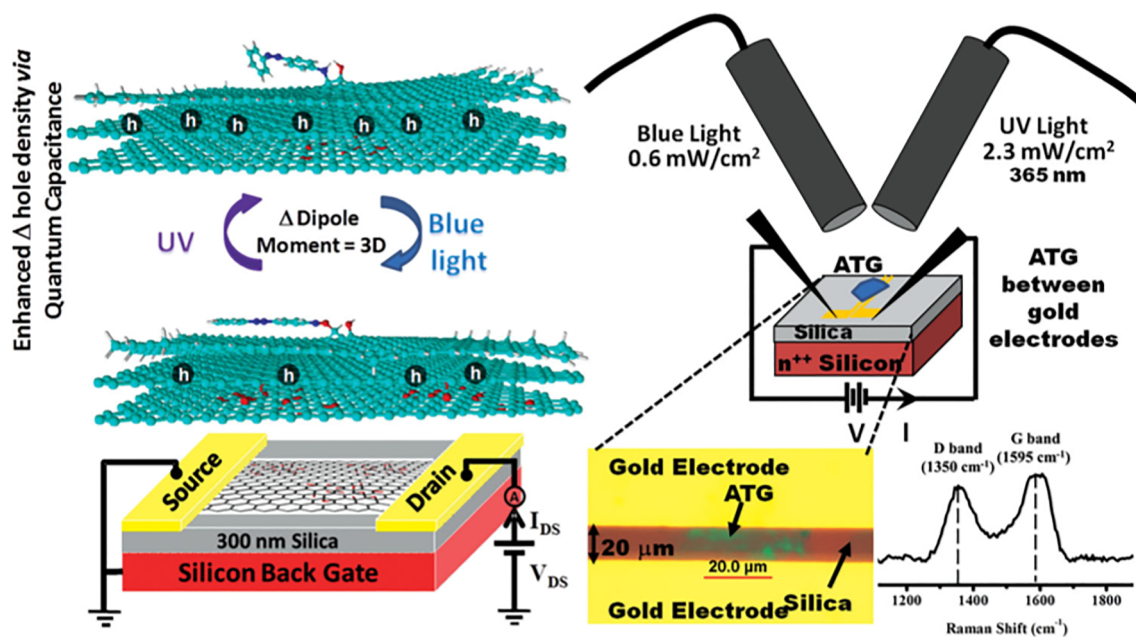


Fig. 16. Representative model showing azobenzene molecules covalently bonded on the sp^3 regime of functionalized graphene. The azobenzene group changes its configuration on graphene (trilayer) when exposed to UV (cis) and blue light (trans). This mechanical motion of azobenzene modulates the density of holes in ATG. Bottom right: The optical image of ATG device between the gold electrodes $20\ \mu\text{m}$ apart. The Raman spectrum of the ATG sheet shows the D and G peak representing the graphenic backbone. Since graphene is functionalized, the Raman spectrum shows a D peak at $1350\ \text{cm}^{-1}$. No appreciable 2D peak was observed. Reproduced with permission needed from Ref. 285. Copyright 2013 Wiley.

arene via diazonium chemistry. Then, the modified nanosheets were mixed with the azide-terminated azobenzene derivative and α -cyclodextrin (α -CD). The azobenzene-derivative was self-assembled into the cavity of α -CD forming a mechanically interlocked architecture, which was grafted on the graphitic surface via a Huisgen [3 + 2] cycloaddition reaction, as described in Fig. 15. Raman spectroscopy provided direct evidence for the chemical attachment of the azobenzene-derivative by detecting the two new modes at 2000 and $2270\ \text{cm}^{-1}$ attributed to the azobenzene unit. The presence of the mechanically interlocked [2]-rotaxane array was evaluated by thermogravimetric analysis and the loading was as high as 40.2%. It should be noted that the rotaxane array provides also enhanced stability of the ensembles in liquid media, due to the presence of sulfonic groups and the presence of the α -CD. As long as the system is irradiated with ultraviolet light, the *trans*-to-*cis* isomerization occurs, pushing the α -CD along the molecular wire connecting the azobenzene with the graphene. Monitoring the absorbance of the ensembles at $370\ \text{nm}$, after exposure to visible and ultraviolet irradiation, a photoresponsive reversible behavior was evident for up to 5 cycles.

Trans-to-*cis* isomerization of azobenzene covalently grafted on graphene was also utilized for the modulation of the dipole moment [285]. A trilayer GO was covalently modified by an amino-terminated azobenzene via amidation and deposited on a silica dielectric substrate (Fig. 16). Under UV irradiation, *trans*-to-*cis* isomerization occurs and induces the generation of an effective gating voltage, since 6 units of holes are produced per azobenzene molecule and constitute an overall hole density increment by $440 \times 10^3\ \text{holes}/\mu\text{m}^2$. With this design a high quantum capacitance of $72.5\ \mu\text{F}/\text{cm}^2$ was observed, indicating the high sensitivity of the reversible dipole moment change.

Moving from the photoinduced structural transitions, pyrene was investigated as a tunable probe based on its folding/unfolding properties [286]. Pyrene molecules having an alkyl-chain terminated to an amine were used for the chemical attachment to GO. Pyrene molecules have strong tendency to form excimers by strong intermolecular attractive π - π interactions. The latter effect was investigated for its impact on the generated photocurrent upon photoexcitation of the pyrene-graphene oxide ensembles 4-GON, while sodium dodecylsulfonate (SDS) was used as blocking agent for the pyrene-pyrene interactions. Pyrene-pyrene stacking within the ensembles results to lower fluorescence emission intensity due to fast deactivation of the excited states via electron transfer to graphene (Fig. 17a). In contrast, incorporation of SDS disturbs the excimer formation and generates fully unfolded pyrene monomers (4-GON/SDS), resulting with higher fluorescence emission intensity due to deactivation directly to the ground state, without electronic communication with the nanosheets (Fig. 17b). Complementary time-resolved fluorescence spectroscopy studies revealed that the lifetime of the singlet excited state of unfolded pyrene moieties within the pyrene-GO was $\sim 75\ \text{ps}$, whereas in the folded state the corresponding lifetime found to be below $30\ \text{ps}$. Evidently, the excimer formation mediates the photoinduced electron/energy transfer from the photoexcited pyrenes to the nanosheets. Photocurrent generation was measured by fabrication of photoelectrodes by deposition of the pyrene-GO on ITO electrodes. As shown in Fig. 17c, incorporation of SDS strongly reduces the output of the photoelectrode highlighting the importance of the π - π interactions within the pyrene units of pyrene-GO ensembles. In accordance to the photocurrent yielded differences, the quantum efficiency of the photoelectrodes in the visible region was higher in the absence of SDS, namely in the case where pyrenes adopt the folded conformation (Fig. 17d).

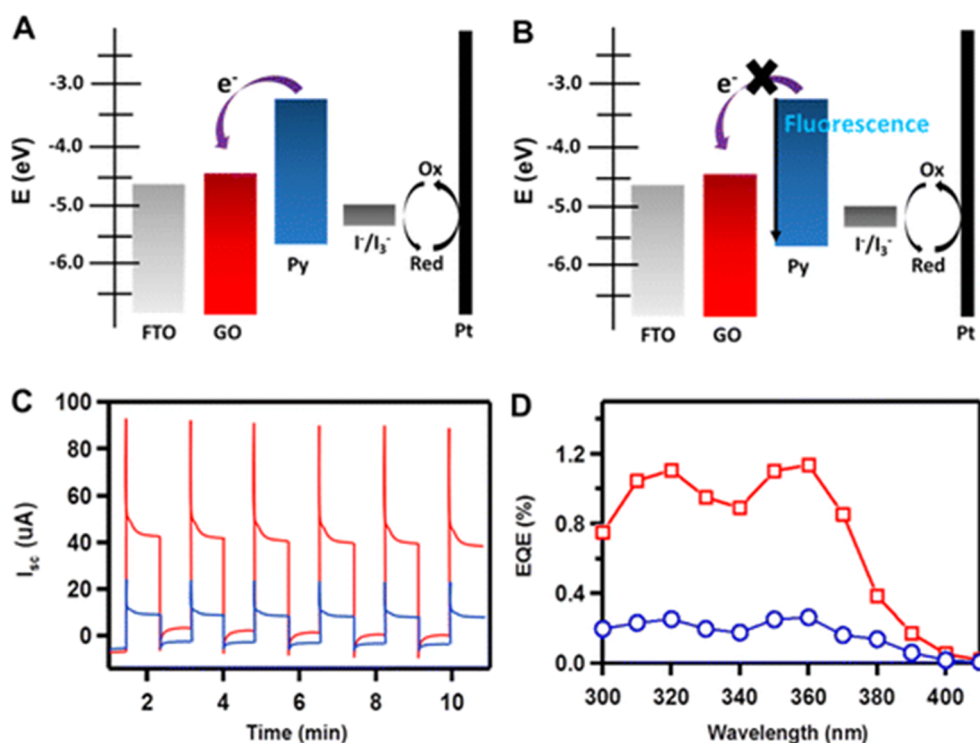


Fig. 17. Schematic illustration of the energy level with respect to vacuum level for (a) 4-GON, and (b) 4-GON/SDS. The arrows indicate electron flows. Photocurrent density (c) and incident photon to current conversion efficiency (d) response under white light illumination at 100 mW/cm^2 . Reproduced with permission from Ref. 286. Copyright 2015 American Chemical Society.

4.1.3. Solar energy conversion

One of the most active research areas in optoelectronics is the exploitation of the photovoltaic effect towards efficient solar cells. The quest for non-silicon materials was met by the isolation and manipulation of graphene sheets. Atomically thick graphene absorbs a higher portion of light ($\sim 2.3\%$) [20] than the corresponding of a silicon layer of equal thickness ($\sim 0.03\%$) [287] and despite the absence of a bandgap it can be functionalized with a great variety of molecules.

Nanodevice fabrication requires highly quality graphene, nevertheless the cost of CVD grown or (micro)mechanically exfoliated graphene is extreme high. In this respect, the quest for solution processable graphene-based functional materials has emerged. Graphene oxide is the most common graphene platform offering the advantage of high yield and dispersibility in liquid media. Spin-coated GO on ITO substrates and UV-treatment for cleaning the surface from adsorbed organics is a prominent approach for the deposition of organic light emitting diodes [242]. Moreover, graphene oxide was realized as hole transport material in polymer solar cells by interpolating the active layer, poly(3-hexylthiophene) (P3HT):phenyl- C_{61} -butyric acid methyl ester (PCBM), and the transparent conductive ITO anode [288]. Also, laser-assisted reduction (photoreduction) of GO was also proposed as an alternative way of nano-manipulation of the nanosheets and the potential of substituting the ITO layer by graphene materials setting a 1.1% PCE [289]. Poly(3,4-ethylenedioxythiophene) polystyrene sulfonate, more commonly known as PEDOT:PSS, is a mixture of two ionomers with extended use in the fabrication of transparent electrodes as hole transport layer with improved chain dispersibility when it is covalently attached on graphene [290]. The covalent attachment was performed by employing an alkyne terminated GO derivative and a PEDOT- N_3 :PSS mixture and the click Huisgen cycloaddition reaction between the two components. Interestingly, the formation of the triazole rings improved the conductivity of the composite and decreased the agglomeration of the PEDOT:PSS blend, however, the overall thermal stability was also decreased due to instability of the triazole rings.

Graphene nanosheets have been widely explored for the fabrication of dye sensitized solar cells (DSSCs) [37]. Structurally defected graphene, derived by thermal exfoliation of GO was successfully introduced in as counter electrode, outperformed by only 10% the classic platinum based electrodes [291]. Finally, thermally reduced graphene was also scrutinized as a substituent for the ITO electrodes in DSSCs yielding a PCE of 0.26%, nevertheless lower to the reference device fabricated with a ITO anode (0.84%) [241]. However, chemically reduced graphene covalently decorated by hemin showed improved efficiency as counter electrodes for DSSCs [292]. In this case, GO treated with ethylenediamine under microwave irradiation gave amine terminated nanosheets, which were then coupled with the carboxylic acids of hemin via carbodiimide mediated condensation. The hybrid material was subsequently treated with hydrazine to reduce the remaining oxygen functionalities present, furnishing the hemin-RGO ensembles. FT-IR spectroscopy and TGA analysis verified the covalent incorporation of hemin and the success of the reduction step. The as-prepared material was stable in DMF and acetone dispersions, enabling the drop-casting deposition on FTO glass substrates for the DSSC fabrication. Impedance spectroscopy shed light to the electron transport properties of hemin-RGO versus the I_3^-/I^- electrolyte.

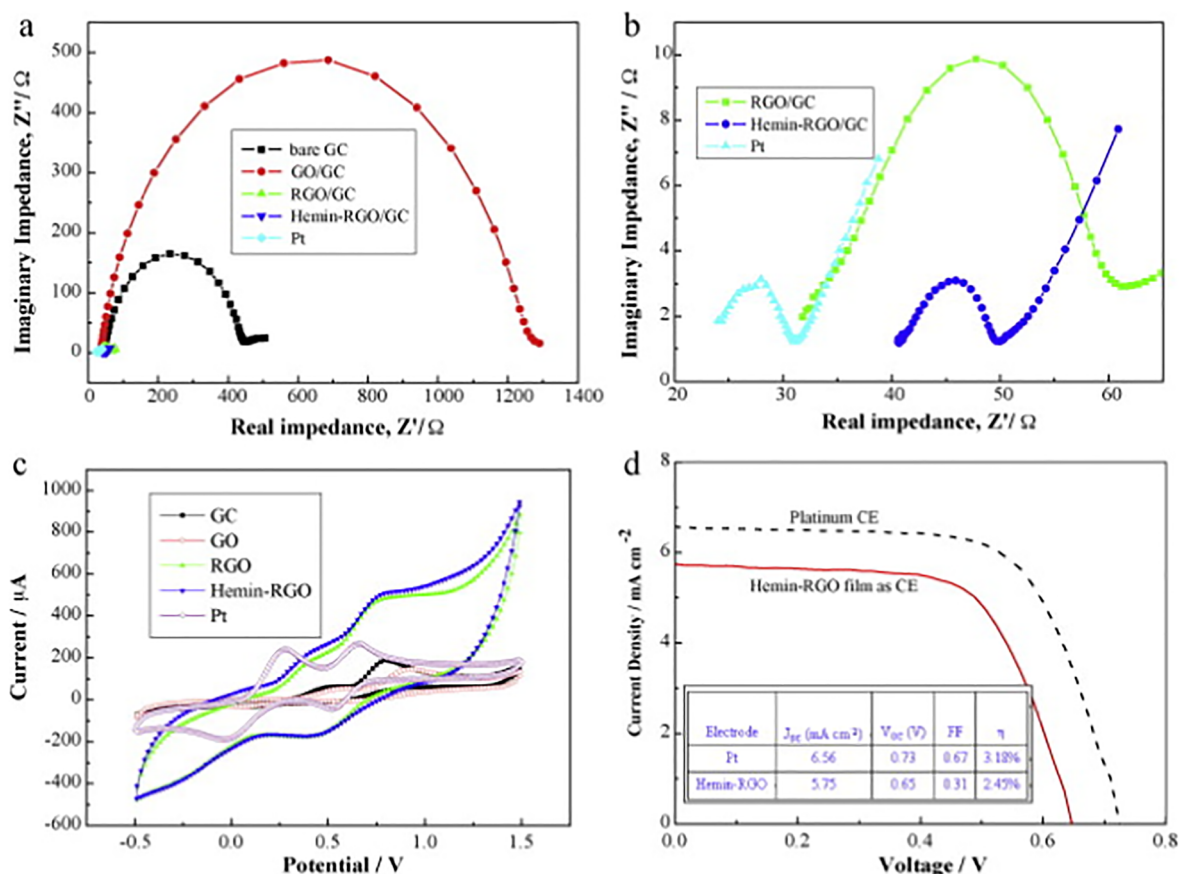


Fig. 18. a) Nyquist plots for bare GC, GO/GC, RGO/GC, hemin-RGO/GC, and Pt in acetonitrile solution of 10 mM LiI and 1 mM I₂. (b) Magnified Nyquist plot of RGO/GC, hemin-RGO/GC and Pt. (c) CV curves for bare GC, GO/GC, RGO/GC, hemin-RGO/GC and Pt. (d) Current-voltage characteristics of DSSCs with hemin-RGO and Pt counter electrodes. The inset exhibits the current-voltage parameters of DSSC with graphene and platinum counter electrodes under simulated solar illumination. Reproduced with permission from Ref. [292]. Copyright 2012 Elsevier.

Nyquist plots revealed very low charge transfer resistance (R_{CT}) at the counter electrode/electrolyte implying a facile I₃⁻ to I⁻ reduction (Fig. 18a, b). Specifically, the value recorded for hemin-RGO (9 Ω) is comparable to counter electrodes prepared from platinum on FTO substrates (7 Ω). Moreover, from the comparable I-V characteristics of DSSCs, having Pt or hemin-RGO counter electrodes (Fig. 18d), the potential of graphene-based hybrids for substituting platinum materials was highlighted.

Activation of GO by SOCl₂, followed by attachment of an amine-terminated ethylenedinitrobenzene (EDNB), afforded ink-like dispersions used for the preparation of organic ternary solar cells with the EDNB-graphene being the electron-cascade acceptor material, namely mediating the transfer of charges between the poly[N-9'-heptadecanyl-2,7-carbazole-alt-5,5-(4',7'-di-2-thienyl-2',1',3'-benzothiadiazole)] (PCDTBT) electron donor and the [6,6]-phenyl-C₇₁-butyric-acid-methylester (PC₇₁BM) electron acceptor [293]. The interfacial interaction of the EDNB-graphene with the photoactive layers generated a more efficient exciton dissociation and provided a conductive path between them. Under the same chemical strategy, the chemical incorporation of a tetraphenylporphyrin (TTP-NH₂) on GO showed enhanced photocurrent gain, as compared to the individual species [294]. Specifically, the on/off density of the recorded photocurrent was 47 mA/cm², which is 6-fold higher than the corresponding simply electrostatically stacked porphyrin/graphene ensembles. The strong intrahybrid interaction was also evidenced by the 59 nm red-shift of the absorption on the Soret band of the TPP within the TPP-graphene ensembles as well as from photoluminescence assays where the emission of TPP was found quenched and blue-shifted.

Moreover, an analogous TPP-graphene derivative was exploited as an electron cascade material in ternary organic solar cells [295]. In this case, TPP-graphene was introduced into the sandwich-like layered structure of the solar cell as layer interfacing with the poly [4,8-bis (2-ethylhexyl)oxy]benzo[1,2-b:4,5-b']dithiophene-2,6-diyl3-fluoro-2-[(2-ethylhexyl) carbonyl]thieno [3,4-b]thiophenediyl (PTB7) electron donor and the PC₇₁BM electron acceptor. Compared to the reference device, where the TPP-graphene was not introduced into the blend, the impact of TPP-graphene was beneficial, since a 16% enhancement to the recorded PCE (8.81%) was achieved. A hydroxyl terminated region-regular poly(3-hexylthiophene) (rrP3HT) electron donor was also covalently incorporated on acyl activated graphene oxide nanosheets, furnishing rrP3TH-graphene oxide ensembles, which utilized as active layer in bulk heterojunction (BHJ) solar cells, with C₆₀ as the electron acceptor [296]. The observed power conversion efficiency was as high as 0.61%, which is a 200-fold increment as compared to rrP3HT/C₆₀ blends, highlighting the impact of the graphene nanosheets on the separation of the photogenerated excitons.

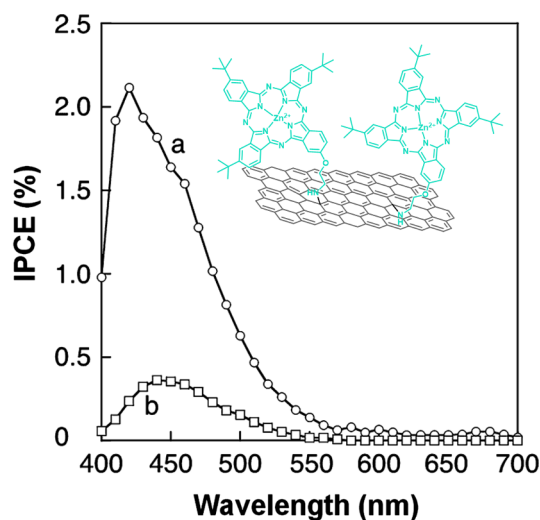


Fig. 19. Photocurrent action spectra of (a) OTE/SnO₂/ZnPC-graphene and (b) OTE/SnO₂/graphene (two-electrode system). Electrolyte: 0.5 M LiI and 0.01 M I₂ in acetonitrile. Reproduced with permission from Ref. [298]. Copyright 2012 American Chemical Society.

Other sources of graphene have been also scrutinized for the preparation of photoactive layers for solar cells. Brominated graphene, prepared by treatment of graphene oxide with bromine, was covalently functionalized by in-situ grafting-to polymerization. Briefly, the brominated graphene was introduced in a mixture of 9,9-dihexylfluoren-2,7-ylidiboronic acid and 4,7-dibromo-2,1,3-benzothiadiazole and a Pd-catalyzed Suzuki cross-coupling reaction was performed [297]. Despite the problematic processing of the PFBH-graphene active layer, due to strong aggregation tendency leading to low PCE (0.26%), the overall approach is another way to access functional materials in less synthetic steps.

Apart from BHJ solar cells, graphene materials have been tested in photoelectrochemical cells as photoanodes. More specific, exfoliated graphene covalently decorated by (2-aminoethoxy)(tri-*tert*-butyl) zinc phthalocyanine (ZnPC) was electrodeposited on tin oxide (SnO₂) coated glass substrates and the incident photon to current efficiency (IPCE) was recorded in I⁻/I₃⁻ electrolyte under broadband visible light irradiation [298]. The maximum IPCE value (2.2%) was observed at 420 nm, while on/off photocurrent studies revealed a steady gain of 10 mA/cm² (Fig. 19). Complementary nanosecond transient absorption spectroscopy and electron paramagnetic resonance spectroscopy shown the photoinduced generation of the ZnPC^{•+}-graphene^{•-} charge separated state, which is responsible for the enhanced current density under visible light irradiation. Covalent incorporation of the ZnPC was overall beneficial for the IPCE properties, since the simply mixed individuals resulted to a low 0.3%. Other metallophthalocyanines were also utilized [299].

Following an analogous approach, GO was decorated by TPP-NH₂ via carbodiimide chemistry, furnishing TTP-graphene ensembles [300]. The incorporation of the TPP was validated by FT-IR and TGA analysis, while UV-Vis and photoluminescence spectroscopy showed a 2 nm bathochromic shift of the Soret band and strong emission quenching accompanied by a blue-shift, respectively, suggesting strong intra-hybrid electronic interactions. Complementary time correlated single photon counting (TCSPC) spectroscopy revealed a shorter lifetime for the covalently bound ¹TPP* (675 ps, 1.6 ns), while nanosecond transient absorption spectroscopy provided evidence for the photoinduced charge separation and the life time of the TPP^{•+}-GO^{•-} separated state (45 ns). A maximum IPCE value of 1.3% was recorded at 420 nm, where the maximum absorbance of the TPP is present.

Another approach for chemically attaching porphyrins on GO was realized by pre-functionalization with iodobenzene units, based on a diazonium chemistry protocol, followed by reaction with a boronylated zinc porphyrin chromophore [301]. X-ray photoelectron spectroscopy was employed to monitor the pre-functionalization step and the porphyrin addition by the iodine content. For the iodoarene-functionalized nanosheets the iodine content was 2.25%, while for the porphyrin-GO hybrid material was diminutive (~0.02%) indicating the success of the coupling reaction. UV-Vis absorption spectrum of the porphyrin-GO ensemble displayed the characteristic Soret band of the porphyrin, red-shifted by 3 nm proving electronic communication at the ground state. The photo-induced phenomena taking place were probed by transient absorption spectroscopy and no peak related to the oxidation of the porphyrin was evident, thus energy transfer from the singlet excited of the porphyrin to the nanosheets is the dominant deactivation pathway. Moving to the photoelectrochemical properties of the ensembles, the hybrid material was electrodeposited on FTO substrates and tested in I₃⁻/I⁻ electrolyte. A 3% IPCE value was recorded at 400 nm, where the porphyrin absorbs the major portion of visible light.

Taking advantage of the intra-hybrid electronic communication within porphyrin-graphene ensembles under photoexcitation and by employing plasmonic nanoparticles to benefit from the plasmon resonance absorption effect, further improvements in the photogenerated current can be achieved [302]. Moreover, utilization of different redox mediators, i.e. methyl viologen and nucleosides, may induce additional improvements. In this respect, water soluble 5-[4-(succinimide-N-oxycarbonyl)phenyl]-10,15,20-tris(N-methylpyridinium-4-yl) porphyrin tri-iodide (Por) was covalently incorporated on graphene, mixed with gold nanoparticles (GNP) and redox mediators (i.e. methyl viologen) and drop-casted on clean ITO electrodes as shown in Fig. 20. Irradiation of the electrodes

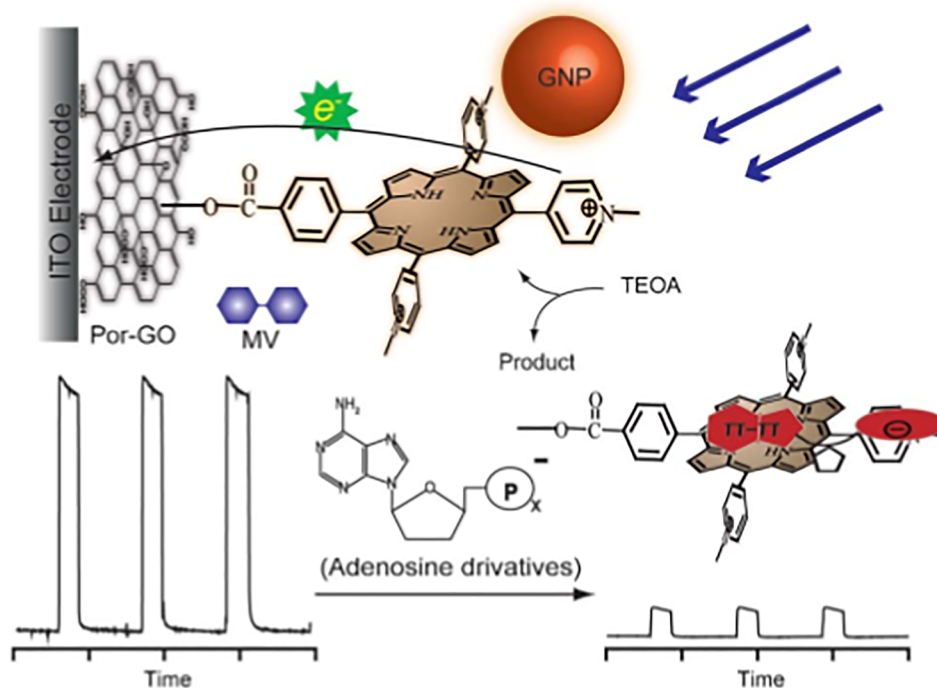


Fig. 20. An illustration of photocurrent generation on the Por-GO-GNP-MV functionalized surface and the photocurrent decrease induced by its interaction with nucleotide. Reproduced with permission from Ref. [302]. Copyright 2013 Royal Society of Chemistry.

coated by the Por-GO/MV/GNP bulk heterojunction showed the maximum photocurrent output and interestingly the presence of GNPs enhances by 6 times the recorded values as compared when the control Por-GO/MV photoelectrode was used.

As previously discussed, hybrid Por-GO/MV/GNP electrodes were studied as photoanodes. Using triethanolamine as hole scavenger and different adenosine derivatives (adenosine, AMP, ADP, ATP) as electron acceptors, the quenching of photocurrent was also investigated. As witnessed the observed photocurrent decreases in the order AMP > ADP > ATP > adenosine. In fact, these photoinduced electrode surface/analyte interactions constitute a process for monitoring the concentration of these nucleotides in solution.

Apart from the already presented covalently functionalized graphenes, there are more examples of chemically modified graphenes with photoactive molecules managing photoinduced processes. We present herein, a series of such nanoarchitectures with potential for optoelectronic applications. In a first example, protoporphyrin IX (PIX) was immobilized via electrostatic interactions on a negatively charged ionic liquid derivative covalently grafted on graphene oxide [303]. Graphene oxide was activated by oxalyl chloride (COCl_2) and then the imidazole-based ionic liquid 1-(3-aminopropyl)imidazole (API) was introduced in the dispersion to promote the formation of an amide bond, as evidenced by FT-IR. After, the imidazole ring was alkylated by 1-bromobutane furnishing the positively charged imidazole ring with bromide as counter anion. PIX, is a negatively charged natural porphyrin bearing two carboxylic groups. Treating the PIX disodium salt with the API-graphene oxide, an exchange of the counter anion occurs leading to the electrostatic stabilization of the negatively charged PIX on the positively charged imidazole rings of the nanosheets. UV-Vis and photoluminescence spectroscopy revealed strong intra-hybrid electronic coupling, which it was also supported by electrochemical studies (DPV).

Graphene nanosheets derived by liquid-assisted exfoliation of graphite have been used for the covalent attachment of (metallo) porphyrins via 1,3-dipolar cycloaddition reactions. (Metallo)porphyrins bearing an aldehyde functionality reacted with N-methylglycine in the presence of exfoliated graphene. The as prepared (metallo)porphyrin functionalized graphene nanohybrids bear one chromophore unit per 235 carbon atoms of the lattice, as calculated by TGA analysis [304]. Raman spectroscopy further supported the chemical disruption of the graphitic lattice due to the cycloaddition reaction, showing the evolution of the D-band and a I_D/I_G around 0.22. For the case of the Pd-metallated porphyrin, XP spectroscopy provided further evidence for the presence of the metallated-chromophore by the characteristic $\text{Pd}3d_{3/2}$ and $\text{Pd}3d_{5/2}$ peaks. Specifically, the observation of the binding energy at 338.5 eV ($\text{Pd}3d_{5/2}$) was assigned to the Pd-N bond, highlighting that the Pd atoms are still coordinated to the porphyrin macrocycle after functionalization. Time-resolved fluorescence spectroscopy showed the fast deactivation of the excited (metallo)porphyrins within the ensembles, while the phosphorescence quantum yield and lifetime were diminished, manifesting the presence of intra-hybrid electron/energy transfer processes.

Oligo(phenylvinylenes) (OPVs) are exceptional organic electron donors which have been employed for the covalent decoration of GO [305]. The design of the employed OPV was based on an amino-terminus for the attachment of GO, whereas the other terminus of the conjugate was a phenyl ring bearing three dodecyloxy substituents for enhanced solubility and the development of

complementary hydrophobic interaction with other nanosheets. As shown by TEM imaging, the covalent incorporation of the OPVs resulted to sandwich-like nanoarchitectures and strong interaction of the organic molecules with the nanosheets, as evidenced by photoluminescence and TCSPC spectroscopy. Such self-organization of modified nanosheets is of great importance for optoelectronics.

Another facile class of organic chromophores are phthalocyanines. Interestingly, metal-phthalocyanines with strong electron accepting properties proved to be able to accept electrons from graphene nanosheets under photoexcitation without being directly conjugated to graphene, but simply covalently bonded [306]. Exfoliated graphene nanosheets covalently functionalized with 4-[(trimethylsilyl)ethynyl]-benzene units via diazonium addition of the corresponding 4-[(trimethylsilyl)ethynyl]-aniline, were used for a click reaction with an azide terminated (2-ethylehexyl)sulfonyl zinc phthalocyanine (ZnPcSO₂). The as prepared ZnPcSO₂-graphene ensembles were fully characterized and the photoinduced phenomena taking place have been evaluated by means of femtosecond absorption spectroscopy. An ultrafast charge separation (1.0 ± 0.5 ps) was observed, manifesting the photoinduced electron transfer from graphene to the electron accepting ZnPcSO₂, setting a milestone for nanoarchitectures where graphene loses electron density upon irradiation.

Along the same lines, a zinc phthalocyanine bearing six *p*-(C₆H₄O*t*-Bu) and a C₆H₄OH group at the periphery of the macrocycle was covalently grafted on exfoliated graphene having carboxylic functionalities incorporated by a 1,3-dipolar cycloaddition reaction [307]. TGA analysis validated the presence of bonded ZnPc molecules on the graphene surface, 6.5% w/w, while FT-IR spectra had the characteristic 1730 cm⁻¹ stretching related to the ester bond formed between the graphene sheets and the chromophore. Strong intra-hybrid electronic communication was unveiled by transient absorption spectroscopy studies. Specifically, excitation of the hybrid material at 387 nm, where the chromophore absorbs light, results to bleaching in the absorption spectra at the region 500–800 nm with distinct features at 650, 735, and 770 nm corresponding to the ground state profile. Further, transient species evolve at 515 and 850 nm representing the absorbance features of the singlet excited state, accompanied by a broad bleaching in the 1000–1400 nm region, implicating the injection of electrons to the conduction band of graphene. The analysis of the photoinduced electron transfer from the photoexcited chromophore to graphene reveals a short-lived and a long-lived component with lifetimes (3.3 ± 0.5) and (270 ± 10) ps, respectively, in DMF. Notably, from these last two examples the diversity of graphene is highlighted, since depending on the materials design, graphene can serve both as electron donor or acceptor.

Beyond monomeric forms of phthalocyanines, an in-situ polymerization method has been reported for the preparation of covalently modified GO nanosheets bearing phthalocyanine polymers [308]. Hence, GO was treated with isophorone diisocyanate (IPDI) to provide IPDI-GO via condensation of one isocyanate unit with either a carboxylic acid or a hydroxyl unit of GO. The second isocyanate group was used for the chemical attachment of 3-aminophenoxypthalonitrile (3-APN), the building block for the phthalocyanine core and linking point of the final polymer phthalocyanine to GO. Finally, excess of a star-shaped triphenoxypthalonitrile and cuprous chloride were added to promote the in-situ polymerization. All intermediate steps were monitored by FT-IR spectroscopy, differential scanning calorimetry (DSC) and TGA. The as prepared hybrid material was tested for its dielectric properties and dielectric constants of 9.04 and 8.16 observed at 100 and 1000 Hz, respectively, showing a potential for future exploitation.

Zinc tetrapyrrolyne porphyrins (ZnPz) is another class of photoactive organic molecule, which was used for the covalent decoration of reduced graphene functionalized by benzoic acid units via diazonium addition of the corresponding 2-aminobenzoic acid [309]. The binding of a ZnPz derivative bearing two alkylamino groups was accomplished by carbodiimide chemistry and the success of the reaction was monitored by FT-IR. In the UV-Vis spectra of the hybrid material, a blue shift of the characteristic bands of the Pz was observed, while the fluorescence emission of the attached Pz was almost fully quenched and blue shifted, suggesting strong intra-hybrid interaction both at the ground and excited states.

Moreover, the in-situ preparation of modified graphene with photoactive homo- and heteropolymers was also reported. A poly(fluorene-perylene) polymer was successfully grown on exfoliated nanosheets functionalized with iodobenzene units via an aryne cycloaddition reaction [310]. The hybrids were examined by Raman, UV-Vis and photoluminescence spectroscopy as well as by electrochemistry. Overall, strong intra-hybrid interactions were unveiled and the material was tested for the photocatalytic reduction of 4-nitrophenol.

In another approach, brominated graphene was used as a grafting-to substrate for the in-situ preparation of polythiophene functionalized graphene nanosheets [311]. The 5-bromo-2-thienylboronic acid was used as a monomer, which furnished polythiophene-graphene covalent ensembles via a Suzuki cross-coupling reaction. In analogous fashion the preparation of a polyfluorene-graphene derivative was also reported [193]. In a different approach, a polyfluorene macromolecule carrying azide functionalities was incorporated on alkyne-functionalized graphene through a [3 + 2] Huisgen cycloaddition [312]. A poly(arylene-ethynylene)-rGO hybrid material exhibited stable photoinduced charge transfer from photoexcited rGO nanosheets to the grafted polymer [313]. Reduced graphene oxide was firstly functionalized by 4-bromobenzyl-diazonium salt and then 1,4-diethynyl-benzene and 1,5-dibromo-3-hexylthiophene were used for the grafting-to polymerization reaction with Pd(PPh₃)₄ and Cu(I) as catalyst and co-catalyst, respectively. The conjugated covalently grafted polymer (PAE) showed strong absorption in the visible region centered at 400 nm and the content of rGO was calculated as high as 15.42 wt% from TGA analysis. Under photoexcitation (365 nm) in solid state, an EPR signal (g = 2.0037) signal was observed suggesting the presence of photogenerated electrons. TCSPC spectroscopy revealed a shorter lifetime for the ¹RGO* excited state within the PAE-RGO ensembles. Molecular orbital approximations showed that the energy level of the conduction band was located on the PAE and the valence band on the rGO providing a negative -energetically favorable- free Gibbs energy for the charge separation (ΔG_{CS} = -2.57 eV). The latter material was tested as a non-volatile memory by taking advantage of the electrical switch arose from the intra-hybrid charge transfer.

Fullerene C₆₀ is the proverbial “fruit fly” of organic solar cells and a highly efficient electron acceptor. Barrejón and coworkers

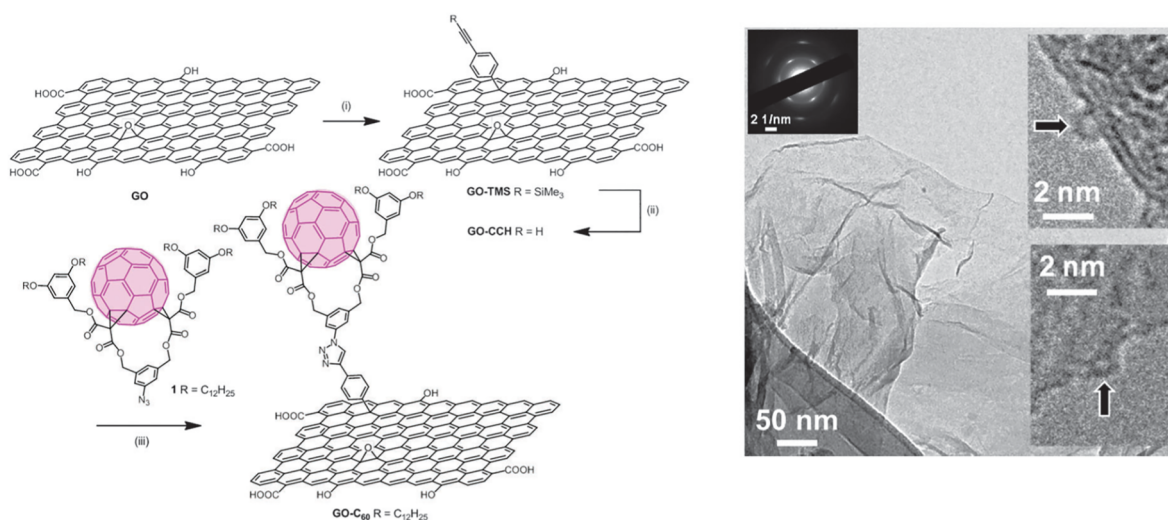


Fig. 21. (left panel) Preparation of GO-C₆₀. Reagents and conditions: (i) 4-(trimethylsilyl)ethynylaniline, isoamyl nitrite, NMP, 70 °C, 24 h; (ii) TBAF, THF/NMP, rt, 1 h; (iii) CuSO₄·5H₂O, sodium ascorbate, NMP, 70 °C, 48 h. (right panel) HR-TEM images of GO-C₆₀ and its corresponding SAED pattern. Insets on the right show spherical C₆₀ units highlighted with arrows. Reproduced with permission from Ref. [314]. Copyright 2014 Royal Society of Chemistry.

prepared C₆₀-functionalized graphene oxide nanosheets via a facile 2-step approach [314]. Initially, ethynylbenzene-functionalities have been incorporated on the nanosheets via diazonium chemistry followed by a click [3 + 2] Huisgen cycloaddition of an azide-terminated fullerene derivative (Fig. 21a), furnishing a hybrid nanomaterial with good solubility in organic solvents. Raman spectroscopy provided information for the success of the diazonium addition, as evidenced by the increment of the I_D/I_G ratio from 0.7 for graphene oxide to 0.86 for the C₆₀-functionalized graphene. During the click chemistry no additional disruption of the honeycomb structure was observed, demonstrating the mild chemical environment during the attachment of the fullerene functionalities. The presence of the triazole rings was validated by X-ray photoelectron spectroscopy, while by the nitrogen content was determined the loading as high as 1 fullerene unit (1 triazole ring) per 161 carbon atoms of GO. HR-TEM microscopy showed the layered morphology of the material and the specific area electron diffraction (SAED) is representative of the hexagonal graphene lattice, while also clearly imaged the C₆₀ cages on the nanosheets (Fig. 21b). By cyclic voltammetry an anodic shift of 0.14 V in the first reduction of the covalently bound C₆₀ was evident and this coupled to its quenched fluorescence at 720 nm constitute a set of indicative data for strong intra-hybrid interactions. Finally, the nature of the intra-hybrid light-induced interactions was unveiled by laser flash photolysis experiments, where transient long-lived C₆₀^{•-} species (1.82 μs) were clearly identified, suggesting photoinduced electron transfer phenomena to take place from graphene to the C₆₀. The hybrid targets the area of organic solar cells and should act as an efficient electron acceptor component improving upon existing materials mainly because of its NIR absorption characteristics.

The high density of carboxylic acids on GO can be exploited for hosting both an electron acceptor and electron donating molecule by means of covalent attachment. In this frame, a zinc phthalocyanine (ZnPc) having an amine terminus and a fullerene derivative having a hydroxyl terminus were covalently introduced via condensation with the carboxylic acids on the surface of GO. Photoinduced phenomena taking place were evaluated by nanosecond transient absorption spectroscopy and complementary electrochemical studies [315]. Using a 532 nm laser for the excitation of ZnPc, the observed spectra clearly shown the formation of the ZnPc^{•+} (absorption band at ~840 nm) and the C₆₀^{•-} (absorption band at ~1000 nm), manifesting the photoinduced charge transfer from the phthalocyanine to the C₆₀ with a calculated lifetime of 0.04 μs, while the charge separation constant was as high as 10⁸ s⁻¹. DPV studies revealed that the ratio of ZnPc:C₆₀ was 1:3, by the 3-fold higher intensity of the peak current of C₆₀, while from the calculated electrochemical gap (0.92 eV) the free-energy changes for the charge separation were also calculated as -0.87 and -0.88 eV for the ¹ZnPc* and ¹C₆₀*, respectively, indicating that the photoinduced separation of charges is exergonic and thus energetically favourable.

Nitrogen-doped graphene, N-graphene, offers an additional chemical functionalization route, namely the N-alkylation reaction of the “pyridinic” nitrogen atoms. To this end, N-alkylation of few layered N-graphene (~4 layers) by bromo-arenes assisted via phase-transfer catalysis (PTC) was presented [199]. Raman spectra (exc. 532 nm) of N-graphene showed an intense D-band indicating the distorted graphitic lattice and the small lateral size of the nanosheets (~20 nm) leading to higher content of edge defects. Upon N-alkylation no further changes were presents. FT-IR spectroscopy displayed the characteristic vibrations owed to the organic addends and XP spectroscopy validated the success of the alkylation. Thermogravimetric analysis allowed to determine the amount of covalently bonded organic units and compare the impact of microwave irradiation using the reaction with 2-bromo-1-(4-chlorophenyl)ethan-1-one (Fig. 22, left panel) as a model. Replacing conventional heating for microwaves gave rise to 3-fold higher loading and shorter reaction times, highlighting the impact of microwave-assisted reaction for the functionalization of graphene [316]. For the rest molecules tested, the differences were scarce, although the process is faster (1 h) than conventional heating (20 h). Following this protocol, the covalent attachment of a porphyrin bromobenzyl-derivative afforded zinc porphyrin-decorated N-

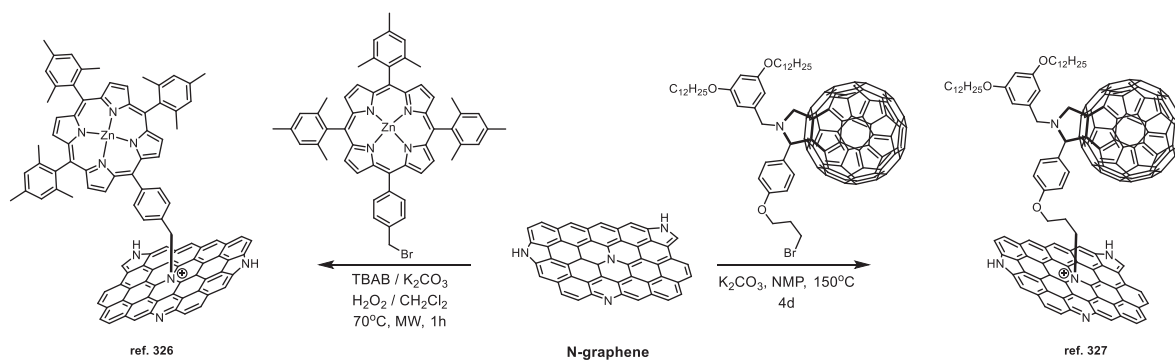


Fig. 22. Covalent functionalization of N-doped graphene with photoactive compounds.

graphene nanosheets (20 %w/w, 1 unit per 295 carbon atoms) with an optical gap around 3.79 eV, namely 0.33 eV smaller than the corresponding of pristine N-graphene (4.2 eV). The UV–Vis absorption spectrum shows a clear peak (Soret band) of the zinc macrocycle, bathochromically shifted by 4 nm as compared to the pristine molecules, suggesting the existence of electronic interactions between porphyrin and the basal plane of N-graphene. Overall, covalent chemistry of N-atoms is a promising approach for bandgap engineering.

In an analogous system, where a C_{60} -pyrrolidine is chemically attached to N-graphene, electron pooling phenomena were unveiled [317] (Fig. 22, right panel). XPS and FT-IR spectroscopy assisted by TGA assays validated the successful formation of hybrids and determined the loading as high as 33 %w/w, while Raman spectroscopy (exc. 532 nm) displayed a downshift of the G-band by 14 cm^{-1} accompanied by the pentagon-pinch band of C_{60} cage at 1471 cm^{-1} . The photophysical properties of the nanohybrids were screened by UV–Vis and PL spectroscopy, where the absorption of the grafted C_{60} -pyrrolidine (416 nm) was found blue-shifted by 16 nm and its emission at 711 nm (exc. 432 nm) was quenched suggesting strong intra-hybrid electronic interactions both at the ground and excited states. Further insights provided by differential pulse voltammetry, showing cathodic shift of the reduction potentials of the fulleropyrrolidine by 30–40 mV, while with the aid of femtosecond transient absorption spectroscopy the N-graphene $^{+}$ - C_{60}^{-} charge separated state was detected. Having addressed the strong interactions within the hybrid nanosheets, electron pooling experiment in the presence of a sacrificial electron donor (1-benzyl-1,4-dihydronicotinamide, BNAH) and methyl viologen (MV^{2+}) as a second electron donor have been performed. Direct electron transfer from BNAH to MV^{2+} is sluggish, nevertheless in the presence of the photoexcited (by visible light) C_{60} -decorated N-graphene electrons are efficiently travel to MV^{2+} , via the charged separated state of the nanoensemble, forming the corresponding MV^{+} as evidenced by monitoring their characteristic absorption centered at 610 nm. These complementary studies on the light-induced charge separation reveal the potential of such nanoarchitectures in solar energy conversion and photocatalysis applications.

Fabrication of a photoactive graphene-based system bearing a bacterial photosynthetic reaction center (RC) was also reported [318]. Reduced graphene oxide nanosheets were initially deposited on ITO electrodes and functionalized by 4-ethynylaniline via diazonium chemistry and the RC isolated from *Rhodobacter sphaeroides* R26 was chemically modified by NHS-PEG₄-azide. The succinimide (NHS) unit directs the covalent binding of NHS-PEG₄-azide to the lysine residues of RC, leaving the azide group free to react with the alkyne functionalized rGO via a Huisgen cycloaddition. As far as the purity and more importantly the integrity of the RC is concerned, it can be evaluated by the absorbance ratio $A_{280\text{nm}}/A_{802\text{nm}}$ and $A_{760\text{nm}}/A_{865\text{nm}}$, which was not affected during covalent grafting on rGO, indicating the non-destructive process. The photoinduced charge separation within RC-RGO was studied by flash photolysis (white light) followed by monitoring the dark monoexponential decay of the fluorescence signal via excitation of the 865 nm band, which is related to the absorbance of the lower excitonic state of the dimer RC. Charge recombination is following the same kinetics (10 s^{-1}) as the native RC, however, the surface concentration of the RC is $2.4 \times 10^{-12}\text{ mol/cm}^2$, calculated by the differential molar extinction coefficient ($\Delta\epsilon_{865\text{nm}} = 105\text{ mM}^{-1}\text{ cm}^{-1}$), is high and comparable to densely packed RC monolayers ($5 \times 10^{-12}\text{ mol/cm}^2$).

Functionalization of graphene nanosheets with Eosin Y [319], optically active helical-substituted polyacetylene chains [320], phenothiazinyl units [321], aza-crown motifs [322] and Eu^{3+} -derivatized silica nanoparticles [323] managing photoinduced electron transfer provides further options for potential (opto)electronic materials. Finally, functionalization strategies based on incorporation of ionic liquids [324] enables the coordination of metal complexes, i.e. iridium(I) [325] and palladium (II) [326].

4.2. Covalently functionalized graphene for medicinal applications

Medicinal applications in principal require graphene derivatives with enhanced stability in aqueous dispersions and at the same time the presence of biocompatible functional groups. Incorporation of biocompatible natural amino acids [327], biodegradable poly (L-lactide) [211] and cyclodextrins [328] onto graphene sheets gave access to some categories of stable graphene-based hybrid materials in aqueous media. As shown earlier, alkyne-terminated (few-layered or CVD) graphenes can be easily prepared by means of diazonium chemistry functionalization. The latter modification allows the post-functionalization of graphene with other functional units via click-chemistry reactions. Implementing an oligoethyleneglycol azide derivative, azido-PEG₄-acid, water dispersible

graphene-based ensembles have been prepared, with the terminal carboxylic acid functionalities contributing to a negative zeta potential (-54.6 mV), while the surface tension (63 mN/m) is indicative of the hydrophilicity of the click-functionalized nanosheets [120]. Nucleophilic attack of azide anions to graphene oxide, followed by click cycloaddition between the azido-graphene and alkyne-terminated glycosides (D-glucose, D-mannose, D-galactose, maltose) afforded also hydrophilic graphenes [329].

Graphene decoration by sugars was accomplished by activating the carboxylic acids of GO with SOCl_2 towards the corresponding GO-COCl, which then reacted with 1,3-diazidoprop-2-ol via esterification. In such way, two azido groups are introduced per each organic unit, however, the overall loading is slightly lower, since the density of carboxylic acids is higher at the edges, whereas epoxides are denser on the basal plane. Poly-L-lysine was also successfully incorporated on graphene oxide resulting to enhanced stability of the functionalized nanosheets in aqueous solutions [330]. Another approach for the preparation of covalently modified nanosheets with enhanced hydrophilicity concerns the simultaneous reduction and functionalization reaction of GO by 4-hydrazinobenzenesulfonic acid [331]. All these chemical manipulations are easily followed by FT-IR spectroscopy and TGA, offering an important toolkit towards covalent graphene derivatives with potential applications in nanomedicine, likewise electrostatic binding of biomolecules.

Exfoliation of graphite fluoride assisted by the cetyl-trimethylammonium bromide (CTAB) surfactant is a feasible way to take advantage of the strong electrostatic forces between the cetyl-trimethylammonium cations and the covalently attached fluorine atoms, with the latter acting as “counter anion” [332]. Moreover, this is a scalable process. Delamination of graphite fluoride, down to 1–2 layers, significantly changes the bandgap of the exfoliated nanosheets, while keeping almost constant the fluoride content to $\sim 25\%$ w/w. Interestingly, the surface of the surfactant-functionalized F-graphene has strong affinity for dopamine, an important biomolecule interplaying at neuron signal transmission. Potentially, this type of nanographenes could be also incorporated to devices for nanomedicine applications.

4.2.1. Biosensing

Boron-doped graphene, prepared by the addition of $\text{BF}_3 \cdot \text{Et}_2\text{O}$ to graphene, has been evaluated for the simultaneous detection of analytes with biological interest as ascorbic acid, dopamine, uric acid and NADH, as well as the explosive trinitrotoluene, commonly known as TNT [333]. For all the examined compounds, higher anodic currents have been recorded, indicating the enhanced electron transfer from the biomarkers to B-graphene, accompanied by enhanced stability in repeated cycles. Electrochemical polymerization of poly(3-aminophenyl boronic acid) in the presence of GO coated gold electrodes affords covalent attachment of the polymer the edges of GO and simultaneous reduction of the oxygen functionalities on the basal plane [334]. The exposed boronic acid functionalities selectively capture sugars, such as fructose and xylitol (germinal diols), at the slightly acid environment of the electrolyte. Taking advantage of the selective complexation of the sugars on the boronic acid functionalized reduced graphene oxide, sensitive sugar sensors have been implemented, using the redox ferrocyanide/ferricyanide pair as agonist agent. The detection limit for fructose was 1×10^{-12} M, while for xylitol was 1×10^{-13} M. In both cases the linearity was up to 10^{-2} M with excellent stability. The same strategy of boronic acid-diol recognition has been also used for the detection of sialic acid (SA), where the low detection limit was as low as 8×10^{-6} M and the linear response was found in the range of $2 \mu\text{M}$ to 1.38 mM [335]. Overall, this approach offers potentiometric methods for analyzing molecules present in samples with biological interest (i.e. serum). An analogous sensing platform prepared by molecular imprinted graphene bearing boronate functionalities has been reported for the covalent recognition of ovalbumin (OVA), a template glycoprotein, and its separation from complex samples [336]. As revealed by circular dichroism the capture of OVA is non-destructive since the captured OVA reserves the pristine features, while the content of the captured macromolecule is proportional to the amount of the boronates, thus can be fine-tuned by increasing the loading -increasing the amount of the monomer- during the synthesis of the sensing platform. Fast rebinding and release of the glycoprotein demonstrates the possibility for future use in clinics.

Sensor-targeting materials can cover a diverse spectrum of applications [337–341]. Specifically, when used in electrochemical sensing methods graphene-based sensors can, potentially cater low-cost, low-power and portability, which are especially important factors when dealing with preventative health technologies [342]. These attributes become increasingly important in neurodegenerative diseases [343] (e.g. Alzheimer’s disease), which are best treated with early intervention therapies and require early diagnosis.

Hydrogen peroxide (H_2O_2) in biological systems reflects the response to pathogens, namely it is produced to promote their oxidative decomposition. In this respect, graphene oxide nanosheets covalently functionalized by polyethyleneimine (PEI) are excellent substrates in order to load functional molecules for sensing H_2O_2 at low concentrations. The covalent incorporation of PEI via carbodiimide chemistry results to positively charged nanosheets capable to host nanoparticles of the anionic iron dye Prussian Blue (PB) which has enhanced electroactivity towards the reduction of H_2O_2 [160].

Following carbodiimide chemistry, one can easily attach dendrimers on the graphene surface towards the realization of bio-sensing materials. Dendrimers are based on repeated diaminoethylene units forming an extended branched network providing enhanced hydrophilicity. Poly(amidoamine) (PAMAM) dendrimers are biocompatible compounds consisting of repeated amine-amido units, forming the so-called 1st-4th generation PAMAM. Such dendrons can be covalently incorporated all over the surface of graphene or at the edges, depending on the selected functionalization process [344]. A 4th generation PAMAM dendrimer, namely having 32 free-terminal amine groups, was electrochemically attached on graphene oxide furnishing modified PAMAM(4th)-rGO electrodes for H_2O_2 sensing [345]. Specifically, as-prepared PAMAM(4th)-rGO electrodes, having free amine groups from the grafted PAMAM(4th), were incubated into a glutaraldehyde solution, followed by washing and a second incubation step into a horse radish peroxidase (HRP) phosphate buffer solution. The HRP was immobilized on the PAMAM(4th)-rGO electrodes via a glutaraldehyde linkage and the major advantage of using the dendrimer is the increased loading in HRP by utilizing the enhanced free amine groups provided by the 4th generation of PAMAM. Interestingly, covalent incorporation of PAMAM(4th) on graphene showed a higher

molecular density (37.51×10^{15} molecules/cm²) than simply casted PAMAM(4th) on glassy carbon (3.33×10^{15} molecules/cm²), meaning that in the prepared hybrids the density of free amine groups is ten times higher. The HRP-PAMAM(4th)-rGO electrodes were tested as amperometric sensors, via recording their amperometric response during periodic addition of the analyte in solution or in spiked serum samples. The linearity of the sensor was in the range of 50–800 μ M at -0.2 V vs NCE and due to the HRP a Michaelis-Menten constant of 853 μ M was also calculated.

Covalently functionalized graphene has been also reported as counterpart of efficient immunosensors. Electrochemically reduced graphene oxide nanosheets functionalized by cysteamine were successfully used for the immobilization of gold nanoparticles mediating the assembly of p53 protein for the detection of the corresponding antibodies, which are crucial for cancer prognosis [346]. Specifically, gold electrodes were initially decorated with aniline units, which served as binding edges for the chemical attachment of a graphene oxide layer via an electrochemical diazonium reaction. Then, the attached GO nanosheet was electro-reduced to restore the conductivity of the layer, leaving carboxylic acid units at the perimeter for the chemical incorporation of the cysteamine ligands for the immobilization of the Au nanoparticles. The detection of p53 antibodies in solution or spiked serum samples was carried out by monitoring the square wave voltammetry (SQW) response of the sensor. Tests were performed in the presence of the [Fe(CN)₆]^{3- / 4-} redox couple and the signal intensity was decaying in respect to the increased amount of the antibodies. Namely, the more the antibodies in the sample, the less was the signal, since p53 antibodies provide steric hindrance blocking the interface between the redox couple in solution and the surface of the electrode. A detection limit down to 0.088 pg/mL was observed with a linear response in the region of 0.1 pg to 100 ng/mL, while the sensor gave reproducible responses showing enhanced stability.

Addition of nitrophenyl units at the perimeter of chemically reduced graphene oxide via diazonium chemistry has been reported as functionalized graphene templates for the development of efficient immunosensors for the detection of deoxynivalenol (DON), a mycotoxin present in cereal samples [347]. The PhNO₂-rGO ensembles were post-treated with gold nanoparticles followed by immobilization of [Ru(bpy)₃]²⁺ via electrostatic interactions with the particles and finally electroreduction (at -920 mV Ag/AgCl) of the nitro- groups to the corresponding amino-groups in order to stabilize the monoclonal deoxynivalenol antibody (DONab). Cyclic voltammetry studies have been performed in order to evaluate the electrochemical response of the Ru(bpy)₃]²⁺/Au/PhNH₂-rGO ensembles. The recorded graphs in the solutions of the [Ru(NH₃)₆]^{2+ / 3+} redox couple were found almost totally suppressed, as compared to electrodes without the ensembles manifesting that the surface of the Ru(bpy)₃]²⁺/Au/PhNH₂-rGO is blocked. After the incubation of the DONab, the Ru(bpy)₃]²⁺/Au/PhNH₂/DONab-rGO electrodes shown an extra decrement to the observed current and was further decreased in the presence of DON molecules in the solution. The latter results were consistent with the complementary amperometric response of the system for the redox couple. The Ru(bpy)₃]²⁺/Au/PhNH₂/DONab-rGO immunosensor was evaluated by electrochemical impedance spectroscopy (EIS) and the maximum charge transfer resistance (R_{ct}) was recorded for a concentration of 2 μ g/ μ L. Going to higher concentration of DON, an inhibition process took place. Another important factor was the pH of the solution in which the immunosensing is recorded. As it was found, the optimum pH is ~ 7 , where the anodic peak in CV graphs of the redox couple drops drastically, suggesting strong binding between the DONab and DON. Concerning the detection range, the sensor exhibited a linear impedometric response between 6 and 30 ng DON/mL and was stable for several days of testing. Moreover, it is a direct method to determine such analytes and challenges other time-consuming techniques likewise the enzyme-linked immunosorbent assay (ELISA).

Chemically reduced graphene was prepared by an ammonia/ascorbic acid thermal treatment, deposited on a glassy carbon electrode and modified with benzoic acid units via diazonium chemistry with the aid cyclic voltammetry (10 cycles from 0 to -1.0 V vs. Ag/AgCl, 200 mV/s). The carboxylic groups of PhCOOH-rGO electrodes were bound the amine-terminated antibody of the anorexigen peptide YY, through carbodiimide chemistry [348]. Then, the hybrid electrode incubated into a casein solution in order to be adsorbed on the surface and block it. Finally, the PhCOOH-antiPYY-rGO/casein electrode was incubated in a solution containing the target PYY antigen and the biotinylated-PYY analogue, forming a competitive system tested in the presence of alkaline phosphatase-labeled streptavidin (AP-Strept) and 1-naphthyl phosphate (1-NPP) as the enzyme substrate. AP-Strept recognizes the biotin-PYY and catalyzes the dephosphorylation of 1-NPP to 1-naphthol. The serum and saliva samples were spiked with biotin-PYY and the amperometric and impedometric response of the immunosensor was evaluated in respect to calibration curves. Optimization of the system is necessary, namely the regulation of a) the inserted carboxyl functionalities affecting which affect the binding of the antigen-PYY and b) the incubation of i) the casein blocking layer, ii) the loading of antigen-PYY and iii) the sample for analysis. Overall, the as fabricated immunosensor provides faster analysis than ELISA and commercial colorimetric kits and its response is linear in the range 10^{-4} - 10^2 ng/mL with a low detection limit of 0.01 pg/mg, values adequate for such analysis in real samples.

Electrochemical addition of p-nitrophenylamine diazonium salt on glassy carbon electrodes was followed by electroreduction of the nitro- to amino groups utilized for the covalent attachment of a top graphene oxide layer via carbodiimide chemistry [349]. The hybrid AP-GC-GO electrodes were reported as an electrochemical sensor for the determination of Cd(II) and Cu(II) cations. XPS spectroscopy gave proof for the incorporation of the azo-derivative on the electrode. Precisely, the 398.3 eV peak was assigned to the amide N-atoms between the aminophenyl-functionalized glassy carbon and the carboxylic acids of GO. Some residual $-\text{NO}_2$ species (401.3 eV) were also present, due to the incomplete electroreduction. The electrochemical sensing properties of the hybrid electrode were monitored with the aid of square wave voltammetry (SWV). A linear response was obtained in the region 5.0×10^{-4} - 5.0×10^{-10} M for both Cd(II) and Cu(II) ions and a significant stability of up to 60 days, without loss of activity, was achieved.

Another feasible approach towards highly selective biosensors is the exploitation of enzymes. L-lactate dehydrogenase (LDH) immobilized on graphene has been proposed as an efficient biomarker for the determination of serum lactate via the electrocatalytic sensing of the re-generated NADH [350]. Diazotization of nitroaniline followed by addition to rGO afforded nitrobenzene-functionalized nanosheets, which electrochemically tuned at -0.06 V to generate the redox pair rGO-PhNHOH/rGO-PhNO. The as prepared graphene-based electrode is highly sensitive for the detection of the oxidation of the NADH generated by LDH catalyzed reduction of

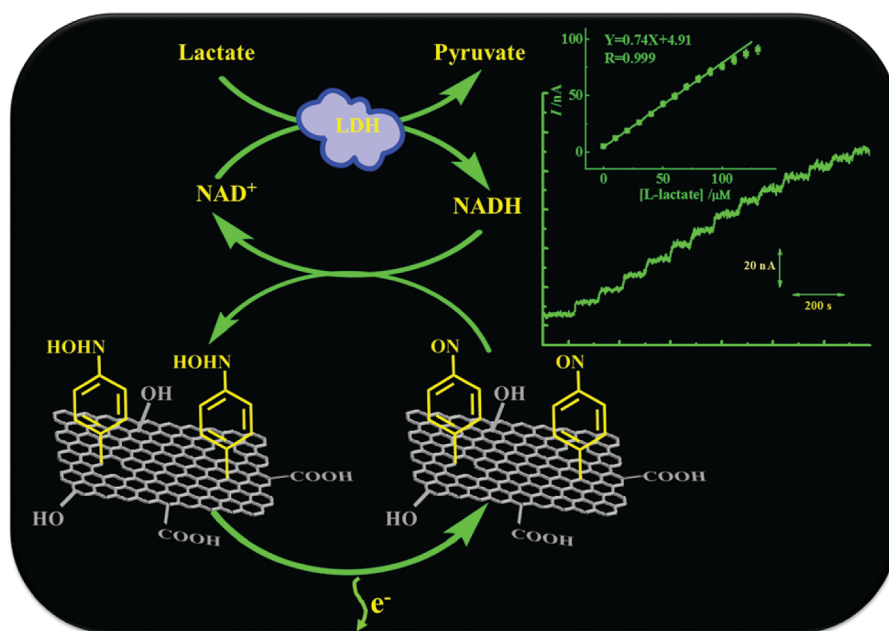


Fig. 23. Schematic illustration of the bioelectrocatalytic sensing of lactate and the corresponding amperometric response obtained at 0.04 V in a stirred solution of 0.1 M PBS (pH 7.2) containing 4 mM NAD^+ . Each addition increased the concentration of lactate by 10 μM . The calibration plot is shown in the inset of the amperometric response. Reproduced with permission from Ref. [350]. Copyright 2016 Royal Society of Chemistry.

L-lactate to pyruvate, as shown in Fig. 23. FT-IR, XPS and Raman spectroscopy verified the successful addition of nitrobenzene units on the graphitic lattice of rGO via the identification of the characteristic vibrations of the PhNO_2 , the presence of nitrogen and the increased I_D/I_G ratio, respectively. AFM microscopy revealed a thickness of 4–8 nm, representing around 3–6 layers of stacked rGO nanosheets. The amperometric response of the hybrid electrochemical sensor was linear down to 90 μM and no interference with other analytes of serum was evident down to 2.5 μM , constituting a competitive system to the clinical method.

Electrografting of N,N' -dimethylphenothiazin-5-ium-3,7-diamine (Azure A) on graphene oxide via diazonium chemistry showed improved efficiency for the oxidation of NADH [351]. More specific, graphene oxide was initially functionalized with thiol terminated derivatives for the stabilization of the nanosheets on gold electrodes. Then, the GO/Au electrodes were functionalized via in-situ electrochemical generation of Azure A radical, furnishing the hybrid AzurA-GO-Au electrodes. For the electrografted Azure A on the GO surface, CV studies showed a stable quasi-reversible redox wave for the dye, in contrast to Azur A electrodeposited on Au, where no such response was evident, suggesting the decreased conductivity of the as-formed Azur A film. Consequently, the good conductivity generated by the diazotization approach favours the monitoring of redox events such as the NADH oxidation, highlighting the potential of such materials for sensing applications.

Functionalization of F-graphene with sulfides has been proposed as an electrochemical sensing probe for single-stranded DNA (ssDNA) macromolecules [180]. As revealed by XPS the atom percentage of fluorine and sulfur was 7 and 5 %w/w, respectively, indicating that the treatment with the sulfur donor (NaSH) results in defluorination of the starting commercially available fluorographite (57% w/w F). Actually, the sulfydryl functionalized F-graphene (F(SH)-graphene) has intense G and D bands in the Raman spectra in sharp contrast to fluorographite, where such bands are absent to the fully sp^3 network. Concerning the sensing properties of the material, the presence of sulfydryl functionalities enhance the hydrophilicity of the surface inducing strong interactions with the hydrophilic ssDNA molecules used as recognition markers for target DNA molecules in solution. In respect to the wild DNA sequences, the F(SH)-graphene/ssDNA electrodes have shown improved response as compared to F-graphite electrodes and non-modified electrodes.

Molecular recognitions can be carried out by imprinted cavities on the surface of graphene-base materials. Poly (methacrylic acid-3-(trimethoxysilyl) propylmethacrylate@GO- N,N' -methylenebisacrylamide) (poly(MAA-g-MAPS@GO-MBA)) is an imprinted monolith prepared by the polymerization of γ -methacryloxypropyl trimethoxysilane (γ -MAPS) in the presence of graphene oxide, followed by addition to a polymerization solution containing N,N' -methylenebisacrylamide (MBA) and methacrylic acid (MAA). Self-polymerization of dopamine on the surface of poly(MAA-g-MAPS@GO-MBA), using minocycline as a reversible template, enabled the preparation of surface imprinted graphene material for the preconcentration of tetracycline antibiotics [352]. This imprinted material was successfully used for the detection of tetracycline analytes in milk samples showing good recognition capacity and enrichment performance for such analytes, as observed by liquid chromatography.

4.2.2. Aptasensing

Aptasensors are another type of biosensors for selective recognition of metal cations, small molecules, macromolecules and cells by aptamers. Graphene oxide layers owning negatively or positively charged groups have been successful incorporated to layer-by-

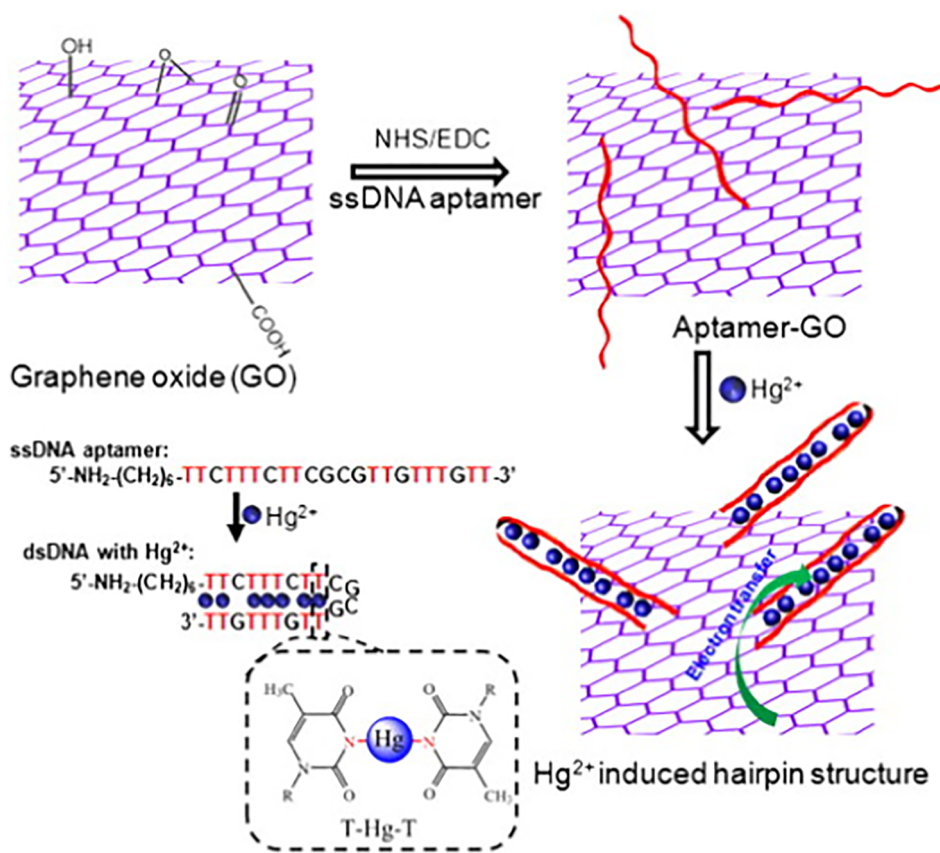


Fig. 24. Operation principle of the label-free detection of Hg^{2+} based on quenching of the fluorescence emission of graphene oxide. Reproduced with permission from Ref. [356]. Copyright 2013 Elsevier.

layer assemblies of aptasensing platforms [353–355].

Covalent attachment of aptamers on graphene oxide was proposed for the preparation of efficient sensing platforms for Hg^{2+} cations based on the fluorescence emission properties of GO [356]. The selected aptamer efficiently binds the cations and a structural transition occurs, namely the linear free aptamer chains are converted to hairpin structures having trapped the cations, as shown in Fig. 24. Utilizing carbodiimide chemistry, the amine-terminated aptamer was chemically grafted on the carboxylic acid moieties of GO and the amide formation was verified by IR spectroscopy. The functionalized nanosheets carrying the aptamer chains have a distinct emission band at 600 nm, which decays in the presence of the cations due to photoinduced transfer of electrons from graphene to the captured cations. The required incubation time was determined to be 5 min, while the proper ionic strength was provided by aqueous 0.3 M NaCl. Concerning the selectivity of the aptamer-GO sensor, it was screened in the presence of various metals (K^+ , Ag^+ , Ca^{2+} , Cd^{2+} , Cu^{2+} , Pb^{2+} , Ni^{2+} , Co^{2+} , Fe^{3+}) and no obvious fluorescence quenching was observed. The response of the biosensor was linear in the range 1–50 nM Hg^{2+} , the detection limit was 0.92 nM, while saturation was reached at 90 nM. Development of label-free aptasensors, was also carried out, for the detection of thrombin [357,358], DNA single strands [359] and cancer cells [360].

Combining two types of aptamers allowed the preparation of graphene-based biosensors with enhanced selectivity for Hg^{2+} and Ag^+ cations [361]. The fabrication of the biosensor was carried out as follows: graphene oxide was electrostatically immobilized on an ammonium-functionalized glass substrate and covered with a polydimethylsiloxane (PDMS) layer (500 μm thickness) having regular punched holes (200 nm diameter). The carboxylic acid groups of the GO were used for grafting the amino-terminated aptamers into the holes of the polymer matrix. After successive washing of the biosensor for removing the DNA probes, the fluorescence (excitation at 530 nm) of each spot/hole was measured prior to the metal binding assays. All measurements were performed with the aid of a microarray scanner by PL imaging of the different spots present on the biosensor, in the absence and presence of the target analytes (Fig. 25), while also in the presence of other metal cations. Under 530 nm excitation the aptamer-GO ensembles display a green emission, 26% quenched as compared to non-modified spots. Incorporation of the Ag^+ and Hg^{2+} analytes results in emission quenching of the corresponding selective aptamer-functionalized spots, due to selective binding and the photoinduced electron transfer from the aptamer-GO to the cation-aptamer complex. For Ag^+ a linear concentration-PL intensity relation was observed in the range of 1 μM to 10 mM, while for Hg^{2+} in the range of 10 pM to 5 mM. The relative quenching efficiency (rQE) for Ag^+ sensing was 28.2% at 1 μM and raised to 78.2% at 10 mM, while the rQE for Hg^{2+} changed from 30.3% (10 pM) to 73.6%

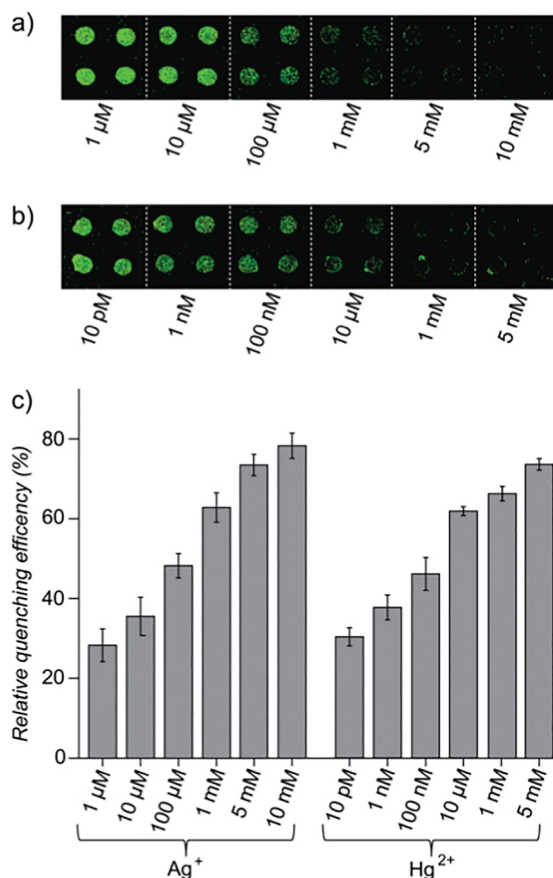


Fig. 25. Scanned fluorescence images of the aptamer-labeled GO with addition of a) Ag⁺ and b) Hg²⁺. c) Relative quenching efficiency of GO depending on the concentration of the Ag⁺ (left part) and Hg²⁺ (right part). Reproduced with permission from Ref. [361]. Copyright 2013 Wiley.

(5 mM). The duplex detection of Hg²⁺ and Ag⁺ cations was not affected by addition of other cations (Mg²⁺, Cd²⁺) highlighting the selectivity of the hybrid biosensor.

Based on the previously discussed fluorescence emission properties of GO, an aptamer-GO hybrid for cocaine sensing was reported [362]. Firstly, GO was immobilized on an APTES-functionalized glass substrate via electrostatic interactions. The first fragment of the aptamer was covalently grafted on the nanosheets via carbodiimide chemistry. Next, the second fragment, which was bound to gold nanoparticles was introduced in order to form a complex with the first fragment. As long as the recognition of cocaine occurs, a conformational change pulls the nanoparticles on the graphitic surface, generating a three-way junction resulting to photoinduced electron transfer from the nanosheets to the nanoparticles, quenching their emission intensity. A confocal microscope equipped with a 543 nm laser used for the emission imaging measurements and the evaluation of the sensing properties of the hybrid material. For 10⁻³, 10⁻², 10⁻¹, 1, 10, 25, and 50 μM cocaine addition to the surface of the sensor, the corresponding QE were as high as 23 ± 3.6%, 36 ± 1.2%, 48 ± 4.3%, 53 ± 1.5%, 57 ± 2.1%, 61 ± 1.4%, and 63 ± 0.9%, respectively, giving a calibration curve with R² = 0.98943. A QE of 56.04% was recorded for 5 μM cocaine in buffer solution, very close to the corresponding QEs for real samples: 55.35% for human plasma, 56.74% for serum, 54.70 for saliva and 56.95% for urine, highlighting the feasibility of the developed biosensing platform. Moreover, the selectivity of the sensor was screened in the presence of pethidine and methadone drugs and no quenching was evident due to their presence.

Detection of macromolecules can be also achieved by aptamer-graphene hybrid nanosensors. Sensing of lysozyme via an aptamer-cRGO platform immobilized on chitosan was reported to allow detection down to 0.45 fM with linear response up to 100 fM [363]. A chitosan layer was used as adhesive for immobilizing the biosensor on a glassy carbon surface. Then the GO electrode was treated with hydrazine, followed by electrochemical activation of the carboxylic acids in the presence of EHS/EDC for the chemical incorporation of the amine-terminated thrombin binding aptamer (TBA). The as-prepared TBA-cRGO electrode was evaluated as the electrochemical platform. Raman spectroscopy verified the reduction process by observing the increased I_D/I_G ratio, showing the structural disorder promoted by the reduction step, while FT-IR validated the chemical incorporation of the TBA. The chemical incorporation of TBA populates the surface of the graphitic nanosheets blocking the interaction with the [Fe(CN)₆]^{3-/4-} redox couple, namely the conductive nanosheets within the hybrid electrode are less accessible to redox species. Incorporation of thrombin enables the recognition by TBA, therefore the intensity of the signal recorded for the [Fe(CN)₆]^{3-/4-} redox couple decreases. Analogous behavior was displayed in the EIS studies. The charge transfer resistance for the [Fe(CN)₆]^{3-/4-} increases as long as the

concentration of thrombin increases, namely the thrombin-TBA recognition blocks the surface of the TBA-cRGO sensor and is less accessible to the reversible oxidation/reduction of the redox probe, resulting to a highly sensitive detection of thrombin. Following the same functionalization protocol, a lysozyme binding aptamer was chemically incorporated on cRGO nanosheets affording a biosensor with a detection limit of 6 fM of thrombin with linear response in the range of 0.01–0.5 pmol/L [364]. The EIS assays were performed also in the presence of $\text{Ru}(\text{NH}_3)_6^{3+}$ showing that the thickness of the sensing material and the electronegativity of the chemical environment possibly contributes to the electrochemical response of the electrochemical biosensor.

Construction of an aptamer-GO hybrid sensor was successfully used for the potentiometric detection of *Staphylococcus aureus* (*S. aureus*) [365]. Graphene oxide was deposited on a glassy carbon electrode and the surface of the electrode was chemically modified by an amide terminated aptamer, via carbodiimide chemistry. A second electrode was prepared by chemical reduction of GO with hydrazine and immobilization of pyrene-terminated aptamer via π - π electrostatic interactions. In these sensors, graphene was used as transduction layer, namely the conductivity difference between GO and cRGO was expected to affect the signal to noise ratio. The evaluation of the hybrid aptasensors was performed by addition of the *S. aureus* in phosphate buffer solution and real-time measurement of the electromotive force (EMF) between a two-electrode system composed by the electrode with the deposited sensor and a double junction Ag/AgCl reference electrode. Glassy carbon electrodes without the aptamer-GO assembly show no response in the presence of *S. aureus*, while the aptamer-GO sensors are highly sensitive due to the selective binding of the microorganism by the aptamer. Control experiments with the Gram-negative *E. coli* and Gram-positive *L. casei* bacteria showed no EMF response from the aptamer-GO sensor, highlighting the selectivity of the sensor and its recognition properties. Further, it was shown that both the presence of the aptamer and graphene transduction layer are needed for the operation of the sensor towards the potentiometric detection of *S. aureus*. Fig. 26 represents the sensing properties of the covalently and non-covalently fabricated sensors, where a higher noise for the covalently grafted aptamer, due to the GO is evident, even though a high detection value of just one colony-forming units (CFU)/mL of the challenging *S. aureus* in 1–2 min was observed. Moreover, the bound *S. aureus* can be washed out from the surface of the sensors by immersion to sodium chloride solutions which induce structural changes to the aptamer, thus releasing the bacteria and restoring a bacteria-free surface.

A click-chemistry approach, based on the incorporation of azide functionalities on graphene oxide and alkyne-functionalized DNA, targets the preparation of tetrahedral DNA superstructures [366]. Graphene oxide was firstly functionalized with chloroethylamine via amide bonding, followed by conversion of the chloride to azide which reacted via [3 + 2] copper catalyzed cycloaddition reaction with the alkyne terminated primary DNA segment. Afterwards, a tetrahedral DNA superstructure was attached to the primary segment through complementary hydrogen bonds between the base pairs. The hybrid graphene/DNA superstructure was immobilized on a gold surface and studied its electrochemiluminescence (ECL) properties. Strong ECL signals have been recorded demonstrating the efficient electron transfer from luminol to the gold surface mediated by the hybrid material and the potential of such bioinspired architectures for biosensors.

Bottom-up synthesized graphene, using a soybean oil based CVD approach on nickel foil, was treated with oxygen plasma to generate carboxylic acid functionalities for the chemical attachment of micro-RNA (mi-RNA) probes as sensors for target mi-RNA biomolecules [367] (Fig. 27). Using the carbodiimide-mediated amidation of graphene with the amino-terminated probe mi-RNAs, the recorded resistance of the hybrid genosensors was $\sim 324 \Omega/\text{sq}$ reserving a small I_D/I_G ratio (0.15–0.25). The as prepared electrochemical genosensors were characterized via electrochemical impedance spectroscopy (EIS), namely the impact of the captured target mi-RNAs to the resistance of the surface charge transport (R_{ct}) for the probe mi-RNA decorated nanosheets was evaluated. As shown in Fig. 27c, R_{ct} increases in the presence of complementary target mi-RNAs, manifesting that the surface of the sensor is blocked and thus the charge transport is impeded, allowing the detection of concentrations down to 10^{-13} M.

4.2.3. Bioimaging, gene and drug delivery

Graphene nanosheets decorated by PAMAM 4th generation dendrimers as carriers for a silicon phthalocyanine (SiPc) and a luteinizing hormone-releasing hormone (LHRH) have been successfully employed as imaging agents for tumors [368]. A low-content GO was prepared by microwave-assisted treatment of graphite with H_2SO_4 and HNO_3 while PAMAM(4th) loaded with SiPc via electrostatic interactions. The latter components were covalently linked by a nucleophilic attack of the free amino groups of SiPc/PAMAM(4th) to the epoxide rings of GO. Finally, the LHRH was covalently inserted to the SiPc/PAMAM(4th)-GO assisted by a maleimide/PEG protocol. The stability of the [SiPc/PAMAM(4th)-LHRH]-GO ensembles in a range of 1–50 $\mu\text{g}/\text{mL}$ was tested by incubation in water, PBS at pH = 7.4 or PBS containing 10% w/v of fetal bovine serum (FBS) at pH = 7.4. After centrifugation, no precipitation and no release of the individuals in the mother liquid was observed. Moreover, SiPc is an excellent candidate for this application, since its high hydrophobic nature restricts its release to the hydrophilic environment of living cells. In order to evaluate the photodynamic properties of the ensembles, singlet oxygen ($^1\text{O}_2$) measurements were carried out by the excitation of the green fluorescence SiPc, within the ensembles, using the Singlet Oxygen Sensor Green® (SOSG) assay. Under monochromatic irradiation (690 nm) a 10-fold increment was observed for $^1\text{O}_2$ generation whereas the local photothermal heating (ΔT) was $\sim 35^\circ\text{C}$ for 20 min irradiation. Prior the in vivo imaging trials on mice, the photodynamic (PDT) and photothermal (PTT) properties of the [SiPc/PAMAM(4th)-LHRH]-GO ensembles were evaluated for their combinatorial PDT-PPT effect on ovarian cancer cells. Under low power (0.3 W/cm^2) 690 nm irradiation the synergic PDT-PTT effect was remarkable reduced and was more efficient for low SiPc concentrations ($< 4.0 \text{ mg}/\text{mL}$). Finally, the [SiPc/PAMAM(4th)-LHRH]-GO ensembles were tested for their ability to target the ovarian cancer cells in-vivo via tail vein IV injection. 12 h after the injection the NIR imaging of the mouse indicates where the tumor is located by the strong green fluorescence of the SiPc loaded on the SiPc/PAMAM(4th)-LHRH]-GO ensembles.

Conjugation of PAMAM dendrons on GO via click-chemistry was also proposed as an efficient biocompatible carrier gene delivery [369]. Azide-functionalized graphene was initially reacted with propargylamine creating a grafting point for the development of the

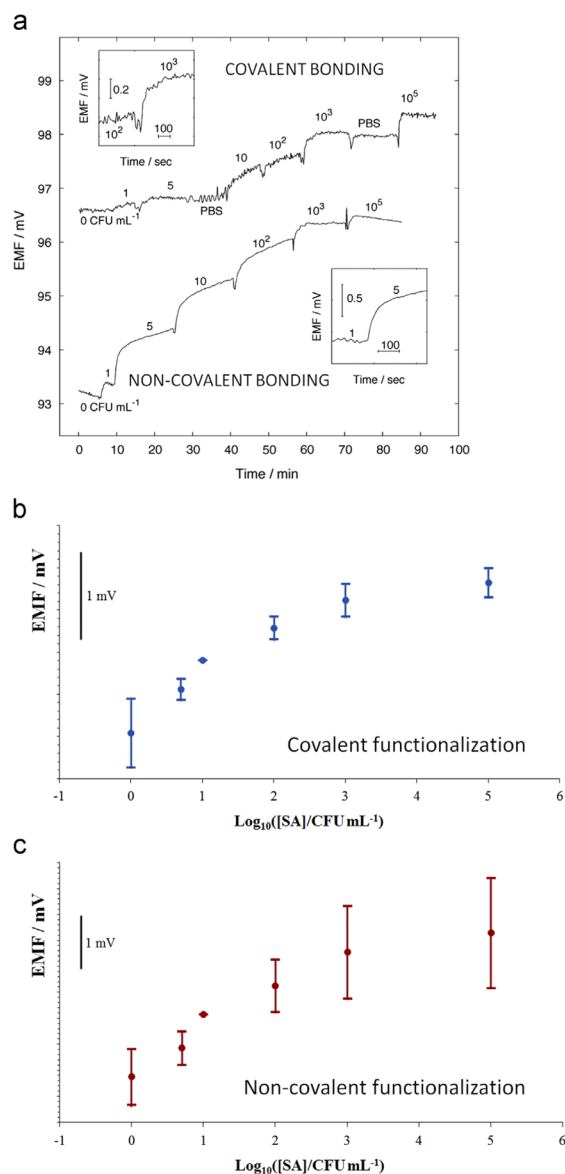


Fig. 26. (a) Aptamer-functionalized aptasensor exposed to stepwise increases of *S. aureus* concentration and the corresponding potentiometric response; numbers above each potentiometric jump represent the final concentration of bacteria. Insets show the detail of two inoculation steps for the covalent and non-covalent functionalization. (b) EMF response versus log of concentration of *S. aureus* for the covalent functionalization. (c) EMF response versus log of concentration of *S. aureus* for the non-covalent functionalization. In (b) and (c) error bars are standard deviation of the response obtained at a given concentration for six different sensors. The sensitivities of the aptasensors are 0.34 mV/decade (covalent functionalization) and 0.55 mV/decade (non-covalent functionalization). Reproduced with permission from Ref. [365]. Copyright 2014 Elsevier.

1st, 2nd and 3rd generation PAMAM dendrons. The immobilization of the plasmic DNA was driven by electrostatic interactions with the amine groups of the PAMAM and was highly improved compared to the physisorption without the presence of the dendrons. Delivery of the desired compounds can also proceed by biocompatible polymers, especially for the case of water-insoluble molecules, likewise anti-cancer drugs [370].

As evidenced for most of the dyes covalently grafted on graphene, upon photoexcitation a minimum fluorescence emission can be observed due to the photoinduced electron and/or energy transfer from the photoexcited dye to the nanosheets. An on/off nanoprobe was fabricated by using GO and coumarin cross-linked by a 2,2'-disulfanedylbis(ethan-1-amine) (DSBA) [371]. The disulfide bond is sensitive to glutathione in living cells, which promotes the dissociation of the S-S bond of DSBA. Actually, in the presence of high levels of glutathione (GSH) in cancer cells the fluorescence probe is "on" and the emission of the coumarin can be detected, consisting the imaging media. The off-to-on response of the nanoprobe was screened in the presence of human serum albumin, bovine serum albumin, glucose, vitamin C and cysteine, however the maximum emission was recorded in the presence of GSH. With the aid of fluorescence microscopy, the imaging of cancer cell cultures was studied as a function of the incubation time. After 1 h incubation the

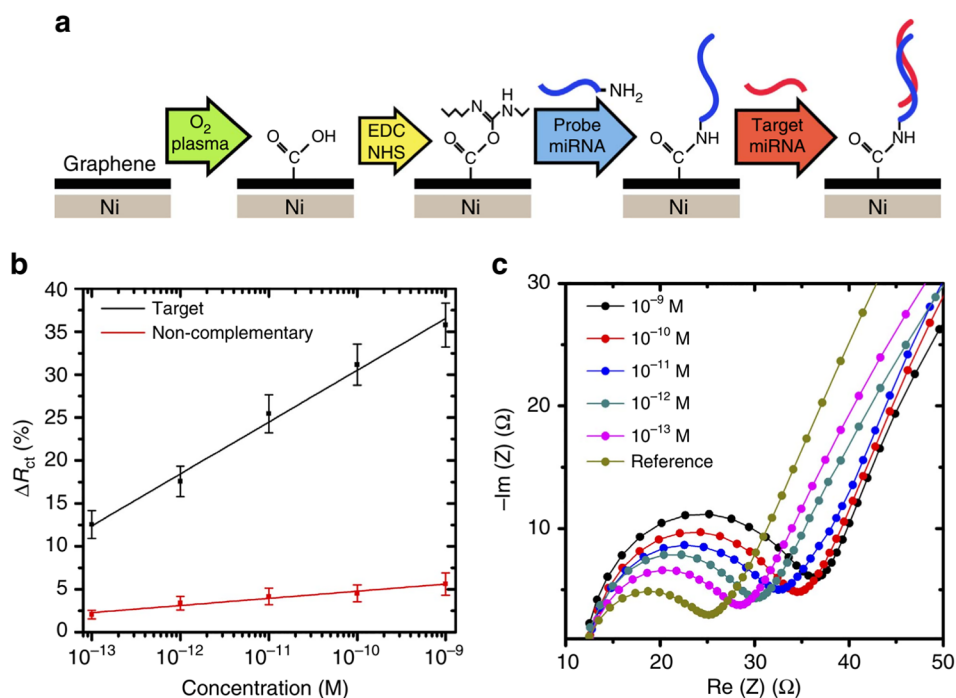


Fig. 27. Biosensor assembly and biosensing performance. (a) Schematic of the functionalization steps involved for the assembly of the graphene-based electrochemical biosensor. (b) Selectivity of biosensor is demonstrated by an increase in R_{ct} with increasing concentration of target miRNA. Error bars represent the s.e. of the mean. (c) Individual EIS curves showing responses of the biosensor to the target miRNA at different concentrations. Reproduced with permission from Ref. [367]. Copyright 2017 Springer Nature.

emission of the released coumarin is well developed. As shown in Fig. 28, the coumarin-graphene probe was also examined in-vivo and developed mice with tumor cells on their back. Within 1 h after the injection, the imaging contrast is already well developed and reaches a maximum after 4 h. Mapping of the intensity shows the accumulation of the nanoprobe within the tumor.

Chelation of the radioactive ^{111}In by a (1,4,7,10-tetraazacyclododecane-1,4,7,10-tetraacetic acid) (DOTA) macrocycle covalently mounted on graphene oxide was reported for the whole body single photon emission computed tomography (SPECT/CT) imaging in mice [372]. Graphene oxide was initially functionalized with triethylene glycol (TEG) diamine via nucleophilic attack to the epoxides and then reacted with the carboxylic acids of DOTA in the presence of a base furnishing the DOTA-GO ensembles, which hosted the radioactive ^{111}In . FT-IR spectra showed the formation of the amide bonds between DOTA and the amine-functionalized GO, while Kaiser test determined the amount of free amines to the GO-NH₂ (670 $\mu\text{mol/g}$) and the DOTA-GO (315 mmol/g), suggesting that 50% of the free amines were grafted to DOTA. AFM imaging showed a thickness of 2–5 nm unveiling the presence of few-layered nanosheets. In Fig. 29, the biodistribution of DOTA[^{111}In]-GO after the intravenous insertion to a mouse is presented. The translocation from liver to spleen was evidenced by the Nano-SPECT/CT imaging of a C57BL/6 mouse, indicating that a rapid and significant urinary excretion followed by accumulation in the spleen. The hybrid system found to be stable for this type of radiolabeling, while intact DOTA[^{111}In]-GO nanosheets have been recovered from the excreted urine, for the first time.

The photochromic behavior of spiropyrans was also integrated to graphene-based materials for in vivo imaging and target delivery [373,374]. Under ultraviolet irradiation, spiropyrans (SP) are transformed to the corresponding merocyanine species (MC) and the structural transition results to bathochromic shift to the electronic absorption spectra, namely absorb light in the region 500–600 nm and emit at 650–800 nm, which is highly appreciated for imaging purposes. In a first example, spiropyran (3% mol) was initially grafted on dopamine-modified hyaluronic acid (HA-SP) and the as prepared HA-SP used for the chemical reduction of GO furnishing reduced graphene covalently functionalized by the HA-SP arrays [373]. XP spectroscopy showed decreased oxygen functionalities, indicative of the reducing step of GO by the HA-SP arrays, accompanied by the presence of the C = O (288.0 eV) peak of HA backbone. Moreover, increased I_D/I_G intensity for the hybrid material was evident in Raman spectra. The hybrid material was tested as a photo-responsive host for the hydrophobic anticancer drug doxorubicin (DOX). DOX was self-assembled on graphene and the SP-to-MC photoinduced structural transition was utilized for imaging the target cells. Fluorescence imaging allowed in-vitro and in-vivo studies, where the presence of DOX was identified by fluorescence mapping of the cell culture or the mice, respectively. Further, DOX-release studies performed to evaluate the rate of release and the viability of the target cancer cells.

Combination of the photo-responsive properties of a spiropyran-conjugated poly(ethyleneglycol)-g-[poly(N-isopropylacrylamide)-co-methylacrylic acid] (SP/DP-PPNM) and those of a pH-responsive boron dipyrromethane-conjugate poly(ethylene glycol)-g-[poly(Nisopropylacrylamide)-co-2-(dimethylamino)ethyl methacrylate (CCDP/BDP-PPDN) was investigated as a tunable multicolor imaging platform [374]. Both conjugates were incorporated onto graphene oxide furnishing covalently modified

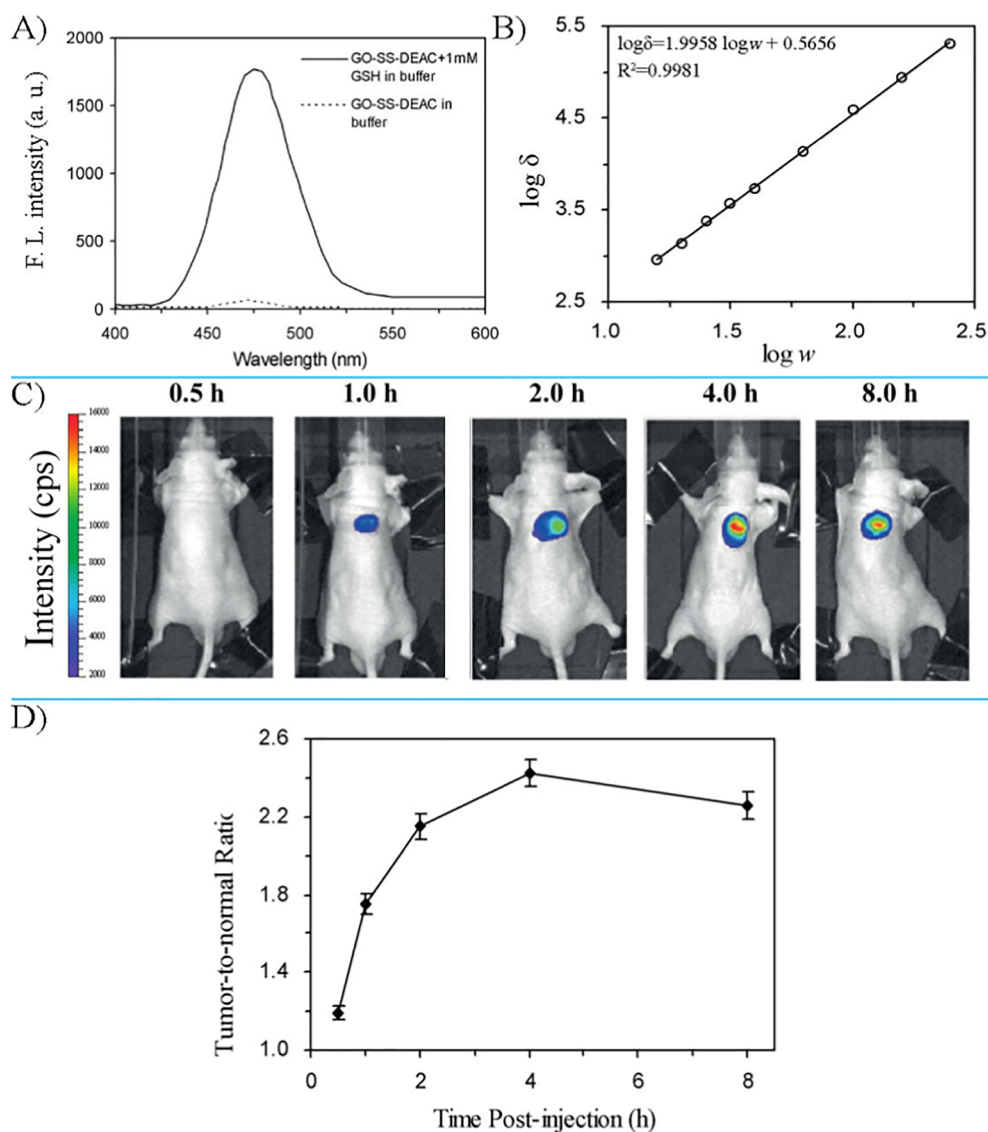


Fig. 28. (A) Two-photon emission spectrum of GO-SS-DEAC (1×10^{-5} M) in PBS with or without 1 mM GSH at pH of 7.0; $\lambda_{\text{ex}} = 800$ nm from a femto-second mode-locked Ti:sapphire laser. (B) The log-log plot of emission intensity (δ) against incident power (w). (C) In vivo NIR images of HeLa tumor-bearing mice at 0.5, 1, 2, 4 and 8 h post intratumor injection with 100 μL of the GO-SS-DEAC nanoprobe solution (2 mg/mL in PBS). A 800 nm pulsed laser diode device was used as the excitation source and fluorescence emission at 480 nm was collected with an emission filter (470 nm/20) put in front of CCD camera. (D) Plot of in vivo tumor contrast at each time point. ($n = 3$). Reproduced with permission from Ref. [371]. Copyright 2014 Royal Society of Chemistry.

rGO nanosheets carrying the two conjugates, as presented in Fig. 30. Accordingly, the bioimaging probe is sensitive to light and pH, resulting in no color (basic pH, no light), only red (basic pH, UV light), only green (acidic pH, no light) and both red and green (acidic pH, UV light) fluorescence output. Zeta potential revealed that under acidic conditions the platform has positive potentials, while the opposite observed for the physiological and alkaline conditions. Under acidic pH the BODIPY-conjugate is protonated and expanded, therefore exposed resulting to enhanced green fluorescence. The expansion of the BODIPY-conjugate at pH 5.0 was also witnessed by AFM imaging studies. Collectively, the hybrid graphene-based platform shows individual fluorescence properties depending on the in vitro or in vivo pH in combination to the stimuli of external UV irradiation.

Other delivery platforms have been reported via covalent functionalization of graphene nanosheets with hydrogels [375], polyethylenimine [376–378], polyethyleneimine-folic acid [379], poly(N-vinyl caprolactam) [380], polyethyleneglycol [381,382], branched polyethylenimine-polyethyleneglycol [383], chitosan [384–386], luminescent nanoparticles [387], while functionalized nanosheets by dextran [388] and polyacrylic acid-fluorescein [389] have been explored as hybrid imaging platforms.

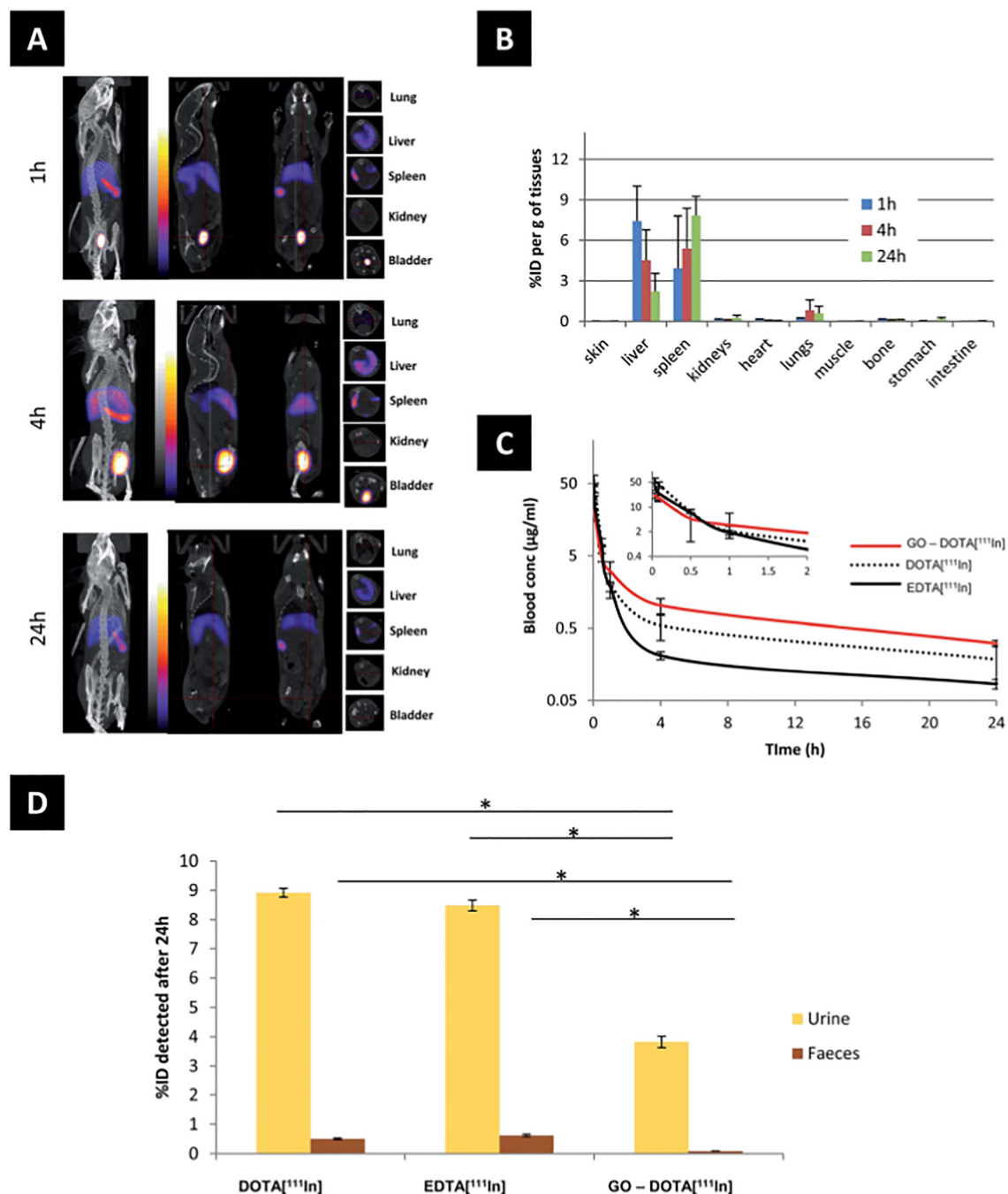


Fig. 29. A) Whole body Nano-SPECT/CT imaging of a C57BL/6 mouse injected with 50 mg of GO-DOTA[¹¹¹In], imaged at different time points (1, 4, and 24 h), showing from left to right whole body, sagittal, coronal and transverse views. (B) Major organ biodistribution, (C) blood profile, and (D) levels of radioactivity detected in urine and faeces after 24 h detected by gamma scintigraphy. Statistical significance * < 0.05 against both controls using Student's *t*-test. Four different mice were used per group. Reproduced with permission from Ref. [372]. Copyright 2015 Royal Society of Chemistry.

4.2.4. Antimicrobial microfiltration of water

Grafting of antimicrobial peptides on graphene oxide through amine coupling was used for the preparation of antimicrobial membranes for the nanofiltration of water samples contaminated by the methicillin-resistant pathogen *Staphylococcus aureus* (MRSA) [390]. Nisin, is a polycyclic antibacterial molecule with exposed amine groups. The amidation of graphene oxide was monitored by FT-IR spectroscopy via the carbonyl vibrations of the newly formed amides and the hybrid material was mixed with polyethyleneglycol (PEG) in order to produce the target membranes. Scanning electron microscope (SEM) imaging, coupled with fluorescence spectroscopy

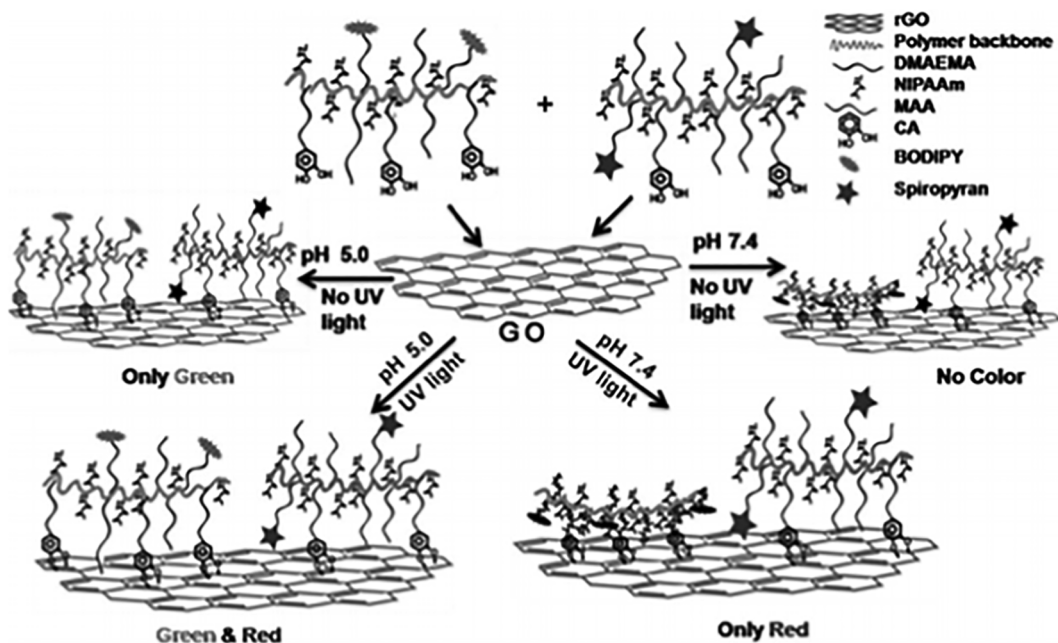


Fig. 30. Illustration of the preparation of CCDP/DBP-PPDN and DP/SP-PPNM/rGO and their response to stimuli as fluorescent probes. Reproduced with permission from Ref. [374]. Copyright 2014 Wiley.

assays, clearly showed the presence of the spherical MRSA (0.6–1 μm) on the membranes, verifying that the filtering of water was successful. Actually, in the filtrated water no MRSA was detected, while also no cultures of MRSA were able to grow.

4.3. Covalently functionalized graphene for environmental applications

Storing lithium cations is a fundamental process for the charge–discharge of lithium ion batteries (LIBs). Graphene oxide nanosheets have been reported as efficient templates for the accommodation of stable radicals [391]. Using a stable nitroxide organic radical, 4-hydroxy-2,2,6,6-tetramethylpiperidin-1-oxyl (4-hydroxy TEMPO), covalently grafted on graphene oxide via esterification allowed the fabrication of a Li^+ storage material tested as anode for LIBs [392]. Li^+ are accommodated on the abundant nitroxide radicals and graphene provides a high interfacial area with the electrolyte, as evidenced by the CV graphs recorded using a typical half-cell configuration with TEMPO-graphene oxide as the anode. Scanning in the region of 0.005–3 V (vs Li/Li^+) revealed the coupled redox peaks at 1.4/2.5 V related to the lithium insertion/extraction process, accompanied by a broad cathodic peak at 0.6 V attributed to the generation of a solid electrolyte interface (SEI) at the surface of the TEMPO-graphene oxide anode. The covalent incorporation of the TEMPO radicals on the graphene oxide excluded the possibility of the active species to be washed out in the electrolyte, allowing the anode material to perform up to 400 stable charge–discharge cycles with high capacity (1080 mAh/g).

Composites consisting of hexylamine-RGO/polyurethane nanocomposite-coated nylon have been proposed as enhanced hydrogen gas barrier films [393]. A simple carbodiimide-mediated addition of triaminoguanidine (TAG) on graphene oxide followed by coordination of metal centers (Cu^{2+} , Ni^{2+} , Co^{2+} and Fe^{2+}) allows the development of thermostable energetic materials [394]. The concept of storing energy meets the quest for storing gases, likewise hydrogen, or capturing gases, likewise CO_2 .

4.3.1. Hydrogen and carbon dioxide capture

Nanoporous materials for hydrogen and carbon dioxide storage is a challenging goal, currently intensively explored. Theoretical proposals for channelled-pillared graphenes suggest that these highly porous graphene networks would be capable to store hydrogen as high as 41 g/L under ambient conditions, meeting the requirements for mobile applications [395]. Graphene-based porous materials could contribute to the development of this technology. Theoretical approximations for graphene oxide nanosheets covalently functionalized by aryl-diboronic acid pillars showed superior ability to store hydrogen, comparable to metallorganic frameworks (MOFs) [157]. Graphene frameworks bearing 1 BDA per 32 graphene carbon atoms (GOF-32 or 1:1 GO:benzyl-diboronic acid) predicted to be the most structurally stable analog with the highest hydrogen uptake (ca. 6.1 wt% H_2 at 77 K and 1 bar), which was higher than any other known porous material. Actually, the latter graphene oxide framework materials were experimentally realised by solvothermal synthesis, where condensation of the benzyl-diboronic acid (BDA) with hydroxyl functionalities of graphene oxide occurs. Tuning the amount of the benzyl-diboronic acid, different d-spacing evidenced by powder XRD analysis. Lower 2θ angles were observed for higher amounts of pillars, whereas other analogous pillars (i.e. benzyl-1,4-diboronic acid) failed to intercalate between the graphene oxide nanosheets. Additionally, prompt gamma activation analysis (PGAA) further supports the intercalation of the diboronic acid derivatives and the 1:1 ratio of GOF-32. Experimental calculation of the GOF-32 BET surface area gave a value

of 470 m²/g (20 m²/g for the GO control) and a H₂ uptake of 1 wt% (0.2 wt% for GO). Further improvements on reducing the oxygen content of GO could increase the hydrogen uptake. GOF-32 was also tested for the CO₂ storage, recording values comparable to amine-functionalized MOFs. In a more recent work, using the same material architecture and focusing on the CO₂ capture properties of the graphene frameworks, higher BET surface values were achieved (560 m²/g) [396]. The absorption capacity for CO₂ was 4.96 mmol/g, higher than amino-functionalized silicas (MCM-48, MCM-41) with high CO₂/N₂ selectivity (48:1).

Covalent grafting of polyethyleneimine (PEI) on hydroxylated three-dimensional graphene was also reported as a hybrid material for superior CO₂ capture [397]. Graphene nanosheets were initially treated with KOH under solvothermal conditions at 180 °C to promote the uniform incorporation of hydroxyl functionalities on the graphitic plane. After purification, the functionalized nanosheets were freeze-dried affording a 3D-porous structure with uniform distribution of the oxygen functionalities, as witnessed by TEM imaging and EDS spectroscopy, respectively. The hydroxylated graphene (HG) was then reacted with aziridine furnishing the PEI-HG ensembles via a ring opening polymerization reaction. Polymer chains were covalently grafted on the nanosheets through the reaction of the aziridine with the hydroxyl groups and EDS spectra also showed the uniform distribution of N-atoms on graphene. XPS further validated the incorporation of the N-rich polymer chains. As long as the PEI content increases the pores of the 3D HG are filled with polymer and the latter is associated with the decreased intensity observed in XRD spectra ($2\theta = \sim 27^\circ$) for the hybrid materials with 0.51–1.98:1 PEI-to-HG ratio (the w/w ratio of the polymerization mixture). BET nitrogen absorption/desorption measurement provided information for the surface area of HG (193.51 m²/g) and HG-PEI ensembles with different w/w ratio. The observed values for 0.51, 1.03, 1.50 and 1.98:1 PEI-to-HG were 119.17, 76.50, 38.93 and 17.05 m²/g, respectively. The wt% of PEI within the PEI-HG ensembles was determined by TGA analysis and found to be 18 wt% for 0.51:1, 28 wt% for 1.03:1, 37 wt% for 1.50:1 and 42 wt% for 1.98:1. Solid state ¹³C MAS NMR studies reveal the formation of carbamate anion species (164.2 ppm) when the PEI-HG material is exposed to CO₂ atmosphere, indicating the interaction of the porous channels with the gas. For PEI-HG the highest CO₂ uptake (4.63 mmol/g at 25 °C/7 atm) was recorded. At higher temperatures (up to 75 °C), the adsorption capacity of the PEI-HG ensembles decrease, representing the ease of gas diffusion into the uniformly distributed PEI chains into the HG channels. Evidently, thermodynamics dominate the kinetic diffusion. Differential scanning calorimetry gave the enthalpy values during the adsorption process, which ranged between 62 and 68 kJ/mol, representative of chemical adsorption which is strong enough to selectively capture the CO₂ over the water molecules. Interestingly, all PEI-HG adsorbents reach half of their total capacity within 1–2 min, while an 80% was reached within 10 min. For reference, MCM-48 adsorbent functionalized by 3-aminopropyl groups, reached this capacity mark after 30 min. Based on the above findings, the PEI-HG adsorbents were investigated for their ability to capture post-combustion CO₂ (simulated flue gas, 10% CO₂). After 30 cycles of heat-driven regeneration mode, only a 1% activity loss was observed and this was attributed to the thermal stability of the ensembles and more specific to the high boiling point of the grafted PEI chains. In the 100–135 °C temperature window, the regeneration process was stable, due to the chemical nature of the adsorption mechanism. Comparison of the prepared material with a MCM-41 modified with PEI reference material, the desorption behavior of the PEI-HG ensembles was better as a fact of the enhanced thermal conductivity of the graphene nanosheets.

4.3.2. Oxygen reduction reaction (ORR)

The oxygen reduction reaction is a core process in clean energy devices such as fuel cells and metal-air batteries in alkaline media and proceed under two different mechanisms: i) a sluggish two-electron reduction of O₂ to peroxide anion (HO₂⁻) and ii) the more preferable fast direct four electron reduction of O₂ to H₂O. Platinum and Pt-based catalysts are the most conventional materials to catalyze the reaction, but apart from the high cost, suffer also from poisoning, agglomeration and poor durability. A quest for alternative materials is dealing with good conversion efficiency, selectivity for the four-electron mechanism, long-term stability and tolerance to other organic fuels (methanol, ethanol). Moreover, high specific surface area and fast charge transport properties are also required. There is a considerable amount of research articles that explore the catalytic activity of graphene (co)doped with heteroatoms (N, O, S, B, P) for electrodes in ORR [398].

In this section, we present covalently functionalized graphenes evaluated as cathodes for the ORR. To investigate the performance of the new catalysts a range of electrochemical techniques have been employed. Usually the working electrode is a glassy carbon electrode, which after polishing, is coated with the graphene-based nanomaterial. Typically, the cyclic voltamograms (CV) are performed in basic aqueous solutions (usually KOH 1 M) once saturated with N₂ and then saturated with O₂. This way, one can see if the observed reduction peaks are solely due to O₂ reduction. In addition, linear sweep voltammetry (LSV) studies in a range of rotation rates and potentials are performed on rotating disc electrode (RDE) in order to reveal the O₂ reduction mechanism on the hybrid material. Utilizing the Koutecky-Levich (K-L) equation, the diffusion limiting current and the number of transferred electrons can be estimated by the slope of the linear graphs. In a similar analysis at rotating ring disc electrode (RRDE), the yield of H₂O₂ (for the case of 2-electron mechanism) can be estimated. Finally, as the fabricated hybrids are (mostly) intended to be employed as cathode electrocatalysts for direct methanol fuel cells (DMFC), it is without surprise to conduct methanol crossover tests, namely to add methanol, while measuring the current density to observe changes that may occur. The stability tests involve either by examining catalyst's activity before and after several cycles of linear sweep voltammetry or chronoamperometry (CA) by estimating the current loss after a considerable amount of time.

Graphene nanosheets have no preferable sites, namely active sites, for the adsorption of oxygen molecules on their surface. Heteroatom doping is the most prominent way to generate active sites by altering the local charge density around the dopants, leading to higher oxygen physisorption and lower onset potentials for electrocatalysis. Sulfur doping has a high potential for the preparation of ORR electrocatalysts due to the unique conformations of the embedded sulfur atoms [399]. However, heteroatom doping is overall a time and energy consuming process lacking scalability. In contrast, molecular doping via covalent chemistry is cheaper, not requiring sophisticated infrastructure and thus feasible for bulk synthesis.

Engineering of the local charge density of graphene was demonstrated by the diazonium addition of nitrobenzene units on rGO [400]. TEM imaging of the functionalized nanosheets showed that the chemical modification did not affect the morphology of rGO, while the successful incorporation of nitrobenzene was confirmed by observing in the XP spectrum the peak of N1s (405.94 eV) representing a molecular loading of 7.58 wt%, in agreement with TGA. Raman analysis showed that I_D/I_G ratio between the D band and G band increased in PhNO₂-graphene compared to the starting rGO, indicating the increased number of defects arising from functionalization. Meanwhile, the G-band of the PhNO₂-graphene was found upshifted by 9 cm⁻¹ corresponding to efficient charge transfer from graphene to the nitrobenzene functionalities. The upshift of the G-band was proportional to the nitrobenzene loading, manifesting the ease of surface engineering of graphene. As expected, local differentiation of charge density would favor the electrocatalysis of ORR and actually its performance was superior, as compared to non-modified rGO. The reduction peak for PhNO₂-graphene appeared at -0.35 V vs SCE, while from the slopes of Koutecky–Levich plots at -0.8 V vs SCE the number of electrons was around 3.1 (2.5 for rGO), a value closer to the 4-electron mechanism. The modified graphene was also stable for over 2000 cycles and resistant to methanol.

Diazotization of thermally and chemically reduced graphene by arenes, with p or n character, resulted to different activity towards the ORR [401]. Besides the push or pull character of the molecular dopants, the impact of the molecular structure of the nanosheets was also evaluated. Chemically reduced graphene was prepared by reduction with NaBH₄, N₂H₄ or NH₄OH in liquid phase. Thermally reduced graphene showed the lowest oxygen content (1.97%) and no nitrogen atoms, as evidenced by XPS, in contrast to chemically reduced graphene, where the oxygen content was higher (6–20%) accompanied by nitrogen atoms (0.09–0.47%). Interestingly, diazotization to t-rGO resulted in higher nitrogen loading ($\Delta N = 4.45$) suggesting higher functionalization degree. The lowest functionalization degree of t-rGO was found for the diazonium addition of the electron donating 4-N (Me)₂PhNH₂, as determined by elemental combustion analysis. For the impact of the added functional units on t-rGO, resistivity measurements at 1 mA were performed and found to be decreased in the order 3,5-NO₂ > 4-NO₂ > 3-NO₂ > 4-CN > 2-NO₂ > 4-N (Me)₂Ph, while pristine t-rGO showed the minimum specific resistivity. Cyclic voltammetry studies in solution containing the [Fe(CN)₆]^{3-/4-} redox couple determined the heterogeneous electron transfer (HET) via the peak-to-peak separation of the reversible oxidation of the couple. For the cyanophenyl-functionalized t-rGO, the most narrow range (127 mV) was observed, thus the faster electron transfer, whereas the 3,5-bisnitrophenyl-functionalized rGO possessed the lowest value presumably due to its highest resistivity. Cyanophenyl-functionalized t-rGO, due to the electron withdrawing properties of the organic unit, gave the best ORR onset (-189 mV vs Ag/AgCl) and the best HER onset (-540 mV vs Ag/AgCl) for the 3- and 4-nitrophenyl-functionalized graphene.

Graphene oxide can be further enriched with carboxylic acids on the basal plane by reaction of the present epoxides with chloroacetic acid [402]. Then the carboxylic functionalities were coupled with 1,4 diaminobutane (DAB) via carbodiimide chemistry, generating cross-linked graphene oxide nanosheets. The remaining oxygen functionalities were reduced by sodium borohydride with slight heating (55 °C). XPS and FT-IR were employed to monitor the described processes. The N1s peak for the cross-linked was shifted to lower energy, compared to pure DAB, indicating the electron transfer from the C atoms of rGO plane to the N atoms of the linker. Imaging of the DAB-rGO network by SEM showed a crumbled porous medium and this morphology was further supported by examination with TEM, where a multilayered structure with a homogeneous distribution of the N atoms in the entire sample was evident. In order to evaluate the porosity of the DAB-rGO network N₂ absorption/desorption analysis showed that the specific surface area (SSA) is 2.6 times higher (289.6 m²/g) than pristine rGO (111.2 m²/g), whereas the pore size distribution of rGO-DAB showed a prominent pore size up to 60 nm, 30-fold increment in respect to rGO. TGA curves recorded under nitrogen atmosphere for rGO-DAB showed superior thermal stability, attributed to the hierarchical porous structure. Moving forward, EIS revealed an enhanced conductivity for the hierarchical structure and LSV essays with the aid of RDE electrode in O₂-saturated 0.1 M KOH solutions allowed to calculate the number of transferred electrons per O₂ involved in ORR as high as 3.85, very close to the 4-electron value (Fig. 31). Complementary measurements with a rotating ring disk electrode (RRDE) determined the yield of generated H₂O₂ as high as 4–5%, almost half, compared to the commercially available Pt/C (9.5%). rGO-DAB and Pt/C catalysts were maintained at an applied potential of -0.3 V for ~8 h at 1600 rpm in an O₂-saturated 0.1 M KOH solution to investigate their long-term stability. A higher relative current of 91.5% that persisted after 30000 s was observed for rGO-DAB compared to the Pt/C electrode, which exhibited a current loss of approximately 57% after the same period. The addition of methanol did not influence the current response of the hybrid, in contrast to the 87% activity decrement of Pt/C.

Malonitrile addition, in the presence of calcium hydride, to the epoxides of graphene oxide followed by addition of hydroxylamine hydrochloride and ammonia aided the preparation of rGO nanosheets decorated with N-hydroxy-imidamide functionalities (NHI) [403]. The as-prepared NHI-rGO was examined with FTIR, SEM, XRD, and Raman spectroscopy. A new band at 1656 cm⁻¹ was present in the FT-IR attribute to the amidoxime group accompanied by an amide II band of N–H at 1378 cm⁻¹. The absence of nitrile and carbonyl stretching frequencies validated the conversion to NHI. XRD and Raman spectroscopy assays verified the reduction of GO during the covalent modification, while SEM imaging revealed a paper-like structure with thin folded sheets. CV graphs, recorded in O₂ saturated aqueous solutions, showed a more positive onset potential for the ORR (-0.1 V vs the Ag/AgCl), compared to GO and electrochemically rGO, while revealed the maximum current density among the materials tested, including the commercial 20 wt% Pt/C. The limiting current density was 40 mA/cm² and the ORR was dominated by the 4-electron mechanism. Obtained from EIS data, the charge transfer resistance of GO was 24797 Ω, for malonitrile-graphene was 22672 Ω and that of NHI-rGO was 2712 Ω, rather comparable to that of 20% Pt/C (1696 Ω). Finally, the NHI covalently modified rGO catalyst was electrochemically more durable than commercial Pt/C as tested over time and the presence of methanol had no effect to its response.

In an attempt to accurately control pyridinic N-content in graphene, Zhong X. et al proposed the incorporation of conjugated pyridine units via [2 + 2] aryne cycloaddition reaction [404]. In this fashion pyridine active sites are introduced out of the basal plane, in contrast to elemental doping where “pyridinic” N-atoms are embedded into the basal plane of graphene. Two different

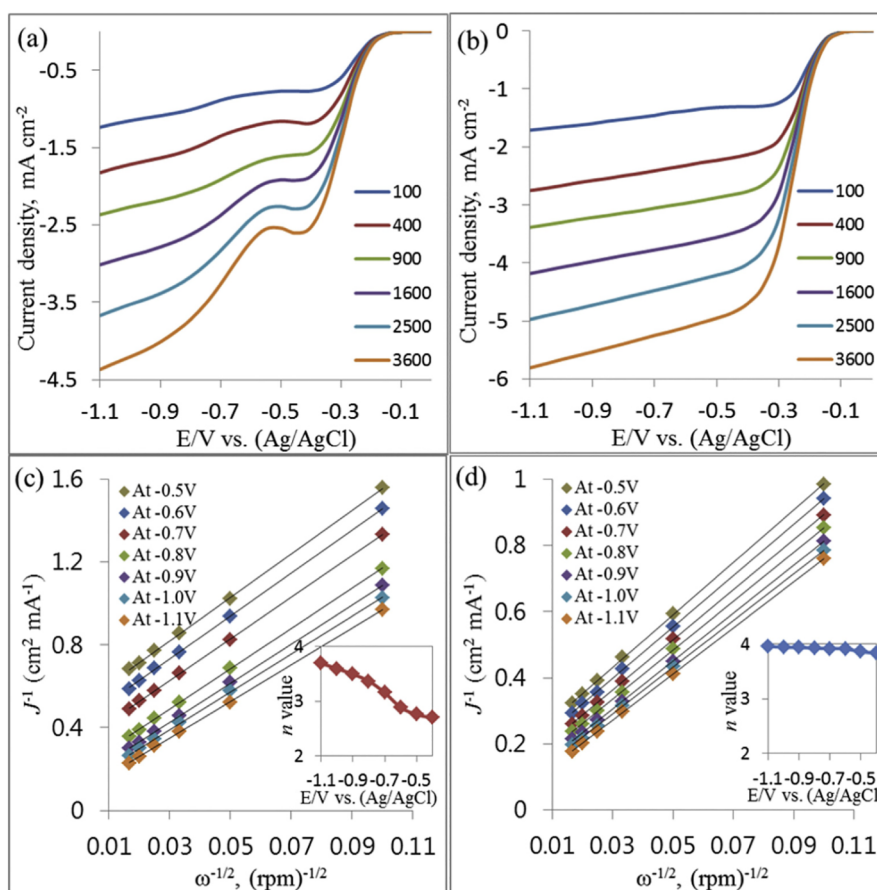


Fig. 31. The LSV for ORR at various rotation speeds on rGO (a) and DAB-rGO (b) in O_2 -saturated 0.1 M KOH at a scan rate of 10 mV/s; Koutecky-Levich plots for rGO (c) and DAB-rGO (d) at different electrode potentials; inset: the calculated electron number per O_2 by the Koutecky-Levich equation. Reproduced with permission from Ref. [402]. Copyright 2017 Elsevier.

pyridine precursors, 3-trimethylsilyl-2-pyridyl trifluoromethanesulfonate and 4-(triethylsilyl)pyridin-3-yl trifluoromethanesulfonate, were employed in order to evaluate the role orientation of the out of plane pyridinic nitrogen. The desired precursor was heated to 80 °C in the presence of cesium fluoride (CsF) and GO, furnishing the corresponding PyNG-2 and PyNG-3 covalently modified graphene. Multilayered modified nanosheets with voile-like structure were revealed by TEM imaging, while the SAED pattern showed that the main lattice of the graphene's skeleton had not been destroyed by the pyridine cycloaddition. By TGA analysis the loading of the organic molecule was evaluated as high as 1 functional pyridine group per 29 carbon atoms, close to the observation by XPS (1:25). AFM studies provided significant information for the stacking through space, since the incorporation of the pyridines increased the space between the folded modified graphene (4.0–4.5 nm) as compared to the starting graphene flakes (3.0–3.3 nm). This increase in height was attributed to externally attached pyridine groups to graphene in the vertical direction, which was also supported by XPS and Raman spectroscopy. Moving to the electrocatalytic properties of the nanoensembles, CV runs of PyNGs performed in O_2 -saturated 0.1 M KOH electrolyte solutions, demonstrated a significant enhancement in ORR electrocatalytic activity. As it can be seen in Fig. 32, PyNG-3, where the nitrogen atom is more exposed to the chemical environment of the solution, had a more pronounced electrocatalytic activity than PyNG-2. LSV studies with RDE (400–2025 rpm) in 0.1 M KOH O_2 -saturated electrolyte unveiled that the ORR mechanism was governed by first order kinetics. Remarkably, the corresponding Koutecky–Levich plots at the electrode potential of -0.6 V revealed that PyNG-3 exhibited higher ORR current in comparison to commercial Pt/C catalyst. The n values for PyNG-3 increased from 3.1 to 3.72 as the applied voltage increased, for PyNG-2 were within the range of 2.2 to 3.4. In addition, PyNG-3 was unaffected by methanol crossover.

Pyridine functionalities have been also utilized as monodentate ligands for the growth of graphene-based metallo-organic frameworks [405]. Specifically, 4-styryl pyridine was introduced on the basal plane of chemically reduced graphene oxide by means of diazonium chemistry, followed by the addition of 5,10,15,20-tetrakis(4-carboxyl)21H,23H-porphyrin (TCPP) and iron chloride ($FeCl_3$). The latter facilitated the conversion of TCPP to the corresponding Fe-TCPP and the assembly of the Fe-TCPP molecules via complexation between the Fe^{+3} cations and the carboxylates at the periphery of Fe-TCPP. At the same time the covalently grafted 4-styryl pyridine on the graphitic basal plane were coordinated to the iron metal centers of the assembled porphyrin network, furnishing the graphene-MOF ensemble. In order to address the impact of the pyridine-functionalized rGO in the metalloporphyrin MOF

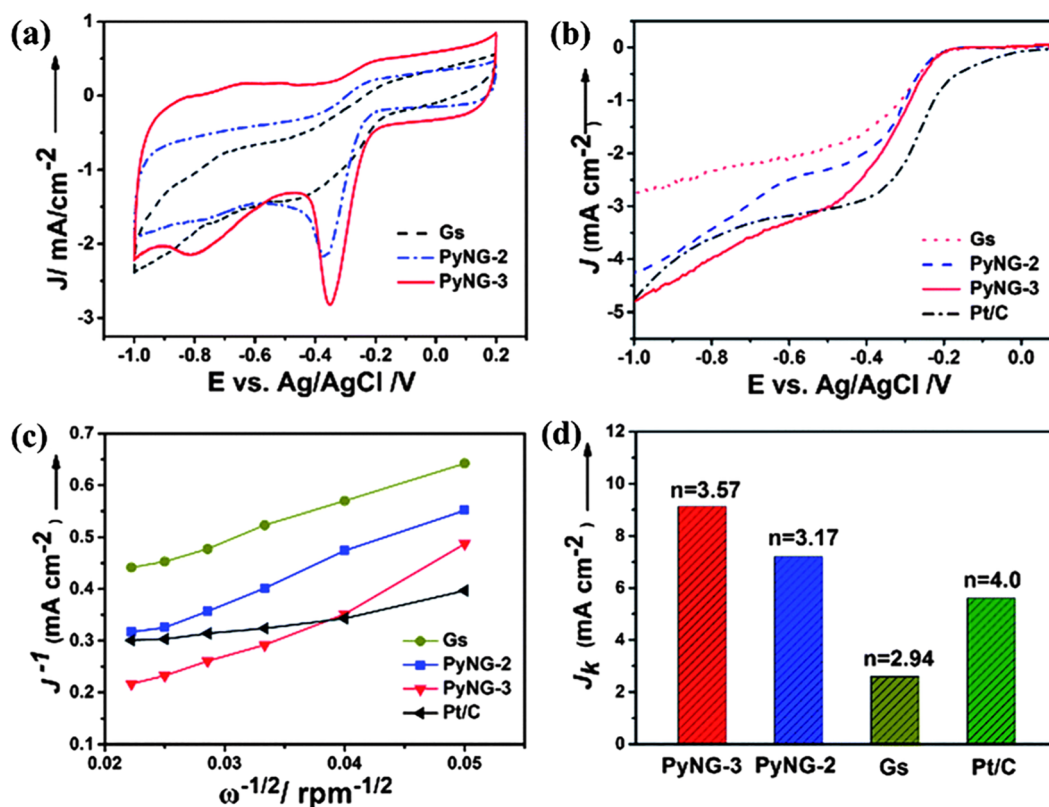


Fig. 32. (a) CVs (100 mV/s) of Gs and PyNGs in O₂-saturated 0.1 M KOH, (b) LSV curves (10 mV/s) for Gs, PyNGs, and Pt/C on an RDE (1600 rpm) in an O₂-saturated 0.1 M KOH solution, (c) Koutecky–Levich plots of Gs and PyNGs at -0.6 V and, (d) kinetic limiting currents of different samples and their corresponding electron-transfer numbers at -0.6 V. Reproduced with permission from Ref. [404]. Copyright 2014 Royal Society of Chemistry.

crystallization, UV–Vis absorption and FT-IR spectroscopy assays were performed. The metalloporphyrin MOF shows a 27 nm red-shift of the Soret band, as compared to the bare TCPP, accompanied by the reduction of the four Q bands to two, due to metal coordination, while in the presence of pyridine-modified rGO the Soret band was heavily blue-shifted by 37 nm, indicating the coordination of the MOF on graphene. FT-IR spectroscopy verified not only the incorporation of iron into the macrocycle, by monitoring the intense Fe–N stretching vibration mode at 1008 cm⁻¹, but also the assembly of the metalloporphyrins to MOF structure by noting the 25 cm⁻¹ down-shift of the vibration frequency of carboxylates located at the perimeter of the macrocycle. The w/w percentage of functionalized graphene is a critical factor to be considered towards the optimization of the ORR efficiency of the hybrid nanomaterial. According to XPS, the amount of nitrogen in the pyridine-functionalized nanosheets ranged between 7.1 and 9.8 wt%. Complementary SEM and XRD studies showed that increasing the content of the graphene sheets resulted in the gradual transformation of the crystalline MOF into an amorphous material, nevertheless the higher content increased the adsorption surface area of the hybrid catalyst (up to 933 m²/g for 50 wt%). Similar effect was observed for the effective surface area as estimated by cyclic voltammetry for the redox reaction of Fe(CN)₆^{3-/4-} and calculated according to the Randles-Sevcik equation. For 50 wt% a well-defined cathodic peak centered at -0.23 V was observed in the CV graph. The ORR kinetics revealed a 4-electron transfer mechanism (between -0.35 to 0.65 V) in contrast to GO or free (Fe-P)_n MOF which was the 2-electron one (Fig. 33).

Nitrogen-dentate ligands covalently attached on graphene have been used for the preparation of palladium catalysts [406]. Accordingly, covalently functionalized graphene oxide nanosheets featuring copper complexes with triazole-pyridine ligands have been proposed as ORR catalysts (Fig. 34) [407,408]. Incorporation of a (tri-isopropyl)silylethynylbenzene units was performed by addition of the corresponding diazonium salt on GO, followed by deprotection of the TMS group of the alkyne terminus by fluoride anions. [407] The as prepared ethynyl-functionalized GO was treated with CuSO₄ and 2-(azidomethyl)pyridine promoting the [3 + 2] Huisgen cycloaddition reaction. Coordination of copper on the triazole-pyridine ligand was promoted by incubation into CuCl₂ solution, yielding the hybrid catalyst RGO-TAmPyCu, as shown in Fig. 34a. The hybrid material was blended with TiO₂ for improved stability in solution and tested as electrocatalyst for the ORR. XPS surveys allowed the determination of the N- and Cu-content (4.47 and 0.95%, respectively) within the hybrid materials, while Raman spectroscopy provided evidence both for the functionalization and reduction step, with the I_D/I_G ratio changing from 0.97 for GO to 1.07 for RGO-TAmPyCu. In oxygen saturated alkaline electrolyte, the covalent RGO-TAmPyCu electrocatalyst outperformed the corresponding physisorbed ensembles and the analogous hybrid materials based on carbon nanotubes.

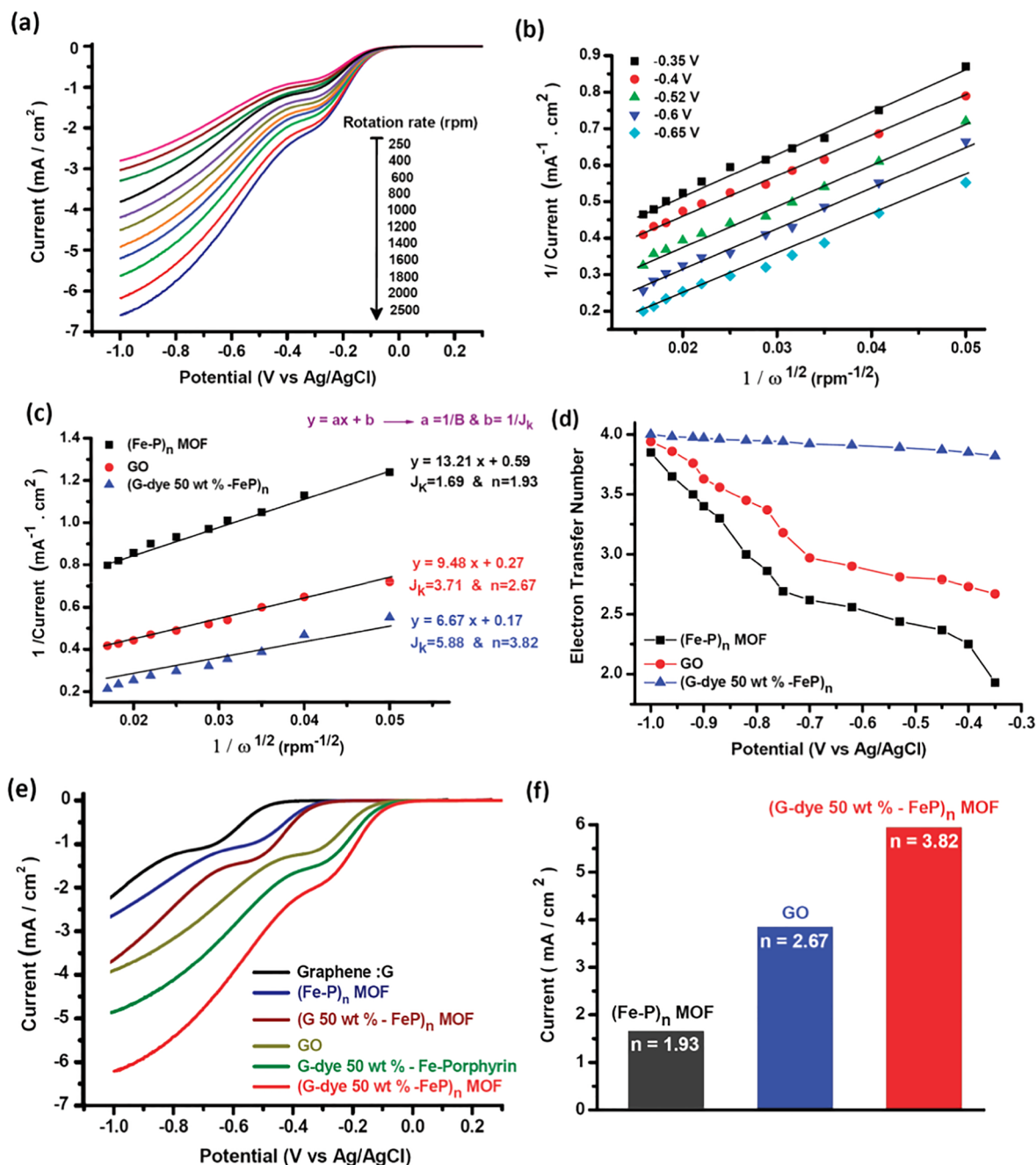


Fig. 33. (a) Rotating disk electrode (RDE) linear sweep voltammograms of (G-dye 50 wt% -FeP)_n MOF in O₂-saturated 0.1 M KOH with various rotation rates at a scan rate of 10 mV/s. (b) Koutecky-Levich plots at different electrode potentials of (G-dye 50 wt% -FeP)_n MOF at different electrode potentials. (c) Koutecky-Levich plots of (G-dye 50 wt% -FeP)_n MOF, (Fe-P)_n MOF and GO at -0.65 V. (d) The dependence of the electron transfer number on the potential for (G-dye 50 wt% -FeP)_n MOF, (Fe-P)_n MOF and GO at various potentials. (e) RDE voltammograms of Graphene, (Fe-P)_n MOF, (G 50 wt% -FeP)_n MOF, G-dye 50 wt% -Fe-Porphyrin, (G-dye 50 wt% -FeP)_n MOF and GO at a rotation rate of 2000 rpm. (f) Electrochemical activity given as the fully diffusion-limited current density (JK) at -0.65 V for (Fe-P)_n MOF, (G-dye 50 wt% -FeP)_n MOF and GO. Reproduced with permission from Ref. [405]. Copyright 2012 American Chemical Society.

Along the same lines, a bio-inspired mimic of laccase enzyme, copper containing oxidase, was prepared for the conversion of molecular oxygen to water molecules [408]. Initially, GO was modified by the diazonium addition of ethynylpyridine units on the basal plane of GO, followed by a click reaction with 2,2'-(1H-1,2,3-triazole-1,4-diyl)dipyridine (TADPy), furnishing the triazole-dipyridine modified GO (GO-TADPy), which was then reduced by hydrazine to the corresponding rGO-TADPy ensembles. Treatment with CuCl₂ allowed the complexation of Cu⁺² and the formation of the biomimic nanocatalyst (Fig. 34b). XPS analysis determined

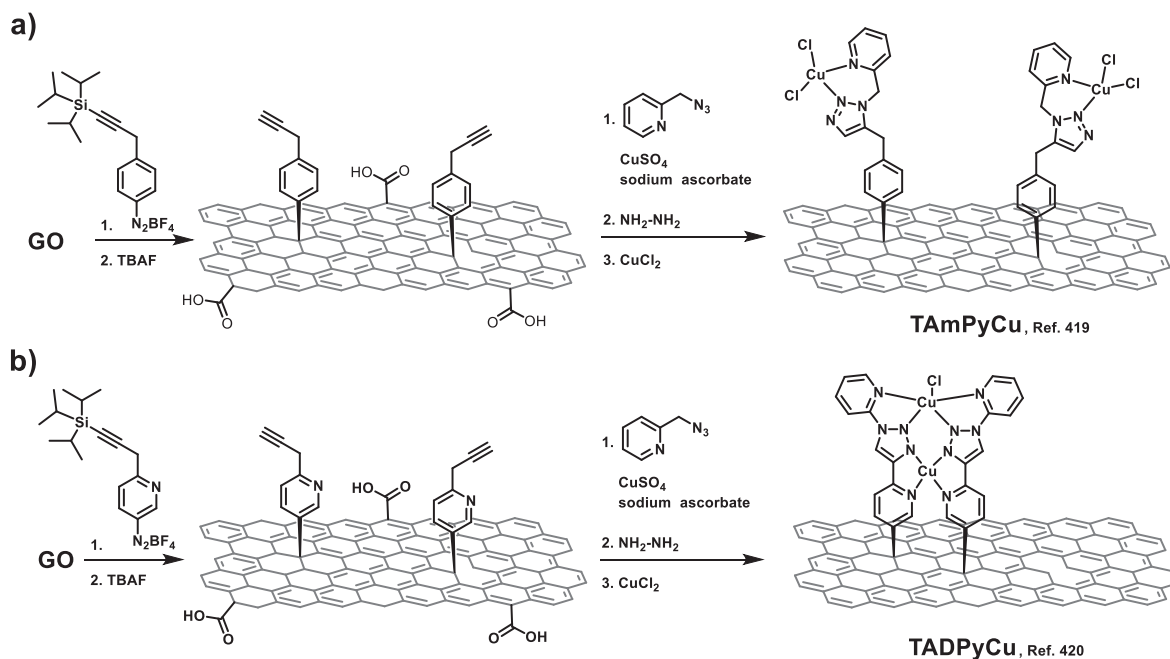


Fig. 34. Incorporation of nitrogen-dentate ligands on graphene oxide by means of diazonium chemistry for the preparation of a) mononuclear and b) binuclear copper complexes for the electrocatalysis of ORR.

the copper content as high as 0.56% and the N-to-Cu ratio approximately 5.8, indicating that the overall covalently attached TADPy ligands mostly coordinated with Cu ions in a 1:1 ratio. Diazonium addition was successful, since the I_D/I_G ratio for GO-TADPy was 1.04 (0.95 for GO) and further increased at the reduction step towards rGO-TADPy (1.12), showing that new domains consisting of conjugated carbon atoms were created by the removal of the oxygen groups. The CV graph of the covalently formed nanohybrids (rGO-TADPyCu) presented a large cathodic current at approximately 0.8 V vs. RHE and the onset potential observed by the RDE electrode was 0.951 V, a more positive value compared to the control catalysts rGO/TAPyCu (non-covalent mononuclear catalyst, 0.917 V), rGO/TADPyCu (non-covalent binuclear catalyst, 0.937 V) and rGO (0.887 V) (Fig. 35a-c). From Koutecky-Levich plots a $n = 3.85$ at the potential range of 0.45–0.6 V suggests a dominant 4-electron reduction process (Fig. 35d), while RRDE studies detected 10% H_2O_2 (2% in phosphate buffer), in sharp contrast to control catalyst which had higher values (Fig. 35e). Overall the rGO-TADPy biomimic was stable for 10,000 cycles and resistant to 2 M methanol (Fig. 35f).

Incorporation of thiol units on fluorographene by reaction with potassium isopropyl xanthogenate was reported as another route for the preparation of thiofluorographene as a template for the immobilization of lipase and catalase enzymes [181]. Initially, xanthogenate anions (nucleophiles) attack the fluorine atoms and substitute them, followed by a two-step treatment at alkaline and acidic conditions, furnishing the thiographene nanosheets. The XP spectrum validated the overall process and allowed the determination of the sulfur content as high as 5.1 at% (F content: 20%). The amount of the immobilized enzyme was proportional to the sulfide amount on graphene. The immobilization of the enzymes is driven by physisorption at the sulfide edges during a vortex shaking of the individual species and as evidenced no deactivation took place, thus can be fully exploited their catalytic properties. Catalase activity of the immobilized enzyme was monitored by UV-Vis spectroscopy, namely by the decreasing of the H_2O_2 absorbance ($\epsilon = 40 M^{-1} cm^{-1}$) at 240 nm.

Cobalt[tetrakis(o-aminophenyl)porphyrin] (CoTAPP) exhibits four aminobenzene groups at the periphery, thus it is likely to polymerize via radical coupling under the diazonium addition conditions, apart from being covalently grafted on the graphene sheets [409] (Fig. 36, left panel). Diazonium addition of CoTAPP to rGO was confirmed with Raman spectroscopy, where the I_D/I_G increased by 14% signifying the conversion of sp^2 carbons to sp^3 carbons during the chemical grafting of CoTAPP. As observed in SEM, CoTAPP within CoTAPP-rGO was well dispersed on the surface of graphene and micro-sized polymerized. The electric resistance of CoTAPP-rGO was below 5.0 Ω as calculated by EIS, while the onset potential for the ORR was + 0.6 V in O_2 saturated acidic media (0.5 M H_2SO_4) following the 4-electron pathway with the n value increasing from 3.5 to 4 in the range of -0.3 V to + 0.2 V.

Another cobalt-porphyrin, cobalt[5,15-(p-aminophenyl)10,20(pentafluorophenyl)-porphyrin] (CoAPFP), was utilized for the covalent modification of graphene oxide via carbodiimide chemistry [410] (Fig. 36, right panel). FT-IR verified the presence of the amide functionalities ($C = O$, 1648 cm^{-1}) generated by the chemical attachment of the porphyrin. The presence of CoAPFP was evident in the UV-Vis absorption spectrum by monitoring the characteristic Soret band (red-shifted by 18 nm as compared to the absorption due to bare CoAPFP), whereas the Raman spectrum showed a red-shift of the G-band, suggesting strong intra-hybrid electronic communication. In order to improve the conductivity of the distorted graphitic lattice, CoAPFP-GO was electroreduced to the corresponding CoAPFP-rGO material, which was tested as catalyst for the ORR (Fig. 37). Electroreduction was performed by 30

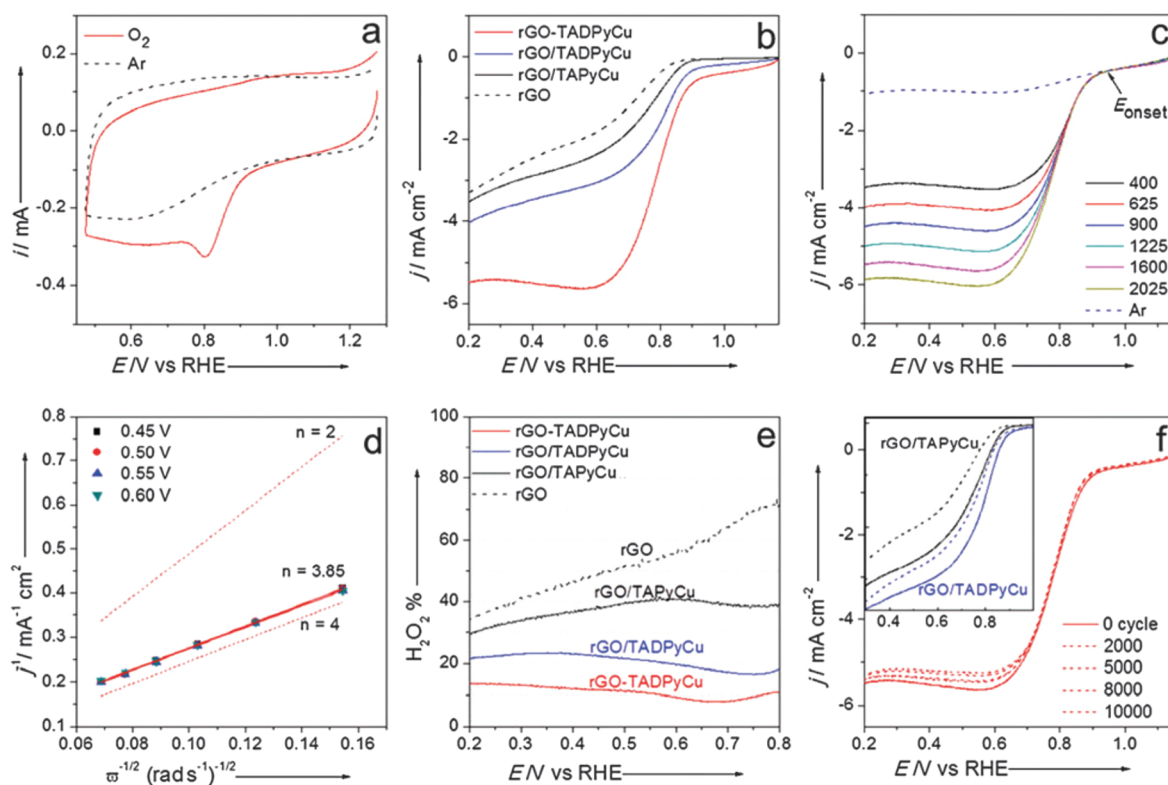


Fig. 35. (a) Cyclic voltammograms of rGO-TADPyCu in Ar (dotted black) and O_2 -saturated (red solid) 0.1 M KOH solutions. (b) Linear scanning voltammograms of rGO-TADPyCu (red), rGO/TADPyCu (blue), rGO/TAPyCu (black) and rGO (dashed black) catalysts in O_2 -saturated 0.1 M KOH. Electrode rotation speed: 1600 rpm. (c) Rotating-disk voltammograms of rGO-TADPyCu in O_2 -saturated 0.1 M KOH solution at the different rotation rates indicated. The dotted line indicates the background when scanned in Ar-saturated solution. (d) Koutecky–Levich plots at different potentials. Theoretical 2-electron and 4-electron reduction processes are shown as dotted lines. (e) Peroxide yield for rGO-TADPyCu (red), rGO/TADPyCu (blue), rGO/TAPyCu (black) and rGO (dashed black) catalysts in O_2 -saturated 0.1 M KOH. (f) ORR polarization plots of rGO-TADPyCu after 0, 2000, 5000, 8000, and 10,000 potential cycles in an O_2 -saturated 0.1 M KOH, respectively. The inset shows ORR polarization plots of rGO/TADPyCu (blue) and rGO/TAPyCu (black) after 0 and 10,000 cycles, respectively. Potential was cycled between 0.575 and 0.975 V at a rate of 50 mV/s. Electrode rotation speed: 1600 rpm. Reproduced with permission from Ref. [408]. Copyright 2015 Royal Society of Chemistry.

repeating cycles over a potential range of 0 to -1.5 V at a scan rate of 50 mV/s. AFM imaging of CoAPFP-rGO indicated that CoAPFP was present on both sides of the nanosheets and via XPS the cobalt ratio was as high as 0.74 atomic %. The ORR efficiency of the as-prepared CoAPFP-rGO was superior than the corresponding one due to the simply mixed rGO and CoAPFP, manifesting the beneficial role of covalent modification. Moreover, in the absence of coordinated cobalt in the porphyrin macrocycle, the reactivity was further decreased, highlighting the role of cobalt cations to the overall catalytic reaction. Within the potential range -0.3 to -0.7 V, the ORR activity recorded for CoAPFP-rGO follows a 4-electron ($n > 3.8$) mechanism, with current density comparable to commercial Pt/C, retaining the 80% of the initially recorded current after 2.5 h of continuous operation and having good resistance to methanol.

Covalent decoration of graphene with iron(II) phthalocyanine has been proposed for the fabrication of efficient cathodes for the ORR (Fig. 38). A first example was carried out by enriching graphene oxide with carboxylic acid functionalities, via HBr/oxalic acid treatment, and grafting of iron(II) tetra-aminophthalocyanine (FeTAPc) via carbodiimide chemistry (Fig. 38, left panel) [411]. The as prepared covalent hybrids were post-treated with hydrazine to reduce the remaining oxygen functionalities on the graphene nanosheets. XPS analysis of the nitrogen functionalities C–N, C=N and NH_2 revealed that in the case of the covalently grafted FeTAPc a shift to higher binding energy was evident compared to free FeTAPc molecules, attributed to charge transfer from the FeTAPc to graphene. Moving to the electrocatalysis of ORR, the current density for the FeTAPc-rGO was higher than that of free FeTAPc, with a well-defined cathodic peak centered at -0.12 V vs. SCE and the K-L plots suggested that the 4-electron mechanism is more likely for the covalent ensembles than the free molecule. From the Tafel plot, the observed lower (41 mV/dec) and higher (396 mV/dec) overpotential regions demonstrated that the rate-determining step was the first electron transfer reaction and the two-electron transfer reaction, respectively. FeTAPc-rGO exhibited good stability with a current loss of 16.5% after 10,000 s and excellent methanol tolerance. Further studies on FeTAPc-based graphene hybrids, prepared by covalent grafting of these molecules on GO via carbodiimide chemistry, showed that the presence of covalently grafted FeTAPc on the rGO nanosheets allows the assembly of FeTAPc to nanoparticles (Fig. 38, right panel) [412]. SEM and TEM imaging assays unveiled that FeTAPc moieties were assembled to nanoparticles homogeneously dispersed on graphene. The overall ORR activity was comparable to that of non-assembled FeTAPc, presented above, however the strong π - π interactions between the FeTAPc molecules emerge new ways for handling the morphology

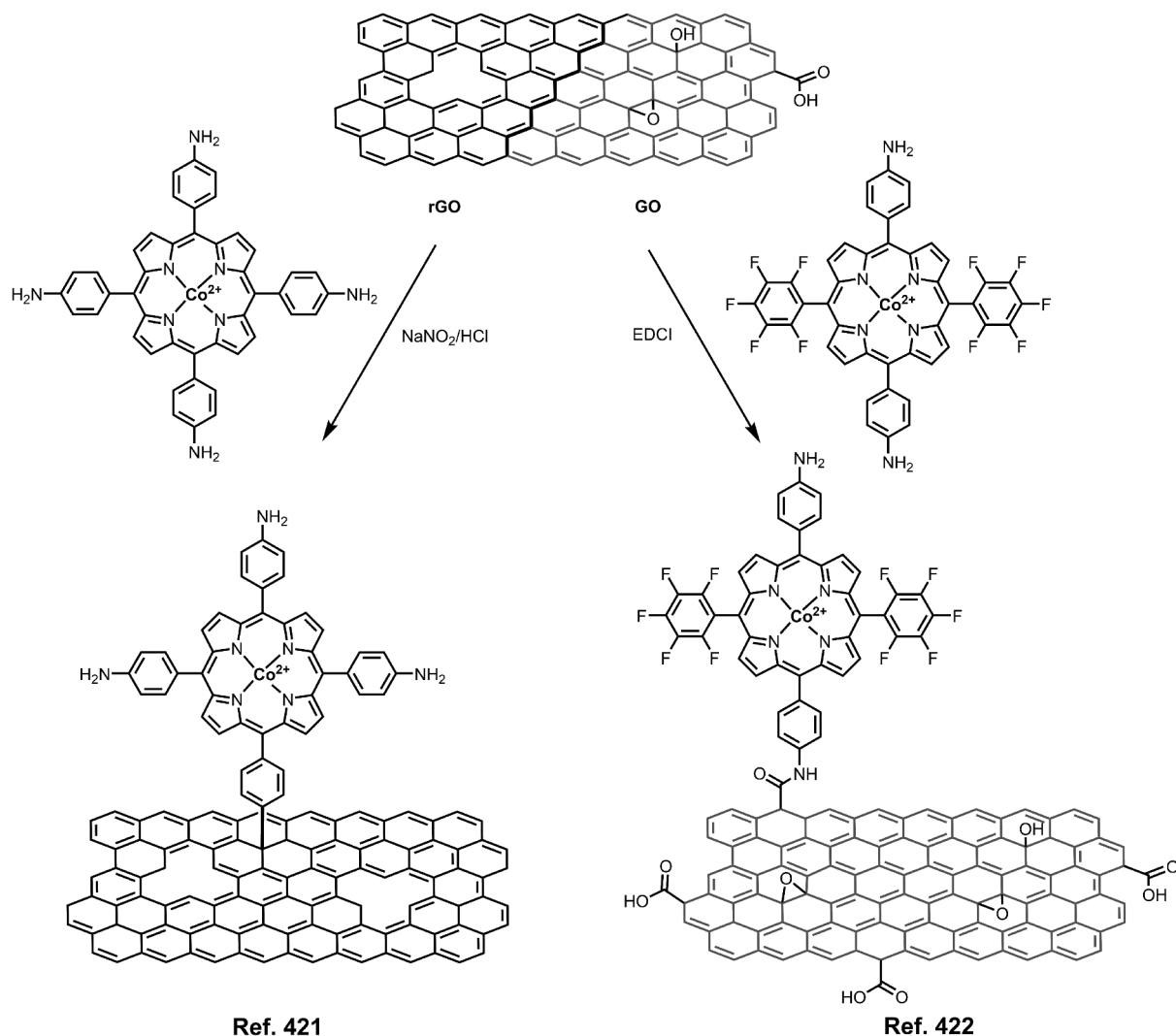


Fig. 36. Functionalization of graphene with cobalt-porphyrins by diazonium addition (left panel) and amide formation (right panel).

at the nanoscale.

Beyond polymeric materials produced by self-assembly, electropolymerization methods have been also exploited for preparing hybrid graphene-based ORR electrocatalysts (Fig. 39). Utilizing the chemistry on the epoxy groups of graphene oxide, 1,5-diaminoanthraquinone (1,5-DAAQ) was successfully attached on the nanosheets and electropolymerized with the aid of cyclic voltammetry [413]. The initially prepared (1,5-DAAQ)-GO ensembles were drop-casted on a polished glassy carbon electrode and subjected to CV runs (-1.3 to $+1.1$ V) in the presence of the monomer under acidic conditions. Accordingly, the negative scan enables the electroreduction of GO, namely the removal of the oxygen species of GO (at ~ -1.1 V), while the positive scan promotes the polymerization of 1,5-DAAQ (Fig. 39a). Overall, this is a handy method to prepare covalent ensembles based on electropolymerized arrays on RGO, while complementary electropolymerization assays assist the characterization of the chemically grafted electropolymerized array. Specifically, the elongation of the polymer chain was found to grow in analogous fashion to polyaniline (PANI), as evidenced by the similar redox peaks at $+0.12$ and $+0.45$ V (Fig. 40), representing the elongation of the polyaniline skeleton within P(1,5-DAAQ)-RGO. Moreover, monitoring the current at $+0.12$ V during the repeating cycles, the rate of electropolymerization decelerated between the 11th and 15th cycle, suggesting the termination of the process. Field emission SEM imaging studies showed a barleycorn-like porous morphology for the P(1,5-DAAQ)-RGO. FT-IR provided significant information both for the incorporation of 1,5-DAAQ and the electropolymerization. The characteristic C=O stretching vibration at 1608 cm^{-1} of 1,5-DAAQ was clearly observed in the spectrum of (1,5-DAAQ)-RGO, accompanied by C-N stretching vibrations of the imino group at 1658 cm^{-1} generated by the chemical attachment on the graphitic lattice and the C-N signature of the free primary aromatic amino group at $\sim 1290\text{ cm}^{-1}$. By Raman spectroscopy, the calculated I_D/I_G ratio for (1,5-DAAQ)-GO was higher than the corresponding of the starting GO, indicating the functionalization/reduction of the nanosheets within the hybrid material. Supportive findings were observed by XPS. Analysis of the N1s peak of the hybrid material showed four peaks with binding energies of 398.5 (=N-), 399.7 (-NH-), 401.3

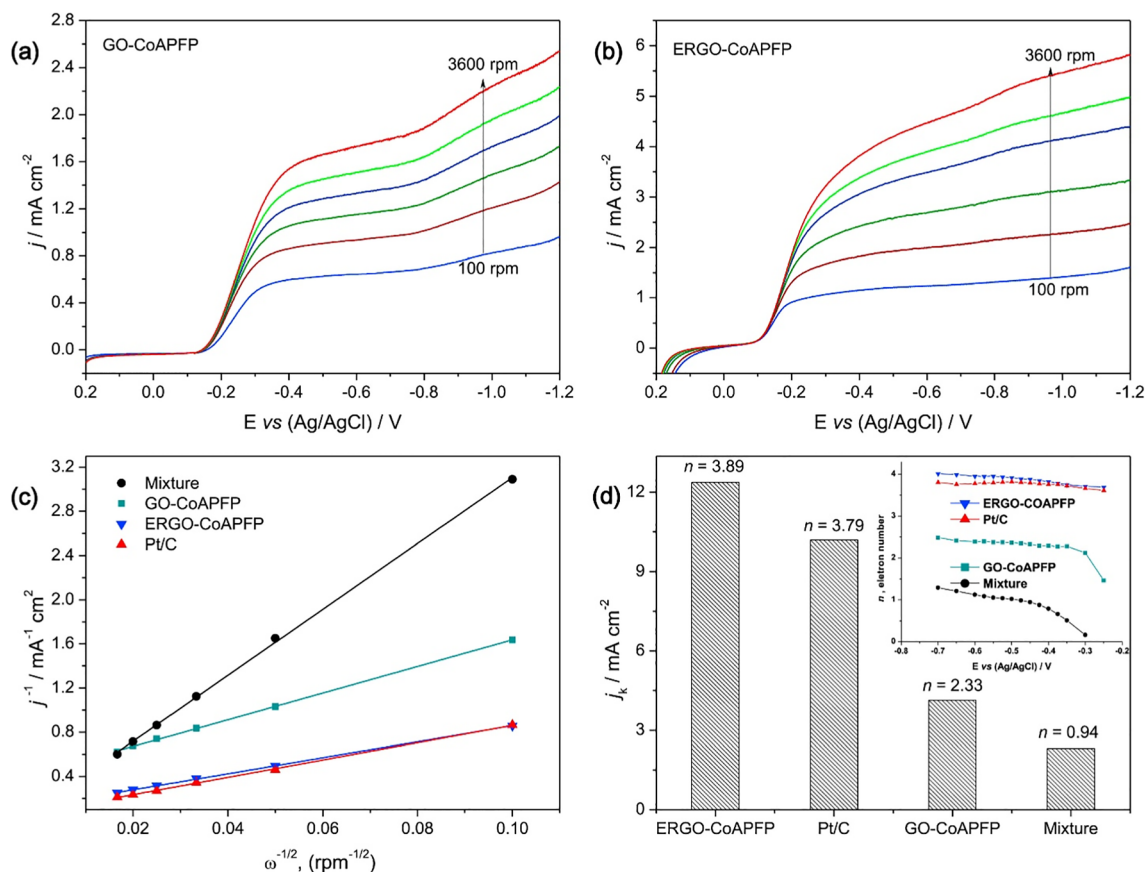


Fig. 37. RDE voltammograms for ORR on the (a) GO-CoAPFP and (b) electroreduced GO-CoAPFP modified electrodes at various rotation speeds (100, 400, 900, 1600, 2500, and 3600 rpm) at a scan rate of 10 mV/s in an O₂-saturated 0.1 M KOH solution. (c) Comparative K-L plots for the ORR catalysis and (d) kinetic-limiting current of the corresponding electron transfer numbers at -0.45 V (the inset shows the electron transfer number at various potentials). Reproduced with permission from Ref. [410]. Copyright 2014 Elsevier.

(protonated primary amine, $-\text{NH}_2^+$) and 403 eV (protonated imine, $=\text{NH}^+$), verifying the success of the proposed polymerization scheme. Investigation of the electrochemical properties of the hybrid material was carried out by analyzing the peak potential separation of the $[\text{Fe}(\text{CN})_6]^{3-/4-}$ redox couple. The anodic (oxidation) and cathodic (reduction) peaks of the redox couple were separated by 73 mV, the lowest recorded value as compared to the reference materials, indicating faster electron transfer kinetics and thus a faster reversible oxidation/reduction mechanism. Electrochemical impedance spectroscopy (EIS) in KCl electrolyte containing the ferrocyanide/ferricyanide probe showed a R_{CT} of 70.6 Ω (close to 51.8 Ω for RGO), highlighting the importance of the reduction step for the conductivity of the ensembles (321.2 Ω for (1,5-DAAQ)-GO). Finally, CV and RDE measurements performed in oxygen-saturated acidic solutions and the ORR efficiency of the hybrid material was evaluated. As derived from the K-L plots, the tested electrocatalyst follows a 2-electron reduction mechanism, namely the electroreduction of dissolved oxygen to hydrogen peroxide, and generated the highest cathodic current density (-3.5 mA/cm^2) among the reference materials (bare glassy carbon, RGO, P(1,5-DAAQ)).

Chemistry on the epoxy groups of GO was utilized for the preparation of polyterthiophene-anchored graphene oxide nanosheets, poly(APT-GO) (Fig. 39b), for the electrocatalysis of ORR [414]. A terthiophene monomer functionalized with a pyrimidine-amine (APT) on the middle ring was chemically introduced on the graphitic surface with the aid of sonic power. The FT-IR spectra of the hybrid APT-GO ensembles has a weakened band at 1265 cm^{-1} (epoxy C-O stretching vibration), as compared to pristine GO, indicating the consumption of the epoxy groups occurred due to the nucleophilic attack by the amine terminated APT monomer. Complementary FT-IR studies on the sonochemical reaction of GO with terthiophene derivatives carrying either a carboxylic or benzoic group shown no impact on the epoxy content, namely no reaction occurred. Moreover, in the spectra of APT-GO the band at 1549 cm^{-1} was attributed to the C-N stretching, emerged by the covalent incorporation of the monomer. Electropolymerization was carried out in the presence of the monomer and three repeating CV cycles in the range 0 to +1.5 V. Comparison of the TGA graphs of APT-GO and poly(APT-GO) revealed enhanced thermal stability for the polymer-GO material, more specifically, the decomposition temperatures were at 185 $^\circ\text{C}$ and 315 $^\circ\text{C}$, respectively. XPS survey after the electropolymerization showed a decreased epoxy content accompanied by a peak at 286.8 eV assigned to the C-N bond formation between the graphene nanosheets and the polymer, while also a chemical composition of 72.3% carbon, 11.3% oxygen, 8.48% nitrogen and 7.85% sulfur, verified the presence of the

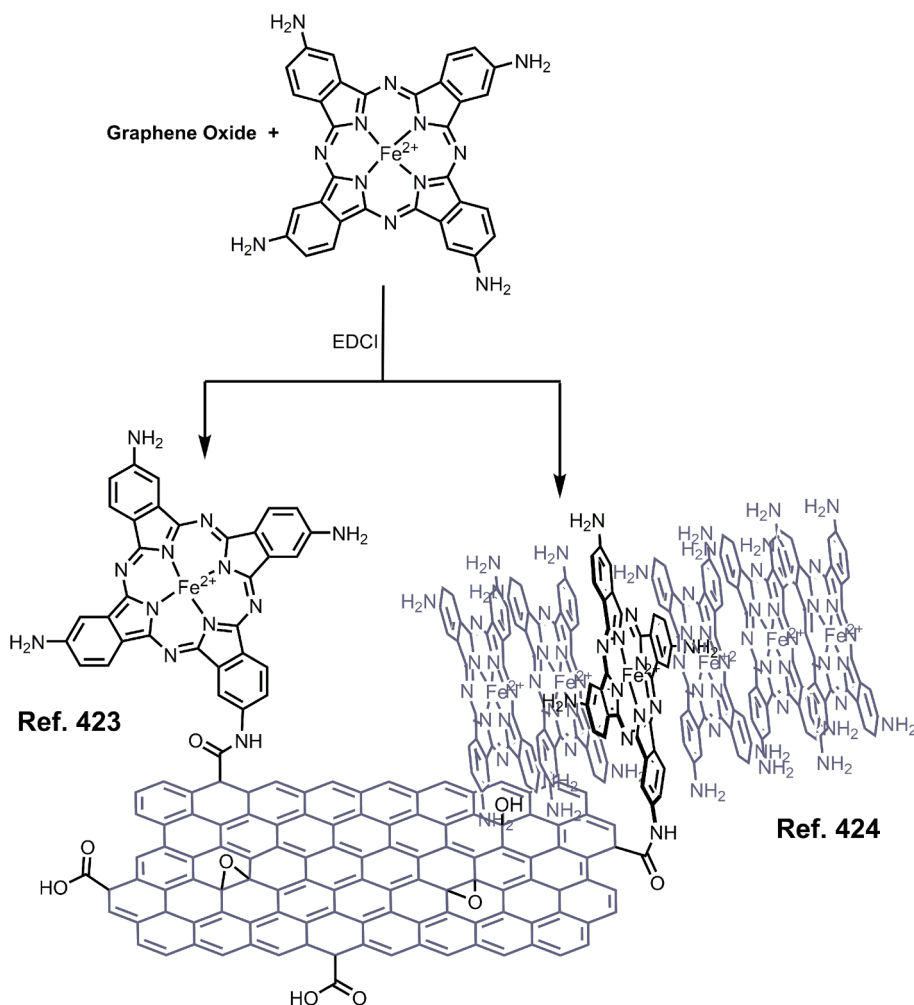


Fig. 38. Covalent grafting of Fe(II)-phthalocyanine on graphene oxide (left panel) and the self-assembly of free Fe(II)-phthalocyanine on the chemically attached ones (right panel).

polythiophene chains. HRTEM imaging of APT-GO and poly(APT-GO) displayed no significant changes to the morphology, although aggregated polythiophene chains were observable. The charge transfer properties were screened by EIS and R_{ct} values as high as 1.52, 0.43 and 0.88 k Ω were recorded for GO, poly(APT) and poly(APT-GO), respectively, while all the Nyquist plots in the frequency range of 100 kHz to 100 mHz form a semicircular arc. The covalent incorporation of the polymer significantly improves the R_{ct} as compared to pristine GO. Poly(APT-GO) tested for the electrochemical reduction of oxygen in alkaline solutions with the aid of RDE setup and a preferable 3.5-electron mechanism observed at -700 mV vs Ag/AgCl.

4.3.3. Hydrogen evolution reaction (HER)

Hydrogen evolution reaction (HER) is a fundamental reaction for the sustainable generation of hydrogen gas from water. Ru-complexes, phthalocyanines as well as non-metal organic dyes have been thoroughly tested in dye-sensitized semiconductor systems for the photoinduced hydrogen evolution [415]. The principal process is the photoexcitation of the sensitizer, the charge separation and the migration of electrons to the photoanode. Similar to ORR, the HER activity of a nanocatalyst varies depending on the experimental conditions (i.e. pH) and the characteristics of the photoanode (i.e. specific surface area, thickness), therefore, the direct comparison of the performance for different hybrids is not a straightforward process.

Triphenylamine (TPA) is a branched amine moiety with strong electron donating and hole-transport properties. 4-Formyl-TPA (TPA-CHO) has been successfully grafted on liquid-assisted exfoliated graphene through 1,3-dipolar cycloaddition [416]. (Fig. 41a) A suspension of exfoliated graphene in NMP containing the TPA-CHO and N-methylglycine allowed to react at 125–135 °C under N₂ for 5 days, furnishing the TPA-graphene ensembles. The absorption of TPA within the TPA-graphene was found at 280 nm, blue-shifted by 19 nm compared to the free molecules, while in the IR spectrum prominent bands at 1022, 1260, and 1095 cm⁻¹ arose from the 5-membered aziridine ring. The I_D/I_G ratio in the Raman spectrum was 0.19 and 0.58 for graphene and TPA-graphene, respectively,

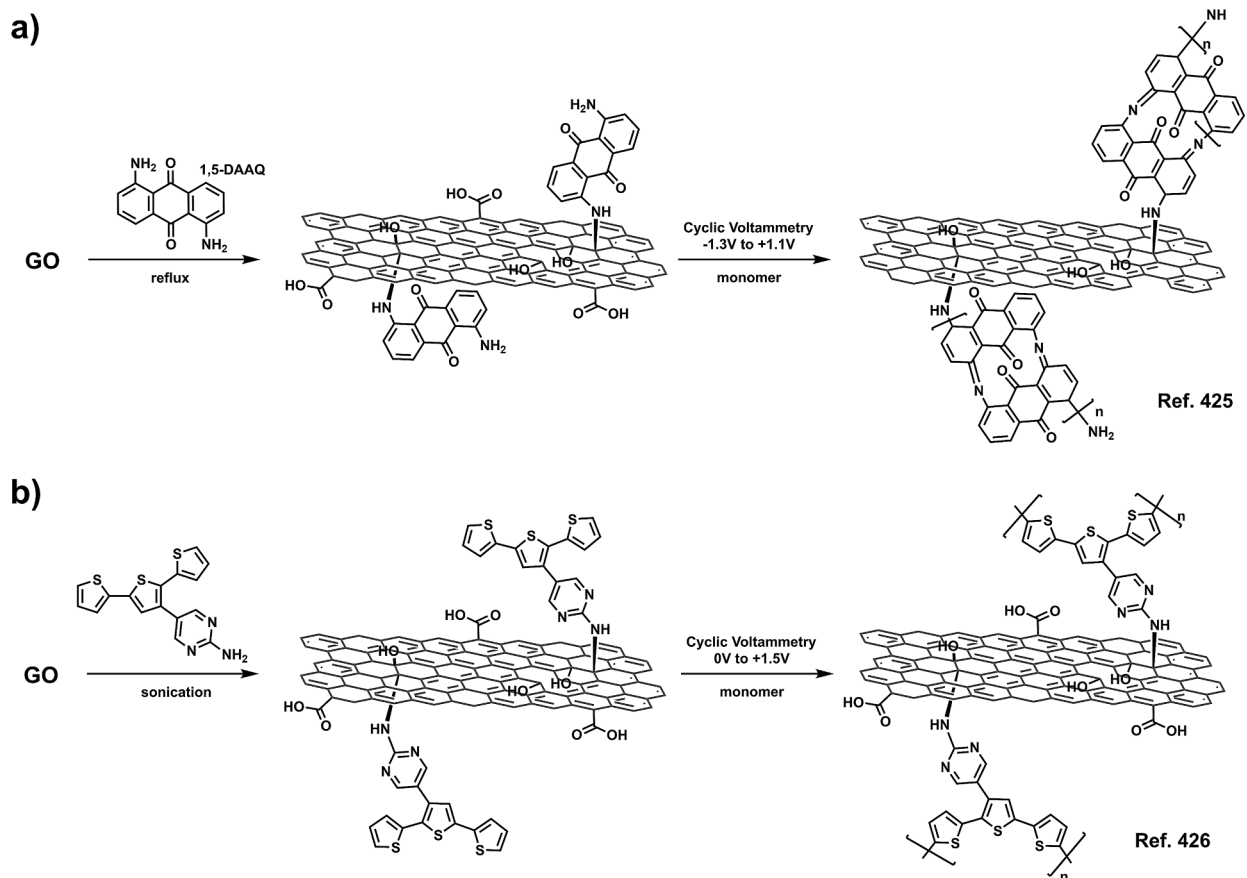


Fig. 39. Chemical functionalization of graphene oxide with a) 1,5-diaminoanthraquinone-based and b) terthiophene-based polymers for the electrocatalysis of ORR.

while the G-band position of TPA-graphene was ca. 2 cm^{-1} lower than that of graphene, suggesting that graphene bears an electron donor component. The as-prepared covalently modified graphene nanosheets were further decorated with 3 wt% platinum nanoparticles, furnishing the hydrogen evolution catalyst TPA-graphene/Pt. By TEM imaging, the average size of Pt nanoparticles was 10–15 nm, while AFM imaging showed a thickness of 4–6 graphene layers. Evaluation of the photoresponse of the hybrid TPA-graphene/Pt was performed by measuring the generated photocurrent under on/off irradiation (GY-10 xenon lamp, 150 W). The catalyst was deposited on a transparent conductive electrode (ITO-coated glass) and the recorded photocurrent density reached $0.18\ \mu\text{A}/\text{cm}^2$, whereas $13.8\ \mu\text{mol}$ of H_2 were generated after 6 h of continuous irradiation ($9.1\ \mu\text{mol}$ of H_2 for TPA-graphene). For TPA-graphene the quantum efficiency was calculated to be $0.3\% \text{ mol E}^{-1}$, while for TPA-graphene/Pt was up to $0.45\% \text{ mol E}^{-1}$. In addition, the hybrid was tested under 30 h of continuous irradiation exhibiting excellent stability and optimum performance at pH 2.

Employing more efficient light-harvesting dyes, such as phthalocyanines, better performance is expected. In this respect, a manganese phthalocyanine (MnPc) was covalently grafted on exfoliated graphene by the 1,3-dipolar cycloaddition of azomethine ylides [417]. In that work, a 4-hydroxybenzene and sarcosine were heated in the presence of exfoliated graphene, furnishing phenoxy-functionalized nanosheets. Accordingly, the MnPcCl was immobilized on the nanosheets via coordination of the manganese (III) center with the monodentate phenoxy ligand (Fig. 41b). As shown in SEM images, the MnPc/graphene possessed a 2D wrinkled surface and thickness, as evidenced by AFM, of around 1.72 nm (ca. 2- to 4-layer graphene). In the IR spectrum, the characteristic vibration peaks of both graphene and MnPc moieties could be detected, as well as a new band centered at 794 cm^{-1} , attributed to Mn–O vibration arising from the coordination. In addition, the UV–Vis absorption spectrum exhibited bathochromic shifts for the coordinated MnPc, further supporting the electronic effects due to coordination of phenoxy-functionalized graphene, which also evidenced by the 63% quenching of the fluorescence emission of the attached MnPc (exc. 600 nm). Analysis of the absorption spectra, precisely via observing the intensity of the characteristic peak of MnPc at 706 nm, the ratio of grafted MnPc was estimated to be ca. 11.9%. MnPc/graphene was also decorated with small (0.8–4 nm by TEM imaging) Pt nanoparticles in order to synthesize MnPc-graphene/Pt as hydrogen evolution catalysts. The photocurrent (GY-10 xenon lamp, 150 W) density of non-coordinated MnPcCl/graphene, in 0.2 M of Na_2SO_4 aqueous solution at $25\text{ }^\circ\text{C}$, was found to be $0.6\ \mu\text{A}/\text{cm}^2$, while that for coordinated MnPc/graphene reached the value of $1.0\ \mu\text{A}/\text{cm}^2$. The recorded increment in current density for the coordinated system is due to lower recombination rate of photogenerated charges, namely slower recombination of the charge-separated state $\text{MnPc}^{\cdot+}$ -graphene $^{\cdot-}$. Moving to the

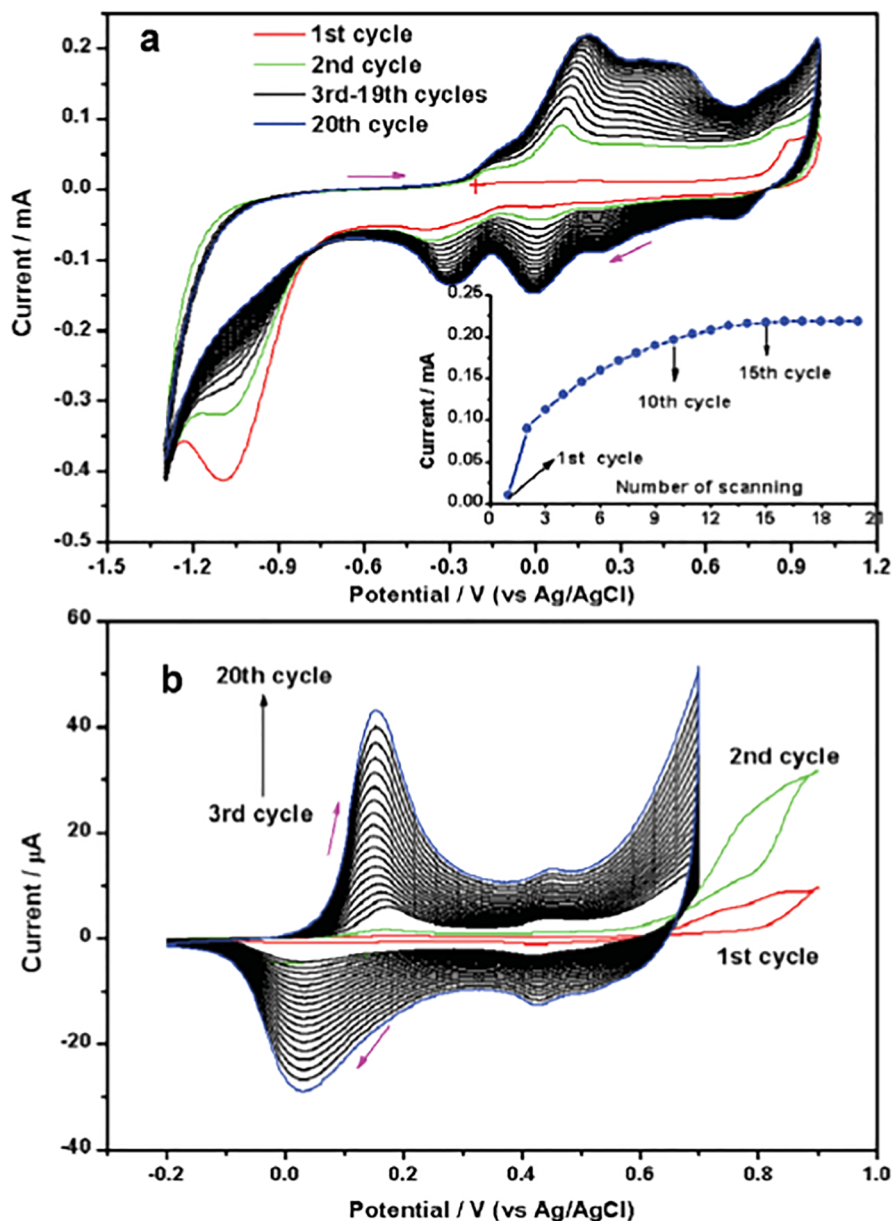


Fig. 40. CVs for the one-step potentiodynamic deposition of P(1,5-DAAQ)/RGO nano hybrid (a) and PANI film (b) in N_2 -saturated 1.0 M H_2SO_4 solution at 50 mV/s. The inset in (a) shows a plot of the anodic peak current (i_{pa}) at 0.12 V vs. scanning number. Reproduced with permission from Ref. [413]. Copyright 2013 Royal Society of Chemistry.

photocatalytic performance of platinum decorated graphene hybrids, under 10 h of UV-Vis light irradiation, the yield of hydrogen production by MnPc-graphene was $7.52 \mu\text{mol}/\text{mg}$ and by MnPc/graphene/Pt was $8.59 \mu\text{mol}/\text{mg}$. Since MnPc has a strong absorption band in the range 650–750 nm, the photocatalytic performance of the MnPc-graphene ensembles, under monochromatic light irradiation at 670 nm was further investigated and the observed quantum yield (0.06% at 670 nm) manifests the potential of this material as an efficient visible/red-light-driven photocatalyst for H_2 production.

Following a modified coordination approach exfoliated graphene carrying a silicon(IV)-phthalocyanine (SiPc) was synthesized, offering the potential for axial coordination of a second graphene sheet carrying a ligand [418]. In more detail, 4-formyl pyridine and sarcosine were heated in the presence of exfoliated graphene, furnishing pyridine-functionalized nanosheets. Accordingly, the $SiPcCl_2$ was immobilized on graphene via coordination of the silicon (IV) center with the monodentate pyridyl ligand. SiPc/graphene retains an extra coordination site on the silicon center, namely the coordination of a second pyridyl-functionalized graphene is favourable towards the formation of the corresponding $SiPc/(\text{graphene})_2$ (Fig. 41c). FT-IR and UV-Vis spectra clearly confirm that the SiPc moieties were anchored on the surface of the graphene flakes. The fluorescence emission spectrum of $SiPc-(\text{graphene})_2$ presented a

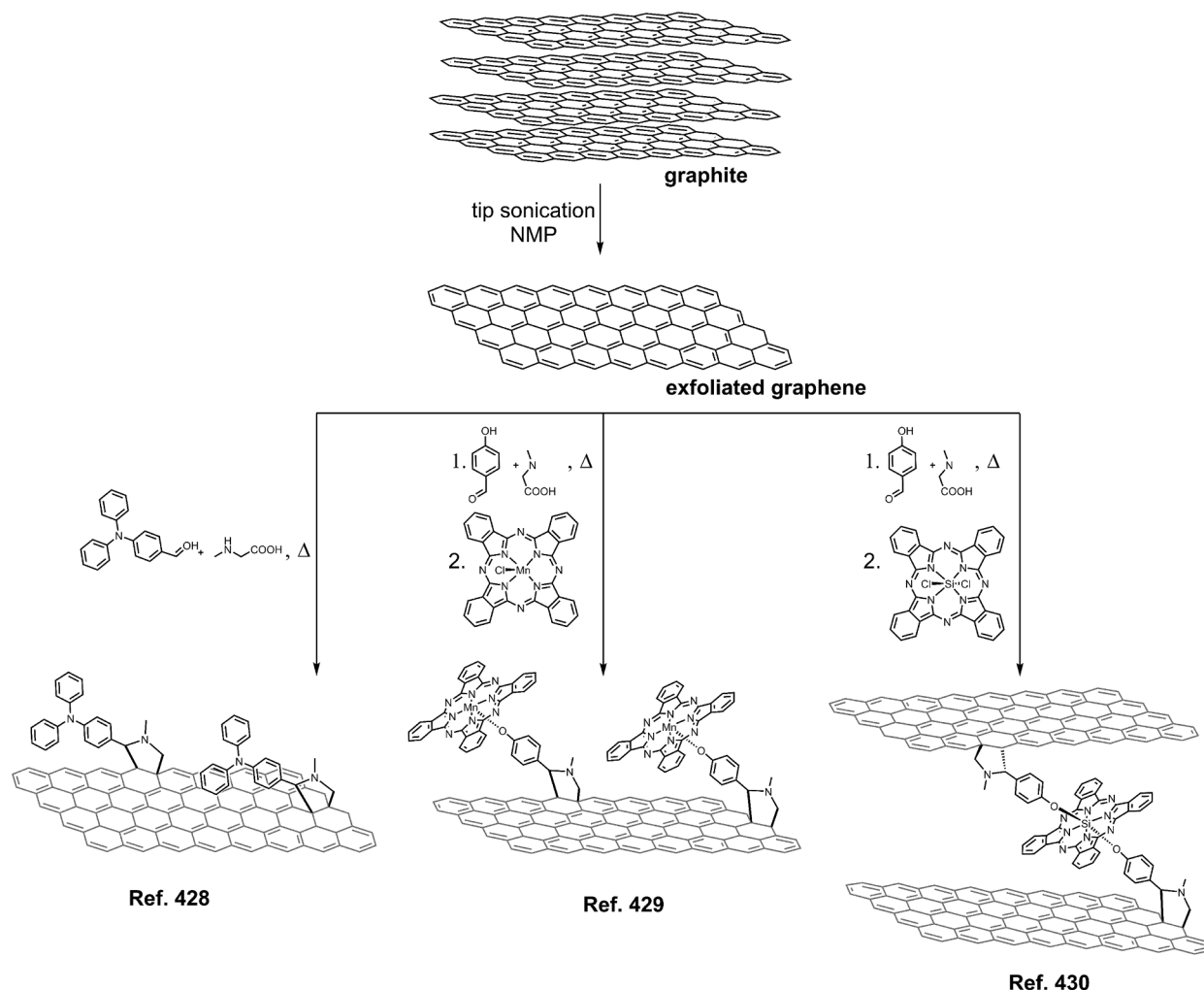


Fig. 41. Covalent modification of liquid-assisted exfoliated graphene via 1,3-dipolar cycloaddition reaction for photoinduced hydrogen evolution.

weak fluorescence emission peak centered at 673 nm compared with the one due to SiPcCl₂, which exhibited a strong fluorescence peak centered at around 700 nm. The quenching efficiency was calculated to be 78%, while the charge transfer efficiency was studied by electrochemical impedance measurements, showing easier charge transfer for the coordinated SiPc than free SiPc. The photocurrent density of SiPc/(graphene)₂ reached ca. 2.23 $\mu\text{A}/\text{cm}^2$ under irradiation in 0.2 M of Na₂SO₄ aqueous solution at 25 °C. The total amount of H₂ evolved from SiPc-(graphene)₂ was 12.6 $\mu\text{mol}/\text{mg}$ while the incorporation of Pt nanoparticles, via photodeposition, further improved the photocatalytic performance reaching 18.2 $\mu\text{mol}/\text{mg}$ under UV-Vis light irradiation. The optimum catalytic efficiency of SiPc/(graphene)₂/Pt was found to be at 5% Pt loading. The calculated quantum yield was 0.33% and 0.14% at 365 nm and 420 nm, respectively, suggesting that SiPc/(graphene)₂/Pt exhibits a consistent and excellent performance for photocatalytic hydrogen production in the whole range of 340–800 nm wavelength light irradiation. Overall, the SiPc/(graphene)₂ ensembles exhibited better photocatalytic performance than MnPc-graphene. The same strategy of axial coordination has been reported for ultrasmall (3–5 nm) N-doped RGO [419]. Following oxidative cutting of carbon nanofibers, ultrasmall GO (usGO) nanosheets were isolated (yield 60%), in sharp contrast to oxidation of graphite. The lateral size and the graphitic lattice were verified by AFM and HRTEM imaging, displaying a 0.8 nm height and 0.242 nm lattice parameter, respectively. Annealing of usGO at 120 °C in the presence of ammonia promoted the incorporation of nitrogen atoms in the graphitic lattice furnishing N-usRGO, namely a 5.6% N-content and a decrement of the O-content to 10% (20% for the usGO), as observed from XPS assays. Then, usGO was covalently functionalized via the [3 + 2] dipolar cycloaddition reaction, as previously described, and the incorporated pyridine moieties were employed for the coordination of a silicon phthalocyanine. Moreover, the N-atoms present within the graphitic lattice offer nucleation points for growing Pt nanoparticles, used as co-catalyst for the photocatalytic hydrogen evolution reaction. The overall impact of N-usRGO as substrate for the fabrication of such hybrid photocatalysts was highlighted by the improvement of the quantum efficiency (1.3% at 365 nm and 0.56% at 420 nm).

Ruthenium complexes as prominent candidates for photoinduced hydrogen evolution and a series of graphene-based ensembles bearing Ru-dyes (Fig. 42) have been reported. In a first example, NMP-assisted exfoliated graphene was covalently modified with

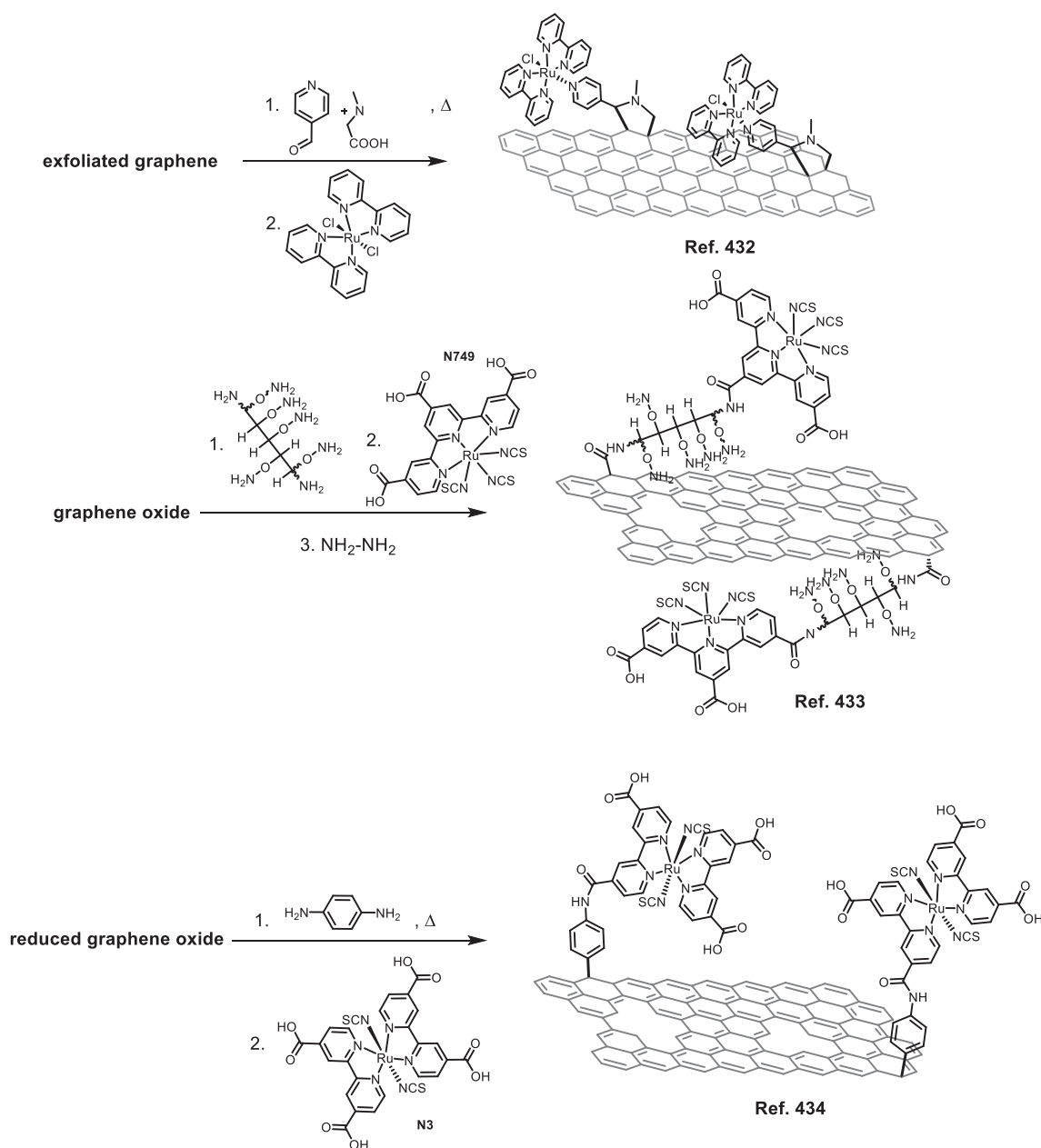


Fig. 42. Covalent modification of graphene with Ru-based dyes for photoinduced hydrogen evolution.

pyridine ligands through an azomethine cycloaddition reaction employing 4-formylpyridine and N-methylglycine followed by coordination of the *cis*-bis(2,2'-bipyridine)dichlororuthenium(II) ($\text{Ru}(\text{bpy})_2\text{Cl}_2$) complex, in refluxing ethanol/acetone (2:1) mixture for 10 h [420]. AFM imaging of the $\text{Ru}(\text{bpy})_2\text{Cl}_2/\text{graphene}$ ensembles showed a higher thickness (~ 1.67 nm) due to the presence of the complexes on the surface of graphene and EDX spectroscopy allowed the examination of the Ru content (0.55% atomic) and the calculation of the functionalization degree (1 Ru-complex per 96C atoms, which is about 1 Ru-complex per 2.5 nm²). FT-IR, Raman spectroscopy and UV-Vis absorption analyses also verified the success of coordination. Interestingly, in the Raman spectrum a downshift of the G-band by 3 cm⁻¹ indicated an electron transfer mechanism from the coordinated complex to graphene. Complementary fluorescence emission spectroscopy provided information for intrahybrid electronic communication at the excited state. Concerning the photocatalytic properties of the ensembles, the photocurrent density of $\text{Ru}(\text{bpy})_2(\text{py})\text{Cl}/\text{graphene}/\text{ITO}$ electrode reached ca. 2.23 $\mu\text{A}/\text{cm}^2$ and the total amount of produced H_2 was 22.5 $\mu\text{mol}/\text{mg}$. The latter was further improved up to 39.3 $\mu\text{mol}/\text{mg}$ by photodeposition of Pt nanoparticles.

The ruthenium dye N749, most commonly known as “black dye”, was covalently attached to rGO in a three-step reaction sequence [421]. Firstly, an amine-terminated six-armed polyethylene glycol (PEG) was attached on the surface of graphene oxide via

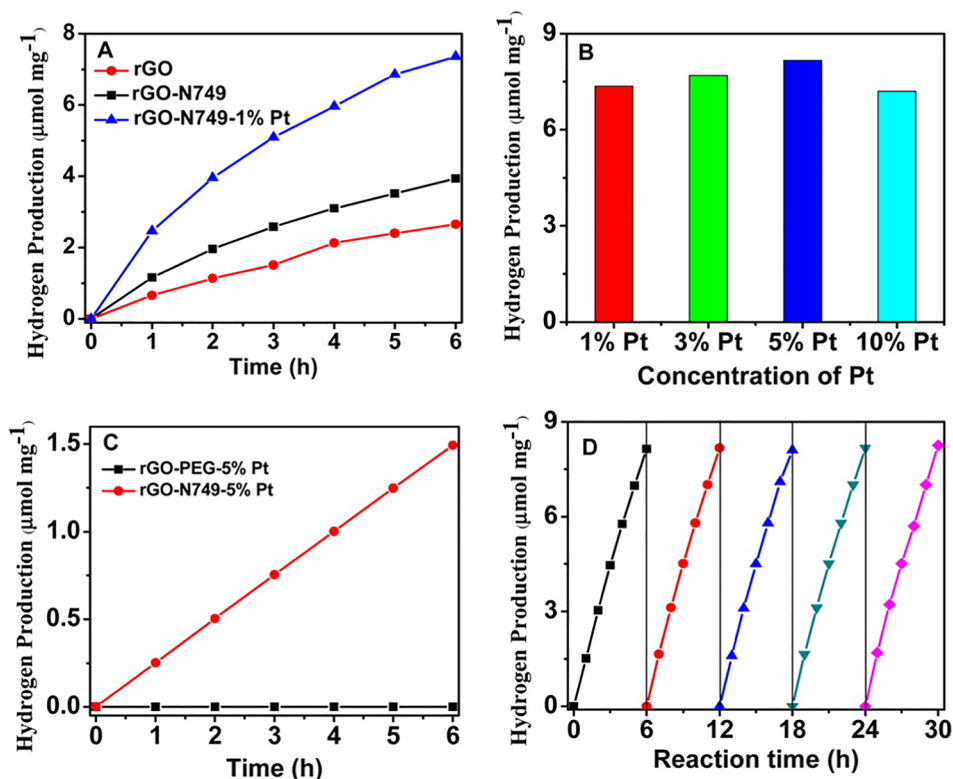


Fig. 43. (A) Hydrogen production by rGO-N749 with and without Pt NPs under UV-vis irradiation. (B) Hydrogen production by rGO-N749 with different loading amounts of Pt NPs (w/w). (C) Hydrogen production by rGO-PEG-Pt and rGO-N749-Pt under visible irradiation ($\lambda > 400$ nm). (D) Stability of rGO-N749-Pt (5 wt% Pt) nanocomposite under UV-Vis light irradiation. Reaction conditions: 1 mg of the catalyst dispersed in 50 mL of 10% TEA solution, pH 10, $T = 25$ °C. Reproduced with permission needed from Ref. [421]. Copyright 2015 American Chemical Society.

carbodiimide chemistry, followed by reduction with hydrazine. The material was dialyzed against deionized water to remove all traces and PEG molecules. The PEG-rGO nanosheets were decorated by N749 dye via condensation of the amine groups of PEG and the carboxylates of the dye. The as prepared N749(PEG)-rGO was then modified by photodeposited Pt nanoparticles, and employed as co-catalyst for hydrogen evolution. Examination by AFM suggested that the formation of N749(PEG)-(rGO)₂ is also possible, since the N749 dye has three carboxylic groups and the PEG units are relatively long and flexible, providing minimum steric hindrance. From UV-Vis spectroscopy assays, the final concentration of conjugated N749 molecules on rGO was evaluated to be 5% based on the dye's absorbance at 615 nm. Compared to free N749, the hybrid N749(PEG)-rGO showed a weak fluorescence emission at the same optical concentration of N749 at 610 nm (quenching efficiency 90%), suggesting efficient photoinduced electron transfer from N749 to the (PEG)rGO. Then, N749-(PEG)rGO/ITO photoelectrodes were fabricated and displayed a steady and reproducible photocurrent response reaching ca. 2.8 $\mu\text{A}/\text{cm}^2$ in a 0.2 M Na_2SO_4 aqueous solution, which was ca. 3 times higher than that of the reference N749/ITO electrode (Fig. 43). Photoirradiation (GY-10 xenon lamp, 150 W) of a dispersion of N749-(PEG)rGO as nanocatalyst in 10% TEA (pH 10) solution produced 3.94 $\mu\text{mol}/\text{mg}$ hydrogen in the first 6 h, while for the optimal Pt loading of 5 wt% under the same reaction conditions, the hydrogen evolution was 8.2 $\mu\text{mol}/\text{mg}$. It should be mentioned here that N749-(PEG)rGO/Pt(5%) had sufficient catalytic stability over the next runs up to 30 h. Using only visible light irradiation, 1.5 $\mu\text{mol}/\text{mg}$ hydrogen was evolved upon 6 h irradiation and the apparent quantum yield at 365 and 420 nm was calculated to as high as 1.09×10^{-8} and 2.46×10^{-8} mol/s respectively.

The N3 dye as another widely used ruthenium dye was scrutinized for the preparation of covalent graphene-based photocatalysts towards hydrogen evolution [422]. Reduced graphene oxide was initially functionalized via diazonium addition of 1,4-phenylenediamine. Then, the N3 dye was grafted via condensation of the carboxylic units and the free amine groups on the graphene nanosheets, furnishing N3-rGO, which was further decorated by photodeposited Pt nanoparticles. The hybrid material consisted of few-layered rGO with well-dispersed Pt nanoparticles, as evidenced by TEM imaging. XPS surveys allowed the determination of the N-atom content (1.7%, 1 aniline per 37 C atoms), however it was difficult to observe the Ru 3d peak. Evidence for the chemical binding of the N3 dye was provided IR spectroscopy through which the characteristic carbonyl amide vibrational bands centred at 1650 and 767 cm^{-1} were identified, while by Raman spectroscopy characteristic modes of the dye appeared at 1023 and 1468 cm^{-1} . The calculated I_D/I_G ratio for N3-rGO was higher (0.82) than that due to rGO (0.78), whereas the G-band within the N3-rGO hybrids was down-shifted by 9 cm^{-1} , suggesting electron transfer from the dye to graphene. Moreover, in the UV-Vis absorption spectrum of N3-rGO a bathochromic shift of the N3 absorption was witnessed, from which (at 538 nm) the ratio of the grafted molecules was found

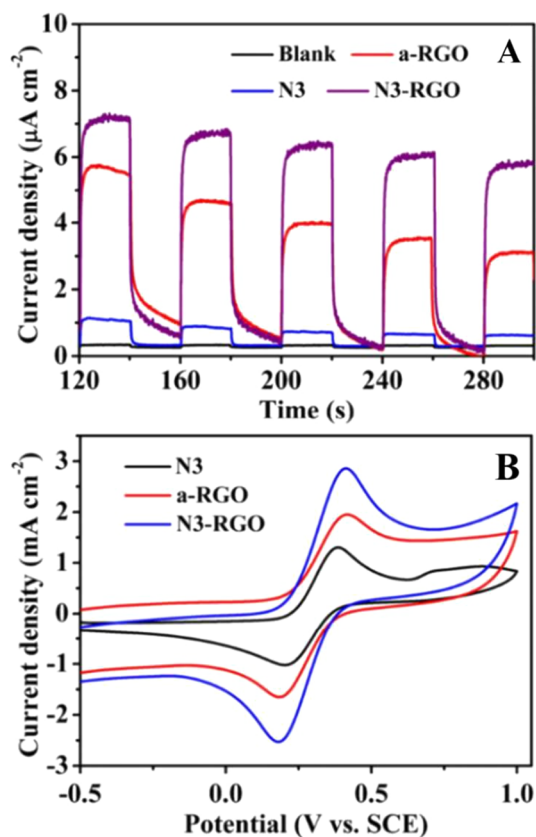


Fig. 44. Photocurrent responses of ITO-electrode, a-RGO (aniline-functionalized rGO), N3 dye, and N3-rGO to UV-Vis irradiation in an aqueous solution containing 0.2 M Na_2SO_4 as supporting electrolyte at 0.4 V vs. SCE. The illumination from a 150 W xenon lamp was interrupted every 20 s. (B) CVs of N3, a-RGO and N3-rGO electrode in 0.2 M KCl/5.0 mM $\text{K}_3[\text{Fe}(\text{CN})_6]/\text{K}_4[\text{Fe}(\text{CN})_6]$ solution. Potential scan rate was 50 mV/s. Reproduced with permission needed from Ref. [422]. Copyright 2016 Royal Society of Chemistry.

ca. 5.7%. The calculated quenching efficiency of N3-rGO was about 65.1% at 383 nm, where free N3 showed a strong emission peak, suggesting efficient photoinduced electron transfer to the graphene sheets. The recorded photocurrent for N3-rGO was 6.2 $\mu\text{A/cm}^2$ under on/off (interval 20 s) UV-Vis irradiation conditions, higher than the corresponding value (3.6 $\mu\text{A/cm}^2$) for the aniline-functionalized rGO (a-RGO) and N3 dye (0.4 $\mu\text{A/cm}^2$) as shown in Fig. 44. Cyclic voltammetry was also employed to examine a-RGO, N3 and N3-rGO, in order to evaluate the conductivity and the energy levels of the hybrid material. The hybrid N3-rGO displayed higher electron density for the redox pair $\text{K}_3[\text{Fe}(\text{CN})_6]/\text{K}_4[\text{Fe}(\text{CN})_6]$ indicating better charge transfer than the individual species and the calculated LUMO of N3 (-4.09 eV) suggests efficient transfer of the photoexcited electrons to the conduction band of rGO (-4.42 eV). Photocatalytic hydrogen evolution assays were performed under continuous UV-Vis irradiation for a period of 7 h. The total amount of H_2 production over rGO was about 2.98 $\mu\text{mol/mg}$, while over N3-rGO was 6.03 $\mu\text{mol/mg}$ and over N3-rGO/Pt was 11.2 $\mu\text{mol/mg}$. Re-examination of the catalysts under strictly visible light irradiation revealed that the H_2 production was almost identical, namely 1.12 and 1.78 $\mu\text{mol/mg}$ for N3-rGO and N3-rGO/Pt, respectively. In addition, the photocatalytic performance of N3-rGO/Pt under monochromatic light irradiation (400 nm) was investigated and the calculated quantum yield at 400 nm was 0.2%.

As earlier described, mimicking enzymes can be an alternative route to address the quest for highly efficient nanocatalysts for energy generation/conversion. Hydrogenases (H_2 ase) belong to a class of enzymes interconverting H^+ to H_2 and their activity resides on their Fe-Fe active center. A p-alkynylbenzene azadithiolate bis-ironhexacarbonyl complex attached on graphene surfaces was investigated as a mimic for the hydrogen evolution reaction [423]. It is noteworthy that the azadithiolate (ADT) motif is essential for the enzymatic activity. The covalent grafting of the Fe-Fe complex on the graphitic surface was promoted via a click-chemistry approach. Precisely, edge plan graphite (EPG) electrodes -also applicable to rGO- were modified with an azide terminated unit, via diazonium addition, which then reacted with the alkyne-terminated H_2 ase mimic via a [3 + 2] Huisgen cycloaddition, giving H_2 ase-EPG. XPS analysis revealed the absence of azide functionalities after the completion of the reaction (6 h) verifying the successful conversion to the corresponding triazoles, while also allowed the calculation of the ratio for triazole N1s and tertiary N1s (3:1) in accordance to the stoichiometry within the H_2 ase-EPG ensembles. Cyclic voltammetry in the presence of the ferrocyanide/ferricyanide redox couple was employed for examining the impact of the covalent attachment over the physisorption of the H_2 ase mimic. For the covalent ensembles, as calculated from the area under the curve of the reversible redox event, the coverage of molecules was as high as 1.43×10^{14} molecules/ cm^2 , two orders of magnitude higher than physisorption, highlighting the importance of covalent

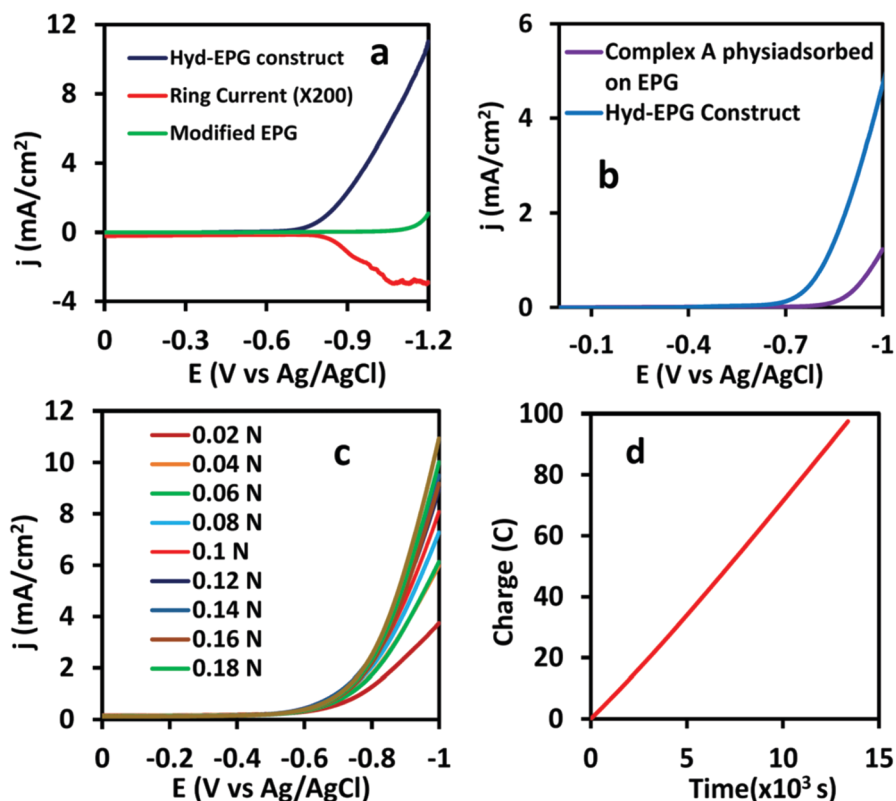


Fig. 45. (a) RRDE data of the Hyd-EPG construct (blue line, indicating H_2 generation and the corresponding Pt-ring current, red line, indicating H_2 detection); the ring held at a constant potential of 0.9 V in aqueous 0.1 N H_2SO_4 ; (b) LSV of the Hyd-EPG construct and complex A physisorbed on EPG; (c) LSV of the Hyd-EPG construct for electrochemical hydrogen generation with increasing acid concentration; (d) controlled potential bulk electrolysis at 0.9 V vs. Ag/AgCl in aqueous 0.2 N H_2SO_4 . Reproduced with permission needed from Ref. [423]. Copyright 2017 Royal Society of Chemistry.

binding. For H^+/H_2 interconversion a RRDE system was employed for the evaluation of the electrochemical reduction of H^+ to H_2 and vice versa. During the positive scan, a large current is detected for the H_2 -ase-EPG electrode with an $E_{\text{on}} = -0.72$ V vs Ag/AgCl (Fig. 45a), better than the physisorbed catalyst (Fig. 45b). Tuning the pH of the solution to higher H^+ concentration increased the generated HER current (Fig. 45c). Finally, controlled bulk electrolysis at -0.9 V vs Ag/AgCl demonstrated the steady consumption of charges under long-term conditions (7.67 C over 1200 s), highlighting the stability of the H_2 -ase-EPG electrodes (Fig. 45d).

4.3.4. Water oxidation and oxygen evolution reaction (OER)

Nile-blue (NB) or Nile-blue A is a biocompatible stain bearing a free amine group. In this respect, this dye can be directly introduced on graphene oxide sheets by means of diazonium addition functionalization [424]. Interestingly, NB-GO can be further exploited for the ORR by growth of NiO nanoparticles on the nitrogen atom locating at the N,N-diethylarene skeleton of the dye. Actually, the affinity of Ni for nitrogen resulted to well dispersed NiO nanoparticles on the graphitic surface, as evidenced by TEM imaging, allowing the immobilization of a stable 4-electron catalyst. Moreover, the NB-GO/NiO hybrid ORR nanocatalyst was further decorated with Pd nanoparticles (by electrodeposition/Ni replacement at +0.48 V) giving rise to a new amperometric sensor for glucose detection in blood serum. Recently, NB-rGO nanosheets decorated with NiO nanoparticles have been evaluated for the electrocatalysis of HER and oxygen evolution reaction (OER) [425]. NiO nanoparticles were well dispersed on the reduced graphene sheets with an average size of 20 nm, the half size of those directly deposited on rGO, as evidenced by TEM imaging. The electrocatalytic properties of NB-rGO/NiO were outperformed by rGO/NiO, probably because NB, which is an electron donor, occupies the unpaired orbitals of Ni and HER becomes unfavourable. In contrast, the latter interaction is favourable for the OER, where an anodic reaction takes place. Eventually, the OER efficiency of NB-rGO/NiO was found to be superior to that of rGO/NiO as evaluated by LSV and EIS electrochemical assays, demonstrating the impact of the intra-hybrid electron transfer phenomena.

Another route to prepare efficient OER electrocatalysts is via coordination of metal cations on appropriately modified graphene. Covalent modification of GO by 2,2'-bipyridine ligands, via diazonium addition of 4-amino-2,2'-bipyridine, enables the examination of a series of metal complexes attached on the graphene lattice [426]. Accordingly, the immobilization of different metal complexes in the form of $\text{M-L}(\text{H}_2\text{O})_4 \text{x}^+$ ($\text{M} = \text{Fe}^{3+}$, Co^{2+} , Ni^{2+} , or Cu^{2+} , $\text{L} = 2,2'$ -bipyridine) was accomplished targeting the water oxidation reaction. In more detail, after the incorporation of the ligand (L) on GO, the hybrid material was electroreduced furnishing the corresponding L-rGO. The complexation of the cations on the L-functionalized graphene was performed by immersing the L-rGO/ITO

electrodes in DMF solution of each metal nitrate to allow coordination at the bipyridine N,N' site. The metalated (M)L-rGO/ITO electrodes were then characterized by Raman and FT-IR spectroscopy, confirming that the ligand was covalently grafted to graphene. OER catalytic performance of the hybrids was investigated by cyclic voltammetry in phosphate buffer with KNO_3 as electrolyte. Enhanced catalytic activity was recorded for the cobalt complexes with a current density of $0.88 \mu\text{A}/\text{cm}^2$ at 1.4 V vs the Ag/AgCl reference electrode, while the current density of Cu and Fe complexes was of the same range, namely 0.28 and $0.2 \mu\text{A}/\text{cm}^2$, respectively, and that of the Ni one was $0.06 \mu\text{A}/\text{cm}^2$. The turn over frequency (TOF) of the graphene-based nanocatalysts bearing complexes with Co, Cu, Fe, Ni was determined to be 2.7, 0.21, 0.24 and 0.1 s^{-1} . However, Co^{2+} coordination to the remaining carboxylate groups of rGO, forming $[\text{Co-COO}]^+$ species, showed to reduce the overall catalytic activity. In this respect, Zn^{2+} was explored in order to achieve a metal exchange at the carboxylate edges, namely remove the Co^{2+} by the electrochemically inactive Zn^{2+} . Evidently, the electrochemical OER activity of $(\text{Co}^{2+})\text{L-rGO/ITO}$ was further improved by 14 s^{-1} higher TOF value, despite the lower current density. The Faraday efficiency for the water oxidation was determined experimentally at a rotating ring-disk electrode and found to be 82.6%, while via multiple CV scans with corresponding ICP-MS analyses the hybrid nanocatalyst exhibited a slow decomposition of the surface-bound catalyst, as evidenced by the observed current density (1st cycle: $636.5 \mu\text{A}/\text{cm}^2$, 3rd cycle: $383.5 \mu\text{A}/\text{cm}^2$), although the TOF was not significantly changed (1st cycle: 17 s^{-1} , 3rd cycle: 19 s^{-1}).

4.3.5. CO_2 reduction reaction

Cobalt-based complexes attract the research interest for electrocatalysis, as previously described for the OER. A copper^{II}-phthalocyanine covalently grafted on GO displayed significant photocatalytic activity towards the reduction of carbon dioxide to methanol [427]. Graphene oxide nanosheets were firstly enriched with carboxylic acids via reaction with chloroacetic acid. The carboxylated GO was then activated by thionyl chloride and heated together with copper (tetrasulfamino)phthalocyanine, furnishing the CoPc-GO ensembles. Incorporation of the chromophore on the nanosheets resulted in increased lateral distance between nanosheets, as evidenced by XRD studies. The characteristic diffraction peak at 10.8° (0 0 1), which represents the interlayer spacing of GO ($\sim 0.74 \text{ nm}$) was absent in the spectra recorded for the hybrid CoPc-GO material, while a new diffraction peak at 26° was found, suggesting that the intercalation effect arose by the chemical attachment of the organic units along the graphene lattice. The presence of the intra-hybrid amide bond was revealed by FT-IR spectroscopy, through the observation of the characteristic $(\text{C}=\text{O})\text{NH}$ stretching vibration at 1654 cm^{-1} , while the XP spectrum clearly displayed the presence of nitrogen. Further supportive evidence for the covalent incorporation of CoPc was provided by Raman spectroscopy and TGA. Investigation of the photocatalytic reduction of CO_2 was carried out using trimethylamine as sacrificial donor in aqueous solution under visible light irradiation. The photocatalytic CO_2 to methanol conversion was monitored by gas chromatography. Calculation of the rate of the photocatalytic reaction was performed for the CoPc-GO ensembles, and compared to that of GO and a physisorbed hybrid CoPc/GO (in 1:1 ratio) employed as reference materials. Covalent bonding between the individual species outperformed the reference physisorbed material. Specifically, the CoPc-GO ensembles found to catalyze the reaction with a rate of $78.7893 \mu\text{mol per g of catalyst per hour}$, while the GC profile of the products showed the presence of 99.17% CO_2 and 0.82% CO after 48 h, without other organic products (i.e. formic acid).

Artificial photosynthesis is among the most challenging nature-mimicking processes. In this respect, a porphyrin photocatalyst bearing anthraquinone units was covalently grafted on reduced graphene oxide and coupled with the enzyme of formate hydrogenase (FH), furnishing a photocatalyst-enzyme hybrid system for artificial photosynthesis of formic acid by carbon dioxide [428]. Reduced graphene oxide was derived by a two-step chemical reduction of graphene oxide by sodium borohydride and concentrated sulfuric acid. The final chemically reduced graphene (CCG) possessed carboxylic units at the periphery and a restored graphene lattice, as evidenced by the theta angle (22.5° , 0.39484 nm), which is close to graphite d-spacing (0.335 nm). Concerning the porphyrin photocatalyst referred as MAQSP, three 1-amino-anthraquinone moieties (AAQ) were linked by 1,3,5-trichlorotriazine (TCT) units to a 5,10,15,20-tetrakis(4-aminophenyl)porphyrin (TAPP) core, leaving one free amine group capable for condensation with the carboxylic acids of CCG. Heating at 130°C a mixture of the two components in DMF, in the presence of triethylamine as a catalyst, the formation of MAQSP-CCG was accomplished, as witnessed by FT-IR spectroscopy ($-\text{NHCO}-$, 1235 cm^{-1}). By TGA analysis the loading of MAQSP as high as 52 %wt was determined. MAQSP-CCG photocatalyst showed a strong Soret absorption at 475 nm and exhibited enhanced and stable photoresponse with current density ca $4.2 \mu\text{A}/\text{cm}^2$. Evaluation towards the artificial photosynthetic production of formic acid from CO_2 was studied by coupling MAQSP-CCG with formate hydrogenase and a rhodium catalyst for the regeneration of NADH. Under photoexcitation the chemically grafted MAQSP molecules transfer photoelectrons to graphene, which then migrate to the rhodium complex and regenerate the consumed NADH for the enzyme catalysed reduction of CO_2 to formic acid, as illustrated in Fig. 46. The efficiency of the multicomponent artificial photosynthesis system was evaluated by the determination of the photogenerated NADH, which was linear with the reaction time and produced with a yield of up to 45.54%, almost doubled as compared with the yield of MAQSP alone. Finally, the amount of formic acid produced in the presence of the MAQSP-CCG ensembles was $110.55 \mu\text{mol}$, while 46.53 and $14.25 \mu\text{mol}$ were generated by $\text{W}_2\text{Fe}_4\text{Ta}_2\text{O}_{17}$, which used as reference catalyst, and free MAQSP, respectively.

Following an analogous design strategy, CCG was covalently decorated by a boron azadipyromethene (BODIPY) derivative [429]. A slight different approach was followed for the covalent grafting of the dye, since CCG was activated by SOCl_2 prior the addition of the BODIPY. The XRD pattern of BODIPY-CCG had a characteristic peak at 25.859° (26° for CCG) suggesting that BODIPY intercalation was responsible for this change, which is in accordance with the increased thickness (1.651 nm , 0.924 for CCG) observed by AFM. The time-correlated single photon counting (TCSPC) technique was employed to investigate the photoinduced dynamics of BODIPY-CCG. From the decay time profiles of the excitation emission of the hybrid (exc. 525 nm) fluorescence emission lifetimes of 597 ps (48.78%), and 1178 ps (51.22%) were deduced, which were lower than the lifetime of intact BODIPY 2156 ps (100%). In BODIPY-CCG, the effective charge separation rate constant was $1.7 \times 10^{11} \text{ s}^{-1}$ and the charge recombination rate

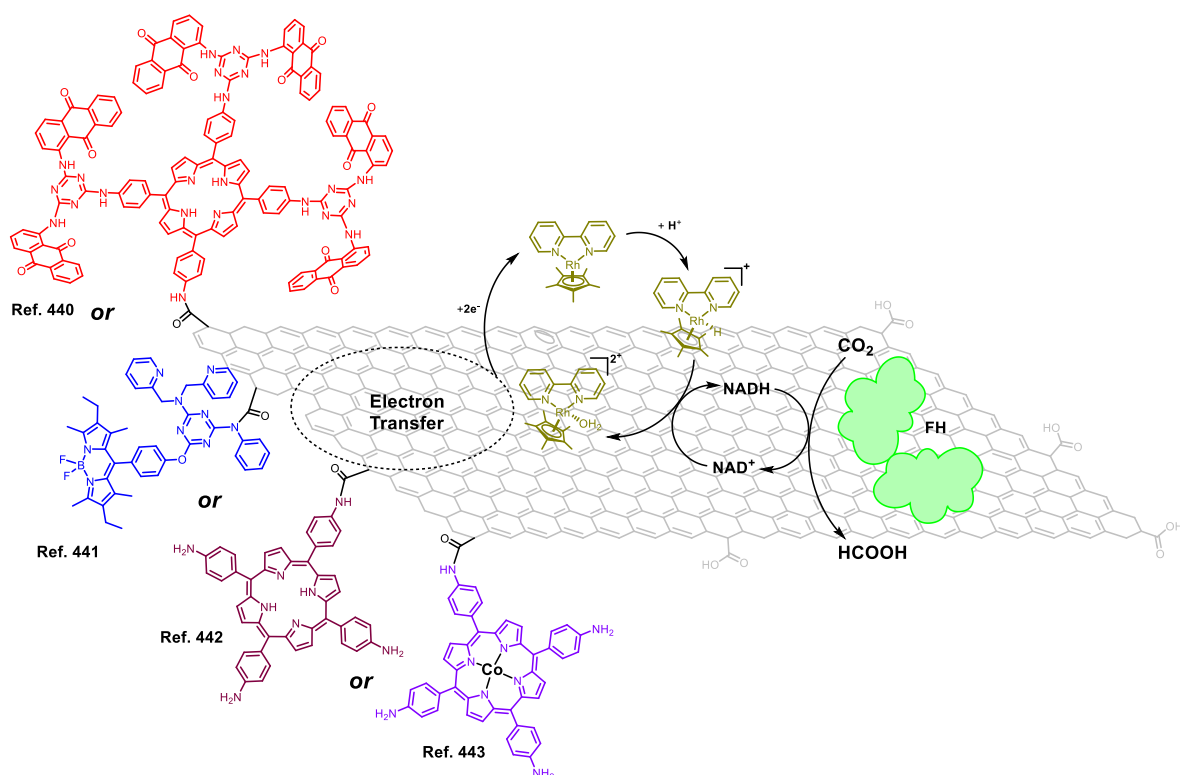


Fig. 46. Illustration of graphene-based hybrid systems employed for the artificial photosynthesis of formic acid.

constant was $1.0 \times 10^{11} \text{ s}^{-1}$, influenced by the extended π -conjugation operating between CCG and BODIPY. Analogous to BODIPY, a TPP-NH₂ was also covalently attached to CCG and both BODIPY-CCG and TPP-CCG photocatalysts were evaluated by recording their photocurrents. Both hybrids showed a stable and reversible photocurrent response with a quick recovery in the dark. Precisely, for BODIPY-CCG a value of $7.5 \mu\text{A}/\text{cm}^2$ was measured, while for TPP-CCG the photocurrent response was $3 \mu\text{A}/\text{cm}^2$. NADH photoregeneration in the presence of BODIPY-CCG was linear with time and yielded up to 54.02%, while TPP-CCG yielded 20.98% of regenerated NADH, respectively. The hybrid was further tested for the production of formic acid from CO₂ and among the four photocatalysts examined, BODIPY-CCG produced the highest amount of formic acid (144.2 μmol) from CO₂ under visible light (Fig. 47).

A tetraamino-TPP derivative was utilized for the preparation of a covalent TPP(NH₂)₃-GO nano hybrid, which was converted to urchin-like microspheres via microemulsion [430]. Water-dispersed TPP(NH₂)₃-GO was added in an octanol oil under agitation. The resulting emulsion was heated instantly in a microwave oven (800 W) for 30 s in order to induce the evaporation of water and assembly of TPP(NH₂)₃-GO to urchin-like microspheres ($\sim 8 \mu\text{m}$), as imaged by SEM and TEM. This nanostructure was inspired by the thylakoid membrane in chloroplasts, where the electron transport chain is arranged side by side for efficient charge transfer. This arrangement of the photosynthetic components results in broadband light trapping and therefore high light harvesting efficiency. Brunauer–Emmett–Teller (BET) analysis indicated large sized open pores in the microspheres and a surface area of $96.4294 \text{ m}^2/\text{g}$ for the reference GO microspheres and $24.3151 \text{ m}^2/\text{g}$ for the TPP(NH₂)₃-GO microspheres. The observed decrement in surface area is attributed to the presence of porphyrin molecules. The urchin like microstructure had a profound effect on light harvesting, elucidating the blackbody behaviour of such a structure. In the UV-Vis diffuse reflectance spectra, the absorption of TPP(NH₂)₃-GO microspheres was extremely high and up to 95% for the entire range tested (400–800 nm). Under simulated sunlight irradiation the hybrid achieved a current density of ca $5.5 \mu\text{A}/\text{cm}^2$, which exceeds that of GO and free porphyrin. The transport of photogenerated electrons from porphyrin to GO, within the urchin-like TPP(NH₂)₃-GO ensembles, was further investigated by ultraviolet photoelectron spectroscopy (UPS) and electrochemical impedance (EIS) spectroscopy. The highest occupied molecular orbital (HOMO) and the lowest unoccupied molecular orbital (LUMO) of TPP(NH₂)₃-GO were calculated to be 3.92 eV and 0.87 eV, respectively, suggesting the occurrence of feasible photocatalytic processes in the visible light region. A detailed examination at the hybrid interface by steady-state absorption, fluorescence emission and femtosecond transient absorption (TA) spectroscopy was conducted, confirming that the optimized urchin-like geometry and covalent bonding allow fast excitation interactions between the moiety and graphene. Finally, the photocatalytic activity of TPP(NH₂)₃-GO microspheres was tested for the visible light-driven photoregeneration of nicotinamide adenine dinucleotide (NADH), yielding up to 51.50%, and for artificial photosynthetic production of formic acid from CO₂, which proved to be highly active, having a 0.5% solar-to-formic acid conversion efficiency, which is much higher than that of natural photosynthesis. The regeneration of NADH was also studied for the case of a covalently grafted cobalt-tetraaminophenyl

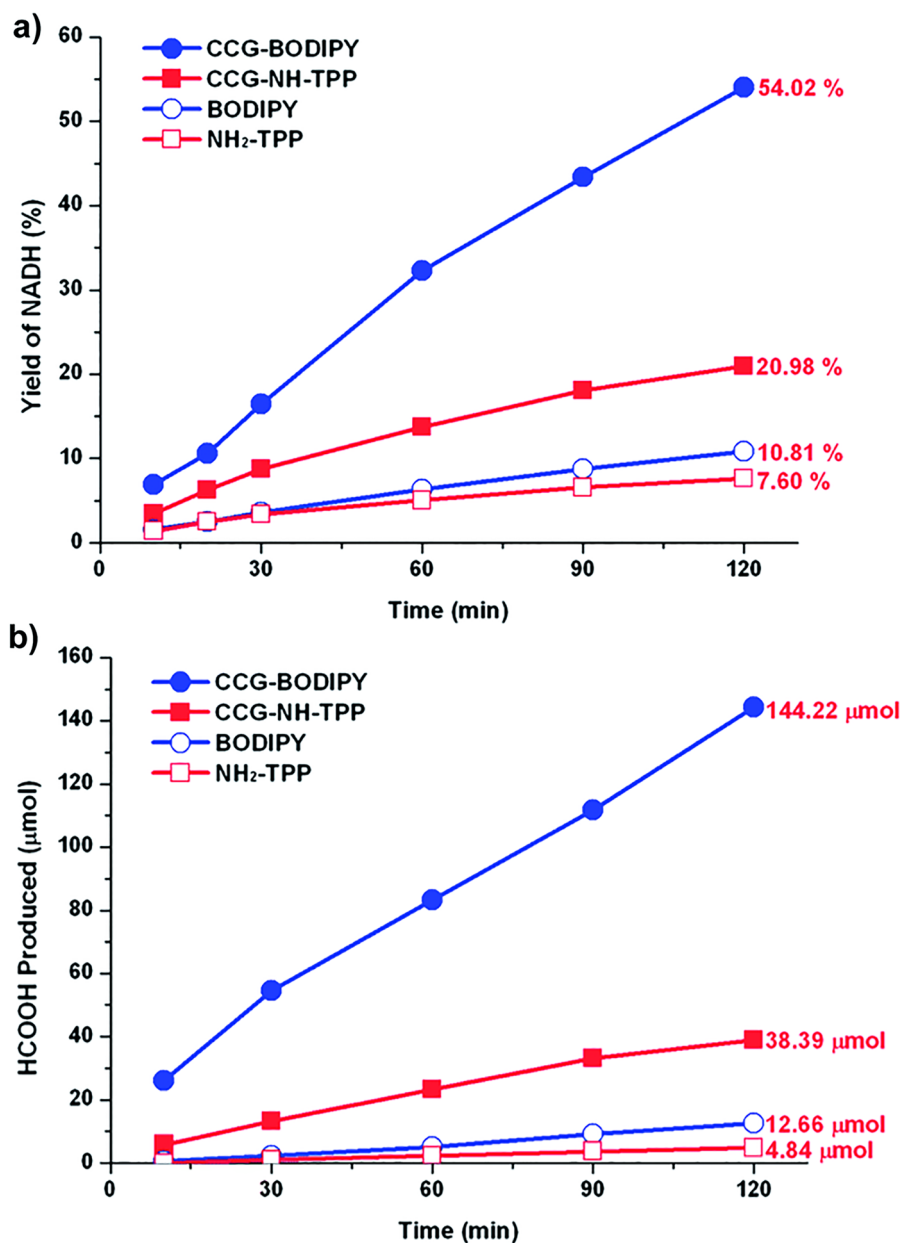


Fig. 47. Photocatalytic activities of BODIPY, CCG-BODIPY, NH₂-TPP, and CCG-NH-TPP photocatalyst for (a) NADH regeneration [β -NAD⁺ (1.24 μ mol), Rh (0.62 μ mol), TEOA (1.24 mmol) and photocatalyst (0.5 mg) in 3.1 mL of sodium phosphate buffer (100 mM, pH 7.0)] and (b) Selective enzymatic production of formic acid from CO₂ (flow rate: 0.5 mL/min) under visible light [β -NAD⁺ (1.24 μ mol), Rh (0.62 μ mol), TEOA (1.24 mmol), photocatalyst (0.5 mg) and formate dehydrogenase (3 units) in 3.1 mL of sodium phosphate buffer (100 mM, pH 7.0)]. Reproduced with permission needed from Ref. [429]. Copyright 2014 Royal Society of Chemistry.

porphyrin on GO [431]. Photoresponse assays revealed a 5-fold increment to the recorded photocurrent, as compared to the one obtained from bare cobalt-porphyrin, a 50% regeneration of NADH (vs 10% for bare cobalt-porphyrin) and a formic acid yield of 96.49 μ mol within a period of 2 h. In that work, methyl viologen (MV²⁺) as electron mediator was employed.

Beyond graphene nanosheets, graphene quantum dots (GQDs) bearing carboxylic acids were covalently decorated with an anthraquinone-isoquinoline (ANP) based dye [432]. Under acidic treatment of graphite with the aid of sonication, GQDs with a lateral size of few nanometers can be isolated. Covalent attachment of the ANP dye on the thionyl-chloride activated GQDs was verified by FT-IR evidenced by the vibrations of the newly formed amide bond at 1640 and 1299 cm⁻¹. The hybrid GQD-based system, ANP-GQDs, showed the highest efficiency for NADH (74.95%) and formic acid (198.96 μ mol) generation, attributed to the enhanced light absorption of ANP-GQDs. The corresponding efficiency of the CCG-based system was significantly lower, manifesting that tuning the size of the graphene lateral dimensions is also critical for the preparation of artificial photosynthetic systems with improved

characteristics.

Another important aspect in such systems is also the morphology of the photocatalyst. In this respect, graphene was grown on Cu foil through CVD and was functionalized by a 1,3-dioxo-1H-dibenzo[de,h]isoquinoline-2[3H]-carbaldehyde (DdIC) via the 1,3-dipolar cycloaddition reaction of in-situ generated azomethine ylides [433]. The resulting DdIC-graphene film on Cu foil showed higher formic acid production from CO₂ than the corresponding conventional spin coated photocatalyst. The covalently attached DdIC showed a blue-shifted absorption band, as compared to unbound DdIC, centred at 415 nm possibly arising from the interactions between DdIC and the CVD-grown graphene film. An increment in the D-band, as observed in the Raman spectrum, was identified in DdIC-graphene, related to the generation of defects during the covalent addition of the chromophore on the graphene lattice. Based on TGA measurements, the loading of DdIC was estimated to be 1 unit per 70 carbon atoms of graphene. The light-driven generation of NADH for a period of 2 h for DdIC-graphene (91.8%) was 225% higher than the conventional coated photocatalyst (40.1%) and ~188% higher than in powdered form (48.9%). Accordingly, DdIC-graphene produced 2.3-fold higher formic acid compared to conventional coating.

Chemical immobilization of ruthenium-based complexes on graphene improves efficiently the photocatalytic properties towards CO₂ reduction. Trinuclear [434] and heteroleptic [435] ruthenium complexes chemically attached on GO allowed the utilization of photoinduced electron transfer processes from the complexes to GO for the CO₂ to methanol conversion. A trinuclear polyazine ruthenium complex was incorporated on phenanthroline-modified GO via coordination. For the ligand-modified GO, a broad absorption feature with a maximum around 400 nm, representing the light capture region of the complex, allowed the exploitation of the hybrid material as a visible light photocatalyst. The presence of grafted phenanthroline ligands was verified by the emerged carbonyl amide stretching vibration signature at 1680 cm⁻¹. The photocatalytic properties of the trinuclear Ru-GO photocatalyst were tested under visible irradiation in DMF/water mixtures with TEA as sacrificial donor. Analysis of the photocatalytic products with GC showed no other products (e.g. CO, CH₄) and the methanol yield was determined as high as 3977.57 ± 5.60 μmol/g (2201.40 μmol/g for GO) after 48 h, while dark experiments produced no organic material highlighting the impact of the photo-induced phenomena taking place within the ensembles. Isotopic labeling of carbon dioxide provided direct evidence for the origin of the produced methanol. This is to say that, ¹³CO₂ replaced ¹²CO₂ and after irradiation of the photocatalytic mixture ¹³CH₃OH was detected as the only product, manifesting the direct photoreduction of carbon dioxide to methanol. Furthermore, the stability of the photocatalyst was investigated by inductively coupled plasma atomic emission spectroscopy (ICP-AES) analysis. After four runs the ruthenium complex content was as high as 4.12 wt%, very close to the content of the freshly prepared hybrid photocatalyst (4.14 wt %).

Following an analogous modification protocol for the preparation of GO having chemically attached a heteroleptic ruthenium complex, a benzimidazole-thiophene ligand was coordinated to a Ru(bpy)₂Cl₂ complex via a microwave assisted reaction and the heteroleptic complex chemically introduced on acyl-chloride activated GO nanosheets [435]. The loading of the as-prepared graphene-based photocatalyst was 0.51 mmol of Ru-complex per gram of catalyst, as derived by ICP-AES. Apart from the different design of the Ru-complex, as compared to the previously described report, it was also found that the photocatalytic methanol production was almost as high as previously, but without using a sacrificial donor. Specifically, the methanol production was determined by GC and found to be 2050 mmol/g after 24 h, without any by-products. The corresponding value for non-functionalized GO was 482 mmol/g after 24 h with a quantum yield of 0.044 (0.180 for Ru-GO). Overall, the chemical incorporation of the complex resulted to the maximum output, as indicated by complementary photocatalytic studies employing GO-COOH, 5% RuCl₃/GO and the free heteroleptic Ru-complex (methanol production: 320, 739 and 1048 mmol/g, respectively).

4.3.6. Oxidation of CO₂ to CO

Covalent modification of graphene with organic units owing high affinity for nanoparticles enables the combination of the properties of graphene with those of nanoparticles. Titania (P25) is a widely explored photocatalyst and forms stable junctions with carboxylic acid terminated molecules. Accordingly, P25 was incorporated on graphene functionalized by the addition of a 4-azido-2,3,5,6-tetrafluorobenzoic acid (PFPA-COOH) [436]. In this study two types of graphene were employed, NMP-assisted exfoliated graphene and CVD graphene. The reaction of graphene with the azide-functionalized organic acid was carried out by heating the reaction mixture at 150 °C for 3 h. Evidence for the successful covalent incorporation of the acid-functionalities on the graphene lattice was observed in the XPS spectra, where characteristic peaks of N1s (401 eV) and F1s (689 eV) were present, whereas the azide-related N1s peaks (402.1 and 405.6 eV, in a 2:1 ratio) were evidenced. Commercial P25 was immobilized on the exposed carboxylates via a solvothermal treatment furnishing well-dispersed nanoparticles (~20 nm) along the graphene surface as imaged by SEM. For the case of the CVD graphene, after the completion of the reaction, the Ni support was etched away by immersing the resulting sample in a solution of FeCl₃/HCl to obtain the free-standing P25-graphene. Electron diffraction studies revealed the rutile [2θ = 27° (1 1 0), 36° (1 0 1), 41° (1 1 1), 44° (2 1 0)] and anatase [2θ = 25° (1 0 1), 37° (0 0 4), 38° (1 1 2), 48° (2 0 0)] phases of P25, accompanied by the intense peak at 2θ = 26.5° which is characteristic of the (0 0 2) hexagonal graphitic carbon lattice. Moreover, EDX analysis provided information for the amount of titanium in the samples, which was up to 2.9 mmol/g. The photocatalytic properties of P25-graphene were evaluated by calculating the amount of carbon monoxide produced during the photoinduced reduction of CO₂ with trimethylamine acting as sacrificial agent for the regeneration of the electron-hole pairs within the catalyst. For the hybrid system, the CO generation was 10-fold higher (1.26 μmol/mg for P25-graphene) as compared to free P25 (0.11 μmol/mg for P25). This was attributed to the higher specific area of the graphene substrate combined to the fine distribution of P25 on the graphene surface, leading to enhanced light absorption and increased number of catalytic sites.

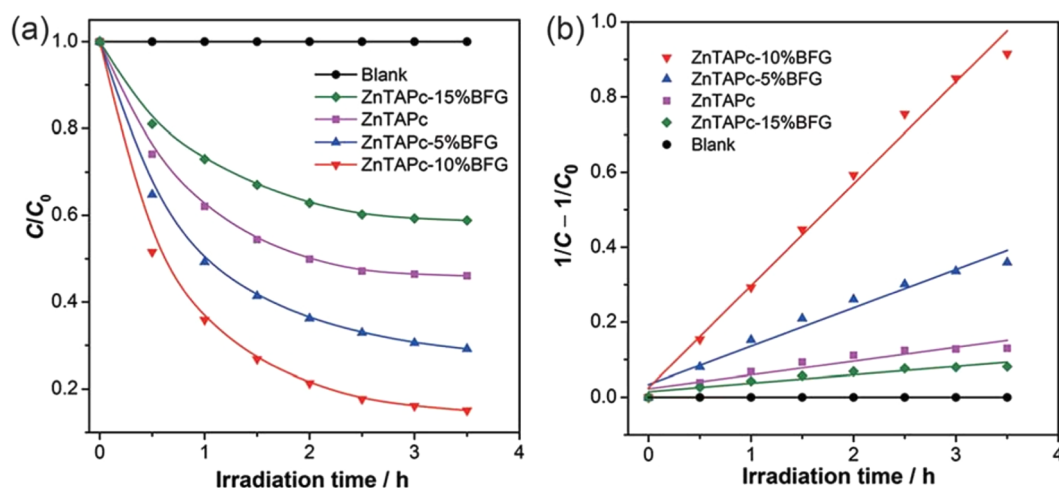


Fig. 48. (a) Photodegradation of RhB on ZnTAPc, the composites and blank. (b) The pseudo-second-order kinetics of RhB photodegradation for ZnTAPc, the composites and blank. Reproduced with permission needed from Ref. [437]. Copyright 2015 Royal Society of Chemistry.

4.3.7. Degradation of water pollutants

The incorporation of benzoic acid units at the edges of rGO, via aryl diazonium functionalization, allowed the covalent attachment of tetrakis(aminophenyl)phthalocyanine (ZnTAPc) on rGO. The so-formed ZnTAPc-rGO hybrid material was tested as photocatalyst for the degradation of rhodamine B (RhB) [437]. Prior to photocatalytic evaluation, the adsorption of RhB from the solution on the surface of the photocatalyst was studied and the calculated adsorption constant (q_e) was found to be 4.13–4.73 mg/g, which is four times higher than that due to bare ZnTAPc (1.04 mg/g). The latter difference is associated to the BET surface of the hybrid material (6.56–8.08 m²/g), which is much higher than the corresponding one of the bare phthalocyanine (1.75 m²/g). Photocatalytic assays were performed by visible light irradiation of a water solution containing ZnTAPc-rGO and RhB and monitored by the UV–Vis absorption of the dye at 553 nm. The highest photocatalytic performance was observed for 10% wt rGO, as shown in Fig. 48, highlighting the optimum ZnTAPc:rGO ratio. Based on complementary photocatalytic assays, a photoinduced decomposition mechanism, where isopropylamine (IPA) and benzoquinone (BQ) were employed as hydroxyl and superoxy radical scavengers, was proposed.

The adsorption of dye molecules onto graphene can be further improved by adopting covalent modification strategies enabling the decoration of graphene with suitable addends, which provide efficient electrostatic interactions between the target dyes and the photocatalyst. In this approach, reduced graphene oxide was modified with a polymeric ionic liquid resulting in enhanced adsorption capacity of charged dyes [438]. By loading 12 wt% poly(ionic) liquid on graphene, the adsorption efficiency for methylene blue (MB) was 1910 mg/g after 19 h at room temperature. Another approach for the enhanced adsorption of MB is the chlorination of graphene oxide, removing 221.4 mg/g after 70 h incubation [175]. Moreover, adsorption of MB was also accomplished by depositing Fe₃O₄ nanoparticles on hydrophilic GO covalently decorated with glucose sugars. The magnetic nanoparticles exhibited high adsorption of the cationic dye with no detection of leaching [439]. Immobilization of gold nanoclusters on functionalized graphene oxide nanosheets also described as an efficient photocatalytic system for the light-induced degradation of water pollutants [440].

5. Conclusions & outlook

The current review presented a complete guide towards chemical functionalization techniques for graphene and a comprehensive list of state-of-the-art applications for a wide variety of graphene hybrids including their performance. This will navigate the interested reader coming into the field through the multitude of synthetic possibilities for graphene functionalization. To the more experienced researcher, the presentation of a variety of active functional groups and their performance in specific applications should offer guidance and inspiration towards more efficient active hybrid materials.

The field of graphene chemistry has shown tremendous advancements fueled by the drive for the realization of the material's potential in various applications. In the last 15 years since its isolation and almost a decade since the Nobel prize awarded to Geim and Novoselov for their discovery, there have been few instances where a novel material has shown so much promise to technologically disrupt so many application fields in such short time. Perhaps as a testament to that, significant funding has been allocated, worldwide, towards development of graphene-based applications, which in turn, produced significant breakthroughs in the understanding of the material's properties, its strengths and its limitations. From the view of a synthetic chemist, graphene presents an elite challenge as a material that is attractive for chemical functionalization aiming at the enrichment of its properties, either physicochemical or optoelectronic. Moreover, this process, intrinsically donates to the material solubility in aqueous or organic solvents, which opens new routes through the gained processability or simply due to its enhanced miscibility in various matrices. Various classical synthetic procedures have been presented for the decoration of graphene with diverse organic moieties.

Chemically modified graphene hybrid materials may present a holistic approach towards many application problems. When coupled with graphene, the virtually infinite library of synthetic functional units, shows tremendous potential to answer key bottleneck issues plaguing today's applications. However, additional advancements are needed on the way to realization of these promises. Up to date, niche protocols have been developed for each of the different graphene analogs (doped, oxidized, etc), nevertheless the lack of a reliable source of graphene, both quantity- and quality-wise, remains an obstacle for up-scale production of materials heading to the market. Secondly, when it comes to the functionalization aspect, key breakthroughs, in yields, functional group variations and material processing are needed to establish graphene hybrids and nanoensembles as the *de facto* materials of choice for the targeted applications. As production costs are inevitably reduced, graphene-based applications are poised to take up market shares in applications previously held by established materials such as e.g. polymers and inorganic metal semiconductors. Nonetheless, such changes will require the justification of cost to performance ratio before such a major shift in infrastructure takes place.

Acknowledgments

This project has received funding from the European Union's Horizon 2020 research and innovation programme under the Marie Skłodowska-Curie grant agreement No 642742. Partial support of this work by the project "National Infrastructure in Nanotechnology, Advanced Materials and Micro-/Nanoelectronics" (MIS 5002772) which is implemented under the "Reinforcement of the Research and Innovation Infrastructures", funded by the Operational Program "Competitiveness, Entrepreneurship and Innovation" (NSRF 2014-2020) Ministry of Development and Investments and co-financed by Greece and the European Union (European Regional Development Fund) is also acknowledged.

References

- [1] Fitzer E, Kochling K-H, Boehm HP, Marsh H. Recommended terminology for the description of carbon as a solid. *Pure Appl Chem* 1995;67:473.
- [2] Cai J, Ruffieux P, Jaafar R, Bierl M, Braun T, Blankenburg S, et al. Fasel R Atomically precise bottom-up fabrication of graphene nanoribbons. *Nature* 2010;466(7305):470–3.
- [3] Dössel L, Gherghel L, Feng X, Müllen K. Graphene Nanoribbons by Chemists: Nanometer-Sized, Soluble, and Defect-Free. *Angew Chem Int Ed* 2011;50(11):2540–3.
- [4] Chen L, Hernandez Y, Feng X, Müllen K. From Nanographene and Graphene Nanoribbons to Graphene Sheets: Chemical Synthesis. *Angew Chem Int Ed* 2012;51(31):7640–54.
- [5] Yang W, Lucotti A, Tommasini M, Chalifoux WA. Bottom-up synthesis of soluble and narrow graphene nanoribbons using alkyne benzannulations. *J Am Chem Soc* 2016;138(29):9137–44.
- [6] Muñoz R, Gómez-Aleixandre C. Review of CVD synthesis of graphene. *Chem Vap Deposit* 2013;19(10-11-12):297–322.
- [7] Hass J, Heer WAD, Conrad EH. The growth and morphology of epitaxial multilayer graphene. *J Phys: Condens Matter* 2008;20(32):323202.
- [8] Seyller T, Bostwick A, Emtsev KV, Horn K, Ley L, McChesney JL, et al. Speck F Epitaxial graphene: a new material. *Phys Status Solidi (b)* 2008;245(7):1436–46.
- [9] Chen J, Duan M, Chen G. Continuous mechanical exfoliation of graphene sheets via three-roll mill. *J Mater Chem* 2012;22(37):19625–8.
- [10] Hernandez Y, Nicolosi V, Lotya M, Blighe FM, Sun Z, De S, et al. High-yield production of graphene by liquid-phase exfoliation of graphite. *Nat Nanotech* 2008;3(9):563–8.
- [11] Lotya M, Hernandez Y, King PJ, Smith RJ, Nicolosi V, Karlsson LS, et al. Liquid phase production of graphene by exfoliation of graphite in surfactant/water solutions. *J Am Chem Soc* 2009;131(10):3611–20.
- [12] Low CTJ, Walsh FC, Chakrabarti MH, Hashim MA, Hussain MA. Electrochemical approaches to the production of graphene flakes and their potential applications. *Carbon* 2013;54(Suppl. C):1–21.
- [13] Chua CK, Pummer M. Chemical reduction of graphene oxide: a synthetic chemistry viewpoint. *Chem Soc Rev* 2014;43(1):291–312.
- [14] Jiao L, Zhang L, Wang X, Diankov G, Dai H. Narrow graphene nanoribbons from carbon nanotubes. *Nature* 2009;458(7240):877–80.
- [15] Kosynkin DV, Higginbotham AL, Sinitskii A, Lomeda JR, Dimiev A, Price BK, et al. Longitudinal unzipping of carbon nanotubes to form graphene nanoribbons. *Nature* 2009;458(7240):872–6.
- [16] Paton KR, Varrla E, Backes C, Smith RJ, Khan U, O'Neill A, et al. Scalable production of large quantities of defect-free few-layer graphene by shear exfoliation in liquids. *Nat Mater* 2014;13(6):624–30.
- [17] Lee C, Wei X, Kysar JW, Hone J. Measurement of the elastic properties and intrinsic strength of monolayer graphene. *Science* 2008;321(5887):385–8.
- [18] Lee J-U, Yoon D, Cheong H. Estimation of Young's modulus of graphene by Raman spectroscopy. *Nano Lett* 2012;12(9):4444–8.
- [19] Mak KF, Sfeir MY, Wu Y, Lui CH, Misewich JA, Heinz TF. Measurement of the optical conductivity of graphene. *Phys Rev Lett* 2008;101(19):196405.
- [20] Bonaccorso F, Sun Z, Hasan T, Ferrari AC. Graphene photonics and optoelectronics. *Nat Photon* 2010;4:611.
- [21] Bolotin KI, Sikes KJ, Jiang Z, Klima M, Fudenberg G, Hone J, et al. Ultrahigh electron mobility in suspended graphene. *Solid State Commun* 2008;146(9):351–5.
- [22] Chen J-H, Jang C, Xiao S, Ishigami M, Fuhrer MS. Intrinsic and extrinsic performance limits of graphene devices on SiO₂. *Nat Nanotech* 2008;3:206.
- [23] Meyer JC, Geim AK, Katsnelson MI, Novoselov KS, Booth TJ, Roth S. The structure of suspended graphene sheets. *Nature* 2007;446:60.
- [24] Morozov SV, Novoselov KS, Katsnelson MI, Schedin F, Ponomarenko LA, Jiang D, Geim AK. Strong suppression of weak localization in graphene. *Phys Rev Lett* 2006;97(1):016801.
- [25] Fasolino A, Los JH, Katsnelson MI. Intrinsic ripples in graphene. *Nat Mater* 2007;6:858.
- [26] Du X, Skachko I, Barker A, Andrei EY. Approaching ballistic transport in suspended graphene. *Nat Nanotech* 2008;3:491.
- [27] Chu Z, He L. Origin of room-temperature single-channel ballistic transport in zigzag graphene nanoribbons. *Sci China Mater* 2015;58(9):677–82.
- [28] Gu Z, Fertig HA, Arovas DP, Auerbach A. Floquet spectrum and transport through an irradiated graphene ribbon. *Phys Rev Lett* 2011;107(21):216601.
- [29] Ackerman ML, Kumar P, Neek-Amal M, Thibado PM, Peeters FM, Singh S. Anomalous dynamical behavior of freestanding graphene membranes. *Phys Rev Lett* 2016;117(12):126801.
- [30] Sarkar S, Bekyarova E, Haddon RC. Covalent chemistry in graphene electronics. *Mater Today* 2012;15(6):276–85.
- [31] Xiang Q, Yu J, Jaroniec M. Graphene-based semiconductor photocatalysts. *Chem Soc Rev* 2012;41(2):782–96.
- [32] Economopoulos SP, Tagmatarchis N. Chemical functionalization of exfoliated graphene. *Chem Eur J* 2013;19(39):12930–6.
- [33] Rodríguez-Pérez L, Herranz MA, Martín N. The chemistry of pristine graphene. *Chem Commun* 2013;49(36):3721–35.
- [34] Wang H-X, Wang Q, Zhou K-G, Zhang H-L. Graphene in light: design, synthesis and applications of photo-active graphene and graphene-like materials. *Small* 2013;9(8):1266–83.
- [35] Eigler S, Hirsch A. Chemistry with graphene and graphene oxide—challenges for synthetic chemists. *Angew Chem Int Ed* 2014;53(30):7720–38.
- [36] Ambrosi A, Chua CK, Bonanni A, Pummer M. Electrochemistry of graphene and related materials. *Chem Rev* 2014;114(14):7150–88.
- [37] Roy-Mayhew JD, Aksay IA. Graphene materials and their use in dye-sensitized solar cells. *Chem Rev* 2014;114(12):6323–48.
- [38] Dreyer DR, Todd AD, Bielawski CW. Harnessing the chemistry of graphene oxide. *Chem Soc Rev* 2014;43(15):5288–301.
- [39] Bonaccorso F, Colombo L, Yu G, Stoller M, Tozzini V, Ferrari AC, et al. Graphene, related two-dimensional crystals, and hybrid systems for energy conversion and storage. *Science* 2015;347(6217):1246501.

- [40] Georgakilas V, Perman JA, Tucek J, Zboril R. Broad family of carbon nanoallotropes: classification, chemistry, and applications of fullerenes, carbon dots, nanotubes, graphene, nanodiamonds, and combined superstructures. *Chem Rev* 2015;115(11):4744–822.
- [41] Narita A, Wang X-Y, Feng X, Müllen K. New advances in nanographene chemistry. *Chem Soc Rev* 2015;44(18):6616–43.
- [42] Yang Z, Ren J, Zhang Z, Chen X, Guan G, Qiu L, et al. Recent advancement of nanostructured carbon for energy applications. *Chem Rev* 2015;115(11):5159–223.
- [43] Zhang X, Hou L, Samorì P. Coupling carbon nanomaterials with photochemical molecules for the generation of optically responsive materials. *Nat Commun* 2016;7(1):11118.
- [44] Li X, Yu J, Wageh S, Al-Ghamdi AA, Xie J. Graphene in photocatalysis: a review. *Small* 2016;12(48):6640–96.
- [45] Bottari G, Herranz MA, Wibmer L, Volland M, Rodríguez-Pérez L, Guldi DM, et al. Chemical functionalization and characterization of graphene-based materials. *Chem Soc Rev* 2017;46(15):4464–500.
- [46] Chronopoulos DD, Bakandritsos A, Pykal M, Zbořil R, Otyepka M. Chemistry, properties, and applications of fluorographene. *Appl Mater Today* 2017;9:60–70.
- [47] Navalón S, Herance JR, Álvaro M, García H. Covalently modified graphenes in catalysis, electrocatalysis and photoresponsive materials. *Chem Eur J* 2017;23(61):15244–75.
- [48] Sturala J, Luxa J, Pumera M, Sofer Z. Chemistry of graphene derivatives: synthesis, applications, and perspectives. *Chem Eur J* 2018;24(23):5992–6006.
- [49] Stergiou A, Karousis N, Tasis D. CHAPTER 2: Non-covalent methodologies for the preparation of metal-free nanocarbons for catalysis. In: *RSC Catalysis Series*, vol. 2018-January; 2018. p. 29–66.
- [50] Sun Z, Yan Z, Yao J, Beiter E, Zhu Y, Tour JM. Growth of graphene from solid carbon sources. *Nature* 2010;468(7323):549–52.
- [51] Ruan G, Sun Z, Peng Z, Tour JM. Growth of graphene from food, insects, and waste. *ACS Nano* 2011;5(9):7601–7.
- [52] Kim KS, Zhao Y, Jang H, Lee SY, Kim JM, Kim KS, et al. Large-scale pattern growth of graphene films for stretchable transparent electrodes. *Nature* 2009;457(7230):706–10.
- [53] Bae S, Kim H, Lee Y, Xu X, Park J-S, Zheng Y, et al. Roll-to-roll production of 30-inch graphene films for transparent electrodes. *Nat Nanotech* 2010;5(8):574–8.
- [54] Boland CS, Khan U, Ryan G, Barwich S, Charifou R, Harvey A, et al. Sensitive electromechanical sensors using viscoelastic graphene-polymer nanocomposites. *Science* 2016;354(6317):1257–60.
- [55] Zohhadi N, Aich N, Matta F, Saleh NB, Ziehl P. Graphene nanoreinforcement for cement composites. In: Sobolev K, Shah SP, editors. *Nanotechnology in construction: proceedings of NICOM5*. Cham: Springer International Publishing; 2015. p. 265–70.
- [56] Lu Z, Hou D, Meng L, Sun G, Lu C. Li Z Mechanism of cement paste reinforced by graphene oxide/carbon nanotubes composites with enhanced mechanical properties. *RSC Adv* 2015;5(122):100598–605.
- [57] Yang Haibin, Cui Hongzhi, Tang Waiching, Li Zongjin, Han Ningxu, Xing Feng. A critical review on research progress of graphene/cement based composites. *Compos A Appl Sci Manuf* 2017;102:273–96. <https://doi.org/10.1016/j.compositesa.2017.07.019>.
- [58] Sreerprasad TS, Bery V. How do the electrical properties of graphene change with its functionalization? *Small* 2013;9(3):341–50.
- [59] Kaila T, Bose S, Mishra AK, Khanra P, Kim NH, Lee JH. Chemical functionalization of graphene and its applications. *Prog Mater Sci* 2012;57(7):1061–105.
- [60] Stergiou A, Gobeze HB, Petsalakis ID, Zhao S, Shinohara H, D'Souza F, et al. Oligothiophene/graphene supramolecular ensembles managing light induced processes: preparation, characterization, and femtosecond transient absorption studies leading to charge-separation. *Nanoscale* 2015;7(38):15840–51.
- [61] Stergiou A, Perivoliotis DK, Tagmatarchis N. (Photo)electrocatalysis of molecular oxygen reduction by S-doped graphene decorated with a star-shaped oligothiophene. *Nanoscale* 2019;11(15):7335–46.
- [62] Kiessling D, Costa RD, Katsukis G, Malig J, Lodermeier F, Feihl S, et al. Novel nanographene/porphyrin hybrids - preparation, characterization, and application in solar energy conversion schemes. *Chem Sci* 2013;4(8):3085–98.
- [63] Economopoulos SP, Tagmatarchis N. Multichromophores onto graphene: supramolecular non-covalent approaches for efficient light harvesting. *J Phys Chem C* 2015;119(15):8046–53.
- [64] Malig J, Stephenson AWL, Wagner P, Wallace GG, Officer DL, Guldi DM. Direct exfoliation of graphite with a porphyrin - creating functionalizable nano-graphene hybrids. *Chem Commun* 2012;48(70):8745–7.
- [65] Geng J, Kong B-S, Yang SB, Jung H-T. Preparation of graphene relying on porphyrin exfoliation of graphite. *Chem Commun* 2010;46(28):5091–3.
- [66] Mann JA, Rodríguez-López J, Abruña HD, Dichtel WR. Multivalent binding motifs for the noncovalent functionalization of graphene. *J Am Chem Soc* 2011;133(44):17614–7.
- [67] Malig J, Romero-Nieto C, Jux N, Guldi DM. Integrating water-soluble graphene into porphyrin nanohybrids. *Adv Mater* 2012;24(6):800–5.
- [68] Ghosh A, Rao KV, George SJ, Rao CNR. Noncovalent functionalization, exfoliation, and solubilization of graphene in water by employing a fluorescent coronene carboxylate. *Chem Eur J* 2010;16(9):2700–4.
- [69] Malig J, Jux N, Kiessling D, Cid J-J, Vázquez P, Torres T, et al. Towards tunable graphene/phthalocyanine-PPV hybrid systems. *Angew Chem Int Ed* 2011;50(15):3561–5.
- [70] Chandra Bikram KC, Das SK, Ohkubo K, Fukuzumi S, D'Souza F. Ultrafast charge separation in supramolecular tetrapyrrole-graphene hybrids. *Chem Commun* 2012;48(97):11859–61.
- [71] Achadu OJ, Nyokong T. Application of graphene quantum dots decorated with TEMPO-derivatized zinc phthalocyanine as novel nanoprobes: probing the sensitive detection of ascorbic acid. *New J Chem* 2016;40(10):8277–36.
- [72] Pakongpan Saithip, Mensing Johannes Philipp, Phokharatkul Ditsayut, Lomas Tanom, Tuantranont Adisorn. Highly selective electrochemical sensor for ascorbic acid based on a novel hybrid graphene-copper phthalocyanine-polyaniline nanocomposites. *Electrochim Acta* 2014;133:294–301. <https://doi.org/10.1016/j.electacta.2014.03.167>.
- [73] Cui L, Lv G, He X. Enhanced oxygen reduction performance by novel pyridine substituent groups of iron (II) phthalocyanine with graphene composite. *J Power Sources* 2015;282:9–18.
- [74] Cui L, Lv G, Dou Z, He X. Fabrication of iron phthalocyanine/graphene micro/nanocomposite by solvothermally assisted π - π assembling method and its application for oxygen reduction reaction. *Electrochim Acta* 2013;106:272–8.
- [75] Kim M, Safron NS, Huang C, Arnold MS, Gopalan P. Light-driven reversible modulation of doping in graphene. *Nano Lett* 2012;12(1):182–7.
- [76] Ramakrishna Matte HSS, Subrahmanyam KS, Venkata Rao K, George SJ, Rao CNR. Quenching of fluorescence of aromatic molecules by graphene due to electron transfer. *Chem Phys Lett* 2011;506(4):260–4.
- [77] Martín-Gomis L, Karousis N, Fernandez-Lazaro F, Petsalakis ID, Ohkubo K, Fukuzumi S, et al. Exfoliation and supramolecular functionalization of graphene with an electron donor peryleneimide derivative. *Photochem Photobiol Sci* 2017;16(4):596–605.
- [78] Kozhemyakina NV, Englert JM, Yang G, Spiecker E, Schmidt CD, Hauke F, et al. Non-covalent chemistry of graphene: electronic communication with dendronized perylene bisimides. *Adv Mater* 2010;22(48):5483–7.
- [79] Le Goff A, Reuillard B, Cosnier SA. Pyrene-substituted tris(bipyridine)osmium(II) complex as a versatile redox probe for characterizing and functionalizing carbon nanotube- and graphene-based electrodes. *Langmuir* 2013;29(27):8736–42.
- [80] Cai X, Tan S, Xie A, Lin M, Liu Y, Zhang X, et al. Conductive methyl blue-functionalized reduced graphene oxide with excellent stability and solubility in water. *Mater Res Bull* 2011;46(12):2353–8.
- [81] Bingel C. Cyclopropanierung von Fullerenen. *Chem Ber* 1993;126(8):1957–9.
- [82] Economopoulos SP, Rotas G, Miyata Y, Shinohara H, Tagmatarchis N. Exfoliation and chemical modification using microwave irradiation affording highly functionalized graphene. *ACS Nano* 2010;4(12):7499–507.
- [83] Jin B, Shen J, Peng R, Chen C, Zhang Q, Wang X, et al. An efficient catalyst for the cyclopropanation of C60, C70, SWNTs, and graphene through the bingel reaction. *Ind Eng Chem Res* 2015;54(11):2879–85.
- [84] Chua CK, Ambrosi A, Pumera M. Introducing dichlorocarbene in graphene. *Chem Commun* 2012;48(43):5376–8.
- [85] Sainsbury T, Passarelli M, Naftaly M, Gnanih S, Spencer SJ, Pollard AJ. Covalent carbene functionalization of graphene: toward chemical band-gap manipulation. *ACS Appl Mater Interfaces* 2016;8(7):4870–7.
- [86] Hu Z, Song C, Shao Q, Li J, Huang Y. One-step functionalization of graphene by cycloaddition of diarylcarbene and its application as reinforcement in epoxy composites. *Compos Sci Technol* 2016;135:21–7.
- [87] Zan W. Chemical functionalization of graphene by carbene cycloaddition: a density functional theory study. *Appl Surf Sci* 2014;311:377–83.
- [88] Hesari M, Workentin MS. Covalent modification of graphene and micro-diamond with redox active substrates via photogenerated carbenes. *Carbon*

- 2015;85:159–67.
- [89] Choi J, Kim K-J, Kim B, Lee H, Kim S. Covalent functionalization of epitaxial graphene by azidotrimethylsilane. *J Phys Chem C* 2009;113(22):9433–5.
- [90] Quintana M, Spyrou K, Grzelczak M, Browne WR, Rudolf P, Prato M. Functionalization of graphene via 1,3-dipolar cycloaddition. *ACS Nano* 2010;4(6):3527–33.
- [91] Neri G, Scala A, Fazio E, Mineo PG, Rescifina A, Piperno A, et al. Repurposing of oxazolone chemistry: gaining access to functionalized graphene nanosheets in a top-down approach from graphite. *Chem Sci* 2015;6(12):6961–70.
- [92] Gribble GW. Mesoionic oxazoles. *Oxazoles: synthesis, reactions, and spectroscopy*; 2003.
- [93] Barrejón M, Gómez-Escalonilla MJ, Fierro JLG, Prieto P, Carrillo JR, Rodríguez AM, et al. Modulation of the exfoliated graphene work function through cycloaddition of nitrile imines. *Phys Chem Chem Phys* 2016;18(42):29582–90.
- [94] Diels O, Alder K. Synthesen in der hydroaromatischen Reihe. *Justus Liebigs Annalen der Chemie* 1928;460(1):98–122.
- [95] Sarkar S, Bekyarova E, Niyogi S, Haddon RC. Diels–Alder chemistry of graphite and graphene: graphene as diene and dienophile. *J Am Chem Soc* 2011;133(10):3324–7.
- [96] Nicolaou KC, Snyder SA, Montagnon T, Vassilikogiannakis G. The Diels-Alder reaction in total synthesis. *Angew Chem Int Ed* 2002;41(10):1668–98.
- [97] Heravi MM, Vavsari VF. Recent applications of intramolecular Diels-Alder reaction in total synthesis of natural products. *RSC Adv* 2015;5(63):50890–912.
- [98] Wilson SR, Yurchenko ME, Schuster DI, Khong A, Saunders M. Synthesis of fluorinated fullerene adducts: reversible solubilization of fullerenes in perfluorinated solvents. *J Org Chem* 2000;65(9):2619–23.
- [99] Isakova A, Burton C, Nowakowski DJ, Topham PD. Diels-Alder cycloaddition and RAFT chain end functionality: an elegant route to fullerene end-capped polymers with control over molecular mass and architecture. *Polym Chem* 2017;8(18):2796–805.
- [100] Delgado JL, de la Cruz P, Langa F, Urbina A, Casado J, Lopez Navarrete JT. Microwave-assisted sidewall functionalization of single-wall carbon nanotubes by Diels-Alder cycloaddition. *Chem Commun* 2004;15:1734–5.
- [101] Mata D, Amaral M, Fernandes AJS, Colaco B, Gama A, Paiva MC, et al. Diels-Alder functionalized carbon nanotubes for bone tissue engineering: in vitro/in vivo biocompatibility and biodegradability. *Nanoscale* 2015;7(20):9238–51.
- [102] Munirasu S, Albuerna J, Boschetti-de-Fierro A, Abetz V. Functionalization of carbon materials using the Diels-Alder reaction. *Macromol Rapid Commun* 2010;31(6):574–9.
- [103] Frolova LV, Magedov IV, Harper A, Jha SK, Ovezmyradov M, Chandler G, et al. Tetracyanoethylene oxide- functionalized graphene and graphite characterized by Raman and Auger spectroscopy. *Carbon* 2015;81:216–22.
- [104] Li J, Li M, Zhou L-L, Lang S-Y, Lu H-Y, Wang D, et al. Click and patterned functionalization of graphene by Diels-Alder reaction. *J Am Chem Soc* 2016;138(24):7448–51.
- [105] Farquhar AK, Fitchett CM, Dykstra HM, Waterland MR, Brooksby PA, Downard AJ. Diels-Alder reaction of anthranilic acids: a versatile route to dense monolayers on flat edge and basal plane graphitic carbon substrates. *ACS Appl Mater Interfaces* 2016;8(35):23389–95.
- [106] Zhong X, Jin J, Li S, Niu Z, Hu W, Li R, Ma J. Aryne cycloaddition: highly efficient chemical modification of graphene. *Chem Commun* 2010;46(39):7340–2.
- [107] Choi E-K, Jeon I-Y, Bae S-Y, Lee H-J, Shin HS, Dai L, et al. High-yield exfoliation of three-dimensional graphite into two-dimensional graphene-like sheets. *Chem Commun* 2010;46(34):6320–2.
- [108] Chua CK, Pumera M. Friedel-Crafts acylation on graphene. *Chem – Asian J* 2012;7(5):1009–12.
- [109] Avinash MB, Subrahmanyam KS, Sundarayya Y, Govindaraju T. Covalent modification and exfoliation of graphene oxide using ferrocene. *Nanoscale* 2010;2(9):1762–6.
- [110] Kalita G, Sharma S, Wakita K, Umeno M, Hayashi Y, Tanemura M. A photoinduced charge transfer composite of graphene oxide and ferrocene. *Phys Chem Chem Phys* 2013;15(4):1271–4.
- [111] Eng AYS, Sofer Z, Sedmidubský D, Pumera M. Synthesis of carboxylated-graphenes by the Kolbe-Schmitt process. *ACS Nano* 2017;11(2):1789–97.
- [112] Liu Y, Deng R, Wang Z, Liu H. Carboxyl-functionalized graphene oxide–polyaniline composite as a promising supercapacitor material. *J Mater Chem* 2012;22(27):13619–24.
- [113] Smaranda I, Benito AM, Maser WK, Baltog I, Baibarac M. Electrochemical grafting of reduced graphene oxide with polydiphenylamine doped with heteropolyanions and its optical properties. *J Phys Chem C* 2014;118(44):25704–17.
- [114] Sarkar S, Bekyarova E, Haddon RC. Reversible grafting of α -naphthylmethyl radicals to epitaxial graphene. *Angew Chem* 2012;124(20):4985–8.
- [115] Sun Z, Kohama SI, Zhang Z, Lomeda JR, Tour JM. Soluble graphene through edge-selective functionalization. *Nano Res* 2010;3(2):117–25.
- [116] Sinitskii A, Dimiev A, Corley DA, Fursina AA, Kosynkin DV, Tour JM. Kinetics of diazonium functionalization of chemically converted graphene nanoribbons. *ACS Nano* 2010;4(4):1949–54.
- [117] Zhu Y, Higginbotham AL, Tour JM. Covalent functionalization of surfactant-wrapped graphene nanoribbons. *Chem Mater* 2009;21(21):5284–91.
- [118] Wu Q, Wu Y, Hao Y, Geng J, Charlton M, Chen S, et al. Selective surface functionalization at regions of high local curvature in graphene. *Chem Commun* 2013;49(7):677–9.
- [119] Bouša D, Pumera M, Sedmidubský D, Šturala J, Luxa J, Mazánek V, et al. Fine tuning of graphene properties by modification with aryl halogens. *Nanoscale* 2016;8(3):1493–502.
- [120] Jin Z, McNicholas TP, Shih C-J, Wang QH, Paulus GLC, Hilmer AJ, et al. Click chemistry on solution-dispersed graphene and monolayer CVD graphene. *Chem Mater* 2011;23(14):3362–70.
- [121] Lomeda JR, Doyle CD, Kosynkin DV, Hwang W-F, Tour JM. Diazonium functionalization of surfactant-wrapped chemically converted graphene sheets. *J Am Chem Soc* 2008;130(48):16201–6.
- [122] Jin Z, Lomeda JR, Price BK, Lu W, Zhu Y, Tour JM. Mechanically assisted exfoliation and functionalization of thermally converted graphene sheets. *Chem Mater* 2009;21(14):3045–7.
- [123] Greenwood J, Phan TH, Fujita Y, Li Z, Ivasenko O, Vanderlinden W, et al. Covalent modification of graphene and graphite using diazonium chemistry: tunable grafting and nanomanipulation. *ACS Nano* 2015;9(5):5520–35.
- [124] Xia Z, Leonardi F, Gobbi M, Liu Y, Bellani V, Liscio A, et al. Electrochemical functionalization of graphene at the nanoscale with self-assembling diazonium salts. *ACS Nano* 2016;10(7):7125–34.
- [125] Chan CK, Beechem TE, Ohta T, Brumbach MT, Wheeler DR, Stevenson KJ. Electrochemically driven covalent functionalization of graphene from fluorinated aryl iodonium salts. *J Phys Chem C* 2013;117(23):12038–44.
- [126] Englert JM, Dotzer C, Yang G, Schmid M, Papp C, Gottfried JM, et al. Covalent bulk functionalization of graphene. *Nat Chem* 2011;3:279.
- [127] Knirsch KC, Englert JM, Dotzer C, Hauke F, Hirsch A. Screening of the chemical reactivity of three different graphite sources using the formation of reductively alkylated graphene as a model reaction. *Chem Commun* 2013;49(92):10811–3.
- [128] Morishita T, Clancy AJ, Shaffer MSP. Optimised exfoliation conditions enhance isolation and solubility of grafted graphenes from graphite intercalation compounds. *J Mater Chem A* 2014;2(36):15022–8.
- [129] Pennetreau F, Riant O, Hermans S. One-step double covalent functionalization of reduced graphene oxide with xanthates and peroxides. *Chem Eur J* 2014;20(46):15009–12.
- [130] Skaltsas T, Mountrichas G, Zhao S, Shinohara H, Tagmatarchis N, Pispas S. Single-step functionalization and exfoliation of graphene with polymers under mild conditions. *Chem Eur J* 2015;21(51):18841–6.
- [131] Luong ND, Sinh LH, Johansson L-S, Campell J, Seppälä J. Functional graphene by thiol-ene click chemistry. *Chem Eur J* 2015;21(8):3183–6.
- [132] Castelaín M, Martínez G, Ellis G, Salavagione HJ. A versatile chemical tool for the preparation of conductive graphene-based polymer nanocomposites. *Chem Commun* 2013;49(79):8967–9.
- [133] Castelaín M, Martínez G, Marco C, Ellis G, Salavagione HJ. Effect of click-chemistry approaches for graphene modification on the electrical, thermal, and mechanical properties of polyethylene/graphene nanocomposites. *Macromolecules* 2013;46(22):8980–7.
- [134] Sarkar S, Niyogi S, Bekyarova E, Haddon RC. Organometallic chemistry of extended periodic π -electron systems: hexahapto-chromium complexes of graphene and single-walled carbon nanotubes. *Chem Sci* 2011;2(7):1326–33.
- [135] Chen M, Pekker A, Li W, Itkis ME, Haddon RC, Bekyarova E. Organometallic chemistry of graphene: photochemical complexation of graphene with group 6 transition metals. *Carbon* 2018;129:450–5.
- [136] Zhang Z, Turner CH. Redox properties of graphenes functionalized with cyclopentadiene-transition metal complexes: a potential redox-active material. *J Phys*

- Chem C 2014;118(42):24633–40.
- [137] Hummers WS, Offeman RE. Preparation of graphitic oxide. *J Am Chem Soc* 1958;80(6):1339.
- [138] Kang JH, Kim T, Choi J, Park J, Kim YS, Chang MS, et al. Hidden second oxidation step of hummers method. *Chem Mater* 2016;28(3):756–64.
- [139] Patel MA, Yang H, Chiu PL, Mastrogiovanni DDT, Flach CR, Savaram K, et al. Direct production of graphene nanosheets for near infrared photoacoustic imaging. *ACS Nano* 2013;7(9):8147–57.
- [140] Chua CK, Sofer Z, Pumera M. Graphite oxides: effects of permanganate and chlorate oxidants on the oxygen composition. *Chem Eur J* 2012;18(42):13453–9.
- [141] Gao X, Jang J, Nagase S. Hydrazine and thermal reduction of graphene oxide: reaction mechanisms, product structures, and reaction design. *J Phys Chem C* 2010;114(2):832–42.
- [142] Hou S, Kasner ML, Su S, Patel K, Cuellari R. Highly sensitive and selective dopamine biosensor fabricated with silanized graphene. *J Phys Chem C* 2010;114(35):14915–21.
- [143] Zhao QS, Li Y, Liu R, Chen A, Zhang GL, Zhang FB, Fan XB. Enhanced hydrogenation of olefins and ketones with a ruthenium complex covalently anchored on graphene oxide. *J Mater Chem A* 2013;1(47):15039–45.
- [144] Zhao Q, Chen D, Li Y, Zhang G, Zhang F, Fan X. Rhodium complex immobilized on graphene oxide as an efficient and recyclable catalyst for hydrogenation of cyclohexene. *Nanoscale* 2013;5(3):882–5.
- [145] Su H, Wu S, Li Z, Huo Q, Guan J, Kan Q. Co(II), Fe(III) or VO(II) Schiff base metal complexes immobilized on graphene oxide for styrene epoxidation. *Appl Organomet Chem* 2015;29(7):462–7.
- [146] Mungse HP, Verma S, Kumar N, Sain B, Khatri OP. Grafting of oxo-vanadium Schiff base on graphene nanosheets and its catalytic activity for the oxidation of alcohols. *J Mater Chem* 2012;22(12):5427–33.
- [147] Sun J, Zhang J, Wang L, Zhu L, Meng X, Xiao F-S. Co-salen functionalized on graphene as an efficient heterogeneous catalyst for cyclohexene oxidation. *J Energy Chem* 2013;22(1):48–51.
- [148] Khatri PK, Choudhary S, Singh R, Jain SL, Khatri OP. Grafting of a rhenium-oxo complex on Schiff base functionalized graphene oxide: an efficient catalyst for the oxidation of amines. *Dalton Trans* 2014;43(21):8054–61.
- [149] Su H, Li Z, Huo Q, Guan J, Kan Q. Immobilization of transition metal (Fe²⁺, Co²⁺, VO²⁺ or Cu²⁺) Schiff base complexes onto graphene oxide as efficient and recyclable catalysts for epoxidation of styrene. *RSC Adv* 2014;4(20):9990–6.
- [150] Li Z, Wu S, Zheng D, Liu J, Liu H, Lu H, et al. Dioxomolybdenum(VI) complex covalently attached to amino-modified graphene oxide: heterogeneous catalyst for the epoxidation of alkenes. *Appl Organomet Chem* 2014;28(5):317–23.
- [151] Zhao Q, Bai C, Zhang W, Li Y, Zhang G, Zhang F, et al. Catalytic epoxidation of olefins with graphene oxide supported copper (salen) complex. *Ind Eng Chem Res* 2014;53(11):4232–8.
- [152] Mahyari M, Shaabani A. Graphene oxide-iron phthalocyanine catalyzed aerobic oxidation of alcohols. *Appl Catal A* 2014;469:524–31.
- [153] Li Z, Wu S, Zheng D, Liu H, Hu J, Su H, et al. Enhanced alkenes epoxidation reactivity of discrete bis(8-quinolino)oxovanadium(IV) or bis(8-quinolino) dioxomolybdenum(VI) tethered to graphene oxide by a metal-template/metal-exchange method. *Appl Catal A* 2014;470:104–14.
- [154] Nasseri MA, Allahresani A, Raissi H. Grafting of a chiral Mn(III) complex on graphene oxide nanosheets and its catalytic activity for alkene epoxidation. *RSC Adv* 2014;4(50):26087–93.
- [155] Li Y, Qi L, Ma H. Preparation of porous polymer monolithic column using functionalized graphene oxide as a functional crosslinker for high performance liquid chromatography separation of small molecules. *Analyst* 2013;138(18):5470–8.
- [156] Yan W, Xu Y. Chen Y Facile and effective functionalization of graphene oxide by boron-oxygen covalent or bingel cyclopropanation reaction. *J Nanosci Nanotechnol* 2015;15(3):2020–6.
- [157] Burrell JW, Gadipelli S, Ford J, Simmons JM, Zhou W, Yildirim T. Graphene oxide framework materials: theoretical predictions and experimental results. *Angew Chem Int Ed* 2010;49(47):8902–4.
- [158] Mercier G, Klechikov A, Hedenström M, Johnels D, Baburin IA, Seifert G, et al. Porous graphene oxide/diboronic acid materials: structure and hydrogen sorption. *J Phys Chem C* 2015;119(49):27179–91.
- [159] Chai N-N, Zeng J, Zhou K-G, Xie Y-L, Wang H-X, Zhang H-L, et al. Free-radical-promoted conversion of graphite oxide into chemically modified graphene. *Chem Eur J* 2013;19(19):5948–54.
- [160] Shan C, Wang L, Han D, Li F, Zhang Q, Zhang X, et al. Polyethyleneimine-functionalized graphene and its layer-by-layer assembly with Prussian blue. *Thin Solid Films* 2013;534:572–6.
- [161] Bourlins AB, Gourmès D, Petridis D, Szabó T, Szeri A, Dékány I. Graphite oxide: chemical reduction to graphite and surface modification with primary aliphatic amines and amino acids. *Langmuir* 2003;19(15):6050–5.
- [162] Vacchi IA, Spinato C, Raya J, Bianco A, Ménard-Moyon C. Chemical reactivity of graphene oxide towards amines elucidated by solid-state NMR. *Nanoscale* 2016;8(28):13714–21.
- [163] Avila-Vega YI, Leyva-Porras CC, Mireles M, Quevedo-López M, Macossay J, Bonilla-Cruz J. Nitroxide-functionalized graphene oxide from graphite oxide. *Carbon* 2013;63:376–89.
- [164] Du G, Nie L, Gao G, Sun Y, Hou R, Zhang H, et al. Tough and biocompatible hydrogels based on in situ interpenetrating networks of dithiol-connected graphene oxide and poly(vinyl alcohol). *ACS Appl Mater Interfaces* 2015;7(5):3003–8.
- [165] Halbig EC, Rietsch P, Eigler S. Towards the synthesis of graphene azide from graphene oxide. *Molecules* 2015;20(12).
- [166] Eigler S, Hu Y, Ishii Y, Hirsch A. Controlled functionalization of graphene oxide with sodium azide. *Nanoscale* 2013;5(24):12136–9.
- [167] Tu Q, Zhao L, Han X, Wang D-E, Yuan M-S, Tian C, et al. visualized method for Cu²⁺ ion detection by self-assembling azide functionalized free graphene oxide using click chemistry. *RSC Adv* 2016;6(98):95628–32.
- [168] Salvio R, Krabbenborg S, Naber WJM, Velders AH, Reinhoudt DN, van der Wiel WG. The formation of large-area conducting graphene-like platelets. *Chem Eur J* 2009;15(33):8235–40.
- [169] Singh SK, Singh MK, Kulkarni PP, Sonkar VK, Grácio JJA, Dash D. Amine-modified graphene: thrombo-protective safer alternative to graphene oxide for biomedical applications. *ACS Nano* 2012;6(3):2731–40.
- [170] Thomas HR, Marsden AJ, Walker M, Wilson NR, Rourke JP. Sulfur-functionalized graphene oxide by epoxide ring-opening. *Angew Chem* 2014;126(29):7743–8.
- [171] Yang Z, Yao Z, Li G, Fang G, Nie H, Liu Z, et al. Sulfur-doped graphene as an efficient metal-free cathode catalyst for oxygen reduction. *ACS Nano* 2012;6(1):205–11.
- [172] Collins WR, Lewandowski W, Schmois E, Walsh J, Swager TM. Claisen rearrangement of graphite oxide: a route to covalently functionalized graphenes. *Angew Chem* 2011;123(38):9010–4.
- [173] Lu P, Zhou R, Guo W, Zeng XC. Amide functionalization of graphene and carbon nanotubes: coverage- and pattern-dependent electronic and magnetic properties. *J Phys Chem C* 2012;116(25):13722–30.
- [174] Chua CK, Sofer Z, Pumera M. Functionalization of hydrogenated graphene: transition-metal-catalyzed cross-coupling reactions of allylic C–H bonds. *Angew Chem Int Ed* 2016;55(36):10751–4.
- [175] Wang C, Zhou J, Chu L. Chlorine-functionalized reduced graphene oxide for methylene blue removal. *RSC Adv* 2015;5(65):52466–72.
- [176] Kita Y, Watanabe N, Fujii Y. Chemical composition and crystal structure of graphite fluoride. *J Am Chem Soc* 1979;101(14):3832–41.
- [177] Bourlins AB, Safarova K, Siskova K, Zbořil R. The production of chemically converted graphenes from graphite fluoride. *Carbon* 2012;50(3):1425–8.
- [178] Dubecký M, Otyepková E, Lazar P, Karlický F, Petr M, Čépe K, et al. Reactivity of fluorographene: a facile way toward graphene derivatives. *J Phys Chem Lett* 2015;6(8):1430–4.
- [179] Whitener KE, Stine R, Robinson JT, Sheehan PE. Graphene as electrophile: reactions of graphene fluoride. *J Phys Chem C* 2015;119(19):10507–12.
- [180] Urbanová V, Holá K, Bourlins AB, Čépe K, Ambrosi A, Loo AH, et al. Thiofluorographene-hydrophilic graphene derivative with semiconducting and gene-sensing properties. *Adv Mater* 2015;27(14):2305–10.
- [181] Sturala J, Hermanová S, Artigues L, Sofer Z, Pumera M. Thiographene synthesized from fluorographene via xanthogenate with immobilized enzymes for environmental remediation. *Nanoscale* 2019;11(22):10695–701.
- [182] Ye X, Ma L, Yang Z, Wang J, Wang H, Yang S. Covalent functionalization of fluorinated graphene and subsequent application as water-based lubricant additive. *ACS Appl Mater Interfaces* 2016;8(11):7483–8.
- [183] Stine R, Ciszek JW, Barlow DE, Lee W-K, Robinson JT, Sheehan PE. High-density amine-terminated monolayers formed on fluorinated CVD-grown graphene.

- Langmuir 2012;28(21):7957–61.
- [184] Li B, He T, Wang Z, Cheng Z, Liu Y, Chen T, et al. Chemical reactivity of C-F bonds attached to graphene with diamines depending on their nature and location. *Phys Chem Chem Phys* 2016;18(26):17495–505.
- [185] Bosch-Navarro C, Walker M, Wilson NR, Rourke JP. Covalent modification of exfoliated fluorographite with nitrogen functionalities. *J Mater Chem C* 2015;3(29):7627–31.
- [186] Bakandritsos A, Pykal M, Błoński P, Jakubec P, Chronopoulos DD, Poláková K, et al. Cyanographene and graphene acid: emerging derivatives enabling high-yield and selective functionalization of graphene. *ACS Nano* 2017;11(3):2982–91.
- [187] Lazar P, Chua CK, Holá K, Zbořil R, Otyepka M, Pumera M. Dichlorocarbene-functionalized fluorographene: synthesis and reaction mechanism. *Small* 2015;11(31):3790–6.
- [188] Chronopoulos DD, Bakandritsos A, Lazar P, Pykal M, Čépe K, Zbořil R, et al. High-yield alkylation and arylation of graphene via grignard reaction with fluorographene. *Chem Mater* 2017;29(3):926–30.
- [189] Mazánek V, Libánská A, Šturala J, Bouša D, Sedmidubský D, Pumera M, et al. Fluorographene modified by grignard reagents: a broad range of functional nanomaterials. *Chem Eur J* 2017;23(8):1956–64.
- [190] Chronopoulos DD, Medved M, Błoński P, Nováček Z, Jakubec P, Tomanec O, et al. Alkynylation of graphene: via the Sonogashira C-C cross-coupling reaction on fluorographene. *Chem Commun* 2019;55(8):1088–91.
- [191] Hossain MZ, Razak MBA, Noritake H, Shiozawa Y, Yoshimoto S, Mukai K, et al. Monolayer selective methylation of epitaxial graphene on SiC(0001) through two-step chlorination-alkylation reactions. *J Phys Chem C* 2014;118(38):22096–101.
- [192] Sun X, Li B, Lu M. A covalent modification for graphene by adamantane groups through two-step chlorination-Grignard reactions. *J Solid State Chem* 2017;251:194–7.
- [193] Gao J, Bao F, Zhu Q, Tan Z, Chen T, Cai H, et al. Attaching hexylbenzene and poly(9,9-dihexylfluorene) to brominated graphene via Suzuki coupling reaction. *Polym Chem* 2013;4(5):1672–9.
- [194] Au H, Rubio N, Shaffer MSP. Brominated graphene as a versatile precursor for multifunctional grafting. *Chem Sci* 2018;9(1):209–17.
- [195] Lai S, Jin Y, Sun X, Pan J, Du W, Shi L. Aqueous-based bromination of graphene by electrophilic substitution reaction: a defect-free approach for graphene functionalization. *Res Chem Intermed* 2018;44(5):3523–36.
- [196] Primo A, Sánchez E, Delgado JM, García H. High-yield production of N-doped graphitic platelets by aqueous exfoliation of pyrolyzed chitosan. *Carbon* 2014;68(Suppl. C):777–83.
- [197] Primo A, Atienzar P, Sanchez E, Delgado JM, Garcia H. From biomass wastes to large-area, high-quality, N-doped graphene: catalyst-free carbonization of chitosan coatings on arbitrary substrates. *Chem Commun* 2012;48(74):9254–6.
- [198] Lazar P, Mach R, Otyepka M. Spectroscopic fingerprints of graphitic, pyrrolic, pyridinic, and chemisorbed nitrogen in N-doped graphene. *J Phys Chem C* 2019;123(16):10695–702.
- [199] Barrejón M, Primo A, Gómez-Escalonilla MJ, Fierro JLG, García H, Langa F. Covalent functionalization of N-doped graphene by N-alkylation. *Chem Commun* 2015;51(95):16916–9.
- [200] Kim M-J, Jeon I-Y, Seo J-M, Dai L, Baek J-B. Graphene phosphonic acid as an efficient flame retardant. *ACS Nano* 2014;8(3):2820–5.
- [201] Some S, Shackery I, Kim SJ, Jun SC. Phosphorus-doped graphene oxide layer as a highly efficient flame retardant. *Chem Eur J* 2015;21(44):15480–5.
- [202] Faezhi-Alamdari R, Haqiqi MG, Zekri N. Immobilized Pd(0) nanoparticles on phosphine-functionalized graphene as a highly active catalyst for Heck, Suzuki and N-arylation reactions. *New J Chem* 2016;40(2):1287–96.
- [203] Poh HL, Sofer Z, Šimek P, Tomandl I, Pumera M. Hydroboration of graphene oxide: towards stoichiometric graphol and hydroxygraphane. *Chem Eur J* 2015;21(22):8130–6.
- [204] Liu J, Ye Y, Xue Y, Xie X, Mai Y-W. Recent advances in covalent functionalization of carbon nanomaterials with polymers: strategies and perspectives. *J Polym Sci Part A: Polym Chem* 2017;55(4):622–31.
- [205] Salavagione HJ, Martínez G, Ellis G. Recent advances in the covalent modification of graphene with polymers. *Macromol Rapid Commun* 2011;32(22):1771–89.
- [206] Remyamol T, John H, Gopinath P. Synthesis and nonlinear optical properties of reduced graphene oxide covalently functionalized with polyaniline. *Carbon* 2013;59:308–14.
- [207] Xiong S, Li Z, Gong M, Wang X, Fu J, Shi Y, et al. Covalently bonded polyaniline and para-phenylenediamine functionalized graphene oxide: how the conductive two-dimensional nanostructure influences the electrochromic behaviors of polyaniline. *Electrochim Acta* 2014;138:101–8.
- [208] Pham TA, Kim JS, Kim D, Jeong YT. Facile preparation of water-dispersible graphene nanosheets by covalent functionalization with poly(3-aminobenzene sulfonic acid). *Polym Eng Sci* 2012;52(9):1854–61.
- [209] Ding P, Su S, Song N, Tang S, Liu Y, Shi L. Highly thermal conductive composites with polyamide-6 covalently-grafted graphene by an in situ polymerization and thermal reduction process. *Carbon* 2014;66:576–84.
- [210] Abdullah N, Hatano K, Ando D, Kubo M, Koshio A, Kokai F. Solubilization of graphene flakes through covalent modification with well-defined azido-terminated poly(ϵ -caprolactone). *J Appl Polym Sci* 2015;132(9).
- [211] Huang W, Wang S, Guo C, Yang X, Li Y, Tu Y. Synthesis and characterization of well-defined poly(l-lactide) functionalized graphene oxide sheets with high grafting ratio prepared through click chemistry and supramolecular interactions. *Polymer* 2014;55(18):4619–26.
- [212] Zong P, Fu J, Chen L, Yin J, Dong X, Yuan S, et al. Effect of aminopropylisobutyl polyhedral oligomeric silsesquioxane functionalized graphene on the thermal conductivity and electrical insulation properties of epoxy composites. *RSC Adv* 2016;6(13):10498–506.
- [213] Yu B, Shi Y, Yuan B, Liu L, Yang H, Tai Q, et al. Click-chemistry approach for graphene modification: effective reinforcement of UV-curable functionalized graphene/polyurethane acrylate nanocomposites. *RSC Adv* 2015;5(18):13502–6.
- [214] Yuan B, Bao C, Song L, Hong N, Liew KM, Hu Y. Preparation of functionalized graphene oxide/polypropylene nanocomposite with significantly improved thermal stability and studies on the crystallization behavior and mechanical properties. *Chem Eng J* 2014;237:411–20.
- [215] Fang X, Liu X, Cui Z-K, Qian J, Pan J, Li X, et al. Preparation and properties of thermostable well-functionalized graphene oxide/polyimide composite films with high dielectric constant, low dielectric loss and high strength via in situ polymerization. *J Mater Chem A* 2015;3(18):10005–12.
- [216] Li H, Shi L-Y, Cui W, Lei W-W, Zhang Y-L, Diao Y-F, et al. Covalent modification of graphene as a 2D nanofiller for enhanced mechanical performance of poly (glutamate) hybrid gels. *RSC Adv* 2015;5(105):86407–13.
- [217] Cao Y, Lai Z, Feng J, Wu P. Graphene oxide sheets covalently functionalized with block copolymers via click chemistry as reinforcing fillers. *J Mater Chem* 2011;21(25):9271–8.
- [218] Ramasamy MS, Mahapatra SS, Cho JW. Functionalization of graphene with self-doped conducting polypyrrole by click coupling. *J Colloid Interface Sci* 2015;455:63–70.
- [219] Roghani-Mamaqani H. Surface-initiated ATRP of styrene from epoxy groups of graphene nanolayers: twofold polystyrene chains and various graft densities. *RSC Adv* 2015;5(66):53357–68.
- [220] Liu Z, Zhu S, Li Y, Li Y, Shi P, Huang Z, Huang X. Preparation of graphene/poly(2-hydroxyethyl acrylate) nanohybrid materials via an ambient temperature “grafting-from” strategy. *Polym Chem* 2015;6(2):311–21.
- [221] Yang Y, He C-E, Tang W, Tsui CP, Shi D, Sun Z, et al. Judicious selection of bifunctional molecules to chemically modify graphene for improving nano-mechanical and thermal properties of polymer composites. *J Mater Chem A* 2014;2(47):20038–47.
- [222] Ramezanzadeh B, Ghasemi E, Mahdavian M, Changizi E, Mohamadzadeh Moghadam MH. Covalently-grafted graphene oxide nanosheets to improve barrier and corrosion protection properties of polyurethane coatings. *Carbon* 2015;93:555–73.
- [223] Han S, Chun BC. Preparation of polyurethane nanocomposites via covalent incorporation of functionalized graphene and its shape memory effect. *Compos A Appl Sci Manuf* 2014;58:65–72.
- [224] Qian X, Song L, Yu B, Yang W, Wang B, Hu Y, et al. One-pot surface functionalization and reduction of graphene oxide with long-chain molecules: Preparation and its enhancement on the thermal and mechanical properties of polyurea. *Chem Eng J* 2014;236:233–41.
- [225] Zhang B, Chen Y, Zhuang X, Liu G, Yu B, Kang E-T, et al. Poly(N-vinylcarbazole) chemically modified graphene oxide. *J Polym Sci, Part A: Polym Chem* 2010;48(12):2642–9.
- [226] Shen B, Zhai W, Tao M, Lu D, Zheng W. Chemical functionalization of graphene oxide toward the tailoring of the interface in polymer composites. *Compos Sci*

- Technol 2013;77:87–94.
- [227] Wan Y-J, Yang W-H, Yu S-H, Sun R, Wong C-P, Liao W-H. Covalent polymer functionalization of graphene for improved dielectric properties and thermal stability of epoxy composites. *Compos Sci Technol* 2016;122:27–35.
- [228] Wan Y-J, Tang L-C, Gong L-X, Yan D, Li Y-B, Wu L-B, et al. Grafting of epoxy chains onto graphene oxide for epoxy composites with improved mechanical and thermal properties. *Carbon* 2014;69:467–80.
- [229] Yousefi N, Lin X, Zheng Q, Shen X, Pothenis JR, Jia J, et al. Simultaneous in situ reduction, self-alignment and covalent bonding in graphene oxide/epoxy composites. *Carbon* 2013;59:406–17.
- [230] Ma J, Meng Q, Michelmora A, Kawashima N, Izzuddin Z, Bengtsson C, et al. Covalently bonded interfaces for polymer/graphene composites. *J Mater Chem A* 2013;1(13):4255–64.
- [231] Guan L-Z, Wan Y-J, Gong L-X, Yan D, Tang L-C, Wu L-B, et al. Toward effective and tunable interphases in graphene oxide/epoxy composites by grafting different chain lengths of polyetheramine onto graphene oxide. *J Mater Chem A* 2014;2(36):15058–69.
- [232] Wan Y-J, Gong L-X, Tang L-C, Wu L-B, Jiang J-X. Mechanical properties of epoxy composites filled with silane-functionalized graphene oxide. *Compos A Appl Sci Manuf* 2014;64:79–89.
- [233] Sun S, Wu P. A one-step strategy for thermal- and pH-responsive graphene oxide interpenetrating polymer hydrogel networks. *J Mater Chem* 2011;21(12):4095–7.
- [234] Li H, Liu L, Yang F. Covalent assembly of 3D graphene/polypyrrole foams for oil spill cleanup. *J Mater Chem A* 2013;1(10):3446–53.
- [235] Ho K-K, Hsiao M-C, Chou T-Y, Ma C-CM, Xie X-F, Chiang J-C, et al. Preparation and characterization of covalently functionalized graphene using vinyl-terminated benzoxazine monomer and associated nanocomposites with low coefficient of thermal expansion. *Polym Int* 2013;62(6):966–73.
- [236] Bekyarova EB, Niyogi S, Sarkar S, Tian X, Chen M, Moser ML, et al. Stereochemical effect of covalent chemistry on the electronic structure and properties of the carbon allotropes and graphene surfaces. *Synth Met* 2015;210:80–4.
- [237] Bekyarova E, Sarkar S, Wang F, Itkis ME, Kalinina I, Tian X, et al. Effect of covalent chemistry on the electronic structure and properties of carbon nanotubes and graphene. *Acc Chem Res* 2013;46(1):65–76.
- [238] Dreyer DR, Park S, Bielawski CW, Ruoff RS. The chemistry of graphene oxide. *Chem Soc Rev* 2010;39(1):228–40.
- [239] Stoller MD, Park S, Zhu Y, An J, Ruoff RS. Graphene-based ultracapacitors. *Nano Lett* 2008;8(10):3498–502.
- [240] Xia F, Mueller T, Lin Y-M, Valdes-Garcia A, Avouris P. Ultrafast graphene photodetector. *Nat Nanotechnol* 2009;4:839.
- [241] Wang X, Zhi L, Müllen K. Transparent, conductive graphene electrodes for dye-sensitized solar cells. *Nano Lett* 2008;8(1):323–7.
- [242] Wu J, Agrawal M, Becerril HA, Bao Z, Liu Z, Chen Y, et al. Organic light-emitting diodes on solution-processed graphene transparent electrodes. *ACS Nano* 2010;4(1):43–8.
- [243] Zhang S, Li Y, Song H, Chen X, Zhou J, Hong S, et al. Graphene quantum dots as the electrolyte for solid state supercapacitors. *Sci Rep* 2016;6:19292.
- [244] Wang H, Hu YH. Graphene as a counter electrode material for dye-sensitized solar cells. *Energy Environ Sci* 2012;5(8):8182–8.
- [245] Echtermeyer TJ, Britnell L, Jasnok PK, Lombardo A, Gorbachev RV, Grigorenko AN, et al. Strong plasmonic enhancement of photovoltage in graphene. *Nat Commun* 2011;2:458.
- [246] Konstantatos G, Badioli M, Gaudreau L, Osmond J, Bernechea M, de Arquer FPG, et al. Hybrid graphene–quantum dot phototransistors with ultrahigh gain. *Nat Nanotech* 2012;7:363.
- [247] Hasan T, Torrisi F, Sun Z, Popa D, Nicolosi V, Privitera G, et al. Solution-phase exfoliation of graphite for ultrafast photonics. *Phys Status Solidi (b)* 2010;247(11–12):2953–7.
- [248] Sun Z, Hasan T, Torrisi F, Popa D, Privitera G, Wang F, et al. Graphene mode-locked ultrafast laser. *ACS Nano* 2010;4(2):803–10.
- [249] Sarkar S, Zhang H, Huang JW, Wang F, Bekyarova E, Lau CN, et al. Organometallic hexahapto functionalization of single layer graphene as a route to high mobility graphene devices. *Adv Mater* 2013;25(8):1131–6.
- [250] Chen M, Tian X, Li W, Bekyarova E, Li G, Moser M, et al. Application of organometallic chemistry to the electrical interconnection of graphene nanoplatelets. *Chem Mater* 2016;28(7):2260–6.
- [251] Song S, Xue Y, Feng L, Elbatal H, Wang P, Moorefield CN, et al. Reversible self-assembly of terpyridine-functionalized graphene oxide for energy conversion. *Angew Chem Int Ed* 2014;53(5):1415–9.
- [252] Ho K-L, Huang C-H, Liao J-H, Zhang W, Li L-J, Lai C-S, et al. Fluorinated graphene as high performance dielectric materials and the applications for graphene nanoelectronics. *Sci Rep* 2014;4:5893.
- [253] Liu Y, Zhou J, Zhang X, Liu Z, Wan X, Tian J, et al. Synthesis, characterization and optical limiting property of covalently oligothiophene-functionalized graphene material. *Carbon* 2009;47(13):3113–21.
- [254] Xu Y, Liu Z, Zhang X, Wang Y, Tian J, Huang Y, et al. Graphene hybrid material covalently functionalized with porphyrin: synthesis and optical limiting property. *Adv Mater* 2009;21(12):1275–9.
- [255] Yamuna R, Ramakrishnan S, Dhara K, Devi R, Kothurkar NK, Kirubha E, et al. Synthesis, characterization, and nonlinear optical properties of graphene oxide functionalized with tetra-amino porphyrin. *J Nanopart Res* 2013;15(1):1399.
- [256] Bala Murali Krishna M, Venkatramaiah N, Venkatesan R, Narayana Rao D. Synthesis and structural, spectroscopic and nonlinear optical measurements of graphene oxide and its composites with metal and metal free porphyrins. *J Mater Chem* 2012;22(7):3059–68.
- [257] Wang A, Yu W, Xiao Z, Song Y, Long L, Cifuentes MP, et al. A 1,3-dipolar cycloaddition protocol to porphyrin-functionalized reduced graphene oxide with a push-pull motif. *Nano Res* 2015;8(3):870–86.
- [258] Wang A, Yu W, Huang Z, Zhou F, Song J, Song Y, et al. Covalent functionalization of reduced graphene oxide with porphyrin by means of diazonium chemistry for nonlinear optical performance. *Sci Rep* 2016;6:23325.
- [259] Zhao X, Yan X-Q, Ma Q, Yao J, Zhang X-L, Liu Z-B, et al. Nonlinear optical and optical limiting properties of graphene hybrids covalently functionalized by phthalocyanine. *Chem Phys Lett* 2013;577:62–7.
- [260] Zhu J, Li Y, Chen Y, Wang J, Zhang B, Zhang J, et al. Graphene oxide covalently functionalized with zinc phthalocyanine for broadband optical limiting. *Carbon* 2011;49(6):1900–5.
- [261] Li Z, He C, Wang Z, Gao Y, Dong Y, Zhao C, et al. Ethylenediamine-modified graphene oxide covalently functionalized with a tetracarboxylic Zn(II) phthalocyanine hybrid for enhanced nonlinear optical properties. *Photochem Photobiol Sci* 2016;15(7):910–9.
- [262] Song W, He C, Dong Y, Zhang W, Gao Y, Wu Y, et al. The effects of central metals on the photophysical and nonlinear optical properties of reduced graphene oxide–metal(II) phthalocyanine hybrids. *Phys Chem Chem Phys* 2015;17(11):7149–57.
- [263] Bai T, Li C-Q, Sun J, Song Y, Wang J, Blau WJ, et al. Covalent modification of graphene oxide with carbazole groups for laser protection. *Chem Eur J* 2015;21(12):4622–7.
- [264] Cao Y, Dong S, Liu S, He L, Gan L, Yu X, et al. Building high-throughput molecular junctions using indented graphene point contacts. *Angew Chem Int Ed* 2012;51(49):12228–32.
- [265] Jia C, Migliore A, Xin N, Huang S, Wang J, Yang Q, et al. Covalently bonded single-molecule junctions with stable and reversible photoswitched conductivity. *Science* 2016;352(6292):1443.
- [266] Jia C, Wang J, Yao C, Cao Y, Zhong Y, Liu Z, et al. Conductance switching and mechanisms in single-molecule junctions. *Angew Chem Int Ed* 2013;52(33):8666–70.
- [267] Xu Q, Scuri G, Mathewson C, Kim P, Nuckolls C, Bouilly D. Single electron transistor with single aromatic ring molecule covalently connected to graphene nanogaps. *Nano Lett* 2017;17(9):5335–41.
- [268] Sun H, Jiang Z, Xin N, Guo X, Hou S, Liao J. Efficient fabrication of stable graphene-molecule-graphene single-molecule junctions at room temperature. *ChemPhysChem* 2018;19(17):2258–65.
- [269] Xin N, Li X, Jia C, Gong Y, Li M, Wang S, et al. Tuning charge transport in aromatic-ring single-molecule junctions via ionic-liquid gating. *Angew Chem Int Ed* 2018;57(43):14026–31.
- [270] Cao Y, Dong S, Liu S, Liu Z, Guo X. Toward functional molecular devices based on graphene-molecule junctions. *Angew Chem Int Ed* 2013;52(14):3906–10.
- [271] Xia CJ, Ye M, Zhang BQ, Su YH, Tu ZY. Switching behaviors of butadienimine molecular devices sandwiched between graphene nanoribbons electrodes. *Jpn J Appl Phys* 2017;56(10).
- [272] Royo M, Antidormi A, Rurall RA. Thermal switch for coherent phonons based on a molecular junction. *J Phys Chem C* 2017;121(19):10571–6.

- [273] Cao L, Li X, Liu G, Liu Z, Zhou G. The spin-charge transport properties for a graphene-based molecular junction: a first-principles study. *Org Electron* 2017;48:357–64.
- [274] Sadeghi H, Sangtarash S, Lambert C. Robust molecular anchoring to graphene electrodes. *Nano Lett* 2017;17(8):4611–8.
- [275] Wang Z-Q, Wei M-Z, Dong M-M, Hu G-C, Li Z-L, Wang C-K, et al. High-performance single-molecule switch designed by changing parity of electronic wave functions via intramolecular proton transfer. *J Phys Chem C* 2018;122(31):17650–9.
- [276] Li J, Merino-Díez N, Carbonell-Sanromà E, Vilas-Varela M, de Oteyza DG, Peña D, et al. Survival of spin state in magnetic porphyrins contacted by graphene nanoribbons. *Sci Adv* 2018;4(2):eaq0582.
- [277] Devi R, Prabhavathi G, Yamuna R, Ramakrishnan S, Kothurkar NK. Synthesis, characterization and photoluminescence properties of graphene oxide functionalized with azo molecules. *J Chem Sci* 2014;126(1):75–83.
- [278] Feng Y, Liu H, Luo W, Liu E, Zhao N, Yoshino K, et al. Covalent functionalization of graphene by azobenzene with molecular hydrogen bonds for long-term solar thermal storage. *Sci Rep* 2013;3:3260.
- [279] Lee JH, Jaworski J, Jung JH. Luminescent metal–organic framework-functionalized graphene oxide nanocomposites and the reversible detection of high explosives. *Nanoscale* 2013;5(18):8533–40.
- [280] Wang D, Ye G, Wang X, Wang X. Graphene functionalized with azo polymer brushes: surface-initiated polymerization and photoresponsive properties. *Adv Mater* 2011;23(9):1122–5.
- [281] Seo S, Min M, Lee SM, Lee H. Photo-switchable molecular monolayer anchored between highly transparent and flexible graphene electrodes. *Nat Commun* 2013;4:1920.
- [282] Min M, Seo S, Lee SM, Lee H. Voltage-controlled nonvolatile molecular memory of an azobenzene monolayer through solution-processed reduced graphene oxide contacts. *Adv Mater* 2013;25(48):7045–50.
- [283] Zhang X, Feng Y, Lv P, Shen Y, Feng W. Enhanced reversible photoswitching of azobenzene-functionalized graphene oxide hybrids. *Langmuir* 2010;26(23):18508–11.
- [284] Yan H, Zhu L, Li X, Kwok A, Pan X, Zhao Y. A photoswitchable [2]rotaxane array on graphene oxide. *Asian J Org Chem* 2012;1(4):314–8.
- [285] Nguyen P, Li J, Sreepasad TS, Jasuja K, Mohanty N, Ikenberry M, et al. Covalent functionalization of dipole-modulating molecules on trilayer graphene: an avenue for graphene-interfaced molecular machines. *Small* 2013;9(22):3823–8.
- [286] Kim H-J, Sung J, Chung H, Choi YJ, Kim DY, Kim D. Covalently functionalized graphene composites: mechanistic study of interfacial fluorescence quenching and recovery processes. *J Phys Chem C* 2015;119(21):11327–36.
- [287] Green MA, Keevers MJ. Optical properties of intrinsic silicon at 300 K. *Prog Photovolt Res Appl* 1995;3(3):189–92.
- [288] Li S-S, Tu K-H, Lin C-C, Chen C-W, Chhowalla M. Solution-processable graphene oxide as an efficient hole transport layer in polymer solar cells. *ACS Nano* 2010;4(6):3169–74.
- [289] Kymakis E, Savva K, Stylianakis MM, Fotakis C, Stratakis E. Flexible organic photovoltaic cells with in situ nonthermal photoreduction of spin-coated graphene oxide electrodes. *Adv Funct Mater* 2013;23(21):2742–9.
- [290] Deetuan C, Samthong C, Thongyai S, Prasertdam P, Somwangthanaroj A. Synthesis of well dispersed graphene in conjugated poly(3,4-ethylenedioxythiophene):polystyrene sulfonate via click chemistry. *Compos Sci Technol* 2014;93:1–8.
- [291] Roy-Mayhew JD, Bozym DJ, Punckt C, Aksay IA. Functionalized graphene as a catalytic counter electrode in dye-sensitized solar cells. *ACS Nano* 2010;4(10):6203–11.
- [292] Xu C, Li J, Wang X, Wang J, Wan L, Li Y, et al. Synthesis of hemin functionalized graphene and its application as a counter electrode in dye-sensitized solar cells. *Mater Chem Phys* 2012;132(2):858–64.
- [293] Bonaccorso F, Balis N, Stylianakis MM, Savarese M, Adamo C, Gemmi M, et al. Functionalized graphene as an electron-cascade acceptor for air-processed organic ternary solar cells. *Adv Funct Mater* 2015;25(25):3870–80.
- [294] Tang J, Niu L, Liu J, Wang Y, Huang Z, Xie S, et al. Effect of photocurrent enhancement in porphyrin–graphene covalent hybrids. *Mater Sci Eng, C* 2014;34:186–92.
- [295] Stylianakis MM, Konios D, Kakavelakis G, Charalambidis G, Stratakis E, Coutsolelos AG, et al. Efficient ternary organic photovoltaics incorporating a graphene-based porphyrin molecule as a universal electron cascade material. *Nanoscale* 2015;7(42):17827–35.
- [296] Yu D, Yang Y, Durstok M, Baek J-B, Dai L. Soluble P3HT-grafted graphene for efficient bilayer–heterojunction photovoltaic devices. *ACS Nano* 2010;4(10):5633–40.
- [297] He J, Bao F, Yan S, Weng F, Ma R, Liu Y, et al. Soluble fluorene–benzothiadiazole polymer-grafted graphene for photovoltaic devices. *RSC Adv* 2017;7(57):35950–6.
- [298] Karousis N, Ortiz J, Ohkubo K, Hasobe T, Fukuzumi S, Sastre-Santos Á, et al. Zinc phthalocyanine-graphene hybrid material for energy conversion: synthesis, characterization, photophysics, and photoelectrochemical cell preparation. *J Phys Chem C* 2012;116(38):20564–73.
- [299] Kumar P, Singh G, Tripathi D, Jain SL. Visible light driven photocatalytic oxidation of thiols to disulfides using iron phthalocyanine immobilized on graphene oxide as a catalyst under alkali free conditions. *RSC Adv* 2014;4(92):50331–7.
- [300] Karousis N, Sandanayaka ASD, Hasobe T, Economopoulos SP, Sarantopoulou E, Tagmatarchis N. Graphene oxide with covalently linked porphyrin antennae: synthesis, characterization and photophysical properties. *J Mater Chem* 2011;21(1):109–17.
- [301] Umeyama T, Mihara J, Tezuka N, Matano Y, Stranius K, Chukharev V, et al. Preparation and photophysical and photoelectrochemical properties of a covalently fixed porphyrin-chemically converted graphene composite. *Chem Eur J* 2012;18(14):4250–7.
- [302] Kong C, Zhang G, Li Y, Li D-W, Long Y-T. Plasmon-enhanced photocurrent monitoring of the interaction between porphyrin covalently bonded to graphene oxide and adenosine nucleotides. *RSC Adv* 2013;3(11):3503–7.
- [303] Karousis N, Economopoulos SP, Sarantopoulou E, Tagmatarchis N. Porphyrin counter anion in imidazolium-modified graphene-oxide. *Carbon* 2010;48(3):854–60.
- [304] Zhang X, Hou L, Cnossen A, Coleman AC, Ivashenko O, Rudolf P, et al. One-pot functionalization of graphene with porphyrin through cycloaddition reactions. *Chem Eur J* 2011;17(32):8957–64.
- [305] Matte HSSR, Jain A, George SJ. A covalently linked graphene-oligo(phenylenevinylene) adduct: self-organization and photo-physical properties. *RSC Adv* 2012;2(15):6290–4.
- [306] Ragoussi M-E, Katsukis G, Roth A, Malig J, de la Torre G, Guldi DM, et al. Electron-donating behavior of few-layer graphene in covalent ensembles with electron-accepting phthalocyanines. *J Am Chem Soc* 2014;136(12):4593–8.
- [307] Ragoussi M-E, Malig J, Katsukis G, Butz B, Spiecker E, de la Torre G, et al. Linking photo- and redoxactive phthalocyanines covalently to graphene. *Angew Chem Int Ed* 2012;51(26):6421–5.
- [308] Wang Z, Wei R, Liu X. Preparation and dielectric properties of copper phthalocyanine/graphene oxide nanohybrids via in situ polymerization. *J Mater Sci* 2016;51(9):1–9.
- [309] Jung CY, Yao W, Park JM, Hyun IH, Seong DH, Jaung JY. Synthesis of A3B zinc tetrapyrrolineporphyrin covalently functionalized reduced graphene oxide. *Tetrahedron Lett* 2015;56(49):6915–8.
- [310] Stergiou A, Tagmatarchis N. Fluorene-erylene diimide arrays onto graphene sheets for photocatalysis. *ACS Appl Mater Interfaces* 2016;8(33):21576–84.
- [311] Yao Y, Gao J, Bao F, Jiang S, Zhang X, Ma R. Covalent functionalization of graphene with polythiophene through a Suzuki coupling reaction. *RSC Adv* 2015;5(53):42754–61.
- [312] Castelaín M, Martínez G, Merino P, Martín-Gago JÁ, Segura JL, Ellis G, et al. Graphene functionalisation with a conjugated poly(fluorene) by click coupling: striking electronic properties in solution. *Chem Eur J* 2012;18(16):4965–73.
- [313] Sun S, Zhuang X, Liu B, Wang L, Gu L, Song S, et al. In situ synthesis and characterization of poly(aryleneethynylene)-grafted reduced graphene oxide. *Chem Eur J* 2016;22(7):2247–52.
- [314] Barrejon M, Vizueté M, Gomez-Escalonilla MJ, Fierro JLG, Berlanga I, Zamora F, et al. A photoresponsive graphene oxide-C60 conjugate. *Chem Commun* 2014;50(65):9053–5.
- [315] Das SK, Kc CB, Ohkubo K, Yamada Y, Fukuzumi S, D'Souza F. Decorating single layer graphene oxide with electron donor and acceptor molecules for the study of photoinduced electron transfer. *Chem Commun* 2013;49(20):2013–5.
- [316] Economopoulos SP, Karousis N, Rotas G, Pagona G, Tagmatarchis N. Microwave-assisted functionalization of carbon nanostructured materials. *Curr Org Chem*

- 2011;15(8):1121–32.
- [317] Barrejón M, Arellano LM, Gobeze HB, Gómez-Escalonilla MJ, Fierro JLG, D'Souza F, et al. N-doped graphene/C60 covalent hybrid as a new material for energy harvesting applications. *Chem Sci* 2018;9(43):8221–7.
- [318] Tangorra RR, Antonucci A, Milano F, Operamolla A, Italiano F, Ragni R, et al. In photoactive film by covalent immobilization of a bacterial photosynthetic protein on reduced graphene oxide surface. *Mater Res Soc Symp Proc* 2015:12–8.
- [319] Li Z, Zhang W, Zhao Q, Gu H, Li Y, Zhang G, et al. Covalently anchored on reduced graphene oxide as an efficient and recyclable photocatalyst for the aerobic oxidation of α -aryl halogen derivatives. *ACS Sustain Chem Eng* 2015;3(3):468–74.
- [320] Li W, Liang J, Yang W, Deng J. Chiral functionalization of graphene oxide by optically active helical-substituted polyacetylene chains and its application in enantioselective crystallization. *ACS Appl Mater Interfaces* 2014;6(12):9790–8.
- [321] Ballesteros-Garrido R, Rodríguez R, Álvaro M, García H. Photochemistry of covalently functionalized graphene oxide with phenothiazinyl units. *Carbon* 2014;74:113–9.
- [322] Ballesteros-Garrido R, de Miguel M, Doménech-Carbó A, Alvaro M, García H. Tunability by alkali metal cations of photoinduced charge separation in azacrown functionalized graphene. *Chem Commun* 2013;49(31):3236–8.
- [323] Zhao C, Feng L, Xu B, Ren J, Qu X. Synthesis and characterization of red-luminescent graphene oxide functionalized with silica-coated Eu³⁺ complex nanoparticles. *Chem Eur J* 2011;17(25):7007–12.
- [324] Yang H, Shan C, Li F, Han D, Zhang Q, Niu L. Covalent functionalization of polydisperse chemically-converted graphene sheets with amine-terminated ionic liquid. *Chem Commun* 2009;26:3880–2.
- [325] Blanco M, Álvarez P, Blanco C, Jiménez MV, Fernández-Tornos J, Pérez-Torrente JJ, et al. Graphene–NHC–iridium hybrid catalysts built through –OH covalent linkage. *Carbon* 2015;83:21–31.
- [326] Park JH, Raza F, Jeon S-J, Kim H-I, Kang TW, Yim D, et al. Recyclable N-heterocyclic carbene/palladium catalyst on graphene oxide for the aqueous-phase Suzuki reaction. *Tetrahedron Lett* 2014;55(23):3426–30.
- [327] Mallakpour S, Abdolmaleki A, Borandeh S. Covalently functionalized graphene sheets with biocompatible natural amino acids. *Appl Surf Sci* 2014;307:533–42.
- [328] Konkena B, Vasudevan S. Covalently linked, water-dispersible, cyclodextrin-reduced-graphene oxide sheets. *Langmuir* 2012;28(34):12432–7.
- [329] Namvari M, Namazi H. Sweet graphene I: toward hydrophilic graphene nanosheets via click grafting alkyne-saccharides onto azide-functionalized graphene oxide. *Carbohydr Res* 2014;396:1–8.
- [330] Shan C, Yang H, Han D, Zhang Q, Ivaska A, Niu L. Water-soluble graphene covalently functionalized by biocompatible poly-L-lysine. *Langmuir* 2009;25(20):12030–3.
- [331] Qiao S-J, Xu X-N, Qiu Y, Xiao H-C, Zhu Y-F. Simultaneous reduction and functionalization of graphene oxide by 4-hydrazinobenzenesulfonic acid for polymer nanocomposites. *Nanomaterials* 2016;6(2).
- [332] Wang Z, Wang J, Li Z, Gong P, Ren J, Wang H, et al. Cooperatively exfoliated fluorinated graphene with full-color emission. *RSC Adv* 2012;2(31):11681–6.
- [333] Tan SM, Poh HL, Sofer Z, Pumera M. Boron-doped graphene and boron-doped diamond electrodes: detection of biomarkers and resistance to fouling. *Analyst* 2013;138(17):4885–91.
- [334] Wu S, Guo H, Wang L, Xin Y, Cheng Y, Fan W. An ultrasensitive electrochemical biosensing platform for fructose and xylitol based on boronic acid-diol recognition. *Sens Actuators, B* 2017;245:11–7.
- [335] Zhou Y, Dong H, Liu L, Liu J, Xu M. A novel potentiometric sensor based on a poly(anilineboronic acid)/graphene modified electrode for probing sialic acid through boronic acid-diol recognition. *Biosens Bioelectron* 2014;60:231–6.
- [336] Luo J, Huang J, Cong J, Wei W, Liu X. Double recognition and selective extraction of glycoprotein based on the molecular imprinted graphene oxide and boronate affinity. *ACS Appl Mater Interfaces* 2017;9(8):7735–44.
- [337] Cheng R, Liu Y, Ou S, Pan Y, Zhang S, Chen H, et al. Optical turn-on sensor based on graphene oxide for selective detection of d-glucosamine. *Anal Chem* 2012;84(13):5641–4.
- [338] Loo AH, Bonanni A, Pumera M. Biorecognition on graphene: physical, covalent, and affinity immobilization methods exhibiting dramatic. *Differences Chem – Asian J* 2013;8(1):198–203.
- [339] Qu Y, Ma M, Wang Z, Zhan G, Li B, Wang X, et al. Sensitive amperometric biosensor for phenolic compounds based on graphene–silk peptide/tyrosinase composite nanointerface. *Biosens Bioelectron* 2013;44:85–8.
- [340] Zhang H, Li ZF, Snyder A, Xie J, Stanciu LA. Functionalized graphene oxide for the fabrication of paraoxon biosensors. *Anal Chim Acta* 2014;827:86–94.
- [341] Wang J, Cheng M, Zhang Z, Guo L, Liu Q, Jiang G. An antibody-graphene oxide nanoribbon conjugate as a surface enhanced laser desorption/ionization probe with high sensitivity and selectivity. *Chem Commun* 2015;51(22):4619–22.
- [342] Turner APF. Biosensors sense and sensibility. *Chem Soc Rev* 2013;42(8):3184–96.
- [343] Ferri CP, Prince M, Brayne C, Brodaty H, Fratiglioni L, Ganguli M, et al. Global prevalence of dementia: a Delphi consensus study. *The Lancet* 366(9503):2112–7.
- [344] Quintana M, Montellano A, del Rio Castillo AE, Tendeloo GV, Bittencourt C, Prato M. Selective organic functionalization of graphene bulk or graphene edges. *Chem Commun* 2011;47(33):9330–2.
- [345] Rao Vusa CS, Manju V, Berchmans S, Arumugam P. Electrochemical amination of graphene using nanosized PAMAM dendrimers for sensing applications. *RSC Adv* 2016;6(40):33409–18.
- [346] Elshafey R, Sijaj M, Tavares AC. Au nanoparticle decorated graphene nanosheets for electrochemical immunosensing of p53 antibodies for cancer prognosis. *Analyst* 2016;141(9):2733–40.
- [347] Sunday EC, Masikini M, Wilson L, Rassie C, Waryo T, Baker GP, et al. Application on gold nanoparticles-dotted 4-nitrophenylazo graphene in a label-free impedimetric deoxyribose. *Immunosensor Sensors* 2015;15(2).
- [348] Guerrero S, Martínez-García G, Serafín V, Agüí L, Yáñez-Sedeño P, Pingarrón JM. Electrochemical immunosensor for sensitive determination of the oncofetal protein YY at grafted reduced graphene oxide electrode platforms. *Analyst* 2015;140(22):7527–33.
- [349] Gupta VK, Yola ML, Atar N, Ustundağ Z, Solak AO. A novel sensitive Cu(II) and Cd(II) nanosensor platform: Graphene oxide terminated p-aminophenyl modified glassy carbon surface. *Electrochim Acta* 2013;112:541–8.
- [350] Manna B, Retna Raj C. Covalent functionalization and electrochemical tuning of reduced graphene oxide for the bioelectrocatalytic sensing of serum lactate. *J Mater Chem B* 2016;4(26):4585–93.
- [351] Gómez-Anquela C, Revenga-Parra M, Abad JM, Marín AG, Pau JL, Pariente F, et al. Electrografting of N', N'-dimethylphenothiazin-5-ium-3,7-diamine (Azure A) diazonium salt forming electrocatalytic organic films on gold or graphene oxide gold hybrid electrodes. *Electrochim Acta* 2014;116:59–68.
- [352] Liu D, Song N, Feng W, Jia Q. Synthesis of graphene oxide functionalized surface-imprinted polymer for the preconcentration of tetracycline antibiotics. *RSC Adv* 2016;6(14):11742–8.
- [353] Jung YK, Lee T, Shin E, Kim B-S. Highly tunable aptasensing microarrays with graphene oxide multilayers. *Sci Rep* 2013;3:3367.
- [354] Kim D-J, Park H-C, Sohn IY, Jung J-H, Yoon OJ, Park J-S, et al. Electrical graphene aptasensor for ultra-sensitive detection of anthrax toxin with amplified signal transduction. *Small* 2013;9(19):3352–60.
- [355] Wang Z, Zhang J, Chen P, Zhou X, Yang Y, Wu S, et al. Label-free, electrochemical detection of methicillin-resistant staphylococcus aureus DNA with reduced graphene oxide-modified electrodes. *Biosens Bioelectron* 2011;26(9):3881–6.
- [356] Li M, Zhou X, Ding W, Guo S, Wu N. Fluorescent aptamer-functionalized graphene oxide biosensor for label-free detection of mercury(II). *Biosens Bioelectron* 2013;41:889–93.
- [357] Gan X, Yuan R, Chai Y, Yuan Y, Cao Y, Liao Y, et al. 3,4,9,10-Perylenetetracarboxylic dianhydride functionalized graphene sheet as labels for ultrasensitive electrochemiluminescent detection of thrombin. *Anal Chim Acta* 2012;726:67–72.
- [358] Yuan Y, Gou X, Yuan R, Chai Y, Zhuo Y, Ye X, et al. Graphene-promoted 3,4,9,10-perylenetetracarboxylic acid nanocomposite as redox probe in label-free electrochemical aptasensor. *Biosens Bioelectron* 2011;30(1):123–7.
- [359] Bonanni A, Ambrosi A, Pumera M. Nucleic acid functionalized graphene for biosensing. *Chem Eur J* 2012;18(6):1668–73.
- [360] Feng L, Chen Y, Ren J, Qu X. A graphene functionalized electrochemical aptasensor for selective label-free detection of cancer cells. *Biomaterials* 2011;32(11):2930–7.
- [361] Liu F, Ha HD, Han DJ, Seo TS. Photoluminescent graphene oxide microarray for multiplex heavy metal ion analysis. *Small* 2013;9(20):3410–4.

- [362] Shi Y, Dai H, Sun Y, Hu J, Ni P, Li Z. Fluorescent sensing of cocaine based on a structure switching aptamer, gold nanoparticles and graphene oxide. *Analyst* 2013;138(23):7152–6.
- [363] Xiao Y, Wang Y, Wu M, Ma X, Yang X. Graphene-based lysozyme binding aptamer nanocomposite for label-free and sensitive lysozyme sensing. *J Electroanal Chem* 2013;702:49–55.
- [364] Wang Y, Xiao Y, Ma X, Li N, Yang X. Label-free and sensitive thrombin sensing on a molecularly grafted aptamer on graphene. *Chem Commun* 2012;48(5):738–40.
- [365] Hernández R, Vallés C, Benito AM, Maser WK, Xavier Rius F, Riu J. Graphene-based potentiometric biosensor for the immediate detection of living bacteria. *Biosens Bioelectron* 2014;54:553–7.
- [366] Wang Z, Ge Z, Zheng X, Chen N, Peng C, Fan C, et al. Polyvalent DNA–graphene nanosheets “click” conjugates. *Nanoscale* 2012;4(2):394–9.
- [367] Seo DH, Pineda S, Fang J, Gozukara Y, Yick S, Bendavid A, et al. Single-step ambient-air synthesis of graphene from renewable precursors as electrochemical genosensor. *Nat Commun* 2017;8:14217.
- [368] Taratula O, Patel M, Schumann C, Naleway MA, Pang AJ, He H. Phthalocyanine-loaded graphene nanoplatform for imaging-guided combinatorial photo-therapy. *Int J Nanomed* 2015;10:2347–62.
- [369] Sarkar K, Madras G, Chatterjee K. Dendron conjugation to graphene oxide using click chemistry for efficient gene delivery. *RSC Adv* 2015;5(62):50196–211.
- [370] Liu Z, Robinson JT, Sun X, Dai H. PEGylated nanographene oxide for delivery of water-insoluble cancer drugs. *J Am Chem Soc* 2008;130(33):10876–7.
- [371] Zhang H, Huang R, Cang H, Cai Z, Sun B. Graphene oxide–coumarin derivative conjugate as activatable nanoprobe for intracellular imaging with one- or two-photon excitation. *J Mater Chem B* 2014;2(12):1742–50.
- [372] Jasim DA, Ménard-Moyon C, Bégin D, Bianco A, Kostarelos K. Tissue distribution and urinary excretion of intravenously administered chemically functionalized graphene oxide sheets. *Chem Sci* 2015;6(7):3952–64.
- [373] Nahain A-A, Lee J-E, Jeong JH, Park SY. Photoresponsive fluorescent reduced graphene oxide by spiropyran conjugated hyaluronic acid for in vivo imaging and target delivery. *Biomacromolecules* 2013;14(11):4082–90.
- [374] Sharker SM, Jeong CJ, Kim SM, Lee J-E, Jeong JH, In I, et al. Photo- and pH-tunable multicolor fluorescent nanoparticle-based spiropyran- and BODIPY-conjugated polymer with graphene oxide. *Chem – Asian J* 2014;9(10):2921–7.
- [375] Ghawanmeh AA, Ali GAM, Algarni H, Sarkar SM, Chong KF. Graphene oxide-based hydrogels as a nanocarrier for anticancer drug delivery. *Nano Res* 2019;12(5):973–90.
- [376] Kim H, Namgung R, Singha K, Oh I-K, Kim WJ. Graphene oxide-polyethylenimine nanoconstruct as a gene delivery vector and bioimaging tool. *Bioconjugate Chem* 2011;22(12):2558–67.
- [377] Chen B, Liu M, Zhang L, Huang J, Yao J, Zhang Z. Polyethylenimine-functionalized graphene oxide as an efficient gene delivery vector. *J Mater Chem* 2011;21(21):7736–41.
- [378] Yan L, Chang Y-N, Zhao L, Gu Z, Liu X, Tian G, et al. The use of polyethylenimine-modified graphene oxide as a nanocarrier for transferring hydrophobic nanocrystals into water to produce water-dispersible hybrids for use in drug delivery. *Carbon* 2013;57:120–9.
- [379] Wei G, Yan M, Dong R, Wang D, Zhou X, Chen J, et al. Covalent modification of reduced graphene oxide by means of diazonium chemistry and use as a drug-delivery system. *Chem Eur J* 2012;18(46):14708–16.
- [380] Kavitha T, Kang I-K, Park S-Y. Poly(N-vinyl caprolactam) grown on nanographene oxide as an effective nanocargo for drug delivery. *Colloids Surf, B* 2014;115:37–45.
- [381] Chen J, Liu H, Zhao C, Qin G, Xi G, Li T, et al. One-step reduction and PEGylation of graphene oxide for photothermally controlled drug delivery. *Biomaterials* 2014;35(18):4986–95.
- [382] Liu G, Shen H, Mao J, Zhang L, Jiang Z, Sun T, et al. Transferrin modified graphene oxide for glioma-targeted drug delivery. In vitro and in vivo evaluations. *ACS Appl Mater Interfaces* 2013;5(15):6909–14.
- [383] Kim H, Lee D, Kim J, Kim T-I, Kim WJ. Photothermally triggered cytosolic drug delivery via endosome disruption using a functionalized reduced graphene oxide. *ACS Nano* 2013;7(8):6735–46.
- [384] Bao H, Pan Y, Ping Y, Sahoo NG, Wu T, Li L, et al. Chitosan-functionalized graphene oxide as a nanocarrier for drug and gene delivery. *Small* 2011;7(11):1569–78.
- [385] Wang C, Mallela J, Garapati US, Ravi S, Chinnasamy V, Girard Y, et al. A chitosan-modified graphene nanogel for noninvasive controlled drug release. *Nanomed Nanotechnol Biol Med* 2013;9(7):903–11.
- [386] Wang C, Ravi S, Garapati US, Das M, Howell M, Mallela J, et al. Multifunctional chitosan magnetic-graphene (CMG) nanoparticles: a theranostic platform for tumor-targeted co-delivery of drugs, genes and MRI contrast agents. *J Mater Chem B* 2013;1(35):4396–405.
- [387] Gao Y, Zou X, Zhao JX, Li Y, Su X. Graphene oxide-based magnetic fluorescent hybrids for drug delivery and cellular imaging. *Colloids Surf, B* 2013;112:128–33.
- [388] Zhang S, Yang K, Feng L, Liu Z. In vitro and in vivo behaviors of dextran functionalized graphene. *Carbon* 2011;49(12):4040–9.
- [389] Gollavelli G, Ling Y-C. Multi-functional graphene as an in vitro and in vivo imaging probe. *Biomaterials* 2012;33(8):2532–45.
- [390] Kanchanapally R, Viraka Nellore BP, Sinha SS, Pedraza F, Jones SJ, Pramanik A, et al. Antimicrobial peptide-conjugated graphene oxide membrane for efficient removal and effective killing of multiple drug resistant bacteria. *RSC Adv* 2015;5(24):18881–7.
- [391] Stathi P, Gournis D, Deligiannakis Y, Rudolf P. Stabilization of phenolic radicals on graphene oxide: an XPS and EPR study. *Langmuir* 2015;31(38):10508–16.
- [392] Du Z, Ai W, Xie L, Huang W. Organic radical functionalized graphene as a superior anode material for lithium-ion batteries. *J Mater Chem A* 2014;2(24):9164–8.
- [393] Bandyopadhyay P, Park WB, Layek RK, Uddin ME, Kim NH, Kim H-G, et al. Hexylamine functionalized reduced graphene oxide/polyurethane nanocomposite-coated nylon for enhanced hydrogen gas barrier film. *J Membr Sci* 2016;500:106–14.
- [394] Yao Q-L, Cohen A, Petrutik N, Shlomovich A, Burstein L, Pang S-P, et al. Highly insensitive and thermostable energetic coordination nanomaterials based on functionalized graphene oxides. *J Mater Chem A* 2016;4(25):9941–8.
- [395] Dimitrakakis GK, Tyljanakis E, Froudakis GE. Pillared graphene: a new 3-D network nanostructure for enhanced hydrogen storage. *Nano Lett* 2008;8(10):3166–70.
- [396] Haque E, Islam MM, Pourazadi E, Sarkar S, Harris AT, Minett AI, et al. Boron-functionalized graphene oxide-organic frameworks for highly efficient CO₂ capture. *Chem – Asian J* 2017;12(3):283–8.
- [397] Liu F-Q, Li W, Zhao J, Li W-H, Chen D-M, Sun L-S, et al. Covalent grafting of polyethylenimine on hydroxylated three-dimensional graphene for superior CO₂ capture. *J Mater Chem A* 2015;3(23):12252–8.
- [398] Wang D-W, Su D. Heterogeneous nanocarbon materials for oxygen reduction reaction. *Energy Environ Sci* 2014;7(2).
- [399] Zhang L, Niu J, Li M, Xia Z. Catalytic mechanisms of sulfur-doped graphene as efficient oxygen reduction reaction catalysts for fuel cells. *J Phys Chem C* 2014;118(7):3545–53.
- [400] Dou S, Shen A, Tao L, Wang S. Molecular doping of graphene as metal-free electrocatalyst for oxygen reduction reaction. *Chem Commun (Camb)* 2014;50(73):10672–5.
- [401] Bouša D, Jankovský O, Sedmidubský D, Luxa J, Šturala J, Pumera M, et al. Mesomeric effects of graphene modified with diazonium salts: substituent type and position influence its properties. *Chem Eur J* 2015;21(49):17728–38.
- [402] Ahmed MS, Kim Y-B. Amide-functionalized graphene with 1,4-diaminobutane as efficient metal-free and porous electrocatalyst for oxygen reduction. *Carbon* 2017;111:577–86.
- [403] Irannejad L, Ahmadi SJ, Sadjadi S, Shamsipur M. Synthesis of N-hydroxy-imidamide-functionalized graphene: an efficient metal-free electrocatalyst for oxygen reduction. *J Iran Chem Soc* 2017;15(1):111–9.
- [404] Zhong X, Yu H, Zhuang G, Li Q, Wang X, Zhu Y, et al. Pyridyne cycloaddition of graphene: “external” active sites for oxygen reduction reaction. *J Mater Chem A* 2014;2(4):897–901.
- [405] Jahan M, Bao Q, Loh KP. Electrochemically active graphene-porphyrin MOF composite for oxygen reduction reaction. *J Am Chem Soc* 2012;134(15):6707–13.
- [406] Fernández-García L, Blanco C, Blanco C, Álvarez P, Granda M, Santamaría R, et al. Graphene anchored palladium complex as efficient and recyclable catalyst in the Heck cross-coupling reaction. *J Mol Catal A: Chem* 2016;416:140–6.
- [407] Wang R-C, Yin T-L, Wei P-J, Liu J-G. A copper complex covalently grafted on carbon nanotubes and reduced graphene oxide promotes oxygen reduction

- reaction activity and catalyst stability. *RSC Adv* 2015;5(81):66487–93.
- [408] Xi YT, Wei PJ, Wang RC, Liu JG. Bio-inspired multinuclear copper complexes covalently immobilized on reduced graphene oxide as efficient electrocatalysts for the oxygen reduction reaction. *Chem Commun* 2015;51(35):7455–8.
- [409] Kim SK, Jeon S. Improved electrocatalytic effect of carbon nanomaterials by covalently anchoring with CoTAPP via diazonium salt reactions. *Electrochem Commun* 2012;22:141–4.
- [410] You J-M, Han HS, Lee HK, Cho S, Jeon S. Enhanced electrocatalytic activity of oxygen reduction by cobalt-porphyrin functionalized with graphene oxide in an alkaline solution. *Int J Hydrogen Energy* 2014;39(10):4803–11.
- [411] Liu Y, Wu Y-Y, Lv G-J, Pu T, He X-Q, Cui L-L. Iron(II) phthalocyanine covalently functionalized graphene as a highly efficient non-precious-metal catalyst for the oxygen reduction reaction in alkaline media. *Electrochim Acta* 2013;112:269–78.
- [412] Cui L, Liu Y, He X. Iron(II) tetraaminophthalocyanine functionalized graphene: synthesis, characterization and their application in direct methanol fuel cell. *J Electroanal Chem* 2014;727:91–8.
- [413] Liu H, Zhang G, Zhou Y, Gao M, Yang F. One-step potentiodynamic synthesis of poly(1,5-diaminoanthraquinone)/reduced graphene oxide nanohybrid with improved electrocatalytic activity. *J Mater Chem A* 2013;1(44):13902–13.
- [414] Naveen MH, Noh H-B, Hossain MSA, Kim JH, Shim Y-B. Facile potentiostatic preparation of functionalized polyterthiophene-anchored graphene oxide as a metal-free electrocatalyst for the oxygen reduction reaction. *J Mater Chem A* 2015;3(10):5426–33.
- [415] Zhang X, Peng T, Song S. Recent advances in dye-sensitized semiconductor systems for photocatalytic hydrogen production. *J Mater Chem A* 2016;4(7):2365–402.
- [416] Li Z, Chen Y, Du Y, Wang X, Yang P, Zheng J. Triphenylamine-functionalized graphene decorated with Pt nanoparticles and its application in photocatalytic hydrogen production. *Int J Hydrogen Energy* 2012;37(6):4880–8.
- [417] Wang D, Huang J, Li X, Yang P, Du Y, Goh CM, et al. Photocatalytic H₂ production under visible-light irradiation based on covalent attachment of manganese phthalocyanine to graphene. *J Mater Chem A* 2015;3(8):4195–202.
- [418] Xiao B, Zhu M, Li X, Yang P, Qiu L, Lu C. A stable and efficient photocatalytic hydrogen evolution system based on covalently linked silicon-phthalocyanine-graphene with surfactant. *Int J Hydrogen Energy* 2016;41(27):11537–46.
- [419] Huang J, Wu Y, Wang D, Ma Y, Yue Z, Lu Y, et al. Silicon phthalocyanine covalently functionalized N-doped ultrasmall reduced graphene oxide decorated with Pt nanoparticles for hydrogen evolution from water. *ACS Appl Mater Interfaces* 2015;7(6):3732–41.
- [420] Xiao B, Wang X, Huang H, Zhu M, Yang P, Wang Y, et al. Improved superiority by covalently binding dye to graphene for hydrogen evolution from water under visible-light irradiation. *J Phys Chem C* 2013;117(41):21303–11.
- [421] Huang J, Wang D, Yue Z, Li X, Chu D, Yang P. Ruthenium dye N749 covalently functionalized reduced graphene oxide: a novel photocatalyst for visible light H₂ evolution. *J Phys Chem C* 2015;119(50):27892–9.
- [422] Wang D, Huang J, Li K, Zhang C, Du Y, Yang P. A robust and efficient visible light driven photocatalyst for hydrogen evolution based on ruthenium dye N3 covalently immobilized on reduced graphene oxide. *RSC Adv* 2016;6(41):34699–707.
- [423] Ahmed ME, Dey S, Mondal B, Dey A. H₂ evolution catalyzed by a FeFe-hydrogenase synthetic model covalently attached to graphite surfaces. *Chem Commun (Camb)* 2017;53(58):8188–91.
- [424] Ansafi AA, Ahmadi Z, Jafari-Asl M, Rezaei B. Graphene nanosheets functionalized with Nile blue as a stable support for the oxidation of glucose and reduction of oxygen based on redox replacement of Pd-nanoparticles via nickel oxide. *Electrochim Acta* 2015;173:619–29.
- [425] Ansafi AA, Sayed Afuni SA, Rezaei B. NiO nanoparticles decorated at Nile blue-modified reduced graphene oxide, new powerful electrocatalysts for water splitting. *J Electroanal Chem* 2018;816:160–70.
- [426] Zhou X, Zhang T, Abney CW, Li Z, Lin W. Graphene-immobilized monomeric bipyridine-Mx⁺ (Mx⁺ = Fe³⁺, Co²⁺, Ni²⁺, or Cu²⁺) complexes for electrocatalytic water oxidation. *ACS Appl Mater Interfaces* 2014;6(21):18475–9.
- [427] Kumar P, Kumar A, Sreedhar B, Sain B, Ray SS, Jain SL. Cobalt phthalocyanine immobilized on graphene oxide: an efficient visible-active catalyst for the photoreduction of carbon dioxide. *Chem Eur J* 2014;20(20):6154–61.
- [428] Yadav RK, Baeg JO, Oh GH, Park NJ, Kong KJ, Kim J, et al. A photocatalyst-enzyme coupled artificial photosynthesis system for solar energy in production of formic acid from CO₂. *J Am Chem Soc* 2012;134(28):11455–61.
- [429] Yadav RK, Baeg J-O, Kumar A, Kong K-j, Oh GH, Park N-J. Graphene-BODIPY as a photocatalyst in the photocatalytic-biocatalytic coupled system for solar fuel production from CO₂. *J Mater Chem A* 2014;2(14).
- [430] Li Q, Zeng Q, Gao L, Ullah Z, Li H, Guo Y, et al. Self-assembly of urchin-like porphyrin/graphene microspheres for artificial photosynthetic production of formic acid from CO₂. *J Mater Chem A* 2017;5(1):155–64.
- [431] Kumar S, Yadav RK, Ram K, Aguiar A, Koh J, Sobral AJFN. Graphene oxide modified cobalt metallated porphyrin photocatalyst for conversion of formic acid from carbon dioxide. *J CO₂ Util* 2018;27:107–14.
- [432] Yadav D, Yadav RK, Kumar A, Park NJ, Baeg JO. Functionalized graphene quantum dots as efficient visible-light photocatalysts for selective solar fuel production from CO₂. *ChemCatChem* 2016;8(21):3389–93.
- [433] Yadav RK, Lee J-O, Kumar A, Park N-J, Yadav D, Kim JY, et al. Highly improved solar energy harvesting for fuel production from CO₂ by a newly designed graphene film photocatalyst. *Sci Rep* 2018;8(1):16741.
- [434] Kumar P, Sain B, Jain SL. Photocatalytic reduction of carbon dioxide to methanol using a ruthenium trinuclear polyazine complex immobilized on graphene oxide under visible light irradiation. *J Mater Chem A* 2014;2(29):11246–53.
- [435] Kumar P, Bansawal A, Labhsetwar N, Jain SL. Visible light assisted photocatalytic reduction of CO₂ using a graphene oxide supported heteroleptic ruthenium complex. *Green Chem* 2015;17(3):1605–9.
- [436] Park J, Jin T, Liu C, Li G, Yan M. Three-dimensional graphene-TiO₂ nanocomposite photocatalyst synthesized by covalent attachment. *ACS Omega* 2016;1(3):351–6.
- [437] Wang Y, Zhou A, Jiang Y, Chen X, He J. Tetraamino-zinc phthalocyanine covalently bound to benzoic acid-functionalized graphene composites for highly efficient visible light photocatalytic activities. *RSC Adv* 2015;5(47):37823–9.
- [438] Zhao W, Tang Y, Xi J, Kong J. Functionalized graphene sheets with poly(ionic liquid)s and high adsorption capacity of anionic dyes. *Appl Surf Sci* 2015;326:276–84.
- [439] Namvari M, Namazi H. Preparation of efficient magnetic biosorbents by clicking carbohydrates onto graphene oxide. *J Mater Sci* 2015;50(15):5348–61.
- [440] Koklioti MA, Skaltsas T, Sato Y, Suenaga K, Stergiou A, Tagmatarchis N. Mechanistic insights into the photocatalytic properties of metal nanocluster/graphene ensembles. Examining the role of visible light in the reduction of 4-nitrophenol. *Nanoscale* 2017;9(27):9685–92.